Wavelet Analysis of Extreme Wind Loads on Low-Rise Structures

by

Isam M. Janajreh

Dissertation submitted to the Faculty of the
Virginia Polytechnic Institute and State University
in partial fulfillment of the requirements for the degree of

Doctor of Philosophy

in

Engineering Mechanics

Prof. Muhammad R. Hajj , Chairman

Prof. Henry W. Tieleman

Prof. Dean T. Mook

Prof. Robert E. Heller

Prof. Saad A. Ragab

Prof. Werner Kohler

January 29, 1998
Blacksburg, Virginia

Keywords: wind loads, pressure coefficients, turbulence intensities, turbulence scales,
wavelets, higher-order statistics, intermittency

Wavelet Analysis of Extreme Wind Loads on Low-Rise Structures

by

Isam Mustafa Janajreh

Committee Chairman: Prof. Muhammad R. Hajj

Engineering Science and Mechanics

(ABSTRACT)

Over the past thirty years, extensive research has been conducted with the objective of reducing wind damage to structures. Wind tunnel simulations of wind loads have been the major source of building codes. However, a simple comparison of pressure coefficients measured in wind tunnel simulations with full-scale measurements show that the simulations, in general, underpredict extreme negative pressure coefficients. One obvious reason is the lack of consensus on wind tunnel simulation parameters.

The wind in the atmospheric surface layer is highly turbulent. In simulating wind loads on structures, one needs to simulate the turbulent character besides satisfying geometric and dynamic similitudes. Some turbulence parameters that have been considered in many simulations include, turbulence intensities, integral length scales, surface roughness, and frequency spectrum. One problem with these parameters is that they are time varying in the atmospheric boundary layer and their averaged value, usually considered in the wind tunnel simulations, cannot be used to simulate pressure peaks.

In this work, we show how wavelet analysis and time-scale representation can be used to establish an intermittency factor that characterizes energetic turbulence events in the atmospheric flows. Moreover, we relate these events to the occurrence of extreme negative peak pressures.

(DEDICATION)

To whom I indebted the most, my family: my parents, Mustafa and Nadida; my sisters Hifa, Wafiqa, Nawal, Wafa', Zenab and Mariam; my brothers Ibrahim, Husam, Hisham and little Wesam; my beloved grandparents Muneira and Ahmad and to my long life partner, my wife, Asimah.

(ACKNOWLEDGMENTS)

I would like to thank my advisor Dr. Muhammad R. Hajj, without his help and constructive comments this work would not have materialized. I thank him for his teaching, his guidance and his reassurance and encouragement. Being his first graduate student gave me the opportunity of experiencing hard work. For this, I deeply thank him. My thanks extend to Dr. Henry W. Tieleman whose experience, hard work and help are greatly acknowledged. His scientific approach, strong comments and constructive ideas have left a positive impact on this work. I also extend my great gratitude to Dr. Saad A. Ragab who taught me my first course in turbulence and who never stopped clarifying and explaining many stumbling points in turbulence. Thanks are also extended to Dr. Robert E. Heller, for his advice throughout my course work and his outstanding teaching. I would like to also thank Dr. Dean T. Mook and Dr. Werner Kohler for their valuable teaching, advising and service on my graduate committee.

I am greatfull to both Dr. T. A. Reinholtd, of Clemson University for providing the model wind tunnel data and Dr. Kishor C. Mehta of Texas Tech University for providing the full scale experimental building data. The financial support for this work from the National Science Foundation under Grant # CMS9412905 is greatly acknowledged.

Contents

List of Figures

List of Tables

Chapter 1

Introduction

1.1 Motivation

The consequences of wind-related disasters that occur in the United States are severe. Such disasters can result in deaths, injuries, property losses, and have a negative impact on the economy. According to the American Association for Wind Engineering (AAWE), the losses caused by high-speed winds, hurricanes and tornadoes, exceeds losses caused by other natural hazards such as earthquakes and floods. Between 1986 and 1993 the estimated losses caused by extreme wind events totaled $41 billion. Based on the National Weather Service [NWS,1992], wind events in 1990 resulted in 124 deaths, 1814 personnel injuries and approximately $1.2 billion in property losses. Hurricane Andrew alone caused 55 deaths in 1992. Another 250,000 persons were left homeless and insured property losses were estimated at $16.5 billion [NIST, 1995]. An example of the severity of damage and losses that can be caused by wind-related disasters in one year is seen in Table 1.1 which shows the insured losses in 1992 as reported by Steinmetz [1993]. These facts serve as evidence of the extreme vulnerability of property, infrastructure and economy in the U.S. to damaging winds.

Based on post-storm evaluation of damage and losses, low-rise structures such as homes, schools and churches are considered the most vulnerable structures according to the AAWE. In the past thirty years, an extensive number of research studies has been conducted to mitigate the wind damage of low-rise structures. The results of many of these studies have found their way into the codes and played an important role in reducing the extent of damage.

Table 1.1: Insured losses in the U.S. in 1992

Wind events	Corresponding insurance losses
Hurricane Andrew	\$16.5 billion
Hurricane Iniki	\$1.6 billion
April storm in Texas and Oklahoma	\$775 million
December storm in the Northeast	\$650 million

However, further improvements are needed in order to reduce the losses. For example, a simple comparison of wind tunnel simulations, code requirements, and full-scale measurements of extreme negative pressure coeffecients near roof corners, roof ridges and leading roof edges shows large discrepancies. The major reason being the lack of consensus on the required wind tunnel simulation parameters, on analysis methods, and on models for design/prediction of wind loads. Such a consensus has been hard to obtain because of the many variables and methods of analysis involved in determining these extreme wind loads. In general, simulating flow parameters such as Reynolds number, turbulence intensities, integral length scales, and roughness parameters have not effeciently improved the prediction of the extreme suction pressures on roofs. Moreover, proposed theoretical models, i.e. strip and quasi steady theories, have failed to predict these extreme pressure coefficients and associated wind loads. This is especially true in the important regions of separation and vortex formation where extreme negative pressure peaks occur.

1.2 Objective

The ultimate goal of this work is to assist in the mitigation against damage to low-rise structures caused by extreme wind storms. Such a goal is achievable if (1) turbulent events in atmospheric wind can be adequately characterized and simulated in wind tunnel model experiments and if (2) a far-field velocity-pressure relation that adequately predicts the low-pressure peaks can be determined. Consequently, characterizing atmospheric turbulence and relating low-pressure coefficients to certain turbulence scale characteristics in the atmospheric boundary layer are the primary objectives of the proposed work. The current models

and descriptions of atmospheric turbulence and the velocity-pressure relation are based on Fourier-domain analysis techniques that have several shortcomings. These shortcomings result from the fact that temporal information is not preserved and that computation of spectral moments requires averaging over many segments, i.e. time periods. In this work, we will discuss these shortcomings and show how they can be overcome by using wavelet analysis. The reason being that wavelet analysis preserves both time and scale information. Based on the wavelet representation, we will be able to examine energetic turbulence events and define an intermittency factor for those events. The time-scale representation will also allow us to trace pressure peaks, that cause extreme wind loads, and relate them to energetic turbulence scales.

All of the results presented here are based on analysis of full scale velocity and pressure measurements obtained from the Wind Engineering Research Field Laboratory (WERFL) at Texas Tech University and on model studies of the Texas Tech Building in the boundary layer wind tunnel at Clemson University. In chapter 2, a brief description of both facilities is given. In chapter 3, the shortcomings of the current simulation parameters are presented. In chapter 4, some shortcomings of the quasi-steady approach for prediction of pressure coefficients from velocity fluctuations are also presented. Because the improvement of the simulation parameters and the analysis procedure are based on the use of wavelet theory, definition of wavelets and pertaining examples are presented in chapter 5. In chapter 6, the intermittency character of turbulence scale in the atmospheric boundary layer is quantified. In chapter 7, it is shown how the extreme negative low-pressure coefficients observed on the roof of the WERFL experimental building are actually related to the intermittent yet energetic events in the incident flow, i.e. the atmospheric surface layer.

Chapter 2

Experimental Setups

Full-scale and related wind tunnel measurements of both pressure and velocity fluctuations are analyzed in this work. In this chapter, the experimental field facility at Texas Tech and the wind tunnel at Clemson University and their associated data acquisition and measurements parameters are described.

2.1 Full Scale Measurements

The full scale data were taken at the Wind Engineering Research Field Laboratory (WERFL) at Texas Tech University. The WERFL facility consists of a metal flat-roof test building and a 49.0m high meteorological tower. The building is mounted on a rigid frame undercarriage on four wheels which allows it to be rotated and to set the building at any azimuth angle relative to the oncoming wind (i.e. perpendicular or oblique). A schematic plan of the building is shown in figure 2.1. The building is equipped with several pressure taps on the roof and along the walls that are connected to differential pressure transducers, each offering a flat frequency response up to 200Hz. Cup-vane anemometers and propeller anemometers are used to measure the velocity at six different elevations. Two sets of cup-vane anemometers are mounted at 4.0 and 49.0m and single cup anemometers are located at 1.0 and 21.0m. Two UVW-propellers are located at 2.5 and 10.0m. These flow measuring devices are limited in their frequency response to about 2Hz and their output was sampled at 10Hz. It is

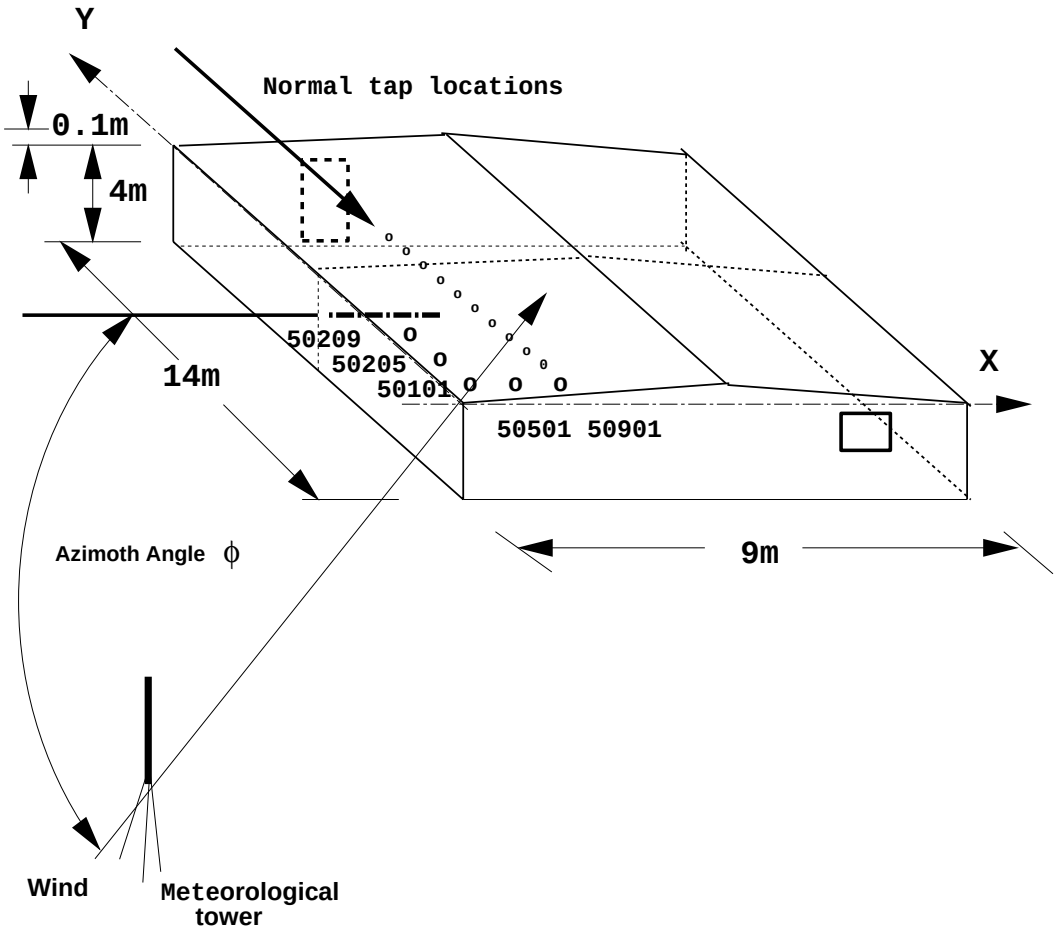

Figure 2.1: Schematic illustration of the WERFL building.

important to note that the vane in the cup-vane anemometer does not follow wind direction changes exactly, but overshoots at times thereby giving erroneous measurements of the wind direction. For a detailed description of the WERFL experimental facility, the reader is referred to Levitan et al. [1992a&b]. The terrain around this experimental facility is flat and open up to 900m radius. Measurement of velocity components and pressure fluctuations are conducted simultaneously for 15 minutes at 10Hz and 40Hz sampling rates, respectively. To establish simultaneous observations of pressure and velocity, the measured pressure were digitally sampled at 10Hz by limiting these observations to those instants for which velocity data are available.

2.2 Wind Tunnel Measurements

Flow simulation and pressure data were obtained from the boundary layer wind tunnel located at the Wind Load Test Facility at Clemson University. The wind tunnel is an open-return type and the test section is 21m long, 3m wide and 2m high. Wind speeds up to 14m/s can be generated by using two blowers. The model experiments were performed on a surface mounted prism with dimensions of 27.5x18.4x8.5cm. This prism is a 1/50 scale model of the (WERFL) experimental building. Although several flow configurations can be employed to simulate the lower part of the atmospheric boundary layer, only two wind tunnel configurations are considered here. In the first configuration, a conventional roughness fetch is used and in the other configuration additional five small spires were placed directly upstream of the model. It has been suggested by Tieleman [1992] and others that a better simulation of the horizontal turbulence intensities and enhancement of their small-scale turbulence content can provide a better prediction of pressure peaks. The first configuration will be referred to as the case without spires and the second as the case with spires.

The pressure measuring instrumentation consists of Setra model differential transducers that are connected to Scanivalve pressure switches. The velocity measurements were taken with standard hot-wire anemometry. The velocity was measured 0.9m upstream from center of the prism which corresponds to the scaled location of the meteorological tower at WERFL. All pressure measurements were taken at the prism's top surface. Both velocity and pressure fluctuations were simultaneously sampled at a rate of 250Hz. Additionally, velocity components data sampled at 2000Hz were used to study the turbulence of the wind tunnel and the influence of the spires on the flow simulation. The later measurements were conducted at the location of the model's center location after the model was taken out from the wind tunnel. Table 2.1 lists the location of the pressure taps on both the model's roof and the WERFL experimental building. The full scale model tap designation is a 5-digit numerate. The first digit 5, is used to designate measurements on the roof of the building. The second two digits indicate the x-coordinate and the last two digits indicate the y-coordinate, both rounded off to the nearest foot. The equivalent SI dimensions are also given in the same table.

Table 2.1: Location of pressure taps on WERFL building and its model.

Tap	WERFL tap locations			Model's tap locations	
	designation #	x (m)	y (m)	x (mm)	y (mm)
1	50900	2.64	0.15	52.8	3.0
2	50901	2.64	0.36	52.8	7.2
3	50902	2.64	0.66	52.8	13.2
4	50903	2.67	0.97	53.4	19.4
5	50904	2.64	1.27	52.8	25.4
6	50905	2.64	1.58	52.8	31.6
7	50907	2.69	2.18	53.8	43.6
8	50909	2.69	2.79	53.8	55.8
9	50913	2.64	4.01	52.8	80.2
10	50918	2.64	5.54	52.8	110.8
11	50923	2.64	7.06	52.9	141.2
12	50101	0.36	0.36	7.2	7.2
13	50901	2.64	0.36	52.8	7.2
14	50209	0.56	2.79	11.2	55.8
15	50501	1.42	0.36	28.4	7.2
16	50205	0.56	1.58	11.2	31.6
17	50509	1.42	2.79	28.4	55.8

Chapter 3

Discussion of Current Analysis and Simulation Procedures of the Atmospheric Turbulence

Wind tunnel model simulations of wind loads have been the primary source for establishing building code provisions. However, a simple comparison of extreme negative pressure coefficients from these simulations and those observed in full-scale measurements show large discrepancies. The major reason behind these discrepancies lies in the fact that matching all flow parameters of the atmospheric boundary layer in the wind tunnel is not easy. This is due to several limitations. In this chapter, we will discuss the simulation parameters that are currently used, their estimation procedures and their shortcomings. These parameters include the mean flow Reynolds number, turbulence intensities, integral length scales, large- and small-scale turbulence, aerodynamic roughness, and spectra of velocity components of the wind.

3.1 Mean Flow Reynolds Number

The difficulty of simulating the mean flow Reynolds number stems from geometric limitations. The full-scale value of the Reynolds number for WERFL field experiment is about $3x10^6$. For extreme wind conditions, this value could increase up to $1.5x10^7$. Thus, for a

1:100 scaled model, the mean flow should be one hundred times as fast as the mean flow of the prototype to satisfy Reynolds number equality. This is not feasible because of compressibility effects and power requirements. The other option is to increase the scale of the model, which requires an extremely large wind tunnel facility. One of the largest facilities where relatively high Reynolds numbers can be obtained is the wind tunnel at Monash University in Melbourne, Australia. Its test section is 12m wide, 4m high and 40m long. In this facility, and for a 1:10 scaled model of the WERFL experimental building, a Reynolds number which is 5 to 10 times larger than the Reynolds number in other wind-tunnels can be achieved. Yet, measurement of the pressure coefficients at the critical locations of flow separation and vortex formation still showed large discrepancies when compared to field results. This is most likely due to the fact that, besides the inability to match full-scale Reynolds number, there is the problem of simulating the turbulence content of the atmospheric wind. This issue is considered in sections 3.2 and 3.4.

3.2 Turbulence Intensities

The local turbulence intensities are defined as

$$\begin{aligned} I_u &= \{\frac{1}{N}\sum_{i=0}^{N-1} {u_i}^2\}^{\frac{1}{2}} /U, \\ I_v &= \{\frac{1}{N}\sum_{i=0}^{N-1} {v_i}^2\}^{\frac{1}{2}} /U, \\ I_w &= \{\frac{1}{N}\sum_{i=0}^{N-1} {w_i}^2\}^{\frac{1}{2}} /U \end{aligned} \tag{3.1}$$

where u, v and w are the fluctuating components of the longitudinal, lateral and vertical velocity components, and U is the local streamwise mean velocity measured at a given height z. Prior to 1990, most wind tunnel simulations focused on duplicating only the longitudinal turbulence intensity. Recent experimental studies strongly suggest that the turbulence intensity of the lateral component is as important Tieleman [1994]. While simulation of these parameters is important, there are two problems. The first problem is that the levels of turbulence intensities could vary rapidly with time. As an example, Table 3.1 shows the

turbulence intensities for the u- and v- wind velocity components measured at Texas Tech between 9:15 a.m. and 2:13 p.m. on February 14^{th} 1992. These intensities were calculated using sampling times of length 820, 410, 205 and 137 seconds. In general, as expected, both intensities decreases with height since the source of turbulence, namely, surface friction has a lesser effect. Moreover, these intensities decrease with the sampling time. It is also clear from these measurements that the turbulence intensities could vary by about 25% for records taken about three hours apart. In wind tunnels, fetch roughness and spires as well as other roughness elements have been used to match the average levels of turbulence intensities observed in the field. The second problem with simulating turbulence intensities is the ability to simulate the distribution of the energy among the different scales. This issue is considered in section 3.4.

3.3 Integral Length Scales

One parameter that has been proposed for characterizing atmospheric turbulence is the integral length scale L_{uu} which represents the average size of the energy containing eddies. By one definition, the integral length scale is proportional to the spectral density function of the velocity fluctuations at zero frequency. This function can be calculated from the auto-correlation function at a fixed point by the following relation

$$S_(\omega) = 4 \int_0^\infty R_{uu}(\tau) cos(\omega\tau) d\tau \tag{3.2}$$

where $R_{uu}(\tau)$ is the auto-correlation function for time delay τ. As ω approaches zero, the spectrum function, $S_{uu}(0)$ becomes

$$S_{uu}(0) = 4 T_{uu} \sigma_{uu}^2 \tag{3.3}$$

where T_{uu} is the integral time scale and σ_{uu}^2 is the variance of the longitudinal velocity fluctuations. With the assumption of frozen turbulence, the integral length scale can be estimated from the integral time scale as

$$L_{uu} = T_{uu} U \tag{3.4}$$

Table 3.1: Variation of turbulence intensities with time height for different segment lengths.

Run(date)	U, m/s	z, m	I_u				I_v			
			820s	410s	205s	137s	820s	410s	205s	137s
430-09:18	8.36		21.6	21.5	20.3	20.8	15.9	13.9	13.6	13.6
432-09:57	9.83		20.7	20.3	20.3	19.7	14.6	14.5	14.1	13.6
437-10:46	10.15		22.1	21.4	21.2	20.9	14.7	14.5	14.3	14.0
438-11:06	11.09	2.5	20.0	20.0	19.9	19.2	15.8	15.7	14.3	13.8
440-13:04	9.57		18.3	17.9	17.4	17.6	13.2	13.1	12.9	12.8
441-13:24	9.61		19.5	17.8	17.5	16.5	14.7	13.2	13.1	13.0
442-13:43	10.06		19.3	19.2	17.0	16.1	14.5	13.7	13.6	13.2
430-09:18	8.99		20.9	20.9	19.7	20.1	17.4	15.8	15.3	15.4
432-09:57	10.68		20.1	19.7	19.6	19.0	16.1	16.1	15.7	15.4
437-10:46	11.00		21.2	20.4	20.3	19.9	16.6	16.4	16.3	16.0
438-11:06	12.11	4.5	19.3	19.3	19.3	18.6	17.0	16.8	15.4	15.0
440-13:04	10.37		17.5	16.9	16.5	16.6	14.6	14.5	14.4	14.2
441-13:24	10.33		19.5	17.7	17.4	16.3	15.9	14.5	14.4	14.2
442-13:43	10.73		19.1	19.1	16.6	15.7	15.5	14.6	14.5	14.2
430-09:18	10.46		19.5	19.5	18.4	18.4	14.1	12.4	11.8	11.8
432-09:57	12.43		18.7	18.0	17.9	17.5	11.7	11.7	11.2	10.9
437-10:46	12.87		19.4	18.3	18.2	17.9	13.1	13.0	12.8	12.7
438-11:06	14.31	10.0	17.3	17.3	17.2	16.5	14.2	14.0	12.9	12.3
440-13:04	11.98		15.1	14.4	13.7	13.9	11.0	10.9	10.8	10.6
441-13:24	11.58		18.1	16.6	16.3	15.5	13.7	12.2	12.1	12.0
442-13:43	11.85		17.5	17.4	15.0	14.1	13.1	12.0	11.9	11.8
430-09:18	13.68		15.4	15.3	14.4	14.8	12.2	10.5	10.1	10.0
432-09:57	16.41		14.1	13.0	12.9	12.5	10.6	10.6	9.9	9.6
437-10:46	17.08		15.0	14.8	14.6	14.3	10.7	10.7	10.5	10.3
438-11:06	18.95	49.0	12.7	12.7	12.6	12.5	12.1	11.5	9.9	9.2
440-13:04	15.15		15.4	14.2	13.3	13.2	11.2	11.1	11.0	10.7
441-13:24	14.71		14.4	13.3	13.0	12.4	11.1	9.9	9.8	9.3
442-13:43	14.53		14.9	14.9	12.0	11.2	11.5	10.8	10.7	10.6

where U is the mean velocity. By substitution, the integral length scale can be obtained from

$$L_{uu} = \frac{US_{uu}(0)}{4\sigma_{uu}^2}. \tag{3.5}$$

In the same manner, one can obtain the lateral and vertical integral length scales.
From the above discussion, it is obvious that the integral length scale depends on the properties of the auto-correlation function at large lags or on the low-frequency components. Streamwise and lateral integral length scales were calculated for velocity records obtained between 9:45 a.m. and 2:13 p.m. at WERFL on February 14^{th} 1992. The results, presented in Table 3.2, illustrate how the length scale can vary by about 200% when using segments lengths of varying durations. Consequently, establishing an integral length scale value for simulation in a wind tunnel test is at least a questionable exercise.

3.4 Small and Large Turbulence Scales

Besides the fact that atmospheric flow is time-varying and the integral length scale varies with segment length and number of averages, experimental evidence has shown that the magnitude of surface pressure is also affected by the distribution of energy among the turbulence scales, namely, the large and small scales. Tieleman and Akins [1996] explained that extreme suction pressures are attributable to the proximity and strength of vortices which are generated by the roll-up of separated shear layers. Because small-scale turbulence controls shear layer development, it must be concluded that this turbulence must also play an important role in controlling the pressures beneath these shear layers. Consequently, both large-scale and small-scale turbulence need to be simulated which is not an easy task. The reason being that the relative ratio of energy of small scales and large scales cannot be easily maintained. Figure 5.5 of Tennekes and Lumley [1982] shows that the Reynolds number based on the integral length scale, Re_L, varies linearly with turbulence Reynolds number, $Re{=}zu^*/\nu$, which is based on height z and friction velocity u^*. On the other hand, the Reynolds number associated with small scales, $Re_l{=}lu^*/\nu$ is proportional to $Re^{\frac{1}{4}}$. For typical values of turbulence Reynolds numbers in the atmosphere and wind tunnel simulations,

Table 3.2: Variation of integral length scales with height for different segment lengths.

Run(date)	z, m	L_{uu}, m				L_{vv}, m			
		820s	410s	205s	137s	820s	410s	205s	137s
430-09:18	2.5	81	80	56	63	384	33	26	25
432-09:57		118	99	100	57	46	45	30	23
437-10:46		122	71	67	64	58	52	45	20
438-11:06		89	89	81	48	297	287	57	34
440-13:04		67	44	32	33	47	45	37	29
441-13:24		280	103	91	56	154	67	65	42
442-13:43		235	236	79	51	103	68	65	54
430-09:18	4.5	95	95	66	71	344	54	23	23
432-09:57		132	107	108	63	42	40	26	20
437-10:46		151	83	80	75	49	43	35	18
438-11:06		88	88	85	51	319	288	44	30
440-13:04		113	46	35	36	54	47	39	26
441-13:24		326	134	123	85	165	66	66	39
442-13:43		275	276	101	67	100	68	65	55
430-09:18	10.0	124	124	90	86	566	103	43	43
432-09:57		197	138	135	113	114	107	44	32
437-10:46		227	120	118	110	69	61	35	31
438-11:06		148	147	145	54	374	338	93	53
440-13:04		176	95	45	54	84	70	60	44
441-13:24		366	189	184	142	254	74	69	50
442-13:43		327	327	115	81	123	75	71	63
430-09:18	49.0	176	168	138	139	787	118	60	56
432-09:57		407	256	220	190	247	246	59	48
437-10:46		255	237	218	190	76	74	36	32
438-11:06		174	174	170	148	814	678	118	43
440-13:04		490	212	173	173	173	144	120	90
441-13:24		556	232	222	144	418	188	162	89
442-13:43		484	475	188	155	289	94	89	80

the turbulence scale ratio, L/l, for the atmosphere is several orders of magnitude larger than that of the simulated flow. This inequality leads to suppression of small-scale turbulence relative to large-scale turbulence. Consequently, Tieleman [1992] proposed increasing the energy of small scales. This is can be achieved by adding spires in the wind tunnel roughness configurations. The results of the work by Tieleman et al. [1992] show that introducing small scales results in improvement of prediction of peak pressure coefficients observed in full scale measurements. However, it is still hard to maintain a duration period for these peaks that is comparable with observed full-scale durations.

3.5 Aerodynamic roughness

The atmospheric boundary layer can be divided into two regions. The lowest is the surface layer region, about 50-100 m height, that is insensitive to the earth rotation and characterized by approximately a constant shear stress. For a near neutrally buoyant atmosphere, the turbulence scales in this region are primarily determined by terrain roughness. The second region extends above the surface layer, up to a height of approximately 1000 m. This region is characterized by vanishing turbulence shear stresses at the upper boundary. The flow in this outer layer is affected by earth's rotation as well as the terrain roughness. Above the atmospheric boundary layer is the free atmosphere where surface friction does not affect the wind. As far as wind loads on low-rise structures is concerned, the surface layer region is the important part. By matching the mean flow of the inner and outer regions of the atmospheric boundary layer, a logarithmic velocity profile can be derived without the assumption of a constant shear stress [Kamail et al. 1994]. This profile is given by:

$$U(z) = \frac{u_*}{k} ln(\frac{z}{z_o}) \tag{3.6}$$

where k is a non-dimensional parameter, known as the von Karman constant, which is equal to 0.4 for the atmospheric boundary layer. In this equation, the constant of integration, z_0, is defined as the aerodynamic roughness. Based on the above equation, recording the wind velocity at two different heights is all that is needed to calculate z_0. By letting $z_r = \sqrt{z_1 * z_2}$ and denoting the mean of the velocities at z_1 and z_2 by $U_r = (U_1 + U_2)/2$, one obtains z_o as

$$z_o = z_r \exp -k u_r(z)/u_* \tag{3.7}$$

Table 3.3: Variation of friction velocity and roughness length with reference heights.

Run(date)	U, m/s				u_*, m/s			z_o, m		
	2.5	4.0	10.0	49.0	$u_{*2.5/4}$	$u_{*2.5/10}$	$u_{*2.5/49}$	$z_{o2.5/4}$	$z_{o2.5/10}$	$z_{o2.5/49}$
430-09:18	8.36	8.99	10.46	13.68	0.514	0.595	0.711	0.012	0.011	0.007
432-09:57	9.83	10.68	12.43	16.41	0.702	0.733	0.876	0.029	0.028	0.020
437-10:46	10.15	11.00	12.87	17.08	0.697	0.769	0.925	0.024	0.022	0.015
438-11:06	11.09	12.12	14.31	18.95	0.845	0.908	1.051	0.043	0.041	0.030
440-13:04	9.57	10.37	11.98	15.15	0.662	0.680	0.747	0.025	0.024	0.021
441-13:24	9.61	10.33	11.58	14.71	0.590	0.554	0.680	0.012	0.012	0.009
442-13:43	10.06	10.73	11.85	14.53	0.554	0.505	0.599	0.005	0.006	0.005

Table 3.3 shows the variations of the friction velocity and aerodynamic roughness length at different heights. The results show significant variations of the roughness length with time, i.e. between 0.005 and 0.043 m over two hours period. This is most likely due to the fact that using velocity observations at two heights is not adequate for estimating z_o. More observations would be needed for an accurate prediction of the roughness parameter, provided also that the atmospheric flow is neutrally buoyant.

Some wind engineers have assumed that the reproduction of the ratio of building height to aerodynamic roughness length, h/z_o, which is referred to as the Jensen Number, is adequate to simulate wind loads on low-rise structures. It is obvious that such a parameter does not guarantee the simulation of turbulence at corresponding heights. Consequently, there is a problem with the use of aerodynamic roughness as a simulation parameter.

3.6 Frequency spectrum of velocity components

It is generally thought that simulating the turbulence in the atmosphere can also be achieved by simulating its frequency spectrum. This is very attractive because obtaining the frequency spectrum of the velocity fluctuations is rather trivial. However, because wind turbulence is in general nonstationary, the spectral estimate is time dependent and frequency components could contribute to other components. Figures 3.1 through 3.8 show the spectra of the longitudinal and lateral velocity components computed over time durations of 15 minutes at heights of 2.5m, 4.0m, 10.0m and 49m respectively. These are the records taken between 9:45

a.m. and 2.13 p.m on February 14^{th} 1992. Along with the measured spectra, the theoretical blunt spectrum function, as proposed by Tieleman [1993] is presented. The average spectrum over a period of two hours is also plotted. The results clearly show that the spectrum is a function of time and averaging over a period of two hours is needed to obtain an estimate of the spectrum that is approximately in agreement with the blunt model. One problem with such velocity spectra is that they cannot be related to peak pressure coefficients observed over few seconds.

In this chapter we have shown how currently used time and frequency domain parameters of the atmospheric boundary layer have limitations. These limitations are due to the fact that many of these parameters are time-dependent. Consequently, records obtained over long periods are needed to obtain good estimates. Unfortunately, such estimates can not be used to predict or simulate peak pressure coefficients that take place over short time intervals of only a few seconds.

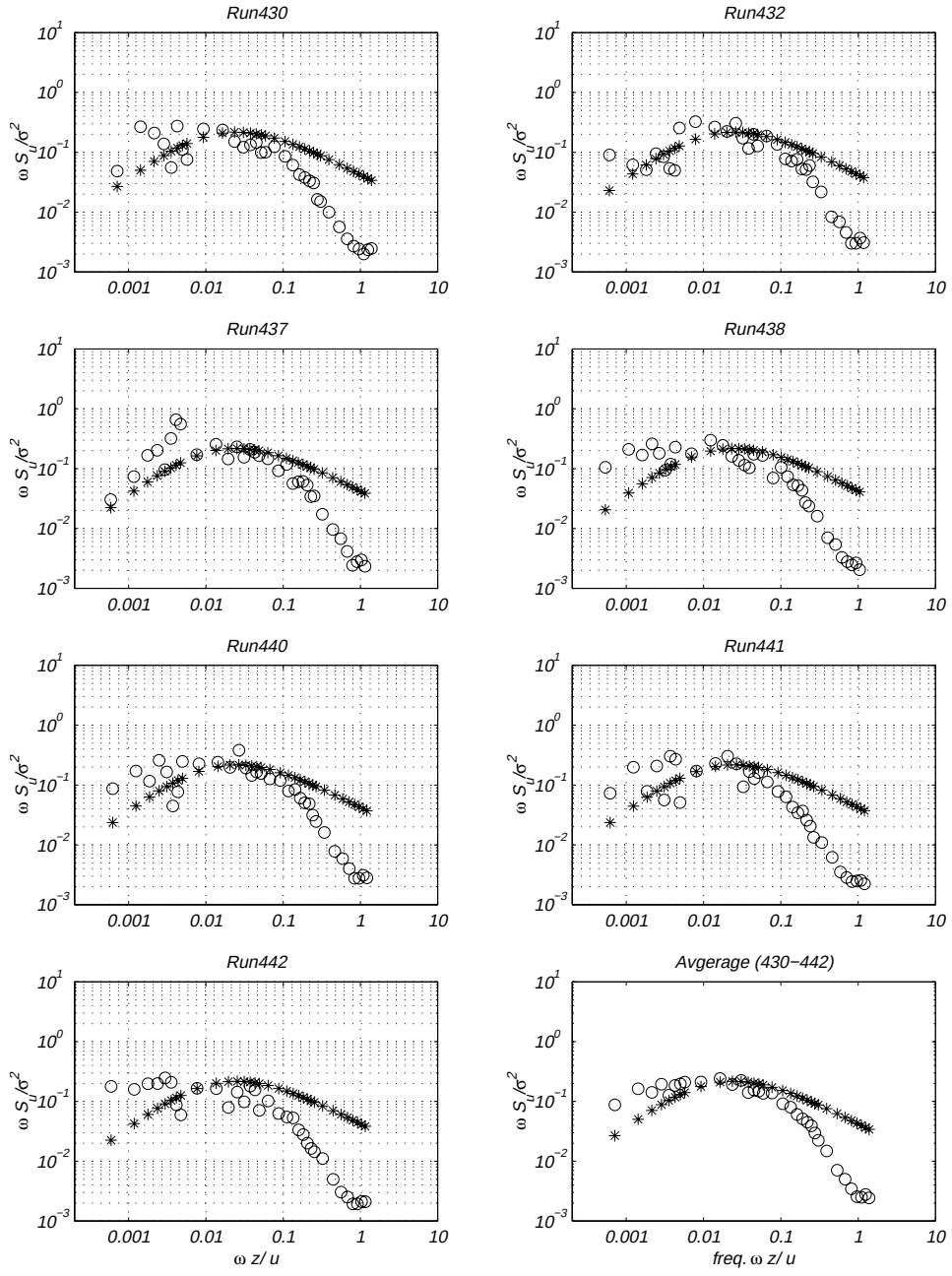

Figure 3.1: Spectra of the $u-$component of the velocity fluctuations at 2.5m height (Runs 430-442). o- Measured spectrum, $*$- theoretical blunt body spectrum [Tieleman, 1995].

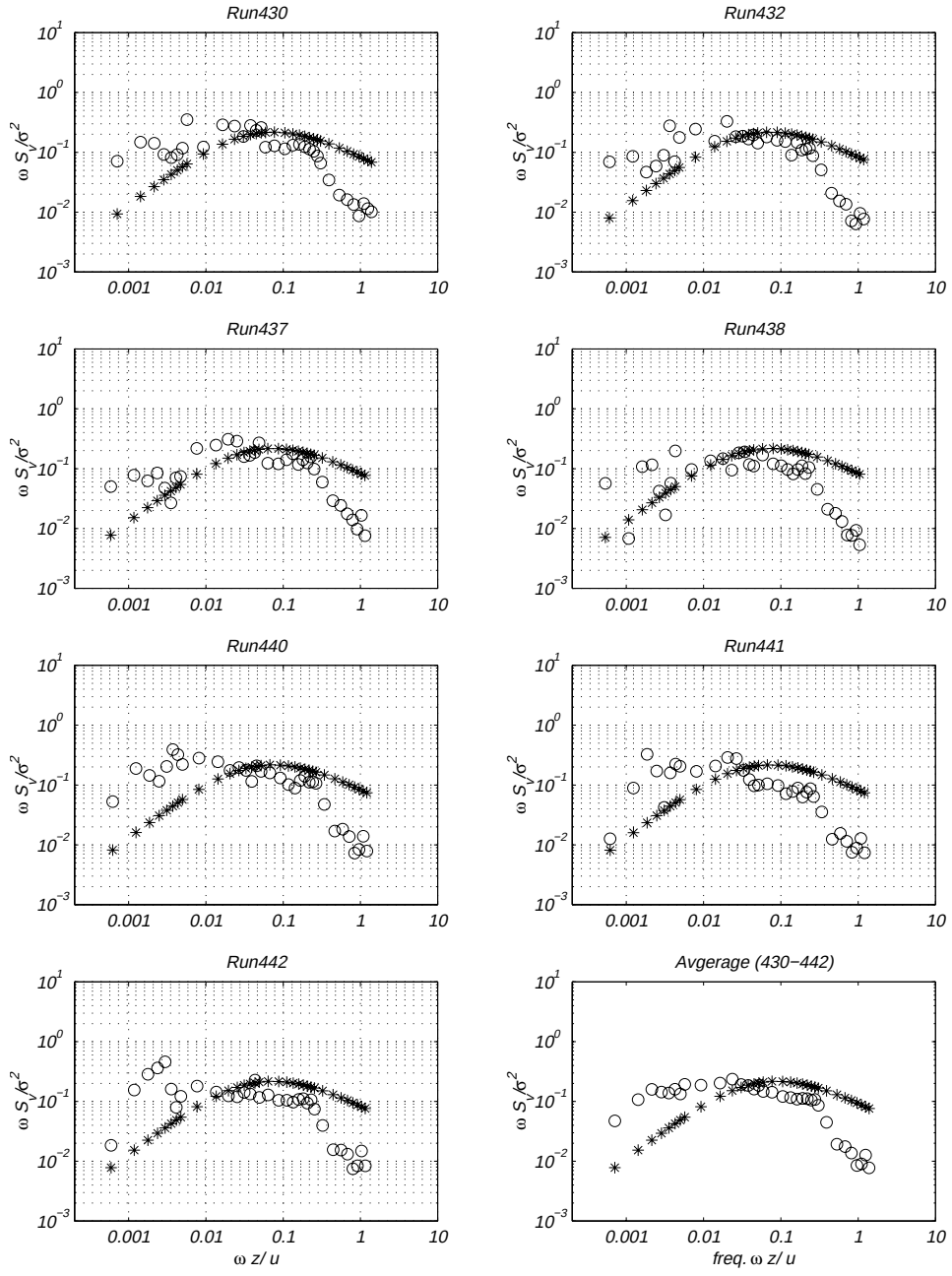

Figure 3.2: Spectra of the $v-$component of the velocity fluctuations at 2.5m height (Runs 430-442). o- Measured spectrum, $*$- theoretical blunt body spectrum [Tieleman, 1995].

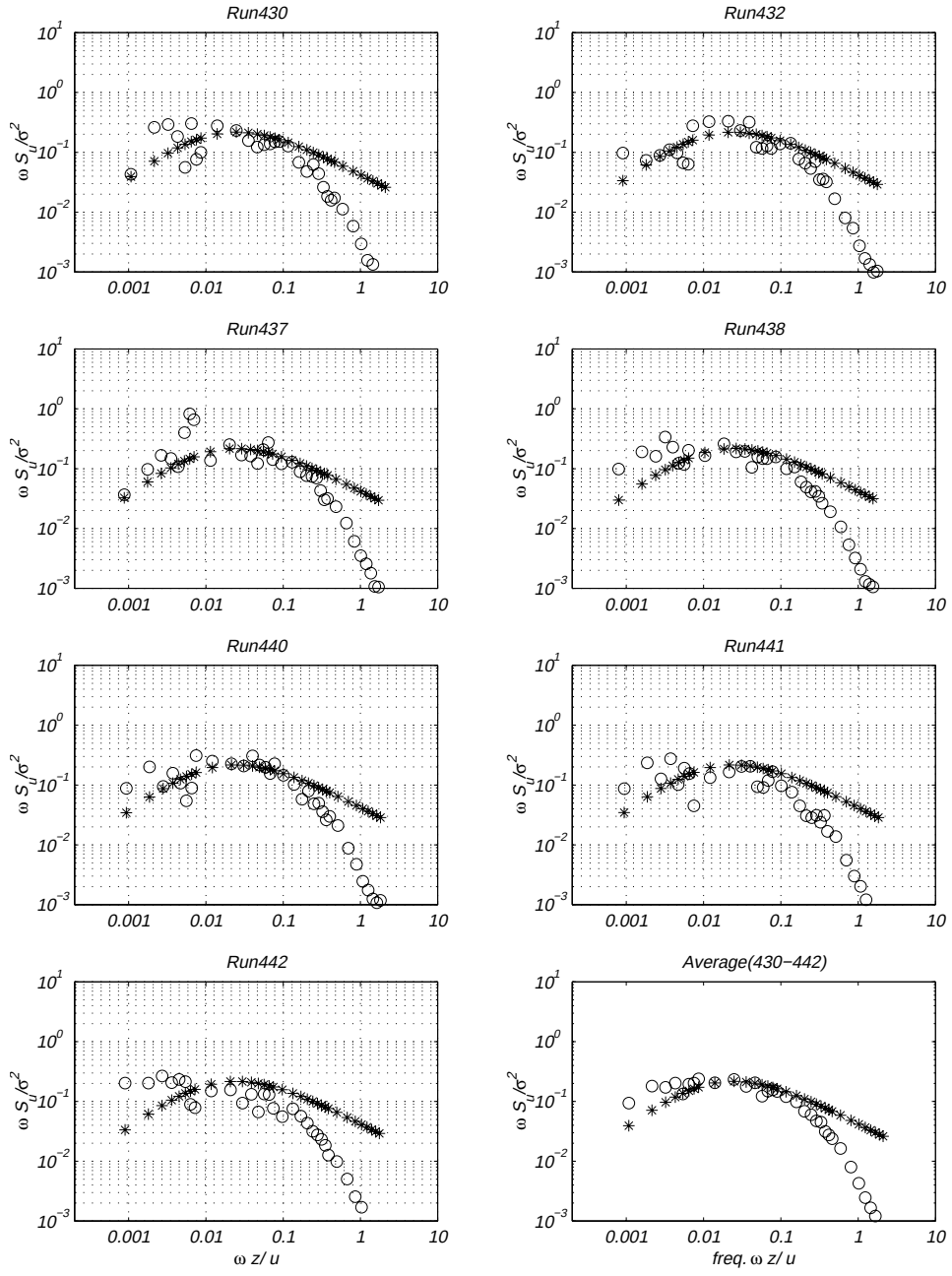

Figure 3.3: Spectra of the $u-$component of the velocity fluctuations at 4.0m height (Runs 430-442). o- Measured spectrum, $*$- theoretical blunt body spectrum [Tieleman, 1995].

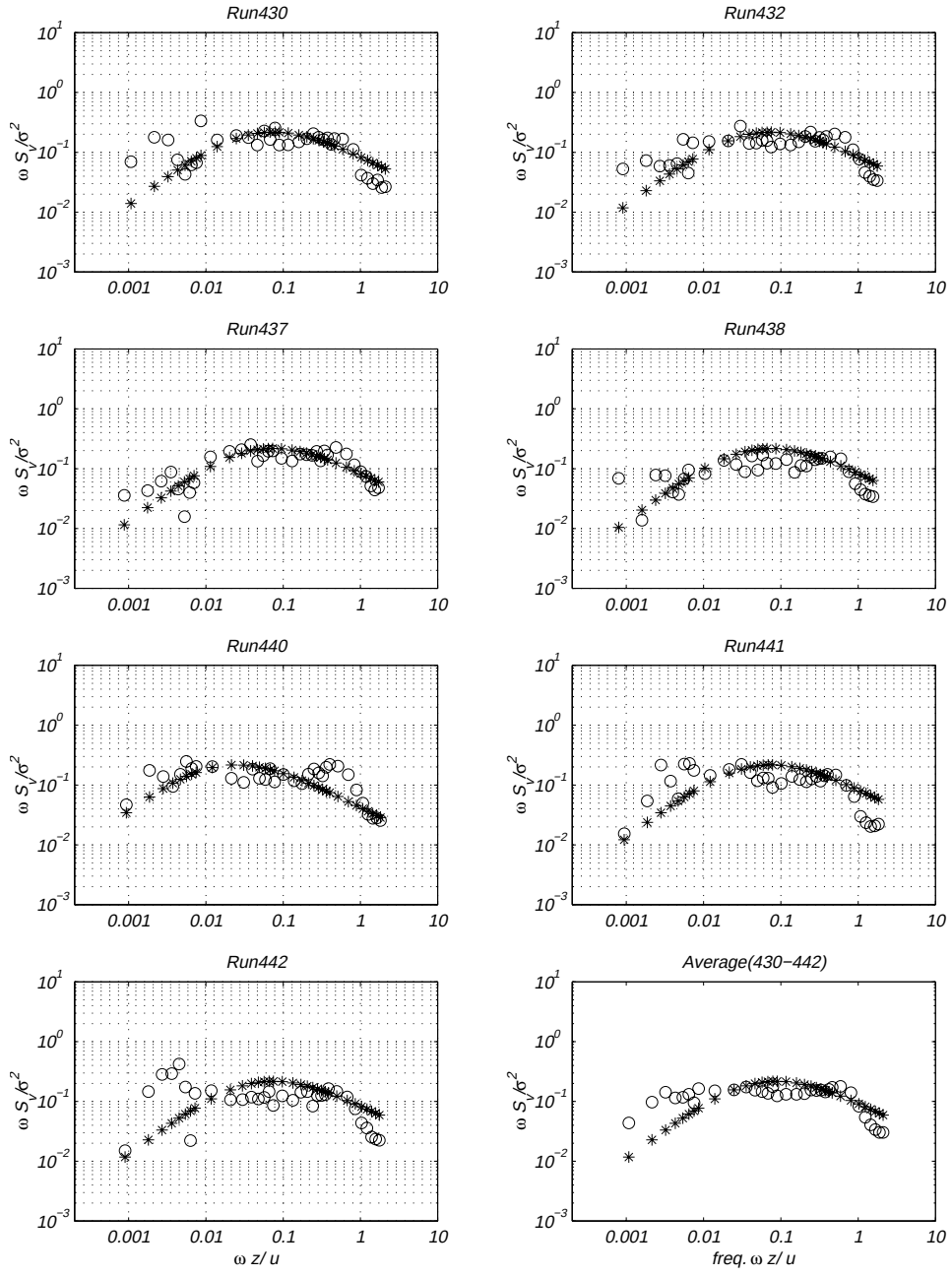

Figure 3.4: Spectra of the $v-$component of the velocity fluctuations at 4.0m height (Runs 430-442). o- Measured spectrum, $*$- theoretical blunt body spectrum [Tieleman, 1995].

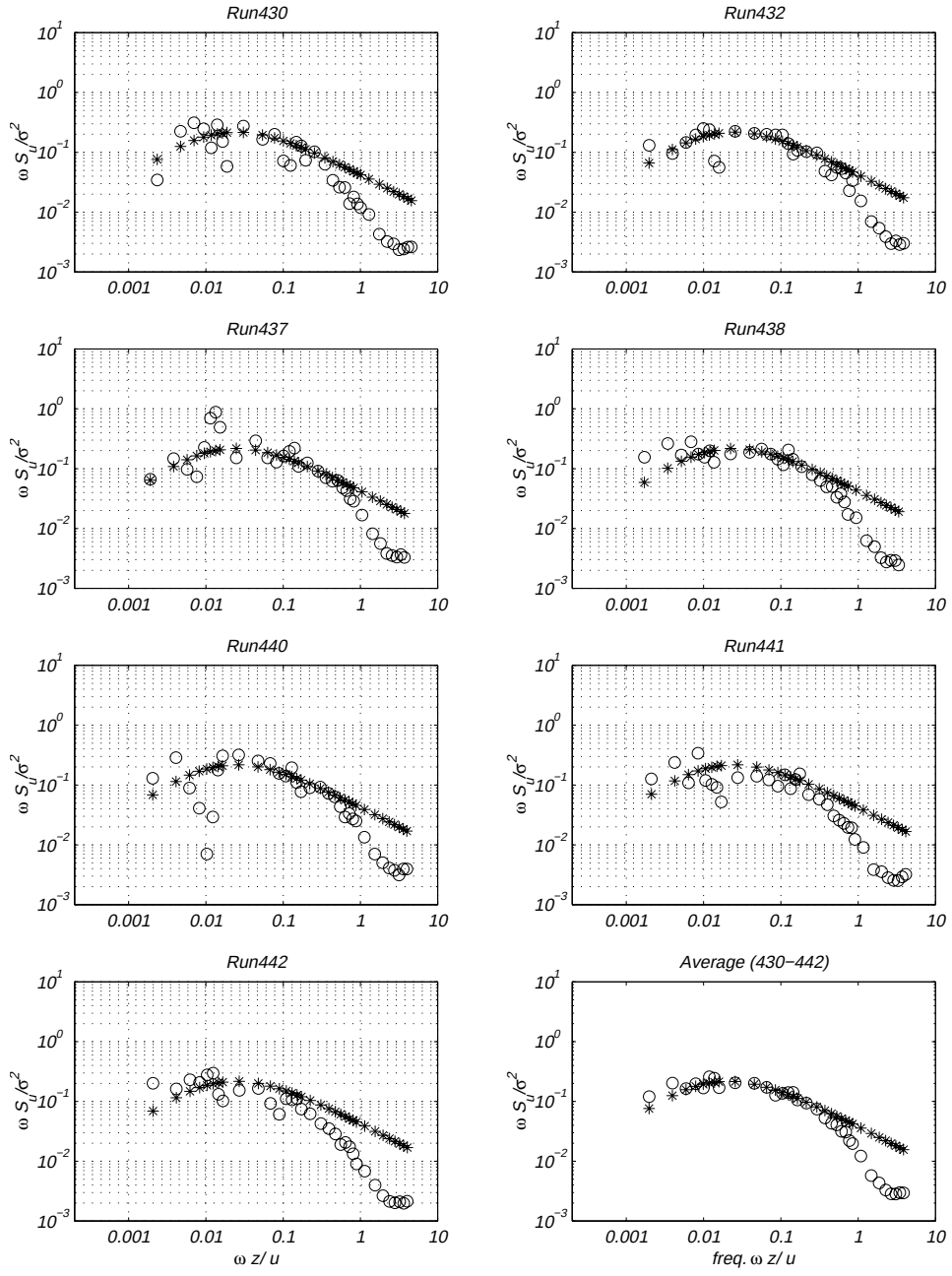

Figure 3.5: Spectra of the $u-$component of the velocity fluctuations at 10m height (Runs 430-442). o- Measured spectrum, $*$- theoretical blunt body spectrum [Tieleman, 1995].

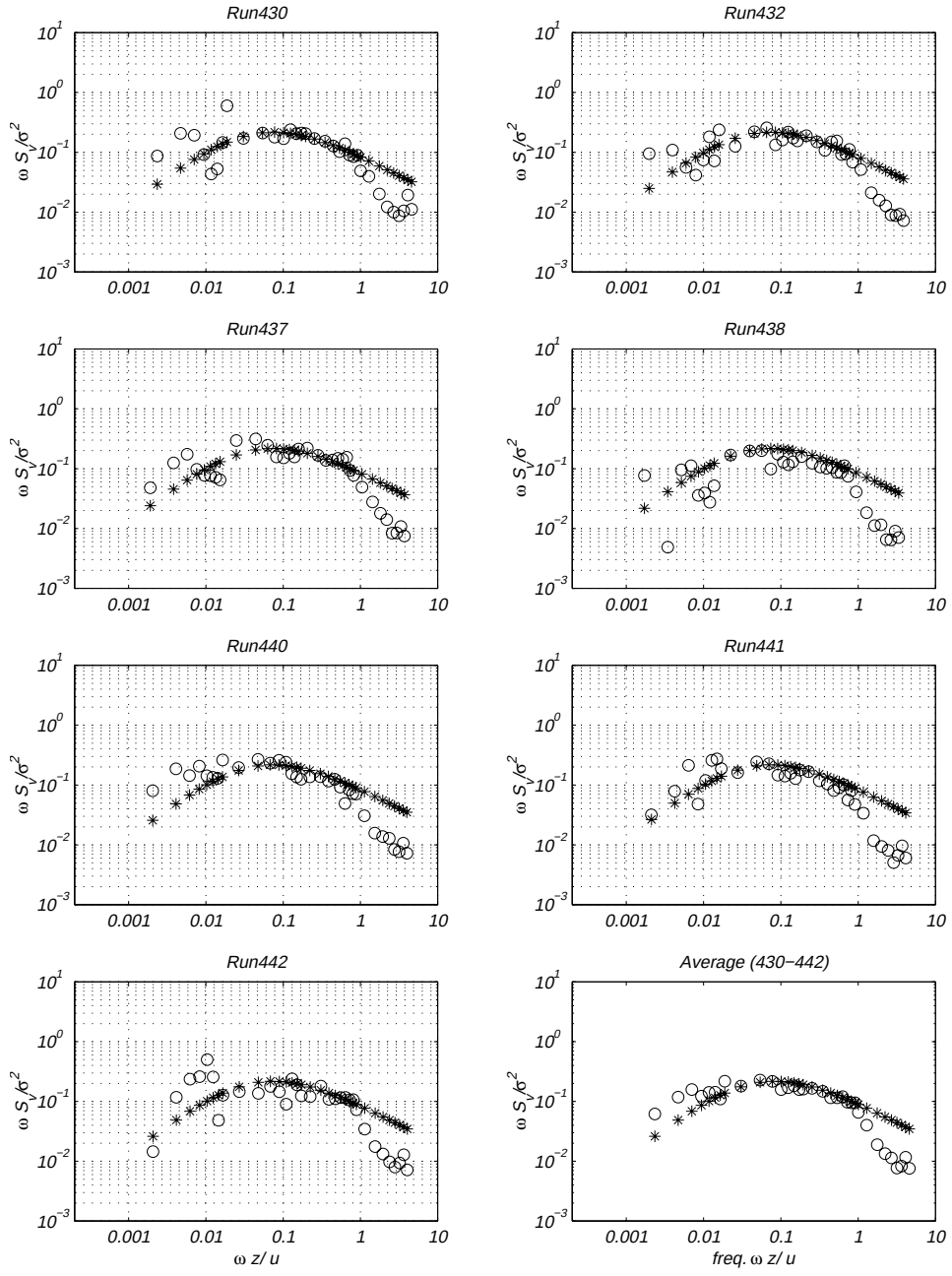

Figure 3.6: Spectra of the $v-$component of the velocity fluctuations at 10m height (Runs 430-442). o- Measured spectrum, $*$- theoretical blunt body spectrum [Tieleman, 1995].

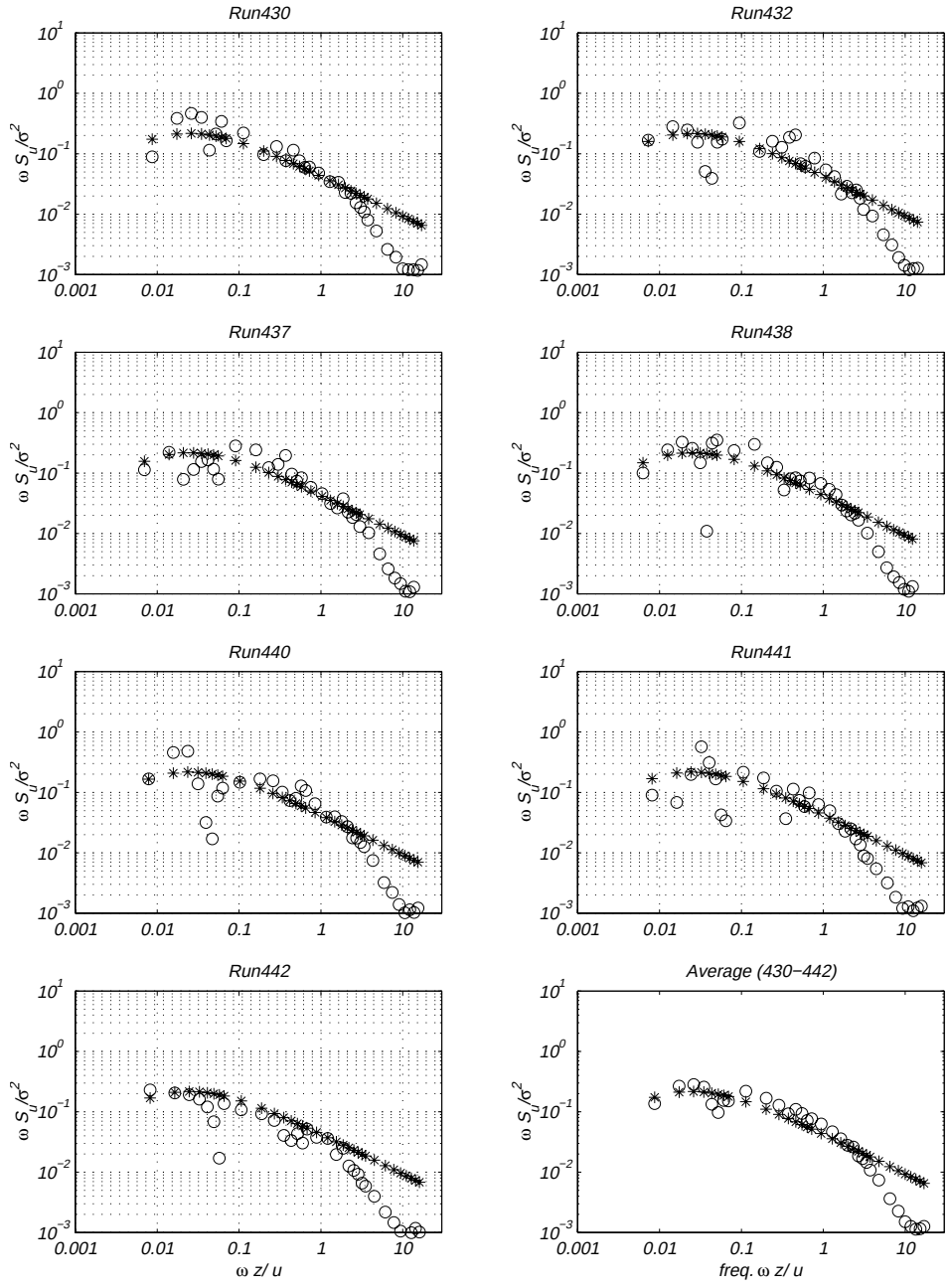

Figure 3.7: Spectra of the $u-$component of the velocity fluctuations at 49m height (Runs 430-442). o- Measured spectrum, $*$- theoretical blunt body spectrum, [Tieleman, 1995].

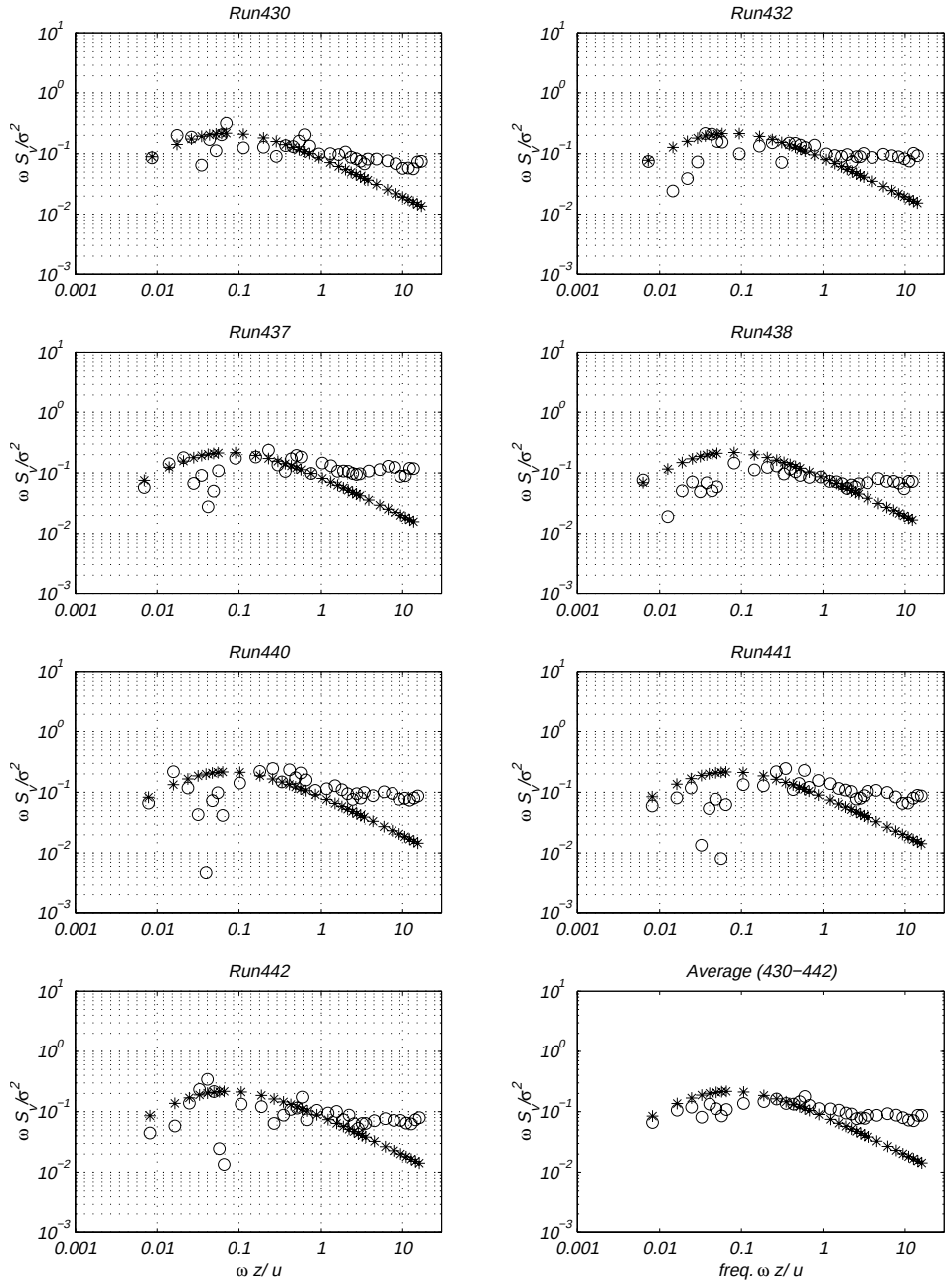

Figure 3.8: Spectra of the $v-$component of the velocity fluctuations at 49m height (Runs 430-442). o- Measured spectrum, $*$- theoretical blunt body spectrum [Tieleman, 1995].

Chapter 4

Shortcomings of Current Analysis Procedure for the Velocity-Pressure Relation

The classical approach to model the relation between velocity fluctuations and pressure coefficients in the atmospheric boundary layer on low-rise structures relies on one of two theories. These are the strip- and the quasi-steady theories. In the strip-theory, it is assumed that the mean pressure is proportional to the wind velocity at the same height. This relation is given by:

$$\overline{p}(z) = \frac{1}{2}\rho U^2(z)\overline{C_p}(\theta) \tag{4.1}$$

where $\overline{p}(z)$ is the mean pressure at height z, U is the mean velocity and $\overline{C_p}$ is the mean pressure coefficient. According to Baines [1963] and Jensen [1965] the strip theory assumption is valid only to determine the mean pressure on the windward face. Consequently, the strip theory could not be used for prediction of suction pressure coefficients on the roof.

In the quasi-steady theory, it is assumed that the surface pressure fluctuations on a structure are proportional to the instantaneous wind velocity and direction. Consequently, the quasi-steady relation is represented by:

$$P(t, \theta(t)) = \frac{1}{2}\rho V^2(t)\overline{C_p}(\theta(t)) \tag{4.2}$$

where $\overline{C_p}(\theta(t))$ is the mean pressure coefficient corresponding to the instantaneous wind direction $\theta(t)$, and $V(t)$ is the magnitude of the instantaneous velocity which is a function

of the wind speed and direction θ.

4.1 Linear Approach and Admittance Function

Over the past twenty years, there has been several simplifications of equation 4.2. The most general velocity-pressure model has been a linearized version of the quasi-steady theory. To obtain this version, the high-order velocity terms of the square of the instantaneous velocity, $V^2(t)$, are neglected, Kawai [1982]. In terms of its components, $V^2(t)$ is written as such:

$$V^2(t) = (U + u(t))^2 + v^2(t) + w^2(t) \tag{4.3}$$

and is approximated by:

$$V^2(t) \simeq U^2 + 2Uu(t)$$

Equation 4.2 is then written as:

$$P(t, \theta(t)) = \frac{1}{2}\rho\big(U^2 + 2Uu(t)\big)\overline{C_p}(\theta(t)). \tag{4.4}$$

Moreover, the fluctuations of wind direction are considered to be linear for small v, u and w which allows one to expand $\overline{C_p}(\theta(t))$ as follows:

$$\overline{C_p}(\theta(t)) \simeq \overline{C_p}(\theta) + \frac{v}{U}\frac{d\overline{C_p}(\theta)}{d\theta_v} + \frac{w}{U}\frac{d\overline{C_p}(\theta)}{d\theta_w} \tag{4.5}$$

where $\theta_v \simeq sin(\theta_v) = \frac{|\vec{\mathbf{v}}|}{|\vec{\mathbf{U}}+\vec{\mathbf{u}}+\vec{\mathbf{v}}|}$ and $\theta_v \simeq sin(\theta_w) = \frac{|\vec{\mathbf{w}}|}{|\vec{\mathbf{U}}+\vec{\mathbf{u}}+\vec{\mathbf{w}}|}$. Upon substituting (4.5) into (4.4) one obtains

$$P(t, \theta(t)) \simeq \frac{1}{2}\rho(U^2 + 2Uu)\big(\overline{C_p}(\theta) + \frac{v}{U}\frac{d\overline{C_p}(\theta)}{d\theta_v} + \frac{w}{U}\frac{d\overline{C_p}(\theta)}{d\theta_w}\big) \tag{4.6}$$

Dividing by the mean dynamic pressure, $\frac{1}{2}\rho U^2$, one can write the instantaneous pressure coefficient as:

$$C_p(t, \theta(t)) \simeq (1 + \frac{2u}{U})\big(\overline{C_p}(\theta) + \frac{v}{U}\frac{d\overline{C_p}(\theta)}{d\theta_v} + \frac{w}{U}\frac{d\overline{C_p}(\theta)}{d\theta_w}\big) \tag{4.7}$$

The rms (σ) value of the fluctuating pressure coefficient derived from the above equation can be further simplified and written as follows:

$$\sigma_{\overline{C_p}} \simeq \Big[\big(2\frac{\sigma_u}{U}\overline{C_p}(\theta)\big)^2 + \big(\frac{\sigma_v}{U}\frac{d\overline{C_p}(\theta)}{d\theta_v}\big)^2 + \big(\frac{\sigma_w}{U}\frac{d\overline{C_p}(\theta)}{d\theta_w}\big)^2 \Big]^{\frac{1}{2}} \tag{4.8}$$

And by substituting components of turbulent intensities as $I_x = \sigma_x/U$, the above equation can be further simplified to give:

$$\sigma_{C_p} \simeq \Big[\big(2I_u\overline{C_p}(\theta)\big)^2 + \big(I_v\frac{d\overline{C_p}(\theta)}{d\theta_v}\big)^2 \Big]^{\frac{1}{2}} \tag{4.9}$$

Note that because the contribution of the turbulence intensity of the vertical component I_w to the σ_{Cp} is small, it was neglected. This assumption is based on the fact that it has been observed that in general near the ground I_w is less than $I_u/2$ or $I_v/2$.

The above linearization is very tempting for two reasons. First, equation 4.9 can be transformed to the frequency domain to give:

$$S_{C_p}(\omega) = 4C_p(\theta)^2 S_u(\omega)/U^2 + (dC_p(\theta)/d\theta_v)^2 S_v(\omega)/U^2 \tag{4.10}$$

here $S_u(\omega)$ and $S_v(\omega)$ are the longitudinal and lateral velocity spectra at corresponding frequencies ω. Hence, a frequency domain relation is obtained between Cp, and u and v components of the velocity fluctuations. The second reason is that if the velocity fluctuations are assumed to be Gaussian, the analysis will result in a Gaussian output for pressure and thus one could statistically predict extreme wind loads. Examining the above relation with full scale data have shown that the pressure spectrum is usually underestimated especially in the high-suction pressure regions (Holscher [1994], Letchford [1992], Kawai [1982]). The discrepancies were attributed then to other interfering parameters such as flow separation, and vortex formation.

In order to compensate for such discrepancies it was proposed to introduce an admittance function in the above spectral relation, which leads to:

$$X^2(\omega) = \frac{U^2 S_{C_p}(\omega)}{4C_p(\theta)^2 S_u(\omega) + (dC_p(\theta)/d\theta_v)^2 S_v(\omega)} \tag{4.11}$$

For ideal quasi-steady conditions, the admittance function is unity across the entire spectrum and any departure from unity would be considered a departure from the quasi-steady conditions.

4.2 Nonlinear Approach and Multivariance Aerodynamic Admittance Functions

Because the linear version of the quasi-steady theory resulted in an inadequate estimation of the pressure spectrum, a modified quasi-steady model has been proposed to account for the nonlinear terms. In this model, the pressure spectrum $S_{Cp}(\omega)$ is related to the velocity components spectra $S_u(\omega)$ and $S_v(\omega)$ and to the spectra of the squares of these components, $S_{u^2}(\omega)$ and $S_{v^2}(\omega)$. This relation is written as [Kawai 1983, Letchford 1993]:

$$\begin{aligned} S_{C_p}(\omega) = \quad & \{4C_p(\theta)^2 \frac{S_u(\omega)}{U^2} + C_p(\theta)^2 \frac{S_{u^2}(\omega)}{U^4} + (dC_p(\theta)/d\theta_v)^2 \frac{S_v(\omega)}{U^2} \\ & + [2(dC_p(\theta)/d\theta_v)^2 + C_p(\theta)^2] \frac{S_u(\omega)}{U^4} \} X^2(\omega) \end{aligned} \tag{4.12}$$

One further modification of the above equation has also been proposed. This modification is based on the fact that introducing only one admittance function, as defined in equation 4.15, assumes that u and v, u^2 and v^2 play equal roles in affecting pressure coefficients. However, Scanlan [1993] showed that the effect of the v-component is more dominant than that of the u-component. In other words, the lateral variation of the wind can provide a significant contribution factor to the wind loading. Thus, one would expect that multivariate admittance functions are better suited than just a single admittance function. In view of this argument, a bilinear model was proposed by Thomas et al. [1992] and Holscher [1994]. In this model, each velocity signal is related to the pressure by independent linear and bilinear transfer functions. A schematic of such a model is shown in figure 4.1. This was considered as a nonlinear improvement of the quasi-steady theory and termed as nonlinear modified quasi-steady theory. The modified version stresses the contribution of velocity components and their squares to the fluctuating wind load in a superposition scheme. The model assumes independent inputs, v and u, with zero mean value and Gaussian stationary stochastic process. Furthermore, it assumes that the output noise is uncorrelated with both inputs. The noise term can be interpreted as the residue between the output signal $y(t)$ and the two input signals $x_1(t)$ and $x_2(t)$ that did not pass through either the linear or the bilinear system. Mathematically, one can express the model as:

$$S_{C_p}(\omega) = S_{y_1 y_1}(\omega) + S_{y_1^2 y_1^2}(\omega) + S_{y_2 y_2}(\omega) + S_{y_2^2 y_2^2}(\omega) + S_{NN}(\omega) \tag{4.13}$$

where $S_{y_1 y_1}(\omega)$ and $S_{y_1^2 y_1^2}(\omega)$ are the contribution of input $x_1(t)$ and its square, and $S_{y_2 y_2}(\omega)$ and $S_{y_2^2 y_2^2}(\omega)$ are the contribution of $x_2(t)$. The residual noise is represented by $S_{NN}(\omega)$. In terms of transfer functions, equation 4.16 can be written as:

$$\begin{aligned} S_{C_p}(\omega) = \quad & \mid H_{11}(\omega) \mid^2 S_{X_1 X_1}(\omega) + \mid H_{12}(\omega) \mid^2 S_{X_1{}^2 X_1{}^2}(\omega) + \\ & \mid H_{21}(\omega) \mid^2 S_{X_2 X_2}(\omega) + \mid H_{22}(\omega) \mid^2 S_{X_2{}^2 X_2{}^2}(\omega) + S_{NN}(\omega) \end{aligned} \tag{4.14}$$

Here $S_{X_1 X_1}$ and $S_{X_2 X_2}$ are the auto-spectra of $x_1(t)$ and $x_2(t)$ respectively, and $S_{X_1{}^2 X_1{}^2}$ and $S_{X_2{}^2 X_2{}^2}$ the auto-spectra associated with the square value of the inputs, ${x_1}^2(t)$ and ${x_2}^2(t)$. $H_{11}(\omega)$, $H_{12}(\omega)$, $H_{21}(\omega)$ and $H_{22}(\omega)$ are the corresponding transfer functions of the inputs X_1, X_1^2, X_2 and X_2^2 to the output Y respectively. S_{NN} is the uncorrelated auto spectrum of the associated noise. Mapping the $u(t)/U$ and $v(t)/U$ as the inputs and $Cp(t)$ as the output, the problem is reduced to a system identification problem of computing four transfer functions. By combining the bilinear model in equation (4.14) with equation (4.12), four admittance functions associated with u, v, u^2, and v^2 can be written as:

$${X_u}^2(\omega) = \frac{\mid H_u(\omega) \mid^2}{4Cp(\theta)^2} = \frac{\mid S_{C_p u}(\omega)/S_{uu} \mid^2(\omega)}{4C_p(\theta)^2} \tag{4.15}$$

$${X_{u^2}}^2(\omega) = \frac{\mid H_{u^2}(\omega) \mid^2}{Cp(\theta)^2} = \frac{\mid S_{C_p u^2}(\omega)/S_{u^2 u^2}(\omega) \mid^2}{C_p(\theta)^2} \tag{4.16}$$

$${X_v}^2(\omega) = \frac{\mid H_v(\omega) \mid^2}{(dCp(\theta)/d\theta_v)^2} = \frac{\mid S_{C_p v}(\omega)/S_{vv}(\omega) \mid^2}{dC_p(\theta)/d\theta_v} \tag{4.17}$$

$${X_{v^2}}^2(\omega) = \frac{\mid H_{v^2}(\omega) \mid^2}{\left[2\left(\frac{dCp(\theta)}{d\theta_v}\right)^2 + C_p(\theta)^2\right]} = \frac{\mid S_{C_p v^2}(\omega)/S_{v^2 v^2}(\omega) \mid^2}{\left[2\left(\frac{dCp(\theta)}{d\theta_v}\right)^2 + C_p(\theta)^2\right]} \tag{4.18}$$

In the next section, we summarize results from several studies that dealt with estimating admittance functions according to both linear and nonlinear models.

4.3 Model and Full-Scale Verification of the Linear Quasi-Steady Theory

Kawai [1982] conducted wind tunnel model studies on a surface mounted prism to verify the validity of the linear quasi-steady theory. The results showed that the quasi-steady approach is only applicable on the windward face and is limited to the low-frequency range. The results also showed that, for the higher frequency components, the estimated pressure should be corrected by a pressure-velocity admittance function. He also noted that one should consider the effects of vortex shedding and wake turbulence in addition to the effect of the oncoming turbulence in evaluating pressures on roofs, the sides and the leeward face. Consequently, the linear admittance function is a function of all of these parameters.
Letchford et al [1992] applied the linear quasi-steady theory and obtained admittance functions for the full-scale measurements of the Texas Tech Building. The results showed significant departures from the theory in particular in the regions of flow separation. In these regions admittance functions of the order of 10 to 100 were obtained, i.e. the theory underpredicted the pressure spectrum on the leading and trailing edges, particularly in the higher-frequency band. In light of these results, Letchford et al. suggested to incorporate nonlinear terms for both pressure coefficients and velocity components. The results of incorporating the second-order terms of the velocity in the quasi-steady theory were insignificant even for large $\overline{C_p}(\theta)$ and $d\overline{C_p}(\theta)/d\theta_v$. The departure from the theory and of full-scale measurements was attributed to building generated and/or wake turbulence which were not considered to be part of the incident flow. One should note here that separating the sources of pressure fluctuations into oncoming and building generated turbulence is not completely true. The reason being that the turbulence in the incident flow affects the development of the separated shear layer.

Tieleman and Hajj [1994] used pressure coefficients, $C_p(\theta(t))$, obtained from wind tunnel measurements to try to predict pressures from velocity measurements in the time domain, i.e using equation (4.2) directly. The results showed that quasi-steady theory could not satisfactory predict the full-scale measured pressure coefficients in regions of flow separation

and vortex development.

Thomas et al. [1992] examined the validity of the modified quasi-steady theory, equation (4.15), for full-scale data obtained from of the WERFL test building at three different locations, middle of the windward wall, next to the roof on the windward and on the roof corner for the quartering wind. Admittance functions X_u^2, X_v^2 $X_{u^2}^2$, and $X_{v^2}^2$ were computed for all of these locations. The results showed continuous attenuation in the relatively high frequency range for the three pressure taps. Moreover, the measured spectrum of $C_p(\theta)$ is significantly underestimated (about 50%) from the model generated spectrum in the higher frequency range. This deviation was again attributed to building generated turbulence or wake which was considered as noise in the model. Holscher [1996] found that the contribution of the nonlinear terms is far less significant than what was reported by Thomas et al. [1992]. According to Holscher only 1% of 60% of the total contribution is due to the nonlinear terms.

In view of all of the unsatisfactory results for the different versions of the quasi-steady theory, we investigated the extent of the linear and the nonlinear relation between spectral components of velocity pressure fluctuations with higher-order spectral moments. The levels of linear and nonlinear coherence, based on these moments, are used to establish the validity of the models proposed by equation 4.10 and 4.12.

4.4 Linear and Nonlinear Coherence between Velocity and Pressure Fluctuations

4.4.1 Frequency-domain Analysis Tools

The extent to which the power in each of two signals are linearly correlated in the frequency domain can be obtained from measurements of the linear coherence. For zero-mean stationary fluctuations $u(t)$ and $p(t)$, representing the fluctuating velocity and pressure signals, the linear coherence function, $\gamma^2{}_{up}(\omega)$, is defined as:

$$\gamma_{up}^2(\omega) = | < P(\omega)U^*(\omega) > |^2 / \{ < |U(\omega)|^2 >< |P(\omega)|^2 > \} \tag{4.19}$$

where $< .... >$ denotes time averaging and $U(\omega)$ and $P(\omega)$ are the complex Fourier amplitudes of $u(t)$ and $p(t)$ respectively. The next higher-order spectral moments to the cross-power spectrum, namely, the cross-bispectrum can be used to quantify the nonlinear coupling among spectral components with different frequencies in two given signals. For velocity and pressure fluctuations, the cross-bispectrum is given by:

$$S_{uup}(\omega_i, \omega_j) =< P(\omega_k = \omega_i \pm \omega_j) U^*(\omega_i) U^*(\omega_j) > \tag{4.20}$$

This cross-bispectrum is a function of two frequency components and measures the degree of coherence among modes with frequencies ω_k in the pressure fluctuations and ω_i and ω_j in the velocity fluctuations. If these modes are independent, their phases are statistically independent and subsequently, the phase of the auto-bispectrum is randomly distributed. The averaging indicated in equation (4.23) by $< .... >$ will then yield near a zero value for the cross-bispectrum. On the other hand, if the three modes are nonlinearly coupled, a phase coherence will exist among them and the averaging will result in a nonzero value for the cross-bispectrum that indicate the strength of the coupling between these modes. The level of nonlinear coherence can then be obtained from the normalized value of the cross-bispectrum. This nonlinear coherence is termed as the cross-bicoherence and is given by:

$$b^2{}_{uup}(\omega_i, \omega_j) = |S_{uup}(\omega_i, \omega_j)|^2 / \{< |U(\omega_i) U(\omega_j)|^2 >< |P(\omega_k)|^2 >\} \tag{4.21}$$

and, by Schwartz inequality, it varies between zero and one.

The above analysis procedure was applied to velocity and pressure fluctuations measured in the Clemson wind tunnel. The details of the experimental setup and locations of pressure taps are given in chapter 2. Two wind tunnel configurations are considered here. One with the conventional spire-roughness configuration which will be referred to as the "no spires" configuration. The other with an additional of five small spires placed directly upstream of the model roof. These small spires were used to obtain adequate simulation of the small scale turbulence [Tieleman et al. 1993]. This setup will be referred to as the "with spires" configuration. Full scale measurements were not used because the time series of the velocity fluctuations could not be classified as stationary and, thus, Fourier domain averaging procedures could not be applied. Two cases are considered here. In one case, the flow is approaching the building at an angle of 90^o degrees with respect to the model leading

edge. Under this condition, a separation region is formed on the roof where the shear layer rolls into a vortex. Eleven pressure taps were placed near the middle of the leading edge and parallel to the mean flow on the model roof. The coordinates of these taps are given in chapter 2. In the second case, the flow is approaching the model at an oblique angle of 45^o. Under these conditions, two corner (delta-wing-like) vortices are formed at the corner of the building. These vortices are responsible for negative pressure coefficients peaks up to -10.

4.4.2 Frequency-domain Velocity-Pressure Coherence

Typical spectra of the pressure fluctuations over the eleven taps for the normal case near the center of the building are shown in figure 4.2. The presented spectra show the normalized energy $\omega S_p/\sigma_p^2$ versus the reduced frequency $\omega z/U$, where σ_p^2 is the pressure variance, z is the model height and U is the mean velocity at the height of the model roof. As expected, the spectra at the low frequencies are different at the various taps. On the other hand, the normalized level of energy of the high frequencies is about the same. It should be noted that, the pressure spectra at all taps are characterized with two maxima centered near normalized frequency of $\omega z/U$=0.008 and 0.5 and with relatively low energy in the normalized frequency band below $\omega z/U$=.0.003. This is true for both the "no spires" and the "with spires" configurations. Figure 4.3 shows the spectra of the pressure fluctuations over four taps in the corner of the roof for the oblique case. Again, both "no spires" and "with spires" configurations show same frequency distribution for the pressure coefficients. It should also be noted that, the pressure spectrum is directly related to the rms value of the pressure coefficients and not to the pressure peaks.

Figures 4.4 and 4.5 show the linear coherence between the frequency components of the u-component of the velocity fluctuations and pressure coefficients for the normal and oblique cases, respectively. It is obvious from these figures that the coherence is negligible for $\omega z/U > 0.01$. While the coherence increases slowly in magnitude for decreasing frequencies below 0.01, the results clearly indicate that the spectral component of the velocity and pressure fluctuations are not linearly related. Moreover, while the presence of spires did not significantly alter the energy distribution content of the pressure fluctuations, it caused a

significant drop in the linear coherence for the low frequencies. On the other hand, we should note that better simulation of the pressure peaks can be obtained when spires were present , Tieleman et al. [1996]. Consequently, using spectral relation to predict pressure peaks is not sufficient.

Figures 4.6 and 4.7 show contour plots of the cross-bicoherence between the velocity and pressure fluctuations for the normal and oblique cases, respectively. As explained above, low values of the cross-bicoherence indicate that there is no direct coupling between frequency components in the velocity to contribute to to frequency components in the pressure coefficients. The plots show that, for all taps, the cross-bicoherence is extremely small, i.e ≤ 0.06, among all frequency components. Hence, a relation based on frequency components between the velocity upstream of the model and the pressure on the roof is not possible.

In this chapter, we have clearly shown the weaknesses for the frequency domain analysis in predicting extreme wind loads. These weaknesses can be summarized as follows:

- Linear admittance functions obtained from different full and model scale experiments showed significant departure from unity. Moreover, there are major discrepancies between nonlinear admittance functions obtained by different research groups for different experiments. Our analysis, using spectral moments, proves that these discrepancies exist because the levels of linear and nonlinear coherence between the frequency components of the velocity and pressure components are very low. This is, most likely, due to the averaging needed in estimating frequency-domain moments. procedures.

- Even if a frequency-domain relation exists, such a relation between rms values could not be used for prediction of extreme pressure coefficients.

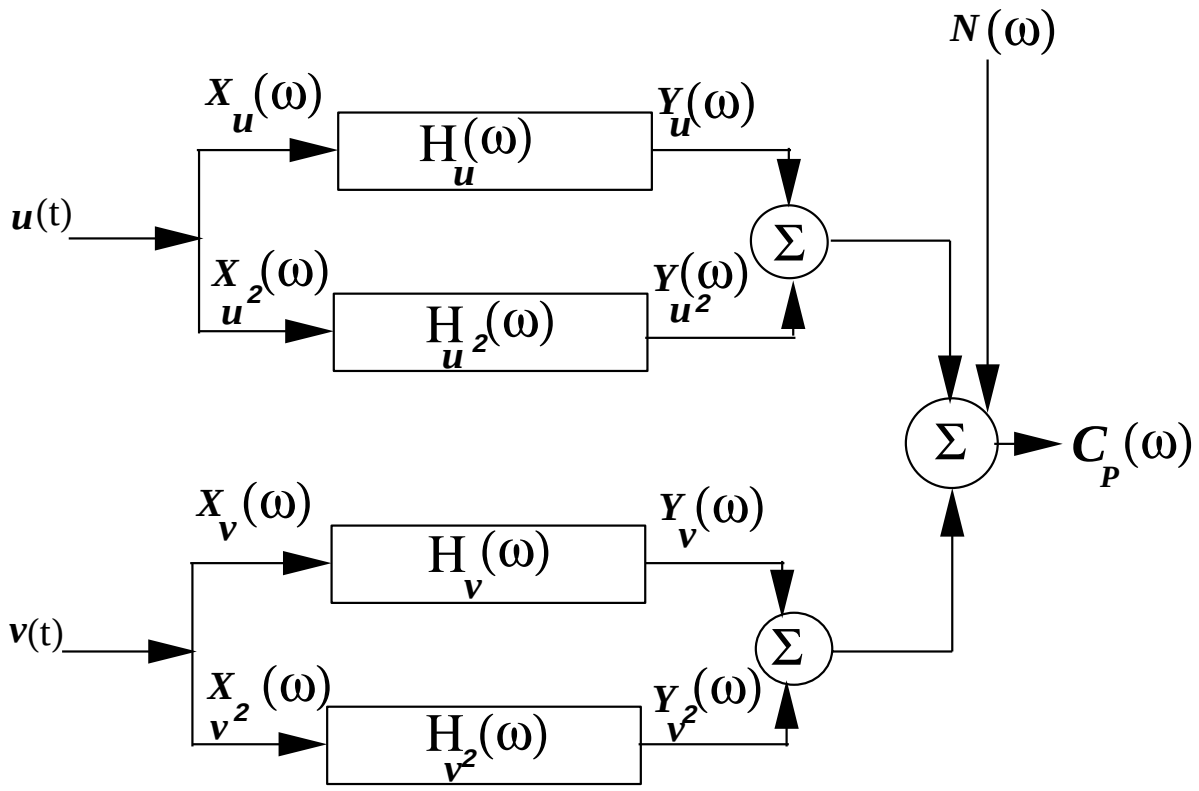

Figure 4.1: Schematic representation of the bilinear model

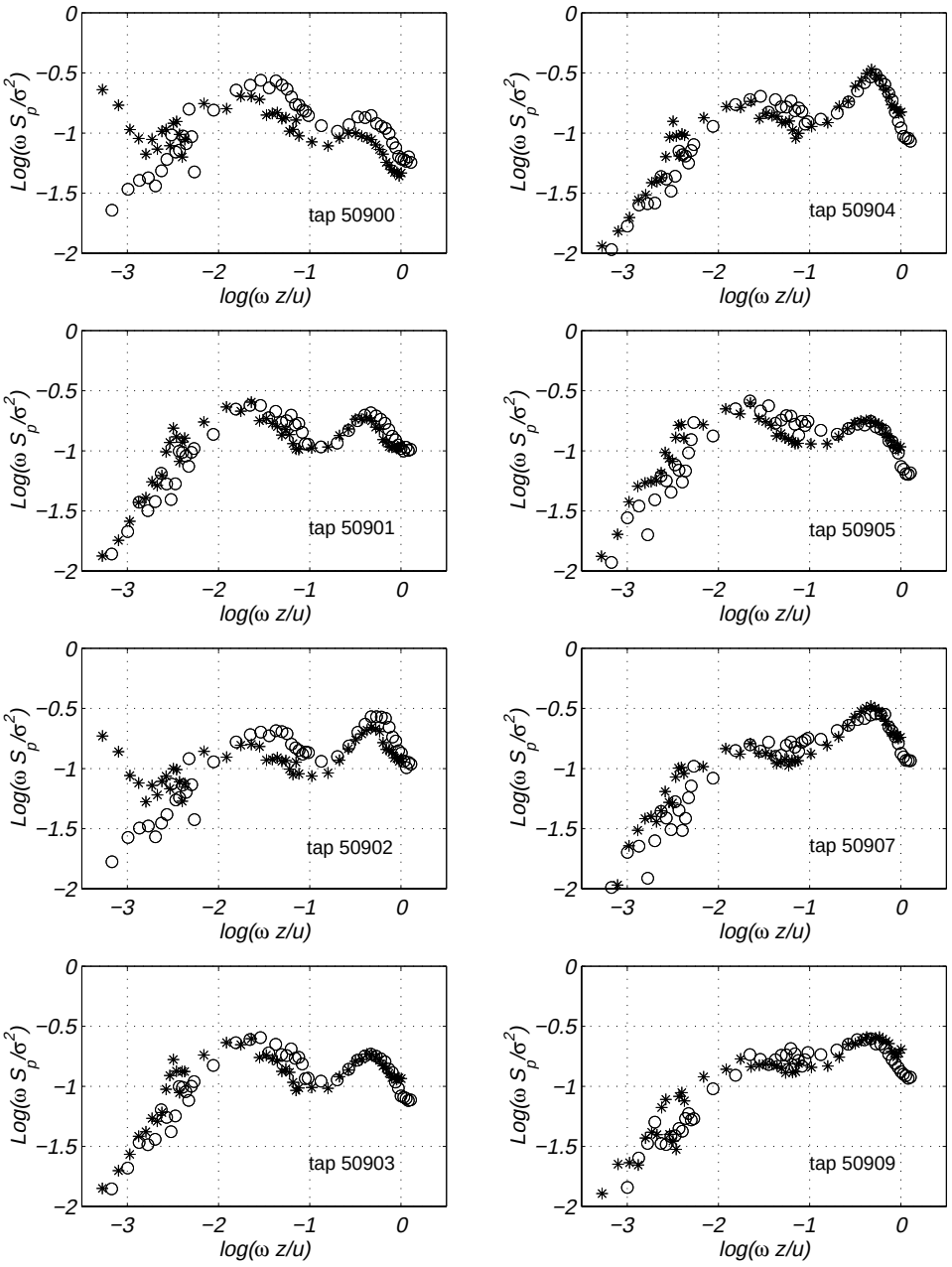

Figure 4.2: Pressure fluctuations spectra, normal incidence case, -o with spires and $*$- without spires.

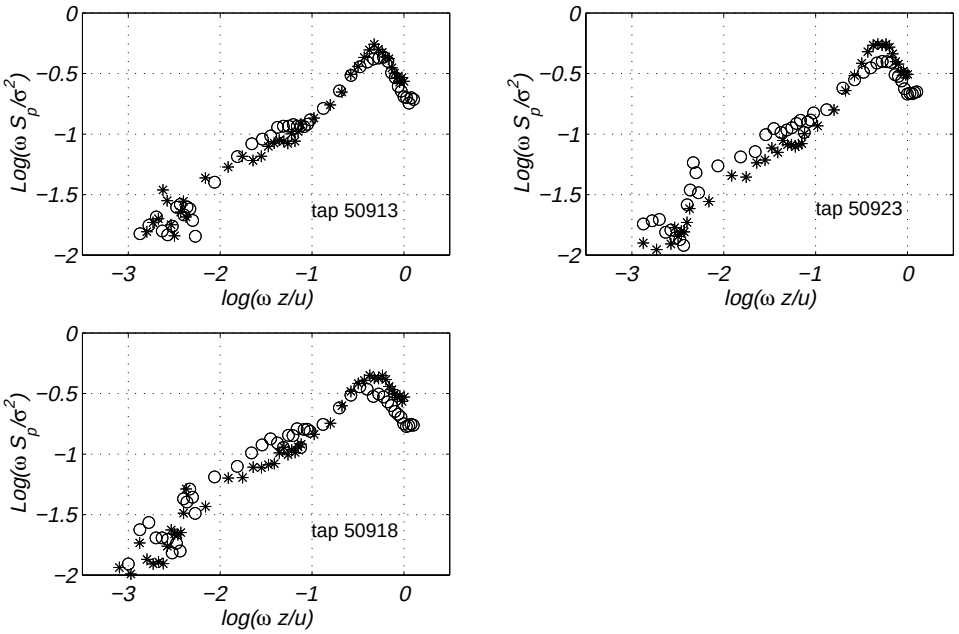

Figure 4.2 cont'd, for caption see previous page.

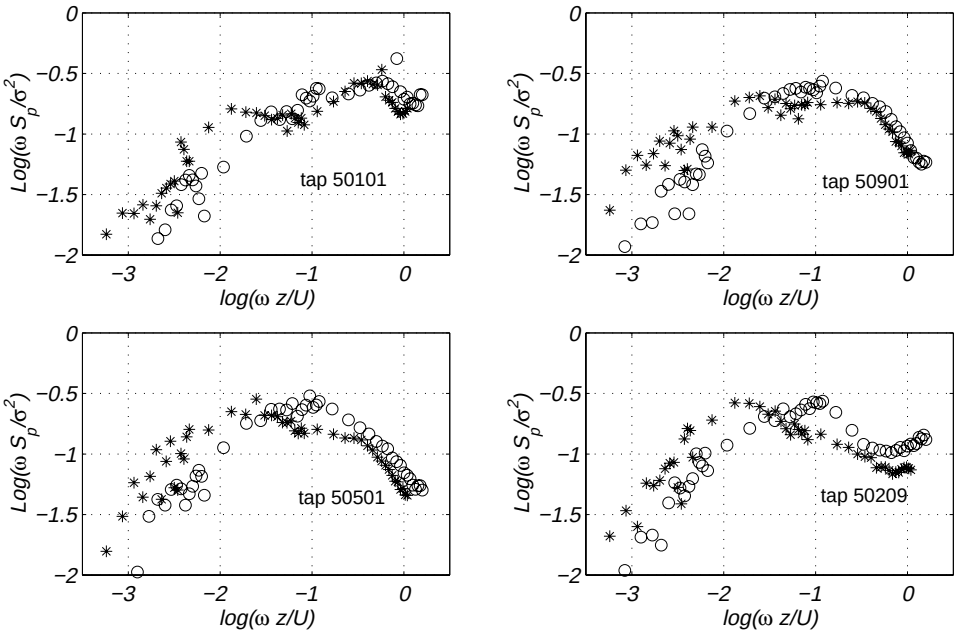

Figure 4.3: Pressures fluctuation spectra, oblique incidence case, o- with spires and $*$- without spires.

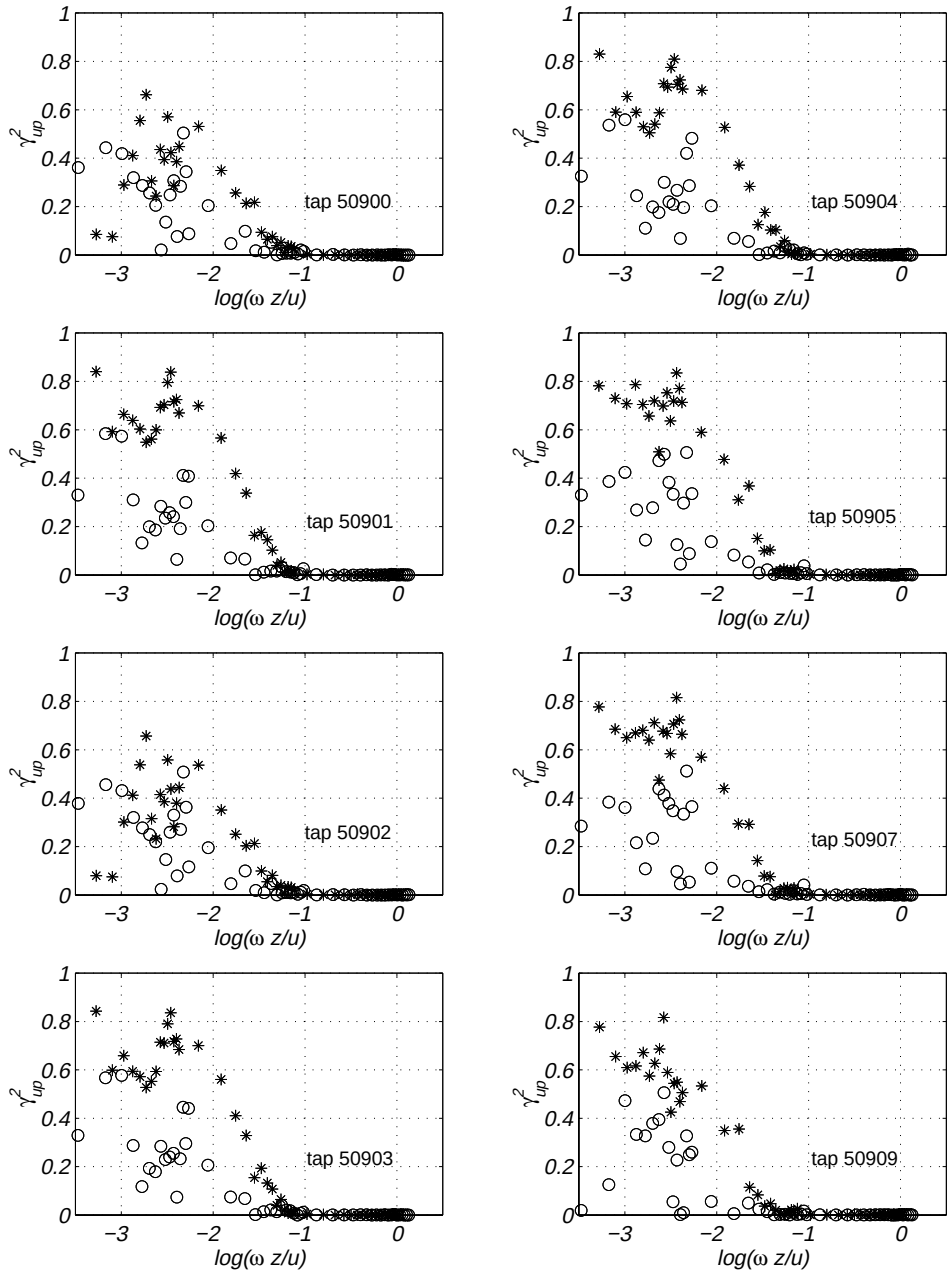

Figure 4.4: Pressures/velocity linear coherence, normal incidence case, o- with spires and $*$- without spires.

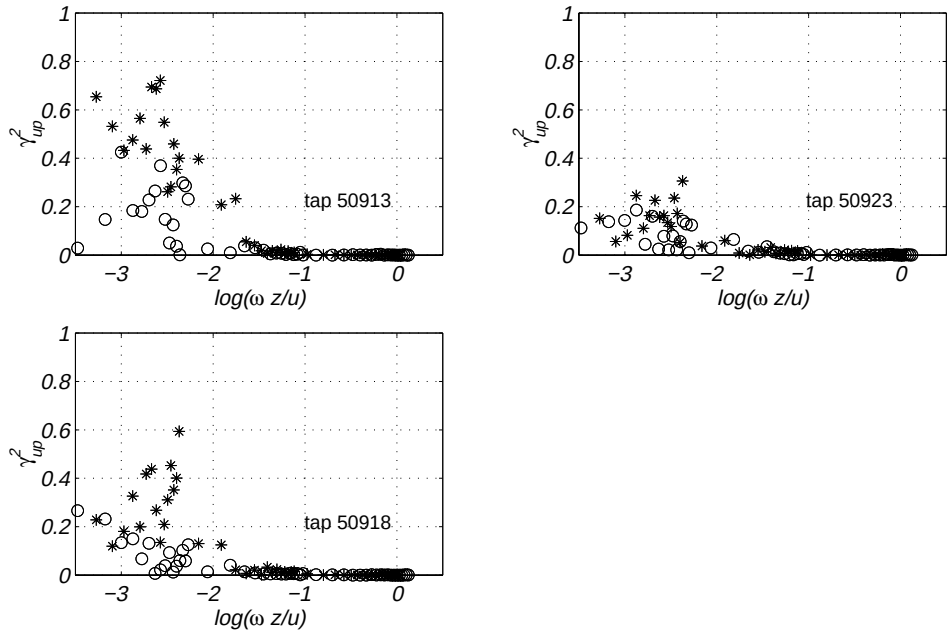

Figure 4.4 cont'd, for caption see previous page.

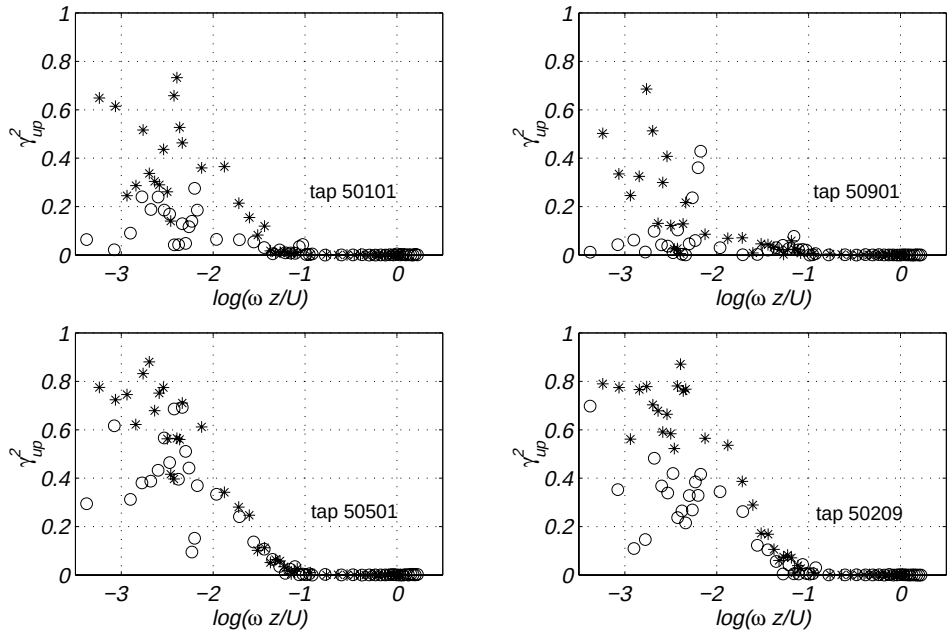

Figure 4.5: Pressures/velocity linear coherence, oblique incidence case, o- with spires and $*$-without spires.

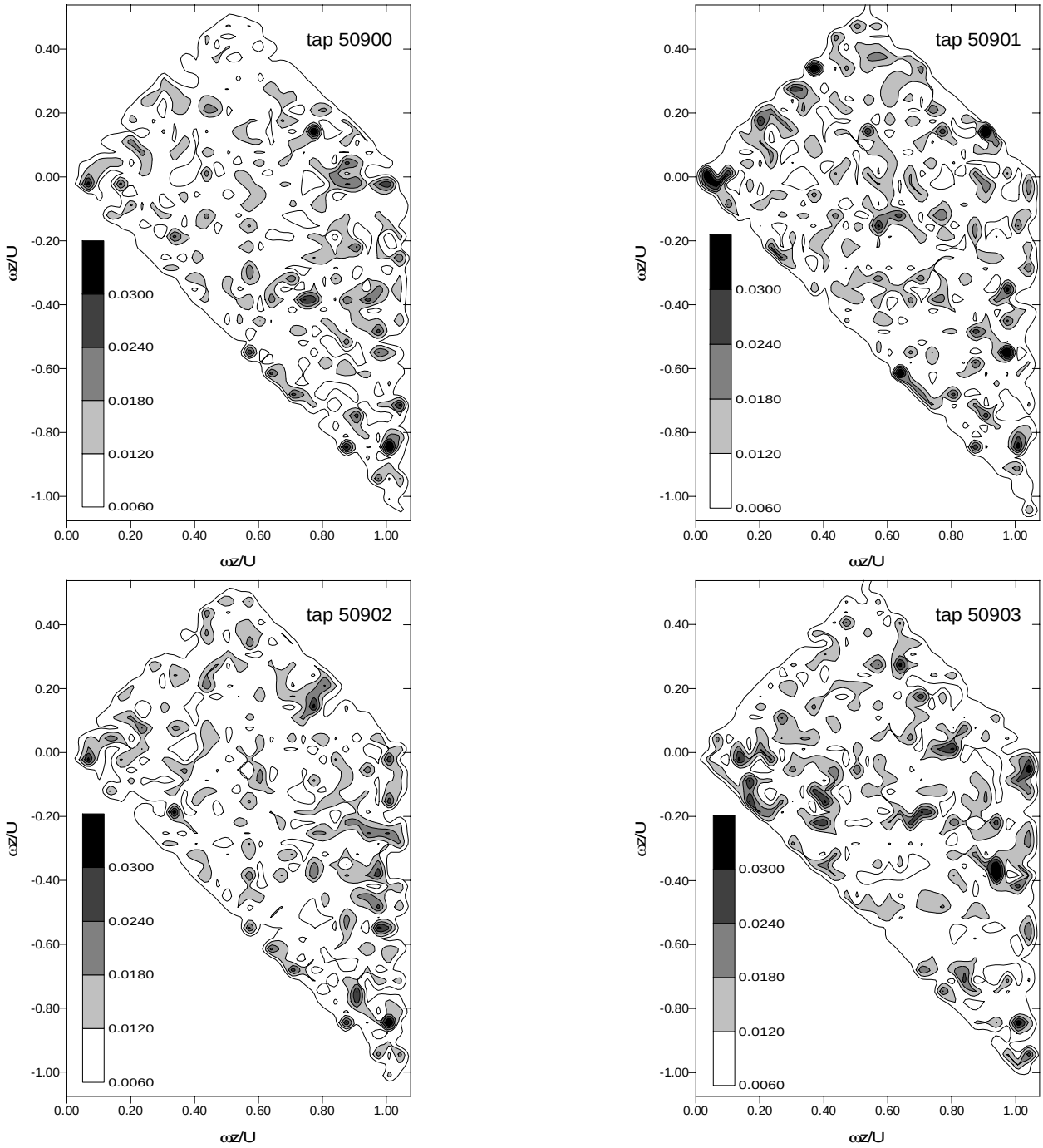

Figure 4.6: Cross bi-coherence of the pressure and the velocity for the normal incidence case, without spires

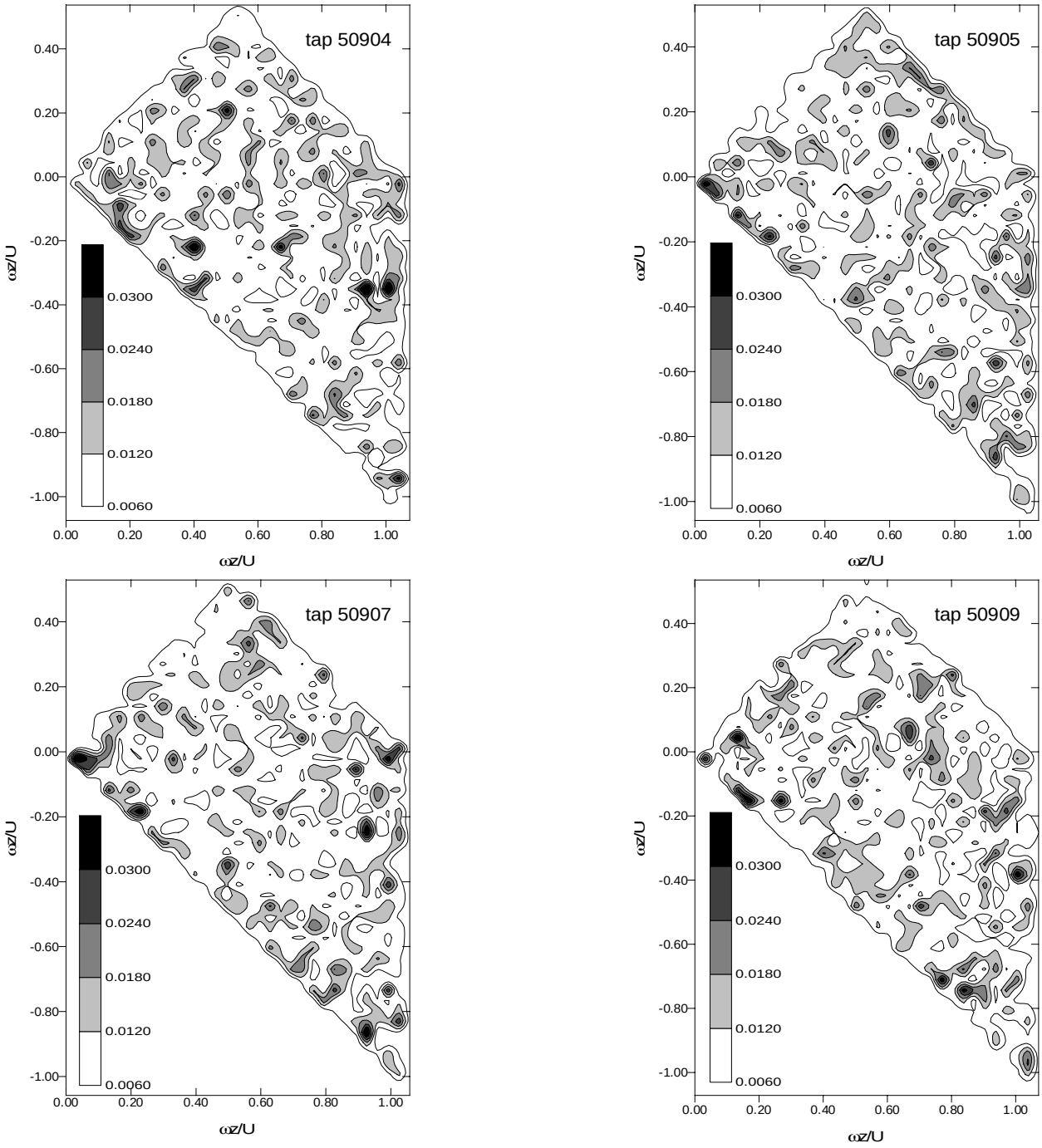

Figure 4.6 cont'd, for caption see previous page.

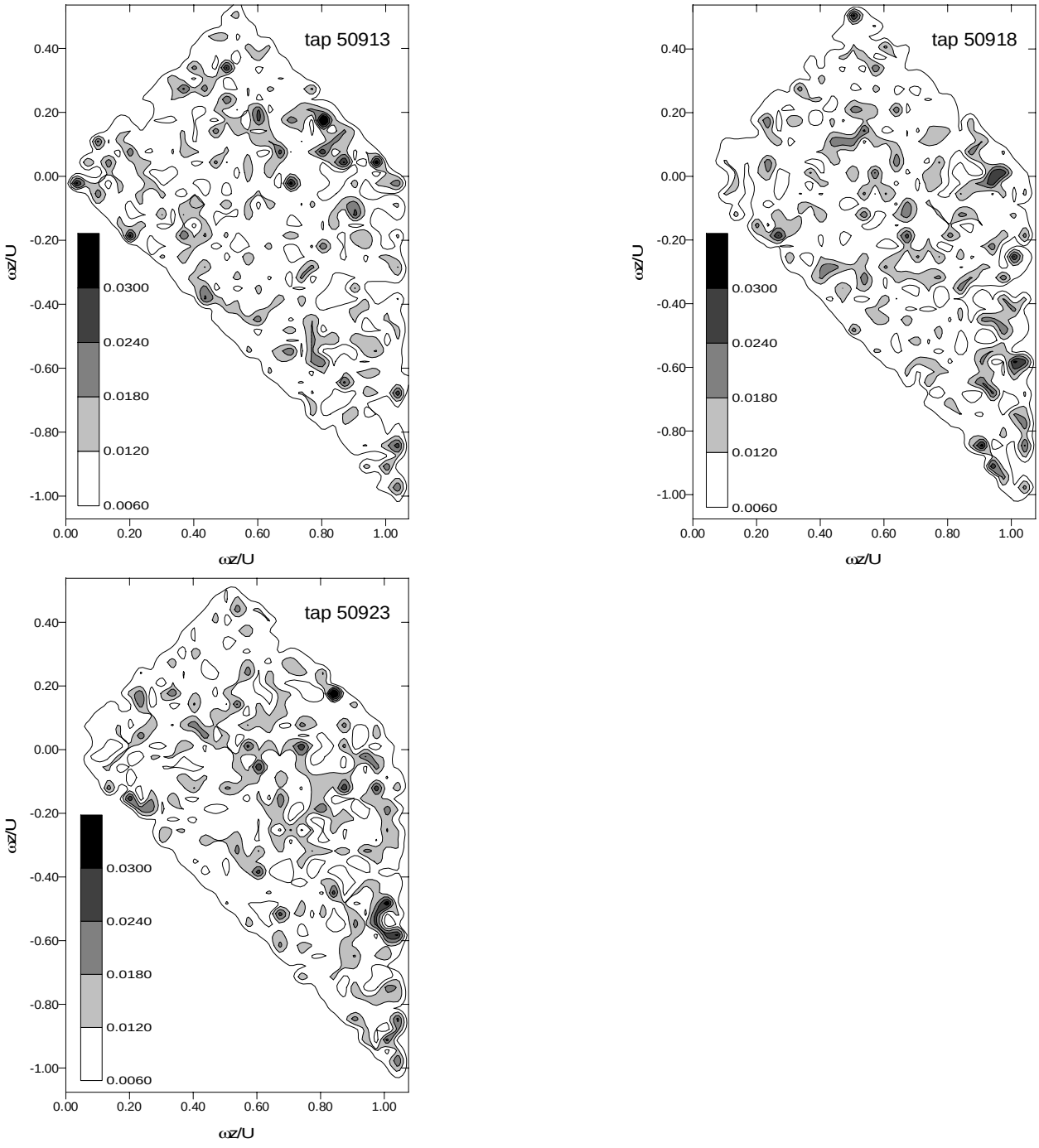

Figure 4.6 cont'd, for caption see previous page.

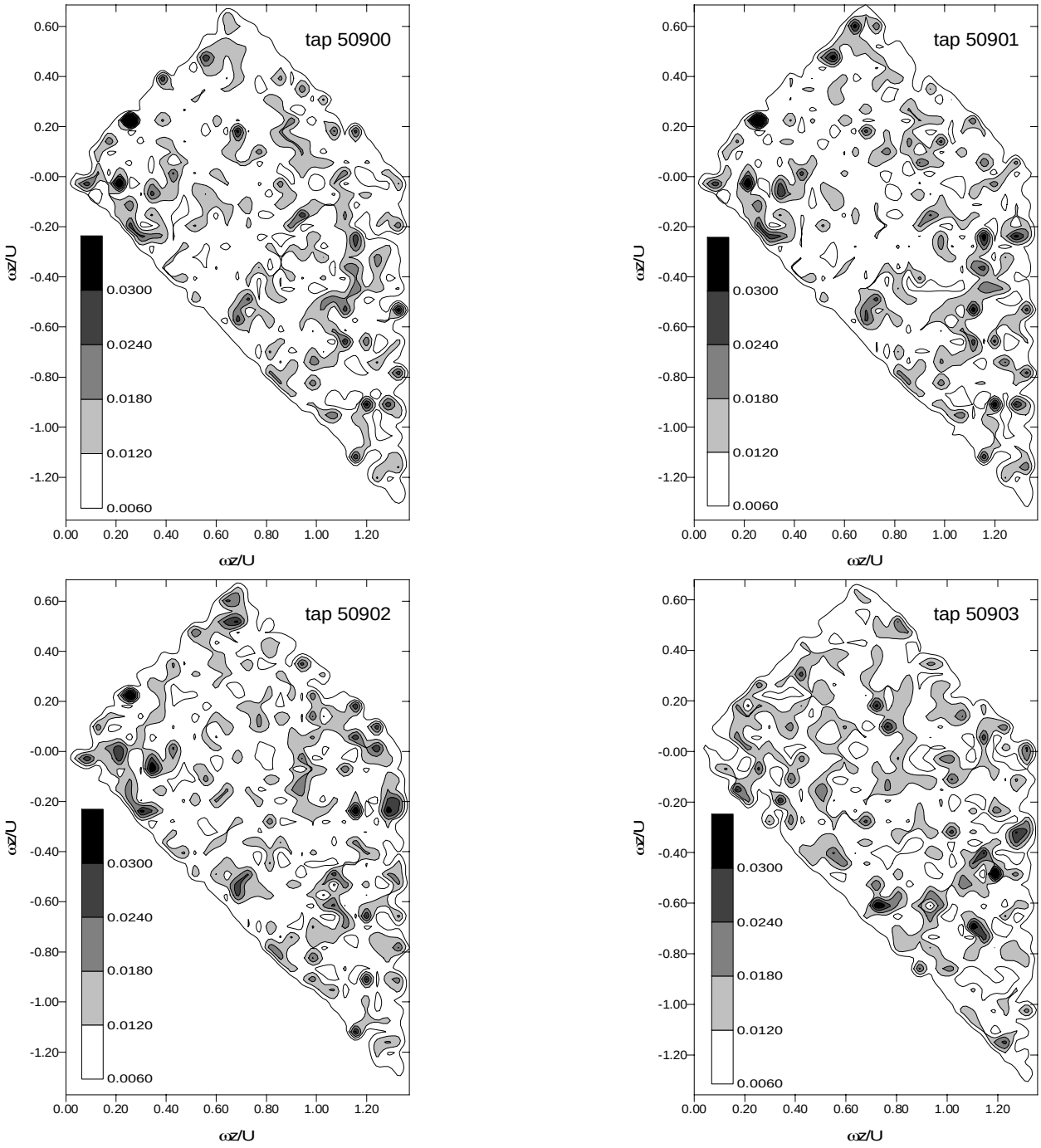

Figure 4.7: Cross bi-coherence of the pressure and the velocity for the normal incidence case, with spires

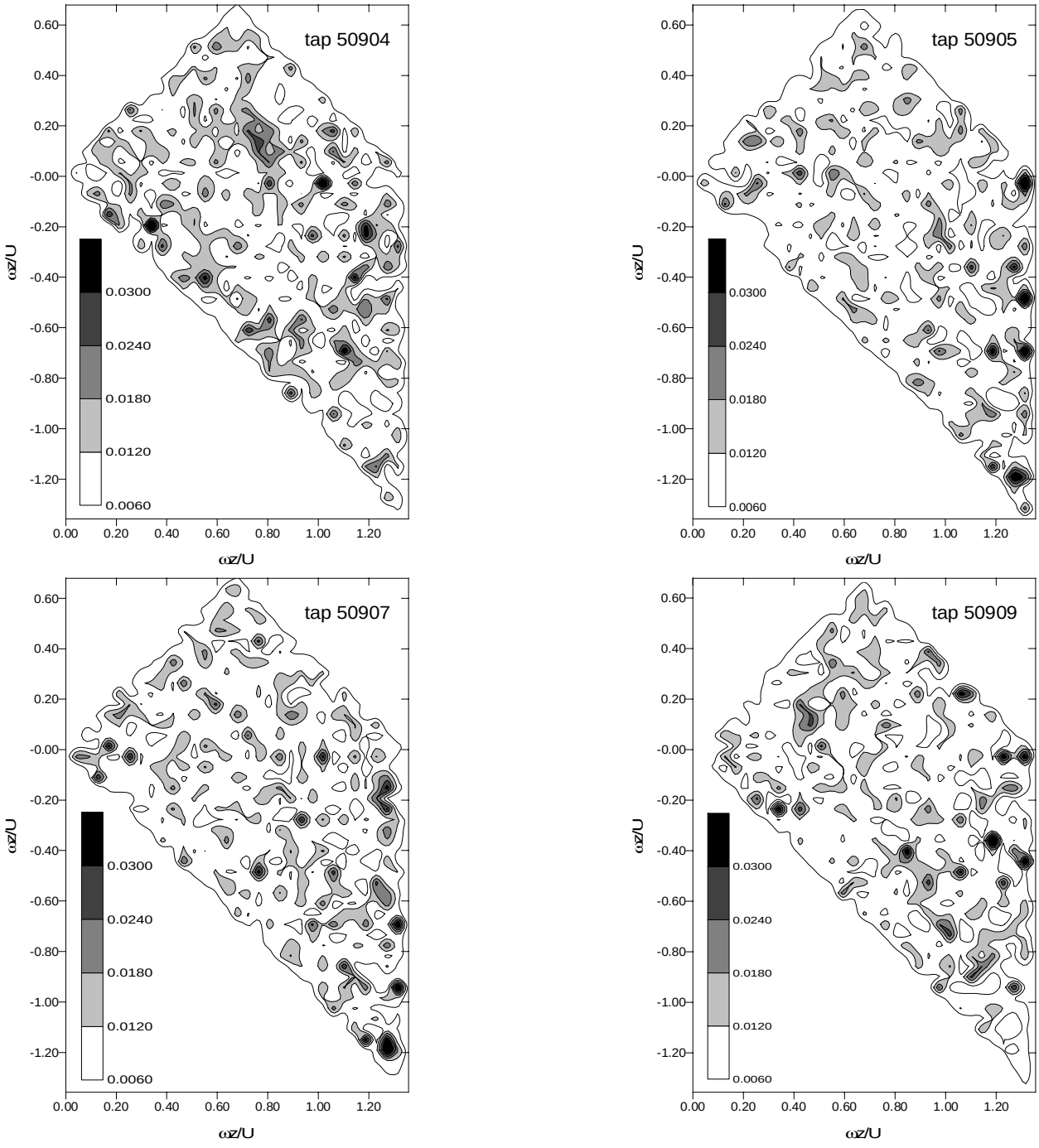

Figure 4.6 cont'd, for caption see previous page.

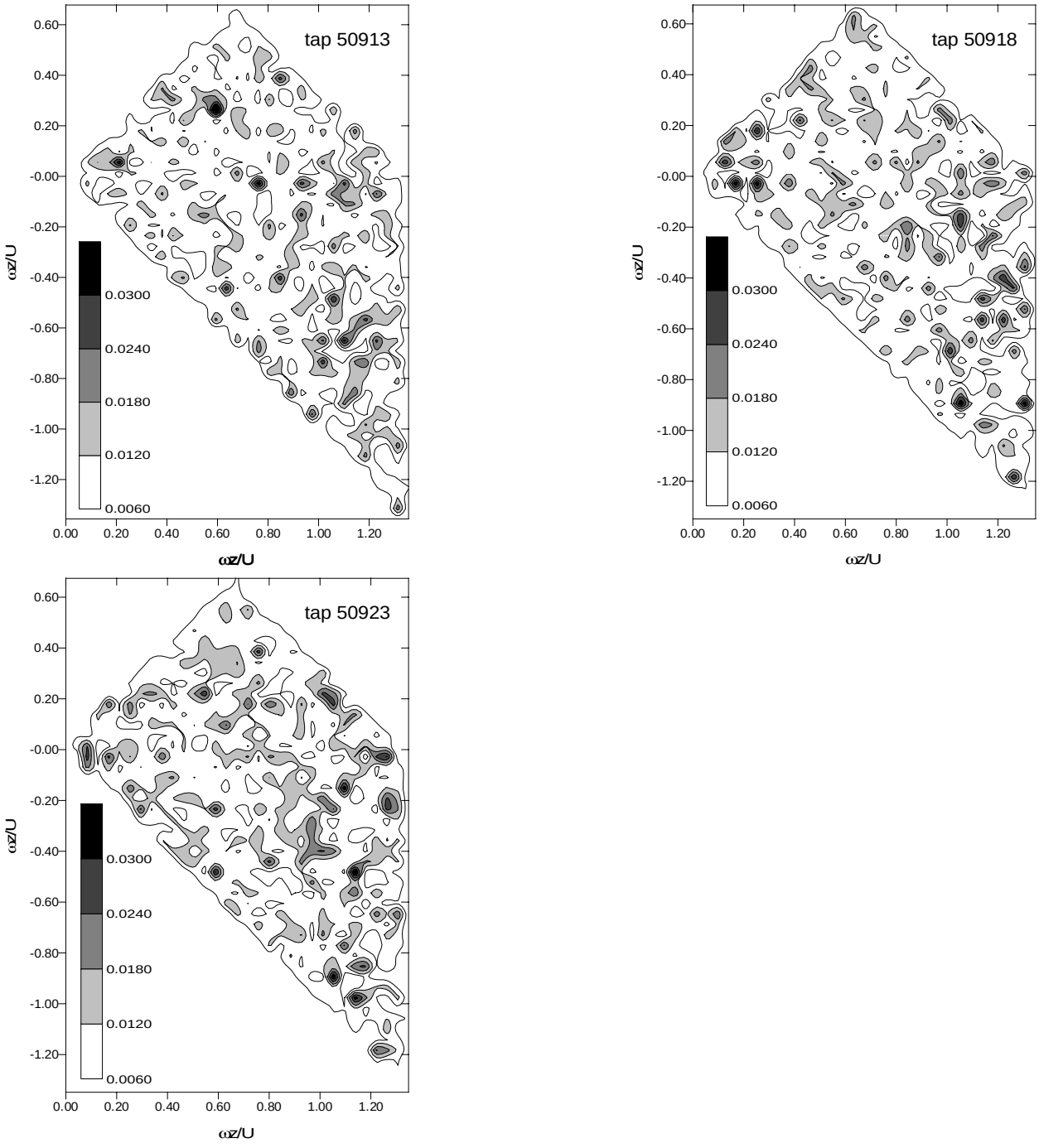

Figure 4.6 cont'd, for caption see previous page.

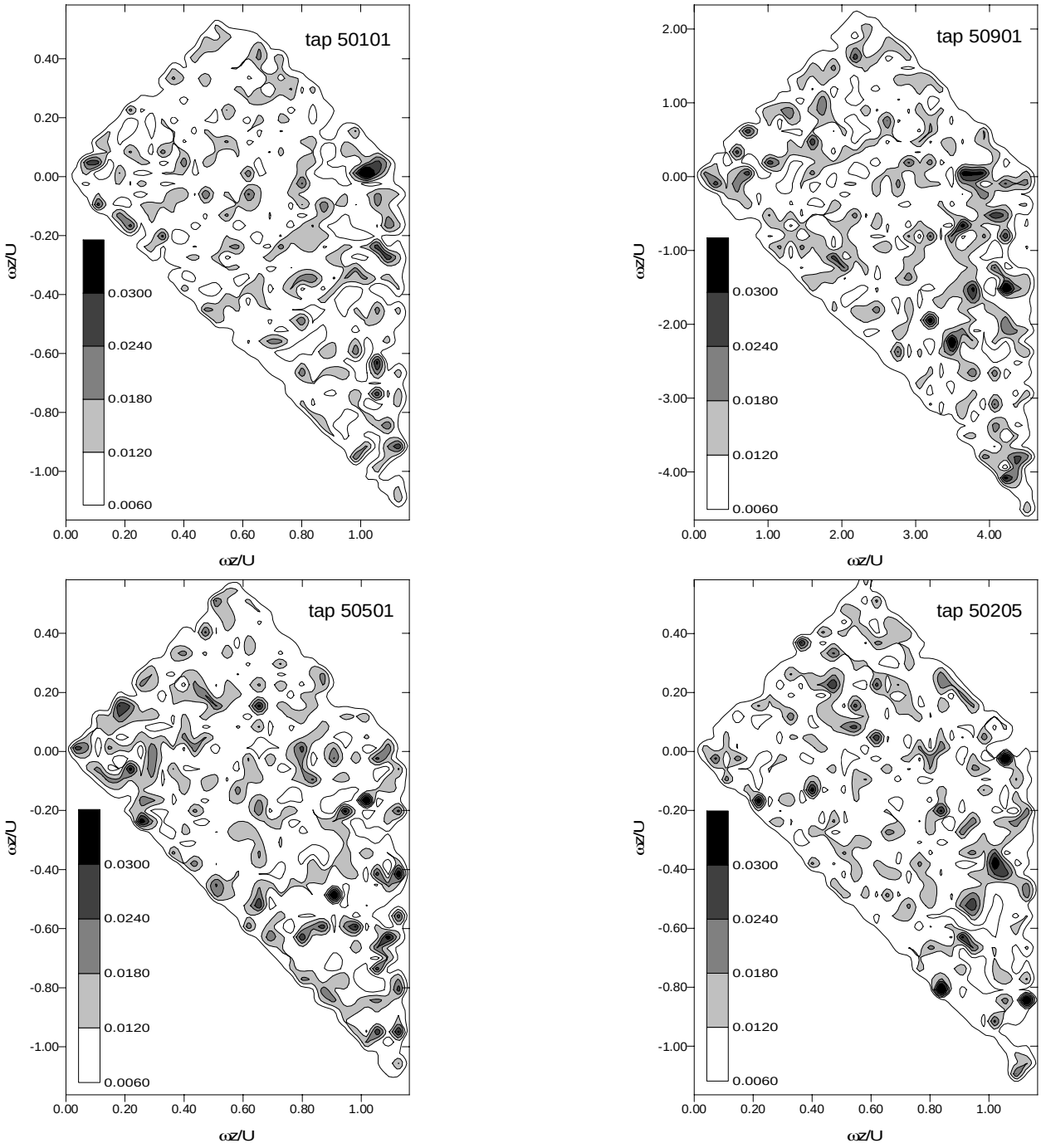

Figure 4.8: Cross bi-coherence of the pressure and velocity for the oblique incidence case, without spires

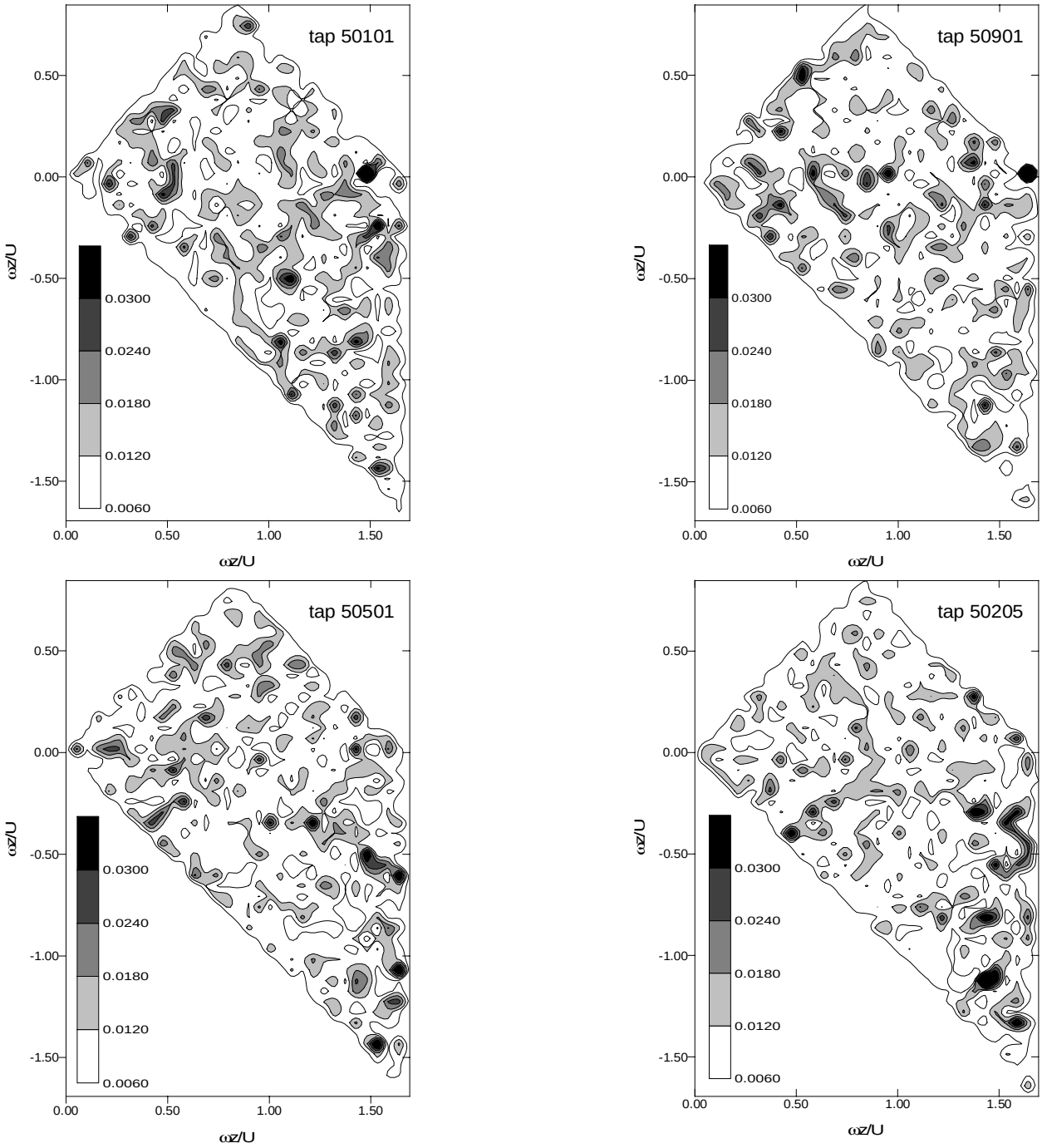

Figure 4.9: Cross bi-coherence of the pressure and velocity for the oblique incidence case, with spires

Chapter 5

Wavelet Analysis, Definitions and Examples

In this chapter, a review of the wavelet transform and its properties is given. Some examples that pertain to the analysis presented in the next two chapters and their interpretations are also provided.

In wavelet analysis oscillating functions of finite duration, called wavelets, are utilized rather than the infinite *sine* and *cosine* functions used in the Fourier decomposition. Because of this property, the wavelet transform has several advantages over the Fourier transform in analyzing atmospheric turbulence and its effects on wind loading on structures. Such advantages arise because item of the property of locality of wavelets in time. Consequently, they are well suited to analyze the nonstationary aspects turbulence fluctuations. Moreover, wavelet analysis can capture short duration peaks which cannot be done by Fourier-domain analysis.

In the remainder of this chapter, we will present wavelet analysis and some examples that illustrate why wavelets should be used for characterizing turbulence in the atmospheric surface layer and studying the velocity-pressure relation.

5.1 Wavelet Theory

When a signal exhibits time varying spectral characteristics, it is said to be nonstationary. For such signals, conventional spectral analysis based on Fourier transform is of limited value. The reason being that the nonstationary signal should be described in a time-frequency or time-scale plane. Such a representation can be obtained by using the wavelet transform. Given a time series $f(t)$, its continuous wavelet transform is defined as:

$$\omega(a,\tau) = a^{-1/2} \int_{-\infty}^{\infty} f(t)\psi^*(\frac{t-\tau}{a})dt \tag{5.1}$$

where $\omega(a,\tau)$ are the wavelet coefficients, $\frac{1}{\sqrt{a}}\psi(\frac{t-\tau}{a})$ are basis functions called wavelets, the * indicates complex conjugate. The above transform gives representation in terms of two parameters a and τ, the first parameter a is associated with scale and the second parameter τ is associated with time. As for the wavelets, $\psi(\frac{t-\tau}{a})$, they are scaled and translated (by varying a and τ) versions of a basic wavelet prototype, referred to as mother wavelet. The basic wavelet prototype, $\psi(t)$ has to be admissible. This condition guarantees that if a function of time is transformed into the time-scale domain with that wavelet, then the inverse transform exists. The wavelet transform is a projection of $f(t)$ onto all scaled and translated versions of the single mother wavelet, $\psi(t)$. Thus, $\omega(a,\tau)$ represents the relative contribution of scales a to the signal at times τ.

In practical situations, the data is discrete , hence, both a and τ need to be discrete. A general form for the discrete wavelet transform is obtained by choosing $a = a_o^m$ and $\tau = n\tau_o a_o^m$. Where a_o and τ_o are constants that represent the base scale and the time resolutions ($a_o > 1$ and $\tau_o > 0$) and the indices m and n are integers. Note that when m and n increase linearly, a and τ change exponentially. Note also that the net translation, τ, depends on the dilation, a_o^m. Because the continuous wavelets are defined for continuously varying scale and time, the wavelets are not orthogonal. Yet, by appropriately discretizing a and τ, one can choose a basic wavelet and obtain a set of wavelets that form an orthonormal basis. In this work, it is proposed to use the orthonormal wavelets to examine the characteristics of turbulence in the atmospheric boundary layer. Mallat [1992], Daubeshies [1993], and Meyer [1994] came up with algorithms that provide orthonormal basis functions. These functions logarithmically represent the scales present in the signal with a coarser time representation

at the larger scales. The dyadic of these functions always reproduces the original signal and, more importantly, the Parseval's theorem, holds, i.e., we have:

$$\int_{-\infty}^{\infty} f(t)^2 dt = \int_{-\infty}^{\infty}\int_{-\infty}^{\infty} \omega^2(a,\tau) da d\tau \tag{5.2}$$

The choice for a_o and τ_o is not arbitrary in order to produce an orthonormal set. If a_o is chosen to be 2 and $\tau_o = 1$ the decomposition is done octave by octave, and one could obtain an orthonormal basis for certain choices of $\psi(t)$. Consequently, the function $f(t)$ can be approximated, by a linear combination of the wavelets, i.e. one can write

$$f(t) = \sum_{m=0}\sum_{n=0} \omega_m[n]\psi_{m,n}(t) \tag{5.3}$$

where the wavelet coefficients $\omega_m[n]$ represents the contribution of scale 2^m over time $n2^m$. By letting,

$$\psi_{mn}(t) = 2^{-m/2}\psi(2^{-m}t - n) \tag{5.4}$$

one can rewrite equation(5.3) as

$$f(t) = \omega_o + \sum_{m=0}^{\frac{logN}{log2}}\sum_{n=0}^{2^m-1} \omega_{2^m+n} 2^{\frac{-m}{2}}\psi(2^{-m}t - n) \tag{5.5}$$

where ω_o is the signal mean value. Notice that the upper limit of n and m is limited by the number of levels ($\frac{logN}{log2}$) which, in turn, is determined by the number of data points N. Based on equation (5.3) and (5.4), one can compute the discrete wavelet coefficients as

$$\omega^m[n] = \sum_{-\infty}^{\infty} 2^{\frac{-m}{2}}\psi(2^{-m}t - n) f(t) \tag{5.6}$$

Squaring both sides of equation (5.3) and integrating over the time domain results in the mean-square value of $f(t)$, i.e.

$$\begin{aligned}\int_{-\infty}^{\infty} f(t)^2 dt = \quad & \omega_o^2 + 2\omega_o \sum_m\sum_n \omega_{2^m+n}\int_{-\infty}^{\infty} 2^{\frac{-m}{2}}\psi(2^{-m}t - n)dt + \\ & \sum_m\sum_n\sum_r\sum_s \omega_{2^m+n}\omega_{2^r+s}\int_{-\infty}^{\infty} 2^{\frac{-m}{2}}2^{\frac{-r}{2}}\psi(2^{-m}t - n)\psi(2^{-r}t - s)dt\end{aligned} \tag{5.7}$$

The second term on the left hand side is zero because the wavelet is an oscillating function with zero mean. The third term can be reduced for orthonormal wavelets to obtain:

$$\int_{-\infty}^{\infty} f(t)^2 dt = \omega_o^2 + \sum_{m=0}^{\frac{log(N)}{log(2)}} \sum_{n=0}^{2^m-1} \omega_{2^m+n}^2 \int_{-\infty}^{\infty} 2^{-m}\psi^2(2^{-m}t - n)dt$$
$$= \omega_o^2 + \sum_{m=0}^{\frac{log(N)}{log(2)}} \sum_{n=0}^{2^m-1} \omega_{2^m+n}^2 (\frac{1}{2^m}). \quad (5.8)$$

By expanding the above equation one gets:

$$\int_{-\infty}^{\infty} f(t)^2 dt = \omega_o^2 + \omega_1^2 + \frac{1}{2}(\omega_2^2 + \omega_3^2) + \frac{1}{4}(\omega_4^2 + \omega_5^2 + \omega_6^2 + \omega_7^2) +$$
$$\frac{1}{8}(\omega_8^2 + \omega_9^2 + ... + \omega_{15}^2) + \frac{1}{16}(\omega_{16}^2 + \omega_{17}^2 + ... + \omega_{31}^2) + ... \quad (5.9)$$

This equation shows the contributions to the mean-square value of a signal from all scales. In this work, we will use Daubechies wavelets to examine time-varying characteristics of the atmospheric turbulence and of the velocity-pressure relation. Daubechies wavelets are specified by a particular set of numbers, called wavelet filter coefficients. Depending on the number of these coefficients, Daubechies wavelets can be either highly localized or highly smooth. Figure 5.1 shows wavelet functions from the wavelet families, DAUB2, DAUB4, DAUB6 and DAUB20 along with their Fourier transform. One should note that all of these wavelet functions are continuous. As the number of the filter coefficients increases the Daubechie wavelets become more smooth and ultimately become close to a harmonic window. On the other hand, the wavelet becomes less local.

5.2 Application of Orthonormal Wavelets

In this section we will generate numerical signals with time-varying characteristics and use Daubechies wavelets to analyze these signals. These examples will help us in the interpretation of the wavelet analysis of atmospheric turbulence and of the velocity-pressure relation.

5.2.1 Wavelet Decomposition and Reconstruction

To show how wavelet analysis works, a discretely sampled function as shown in figure 5.2 is investigated. This function is given by

$$f(t) = \begin{cases} 1 + sin(2\pi\frac{t}{127}) & : & 0 \leq t \leq 127 \\ 0.5 + uniform(rand) & : & 128 \leq t \leq 256 \\ sin(2\pi\frac{20(t-257)}{255}) & : & 257 \leq t \leq 512 \\ 1.0 + sin(2\pi\frac{4(t-513)}{255})sin(2\pi\frac{12(t-513)}{255}) & : & 513 \leq t \leq 768 \\ 1.0 + sin(0.2(2\pi\frac{(t-768)}{231}))^3 & : & 768 \leq t \leq 1000 \\ 1.0 & : & 1001 \leq t \leq 1024 \end{cases}$$

which consists of a large-scale oscillation, random fluctuations, small-scale oscillations, both amplitude and frequency modulations and a constant. The mean value of the signal is unity. The physical domain of the signal is mapped into a record that spans over 2^{10}=1024 units. Figure 5.3 shows a decomposition using DAUB4 wavelet family over $\frac{log1024}{log2} + 1 = 11$ scales. The additional level represents the mean of the signal. This level is denoted by $m = -1$. The second scale, denoted by $m = 0$, represents the largest scale in the signal and is obtained by projecting one wavelet over the whole signal. The third scale denoted by $m = 1$, is obtained by projecting two wavelets onto the signal. This projection is continued until the eleventh scale, denoted by $m = 9$, is obtained by applying 512 wavelets onto the signal.

Thus, as expected, level -1 has a value of 1 which is exactly the mean value of the signal in figure 5.2. At $m = 3$, the wavelet catches the largest signal scale which is defined over $0 \leq t \leq 128$; the random portion of the signal which contains several frequency components is, as expected, captured in several scales, $m = 3$ thru $m = 9$. The high frequency portion of the signal ($256 \leq t \leq 512$) is captured by scale $m = 7$ and the amplitude modulation of the signal part is captured at $m = 6$ and $m = 7$. Some residual of the signal scales usually appears in one higher or lower scale. This is due to the mismatch between the projected wavelet scale and the signal scale. This mismatch could be reduced drastically by increasing the sampling rate. This rate allows higher step-size scale resolution of the wavelet. Frequency modulation at $768 \leq t \leq 1000$ is best represented by wavelet as can be represented by several successive scales $m = 6$ thru $m = 9$ at different times that slide at a rate proportional to the modulations. Finally, the constant portion ($1001 \leq t \leq 1024$) of the signal is seen by the wavelet as very large scale oscillation and thus appears at the relatively large scales $m = 1$

thru $m = 4$.

Figure 5.4 shows a reconstructed signal obtained by adding the successively transformed scales. It is obvious that such a signal can be satisfactorily constructed from the wavelet coefficients. Moreover, the energy of each scale in the signal is represented by the square of the wavelet coefficient. The time variation of this energy is shown in figure 5.5 which maps the magnitude of the wavelet coefficients over scales with $m = -1$ to $m = 9$ at all times. One can see that wavelet coefficients are high at times corresponding to the presence of a certain scale in the original signal. Adding the energy over time will give the total energy content of a certain scale.

5.2.2 Intermittency Representation

One of the objectives of this work is to characterize the time variations of turbulence in the atmospheric boundary layer. This objective will be achieved by dividing the turbulence over small and large scales and by examining the time variations in the energy of each scale. These characteristics are represented by an intermittency factor and corresponding percentage of energy.

Intermittency is, in general, defined as the occurrence of short-time irregular variations in a long regular signal. By this definition, intermittency can be interpreted as the time fraction of turbulence versus non-turbulence or as the time fraction the measuring device sees the variable in a high energy state. Consequently, intermittency can be measured as a time factor or percentage. To explain this idea we consider the two signals shown in figures 5.6.a. and 5.6.b. Figure 5.6.a. shows a sinusoidal time series. In figure 5.6.b. we added a short-time variation to the signal shown in figure 5.6.a. We computed the wavelet coefficients of both signals and calculated the average energy of all scales in those signals. To quantify the intermittency, we considered the following approach: If the measuring device sees the scale's energy at a higher state than a certain threshold, the scale is considered to be intermittent. This threshold was defined as twice the average energy of that scale. The percentage of total time that the device sees the higher energy state is defined as the intermittency factor. This measure, in addition to the percentage of energy contribution by each scale to the total energy, gives a complete picture about intermittency. The significance of the energy

percentage measurement is that it reveals the level of intermittency of energetic scales because a highly intermittent scale could be insignificant if its contribution to the total energy is small. Figures 5.7.a. and 5.7.b. show the intermittency factor and energy percentage contribution of each scale in the signals shown in figures 5.6.a. and 5.6.b., respectively. As expected, the intermittency factor is zero for the sinusoidal signal shown in figure 5.6.a. The total energy of the signal is captured in one scale at $m = 4$. The addition of smaller scale to the sinusoidal signal over 2.34% of the time is captured as 2% intermittency and recorded at smaller scale ($m = 7$) as shown in figure 5.7.b. The total energy of the signal is divided between the periodic scale (73% contribution) and the intermittent scale (27% contribution).

5.2.3 Wavelet representation of the relation between two intermittent variables

The other objective of this work is to establish if there is a relation between the velocity and the pressure on the roof of a building. In chapter 4, we established that Fourier-domain analysis could not adequately establish such a relation. Because wavelet analysis preserves temporal information, we will examine this relation in time-scale domain. As an example consider two signals that experience same variation at the same scale and time, or with a shift parameter if a time lag exist. One should expect that the product of the wavelet coefficients at that scale and time should be large. Figures 5.8.a. and 5.8.b. show two signals that exhibit same scale variation at two time intervals centered at times 4000 and 7700 second, their mean square representation is given in figures 5.9.a. and 5.9.b., respectively. The most energetic scales are captured at $m = 7$ and $m = 9$ at their respective appearance in time. Figure 5.10 shows the product of the wavelet coefficients of the two signals of figure 5.8. The results show that, except at times 4000 and 7700 seconds, where the signals experience the same scale variations the product is very small. Thus, the product of the wavelet coefficients can be used to determine if energetic or intermittent events in two signals take place at the same scale and same time.

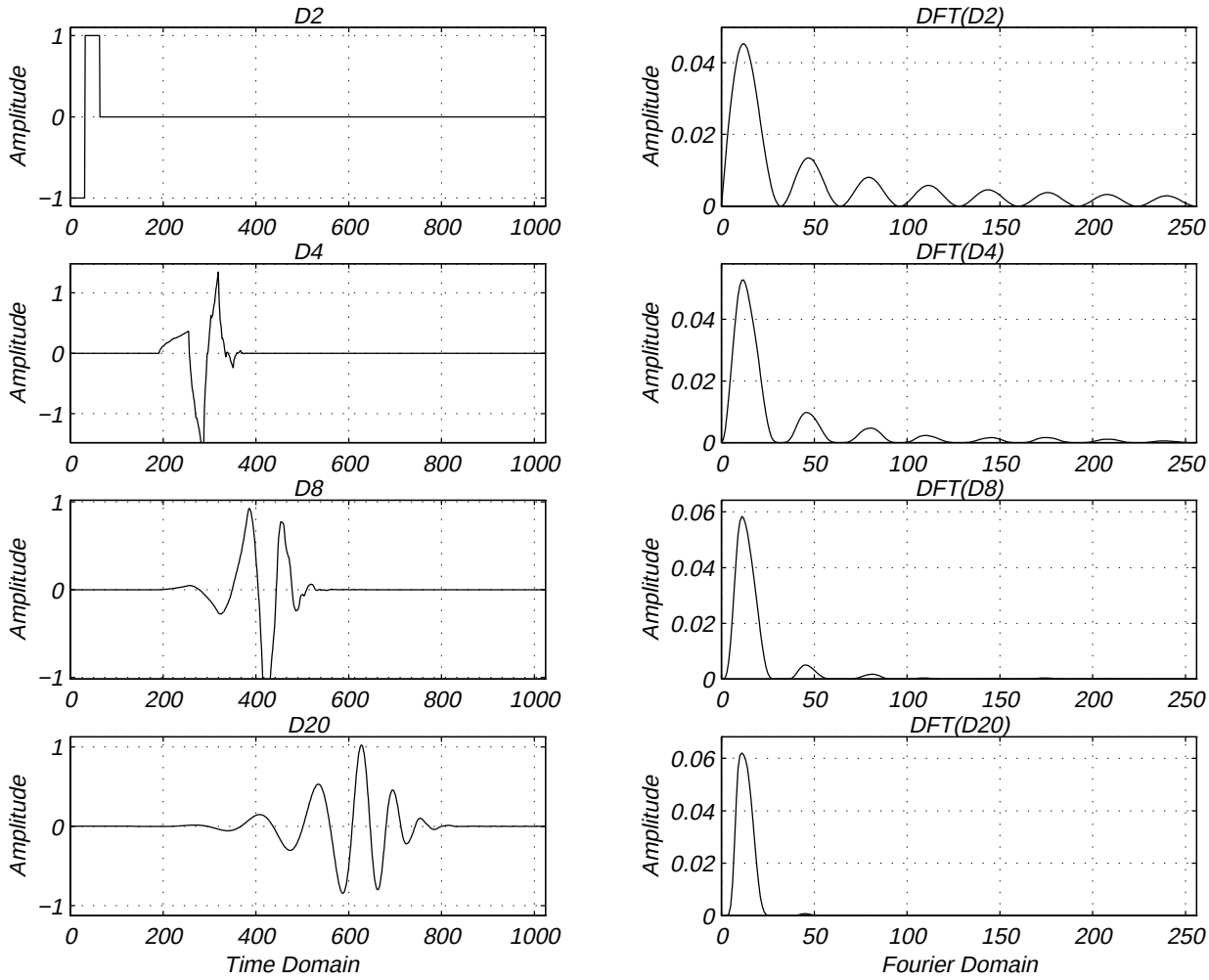

Figure 5.1: Daubechies D2, D4, D8 and D20 wavelets and their Fourier-domain transforms.

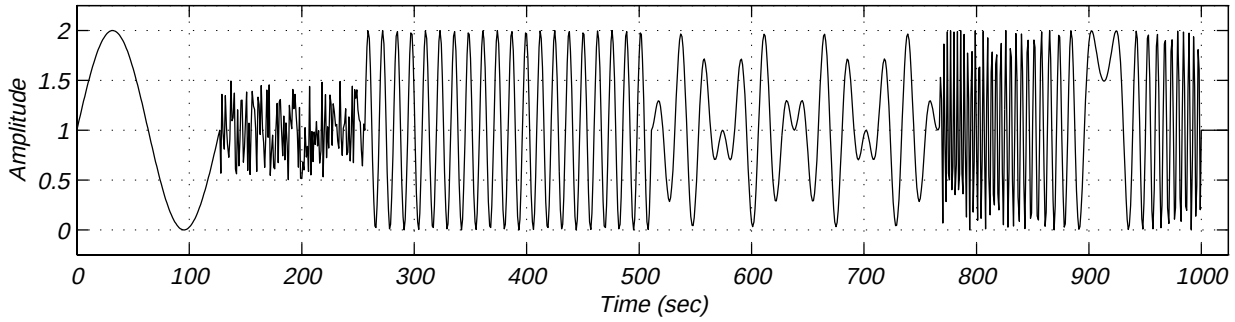

Figure 5.2: Time series of a simulated signal.

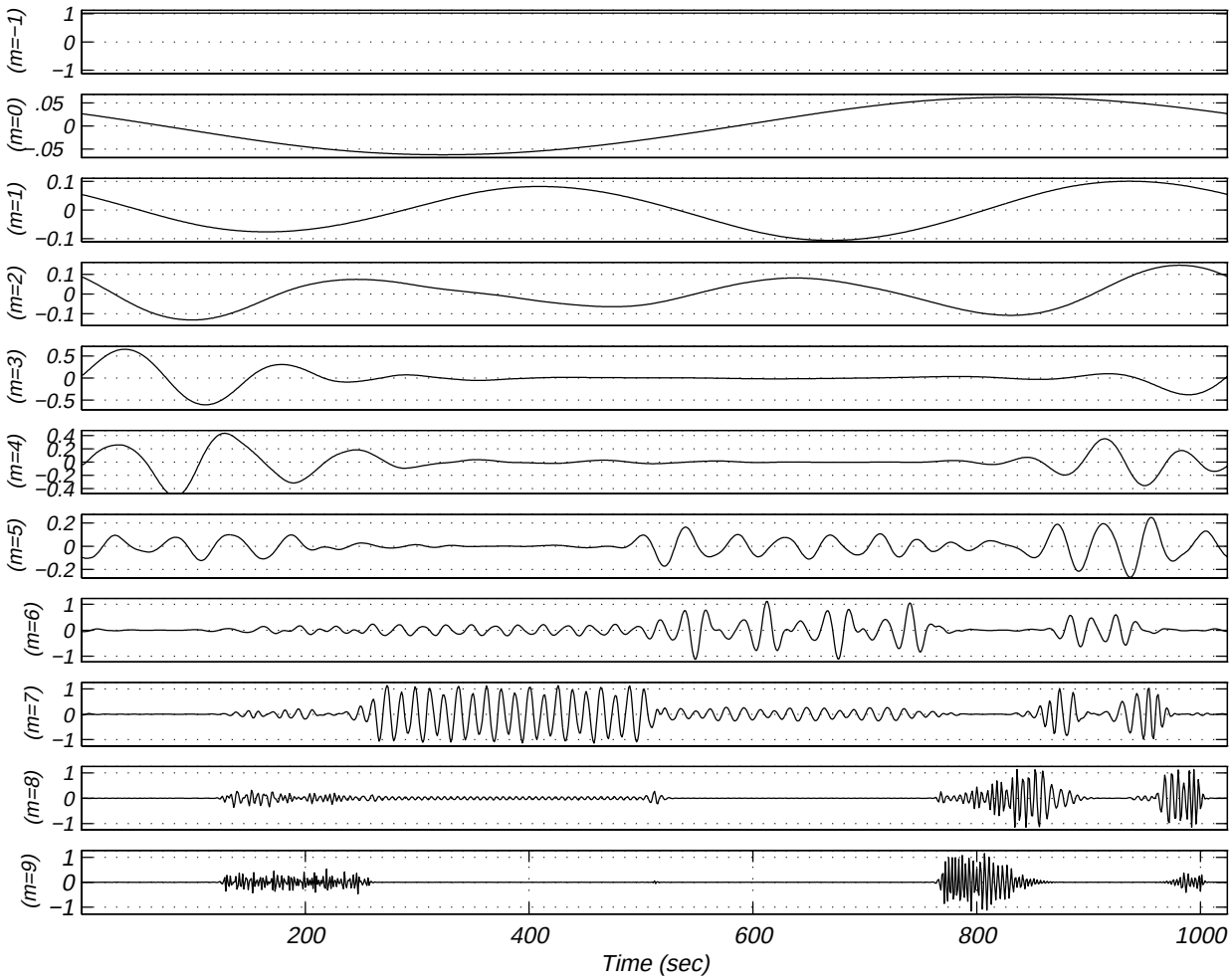

Figure 5.3: Decomposed 11 levels of the time series signal.

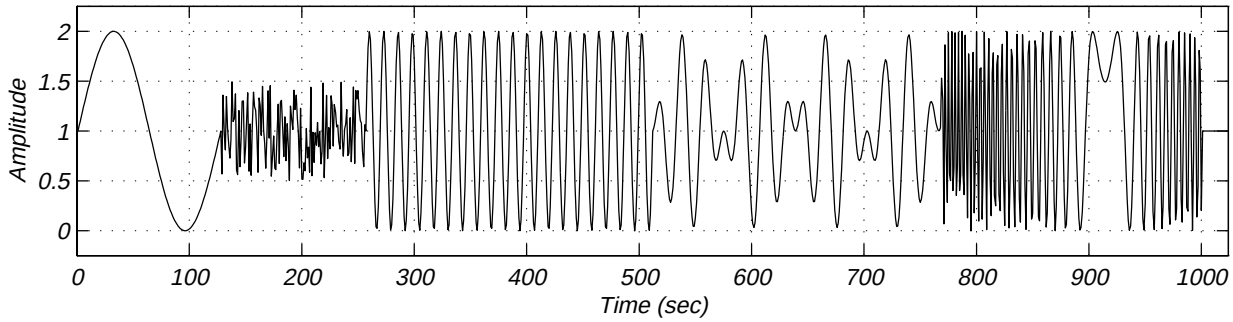

Figure 5.4: Reconstruction of the time series signal.

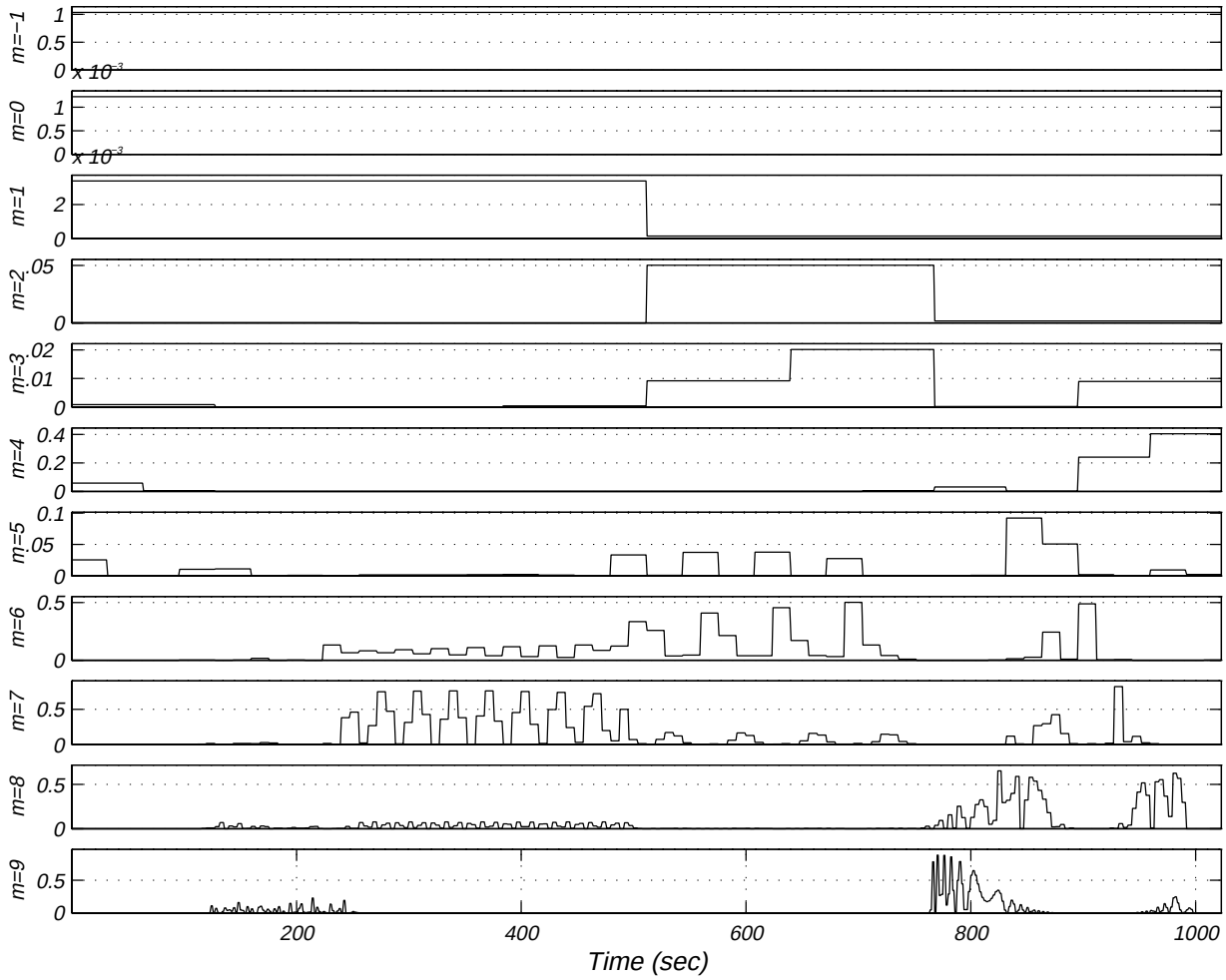

Figure 5.5: Energy representation of the time series signal.

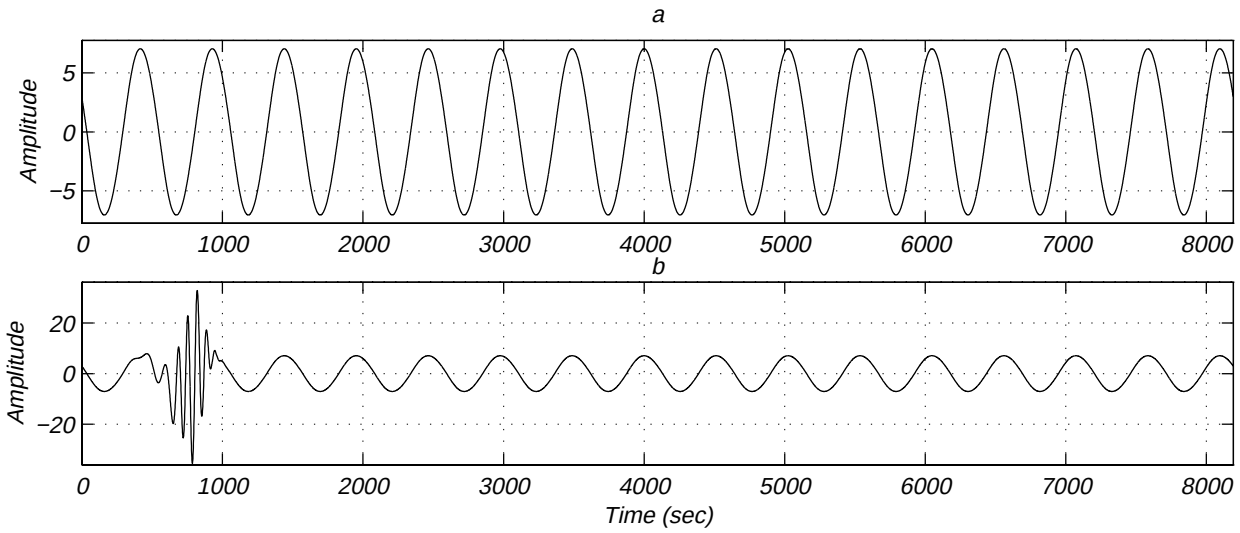

Figure 5.6: Intermittent time series signals.

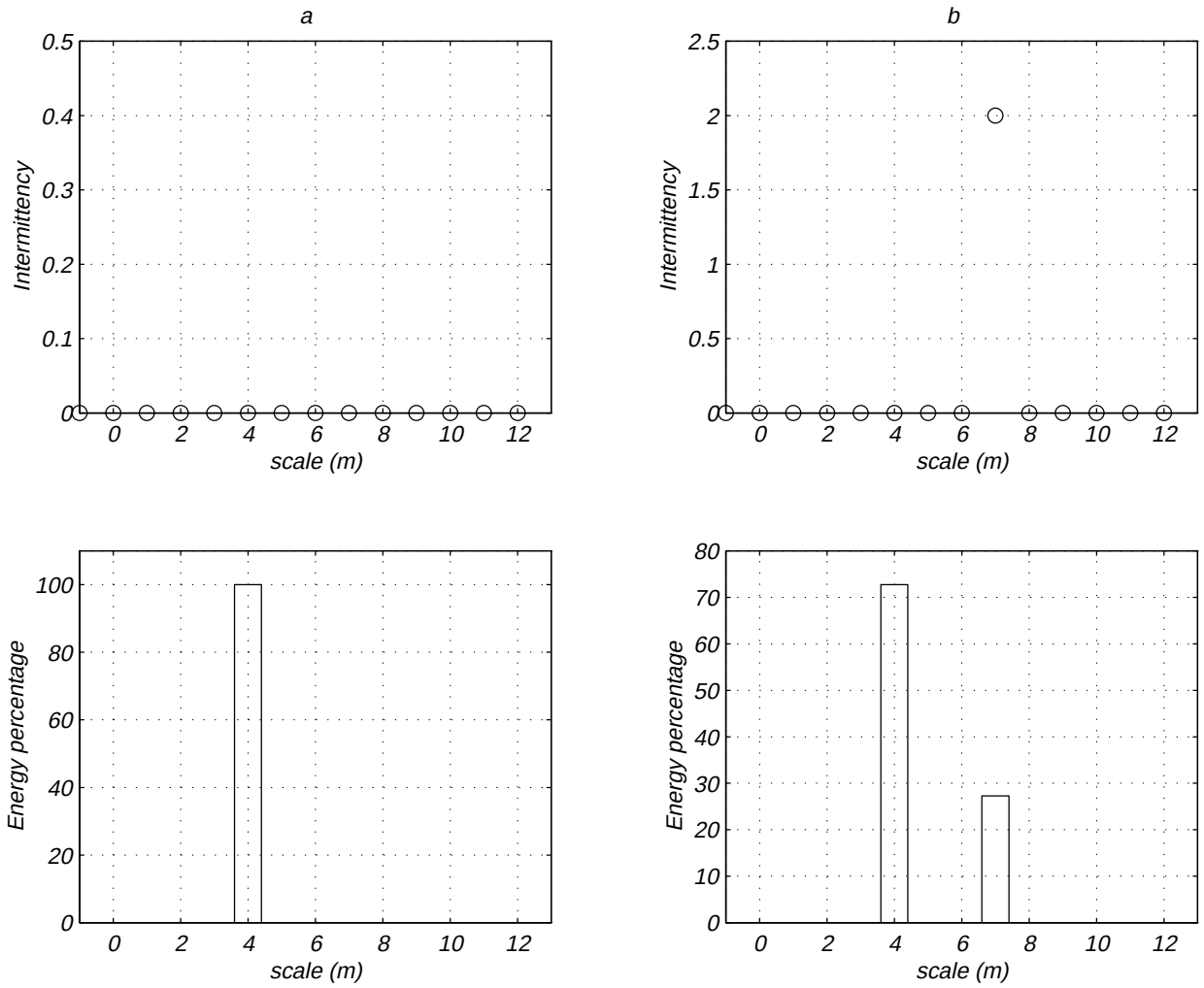

Figure 5.7: Intermittency factor and energy percentage contributions for all scales of the signals in figures 5.6.a. and 5.6.b.

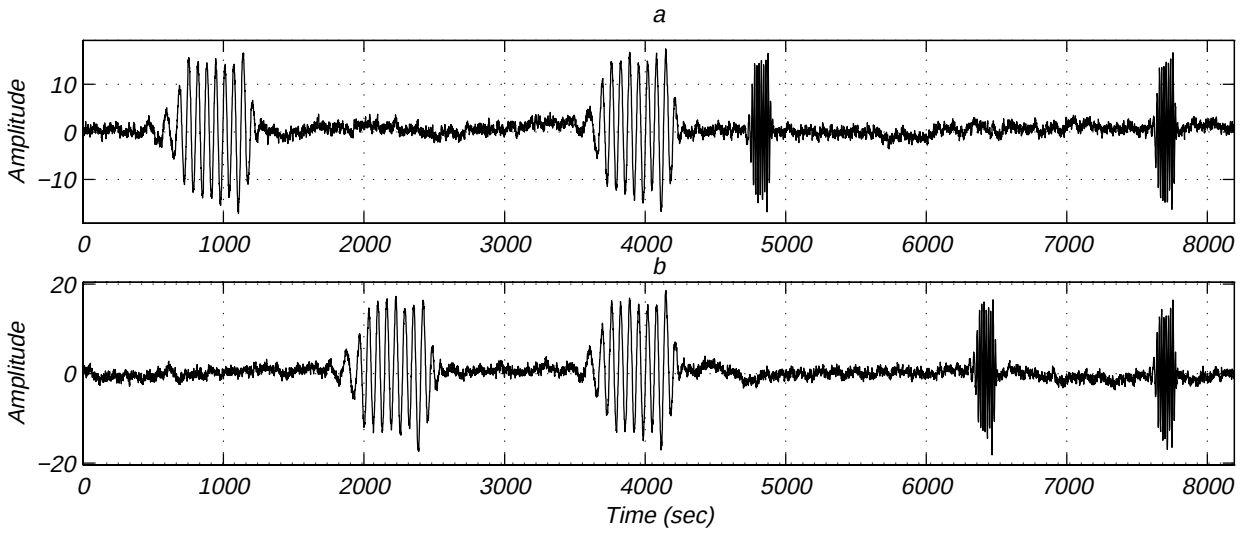

Figure 5.8: Two signals experience variation at the same scale at different times.

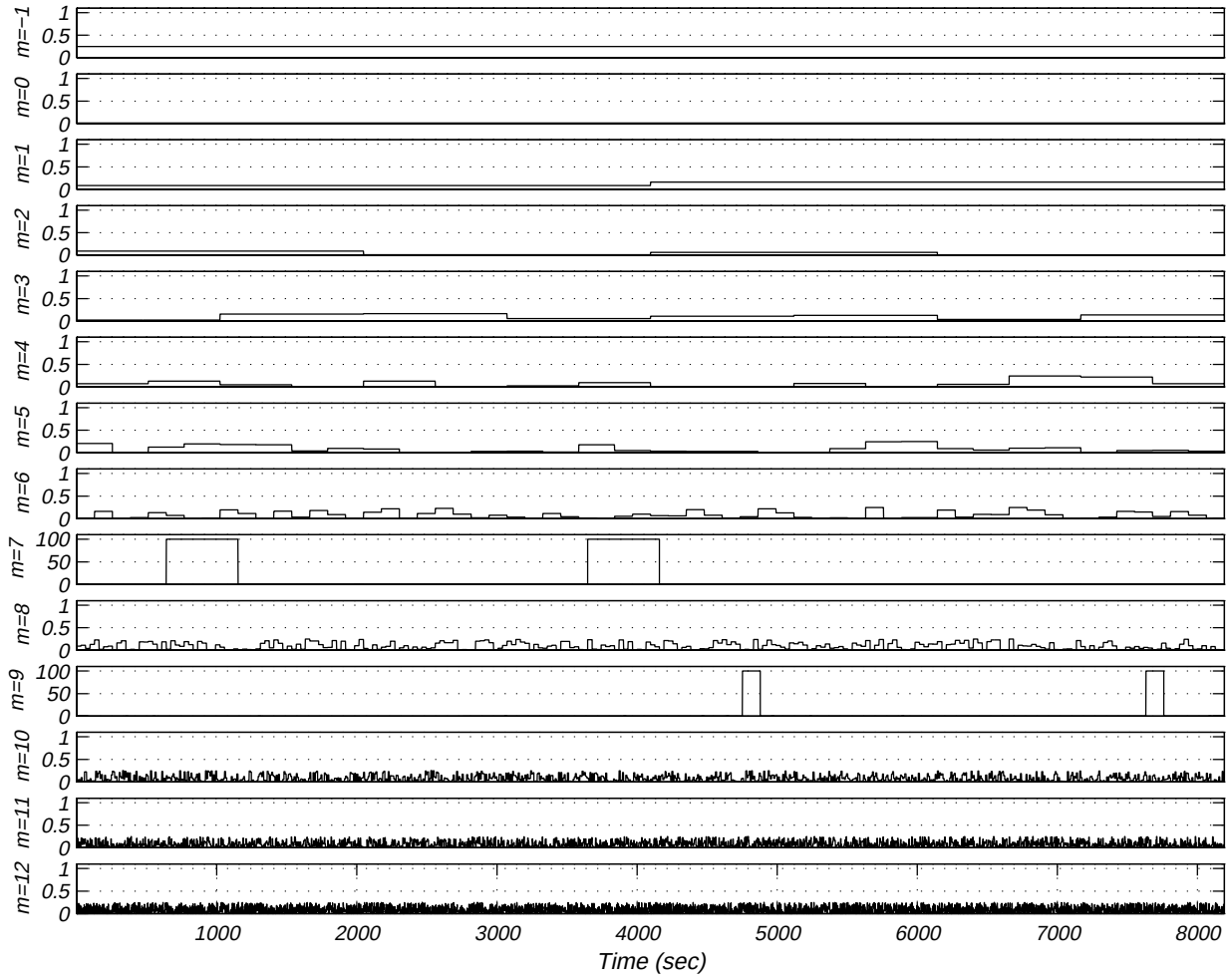

Figure 5.9a: Mean square representation of the 5.8.a. signal.

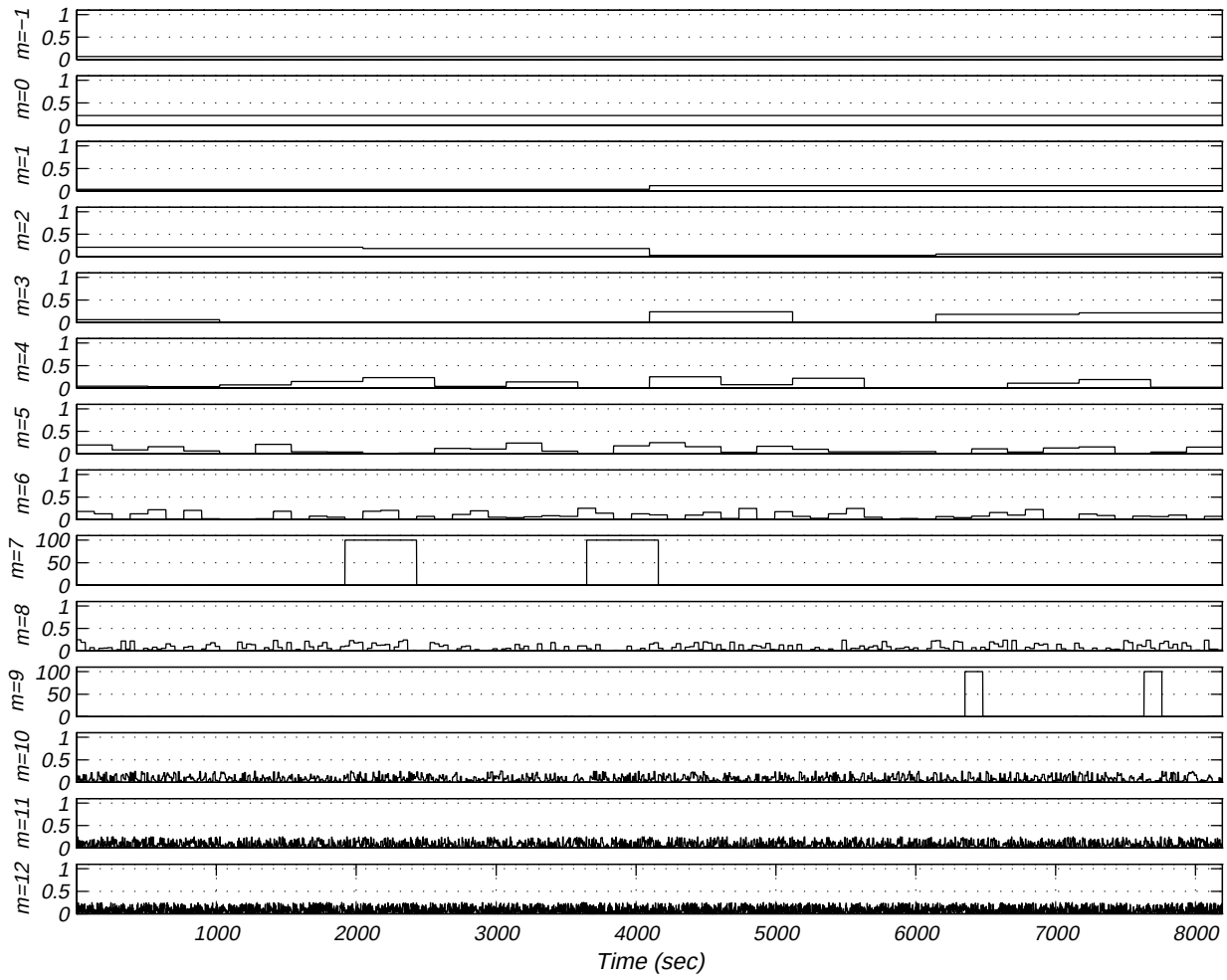

Figure 5.9b: Mean square representation of the 5.8.b. signal.

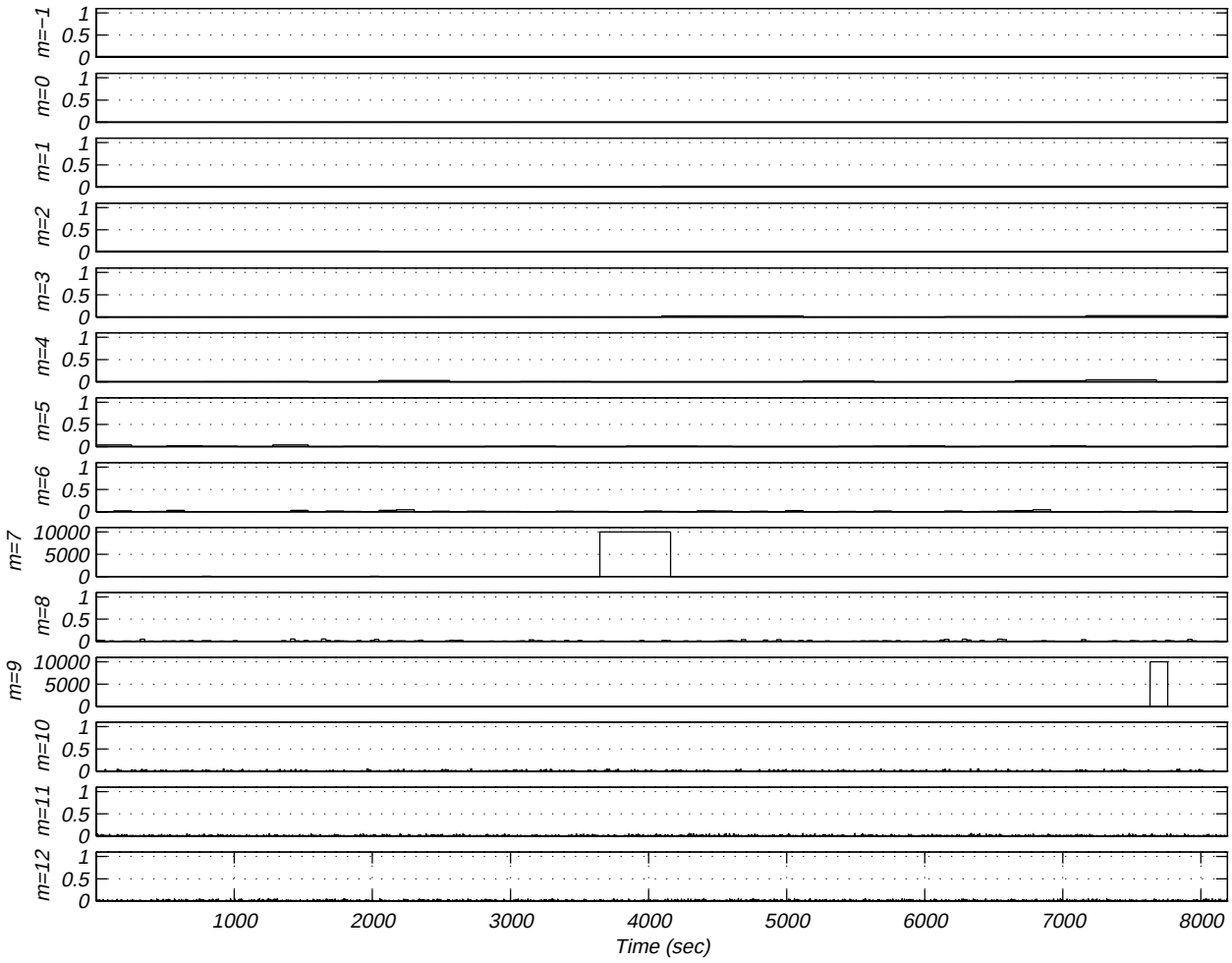

Figure 5.9: Mean square representation of both 5.8.a. and 5.8.b. signal.

Chapter 6

Wavelet Analysis of Turbulence in Atmospheric Boundary Layer

We have established that peak pressure coefficients, which are related to extreme wind loading, depend on the characteristics of the atmospheric turbulence. The atmospheric turbulence is usually made up of coherent structures that can be localized in time and/or space. Thus, it is fair to assume that the turbulence of the atmospheric boundary layer is, in general, nonstationary or nonhomogeneous and one could treat turbulence as an intermittent phenomena. This argument provides our motivation for characterizing atmospheric turbulence with the concept of intermittency.

Understanding turbulence by studying its intermittent behaviour is not a totally new idea. Sandborn [1959] used bandpass filtering to examine intermittency characteristics of a laboratory boundary layer. Conditional sampling has been used to characterize intermittency in fluid flows. As we have explained in the previous chapters, the traditional Fourier spectra, which involves time averaging of moments of data, cannot be applied to obtain time varying characteristics. In this chapter, we use wavelet theory to characterize atmospheric turbulence by an intermittency factor. This factor is based on the variation of the energy content of the atmospheric turbulence scales with time. Such information contributes to our understanding of turbulence in the atmospheric wind and establishes a quantitative value that might need to be simulated in wind tunnels for the purpose of predicting extreme pressure coefficients.

6.1 Wavelet Analysis of Velocity Components of the Surface Layer

Unlike the Fourier transform that maps a time series to a spectrum, the wavelet transform maps the time series to a two-dimensional domain that shows the evolution of scales with time. Figures 6.1 through 6.4 show the $u-$ and $v-$ velocity components of records M15N468, M15N471, M15N086 and M15N087 runs. These records were obtained using a cup-vane anemometer with a 40Hz sampling frequency, yet low-pass filtered at 10Hz, and were taken at WERFL at Texas Tech on February 17^{th} 1992 between 6:37 a.m. and 7:28 a.m. for the M15N468 and M15N471 runs and on April 28^{th} 1991 between 1:11 p.m and 1:45 p.m for the M15N086 and M15N087 runs. By examining the time series of these velocity components, one notices a degree of intermittency or nonstationarity. By intermittency, we mean the presence of specific features such as a peak over a short period of time or a fast increase or drop in magnitude. One could define an intermittency factor, according to the technique presented in chapter 5, for the whole signal. However, we should note that the signal is composed of a wide range of scales or frequencies and it would be better to define an intermittency factor for individual scales. As explained in chapter 5, wavelet analysis allows us to define intermittency factor for each scale.

The Daubechies wavelets as described in chapter 5, were applied to analyze the velocity time records shown in figures 6.1 through 6.4. Each of these records comprises 8192 samples and has a length of 819.2 seconds. Hence, the largest scale that can be characterized is given by m=0 and corresponds to 819.2 seconds (about 0.001 Hz) and the smallest scale is given by m=12 and corresponds to 0.2 seconds (about 5 Hz). Table 6.1 shows the scale index m, scale duration in seconds and frequency range covered by each scale based on our analysis. Analyzing these signals as such is analogous of applying a narrow band-pass filter to the record and determining the energy content over the frequency range of the band pass filter. The next scale implies doubling the center frequency of that filter, applying it to both halves of the signal and determining energy content of these halves. This procedure is repeated by doubling the filter center frequency and applying it onto the equal signal portions until the lowest number of sample points, i.e. two, is reached.

Table 6.1: Scale index and corresponding frequency range.

Scale index (m)	Number of wavelets	Scale duration (sec.)	Center Freq. (Hz)
m=-1	signal mean value	-	-
m=0	1	819.2	$1.22E^{-3}$
m=1	2	409.6	$2.44E^{-3}$
m=2	4	204.8	$4.88E^{-3}$
m=3	8	102.4	$9.77E^{-3}$
m=4	16	51.2	$1.95E^{-2}$
m=5	32	25.6	$3.91E^{-2}$
m=6	64	12.8	$7.81E^{-2}$
m=7	128	6.4	$1.56E^{-1}$
m=8	256	3.2	$3.13E^{-1}$
m=9	512	1.6	$6.25E^{-1}$
m=10	1024	0.8	1.25
m=11	2048	0.4	2.50
m=12	4096	0.2	5.00

Figures 6.5 through 6.8 show the time series of the velocity fluctuations and corresponding magnitudes of the wavelet coefficients for scales m between 1 and 12. Notice that the scale represented by m=1 corresponds to 409.6 seconds and can only be captured twice in a record 819.2 seconds long. As m increases and the scale size decreases more variations in the magnitudes of the wavelet coefficients of the scale can be detected. A close look at these figures show two important points. First, figures 6.5.a, 6.6.a, 6.7.a and 6.8.a show that, for the $u-$component, coefficients of scales with m between 5 and 9, which correspond to frequencies between 0.039 and 0.625 Hz, have the largest magnitudes. On the other hand, the analysis shows that, for the $v-$component, the coefficients with duration less than 6.4 seconds ($m < 7$)have the largest magnitudes. We should note here that the larger coefficient magnitude does not translate into larger contribution to the mean-square value. The reason being that the contribution of each scale involves time integration, see equations 5.7 and 5.9. This notion is very important, because while the large scales have the large contribution to the mean-square value the smaller scale ($m = 5$ to 9 for the $u-$component and $m > 7$ for the $v-$component) might have at certain times larger wavelet coefficients than the large scales. Consequently, these scales are highly intermittent, i.e., at certain times, they might have significant contribution to the turbulence content of the atmospheric flow. Second, it is

obvious from the plots that scales of both $u-$ and $v-$components are highly intermittent. By intermittency, we mean that the magnitude of the wavelet coefficients of a certain scale varies significantly with time. In the next section we propose to quantify the level and duration of energy "pulses" at different scales by the intermittency factor as introduced in section 5.2.2. The role of these pulses in generating negative pressure peaks will be examined in chapter 7.

6.2 Intermittency in Atmospheric Turbulence

6.2.1 Analysis Procedure

In general, intermittency means the occurrence of relatively short irregular bursts in a long regular signal. Such a definition of intermittency has been mostly used in chaos to explain the transition from regular, such as laminar, to chaotic, i.e., turbulent motion. Based on this understanding, intermittency can be defined as the fraction of time the magnitude of a fluctuating signal exceeds some predetermined level, thereby implying that the energy is not evenly distributed in time. Consequently, here we define intermittency factor, as the percentage of time a signal sees the variable in its high energy state.

As explained in the previous sections, one could define an intermittency factor for $u-$ and $v-$ velocity components. Yet, because turbulence fluctuations contain different scales and because these scales range over several orders of magnitude, we have opted to define an intermittency factor for each scale in the $u-$ and $v-$ components. Moreover, in order to estimate the percentage of time where these scales are in their higher amplitude state, it is necessary to define a threshold value and time of integration of energy. In this work, the threshold is defined as twice the average energy content of the scale. The time of integration is taken to be equal to the duration over which the higher energy state takes place. Furthermore, a total energy measure of a certain scale is important because intermittency of high-energy scales should be more important than the intermittency of low-energy scales. Thus, in this work we present the following quantities. The first quantity is the percentage of the total energy each scale contains. This representation is similar to the normalized power spectra because it involves integration over time. The second quantity is the intermittency factor which

defined by the percentage of time a scale is in its higher energy state. The third quantity is the percentage of energy of each scale that is contained during intermittent events. These quantities will not only give relative energy levels of different scales as would be the case of a frequency spectrum they will also give a measure of the time variations in the energies of these scales.

6.2.2 Intermittency Factor

Records M15N468, M15N471, M15N086 and M15N087 were analyzed according to the above procedures. The results are shown in figures 6.9, 6.10, 6.11 and 6.12, respectively. Included in these figures are the percentage of total energy contained in each scale, the intermittency factor and the percentage of energy contained during intermittent events. By examining the energy content of the different scales in the $u-$component of the wind for the four records, it is easy to notice that the percentage of total energy contained in each scale varies with time. This variation implies that the records are nonstationary and is consistent with the results of chapter 3. Yet, one should note that in general most of the energy is contained in scales with m between 2 and 8. Each scale contains somewhere between 10 and 20% of the total energy of the signal. The energy content of the different turbulence scales in the $v-$component exhibits the same characteristics as that of the $u-$components. In general, the percentage of total energy of each scale is different from one record to the other. Yet, it is obvious that most of the energy is contained in scale with m exceeding 2. One should note here that the energy seems to be more evenly distributed among the scales of the $v-$component than among the scales of the $u-$component. Another important note to make is that the small scales ($m > 8$) in the $v-$component contain higher percentage of energy than the $u-$components. This is possibly due to local isotropy.

Figure 6.9, 6.10, 6.11 and 6.12 show also the intermittency factor. This factor gives the percentage of time the wavelet coefficient of a particular scale is larger than twice its average value. The results show that, for the $u-$component, scales with m between 2 and 10 have consistently an intermittency factor between 15% and 25%. For the $v-$component, the intermittency plots show that scales with m above 2 have an intermittency factor of about

15%. Besides measuring the intermittency factor, we show the percentage of the energy of each scale contained during the intermittent events. The results show that about 60 to 70 percent of the energy of each scale appears in less than about 15% to 25% of the time. This result is very important because it shows that in both the $u-$ and $v-$components of the atmospheric wind, most of the energy of the different scales appears in short periods of time. These results are important because simulating such events or turbulence with such characteristics might be necessary for accurate prediction of pressure peaks. These results are also important because they show that considering averaged energy values, as would be estimated from the power spectrum, is not sufficient. We will now study the relation between the high energy events in the wind and the negative pressure peaks.

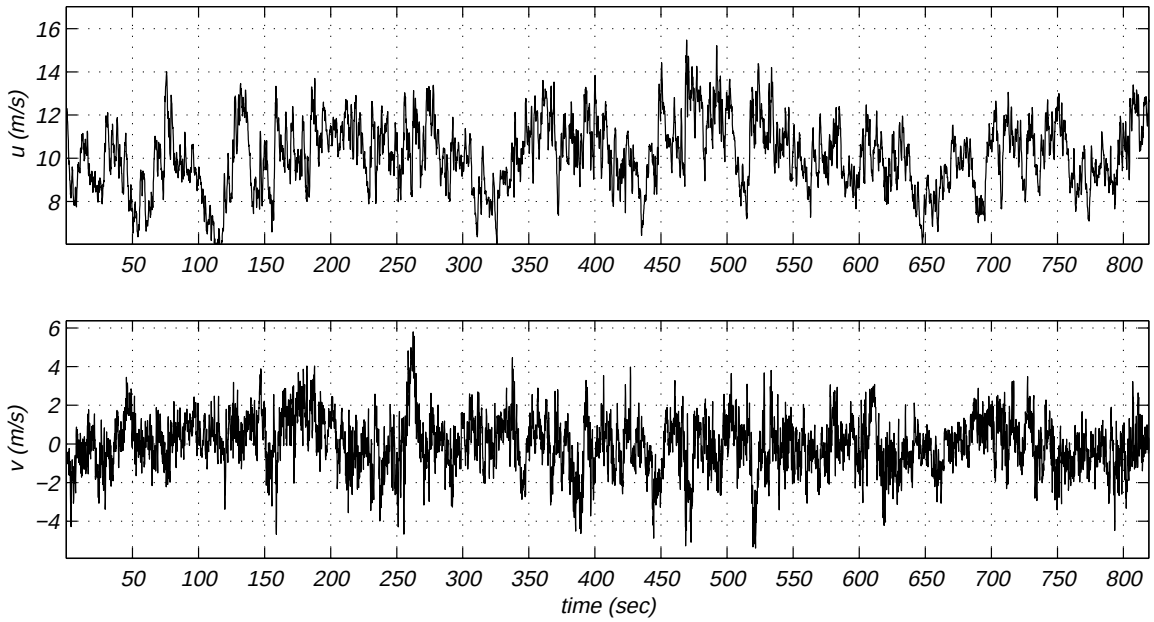

Figure 6.1: Time series of u- and v- velocity components for M15N468 run.

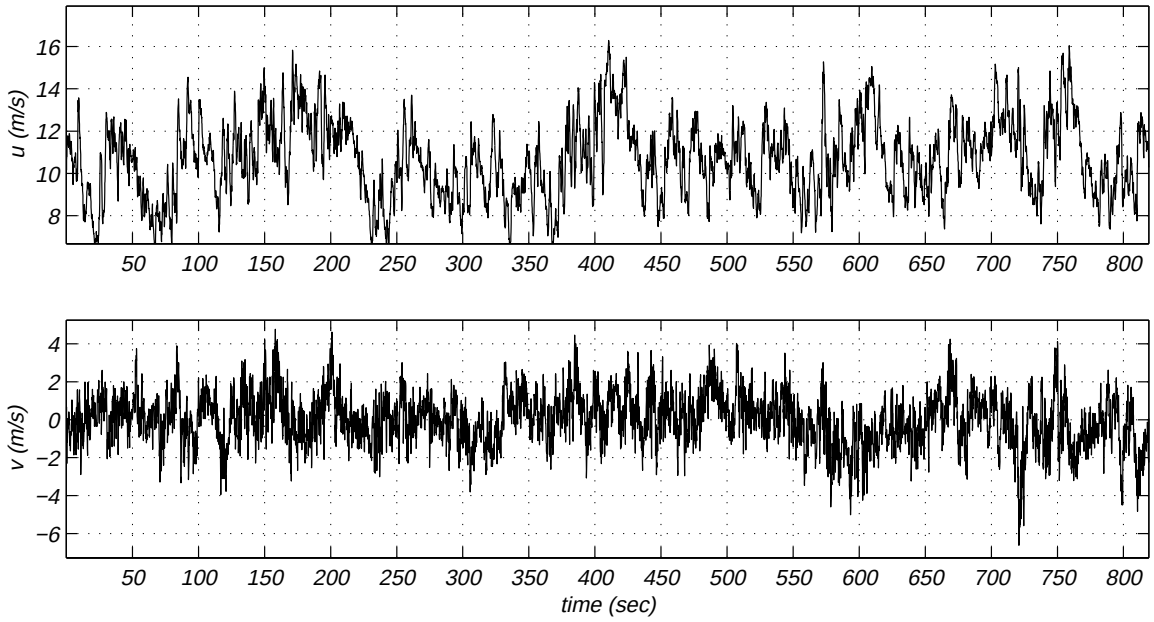

Figure 6.2: Time series of u- and v- velocity components for M15N471 run.

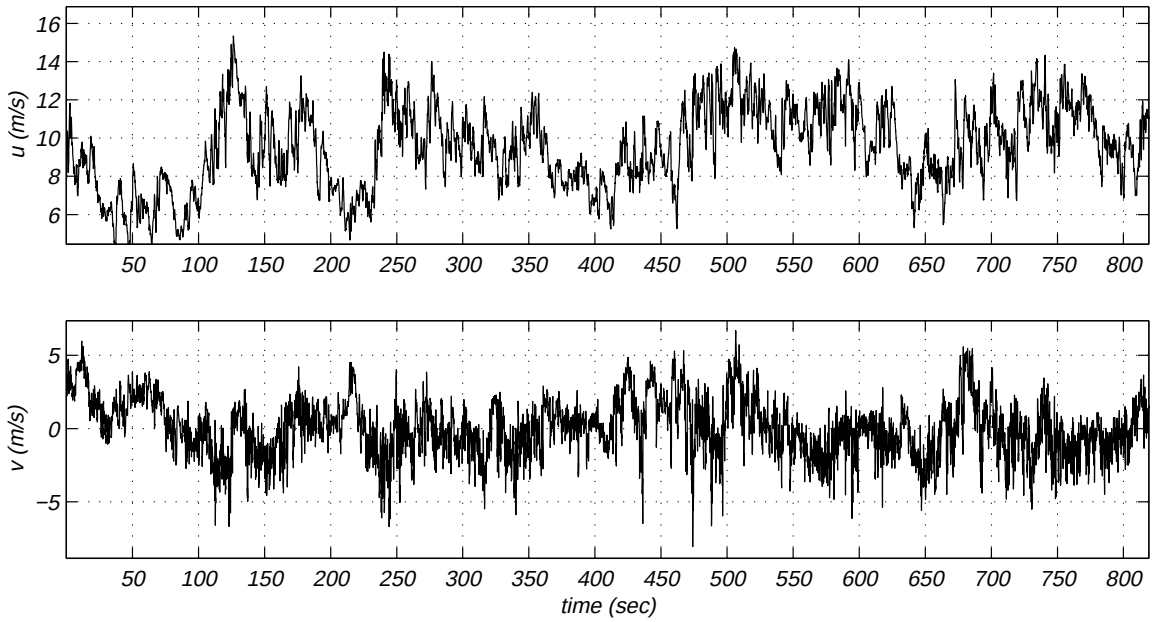

Figure 6.3: Time series of u- and v- velocity components for M15N086 run.

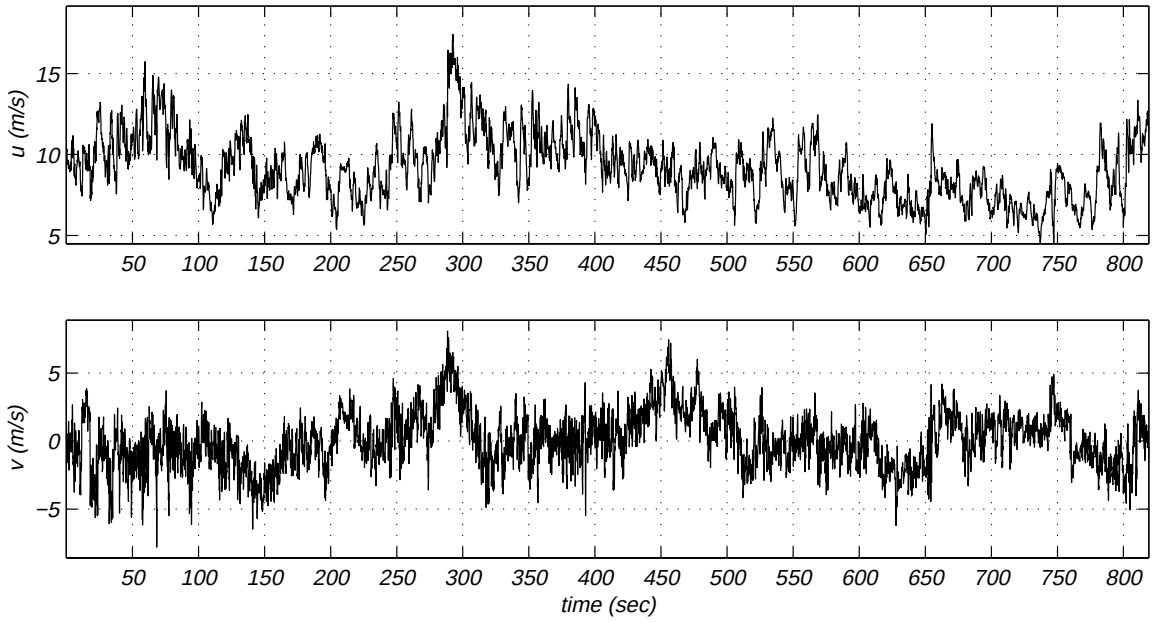

Figure 6.4: Time series of u- and v- velocity components for M15N087 run.

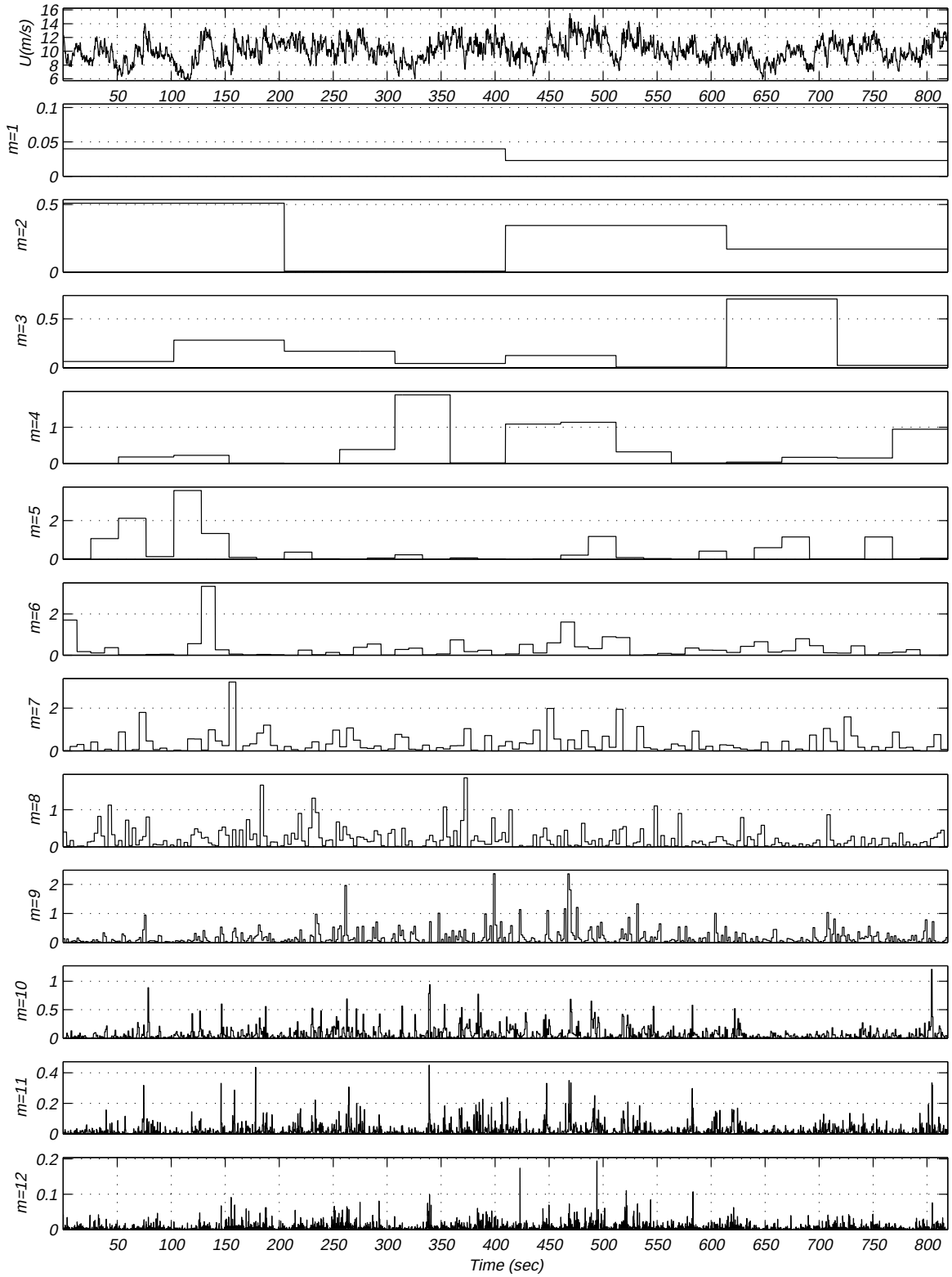

Figure 6.5a: Wavelet coefficients of the longitudinal velocity component for record M15N468.

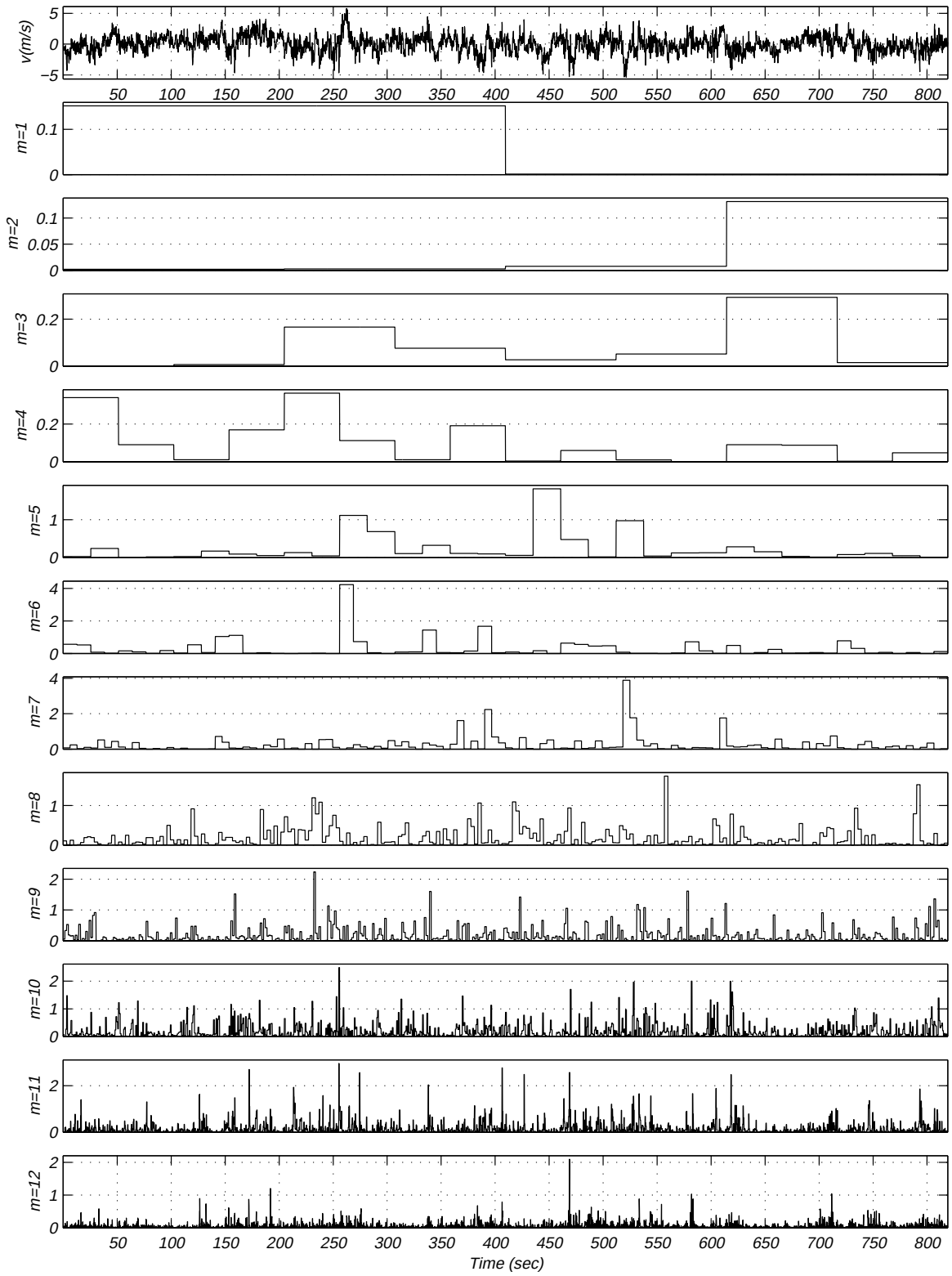

Figure 6.5b: Wavelet coefficients of the lateral velocity component for record M15N468.

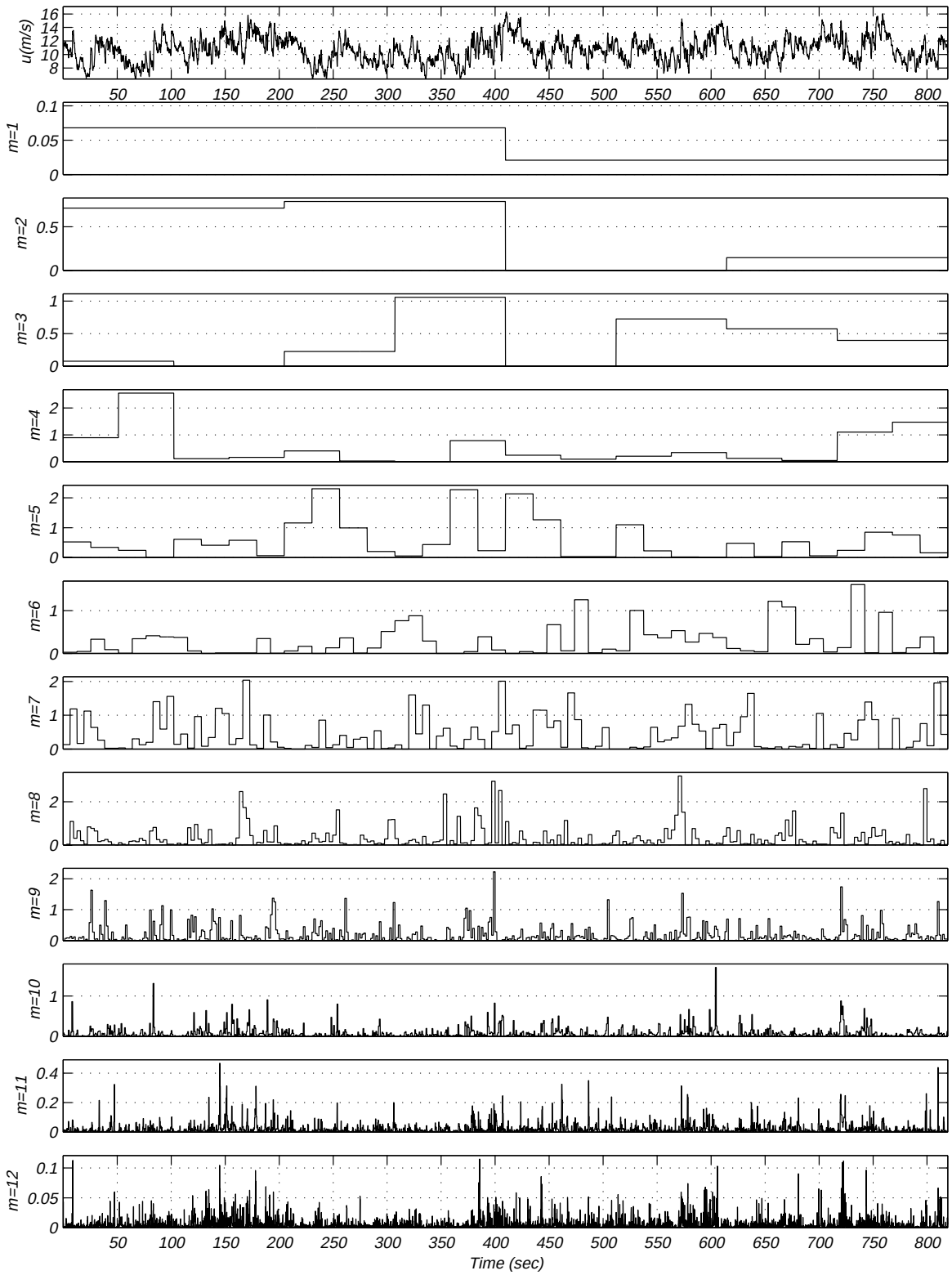

Figure 6.6a: Wavelet coefficients of the longitudinal velocity component for record M15N471.

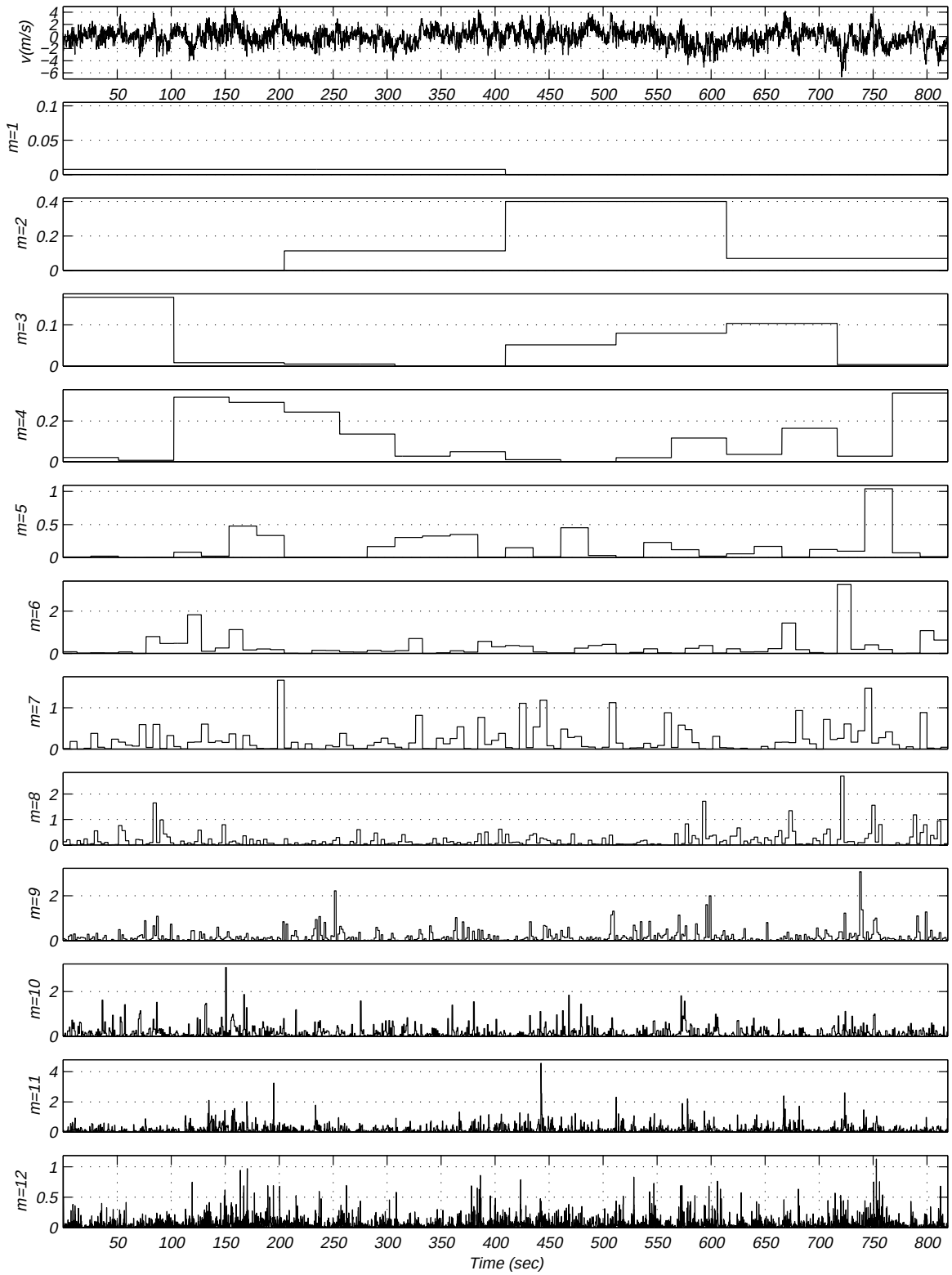

Figure 6.6b: Wavelet coefficients of the lateral velocity component for record M15N471.

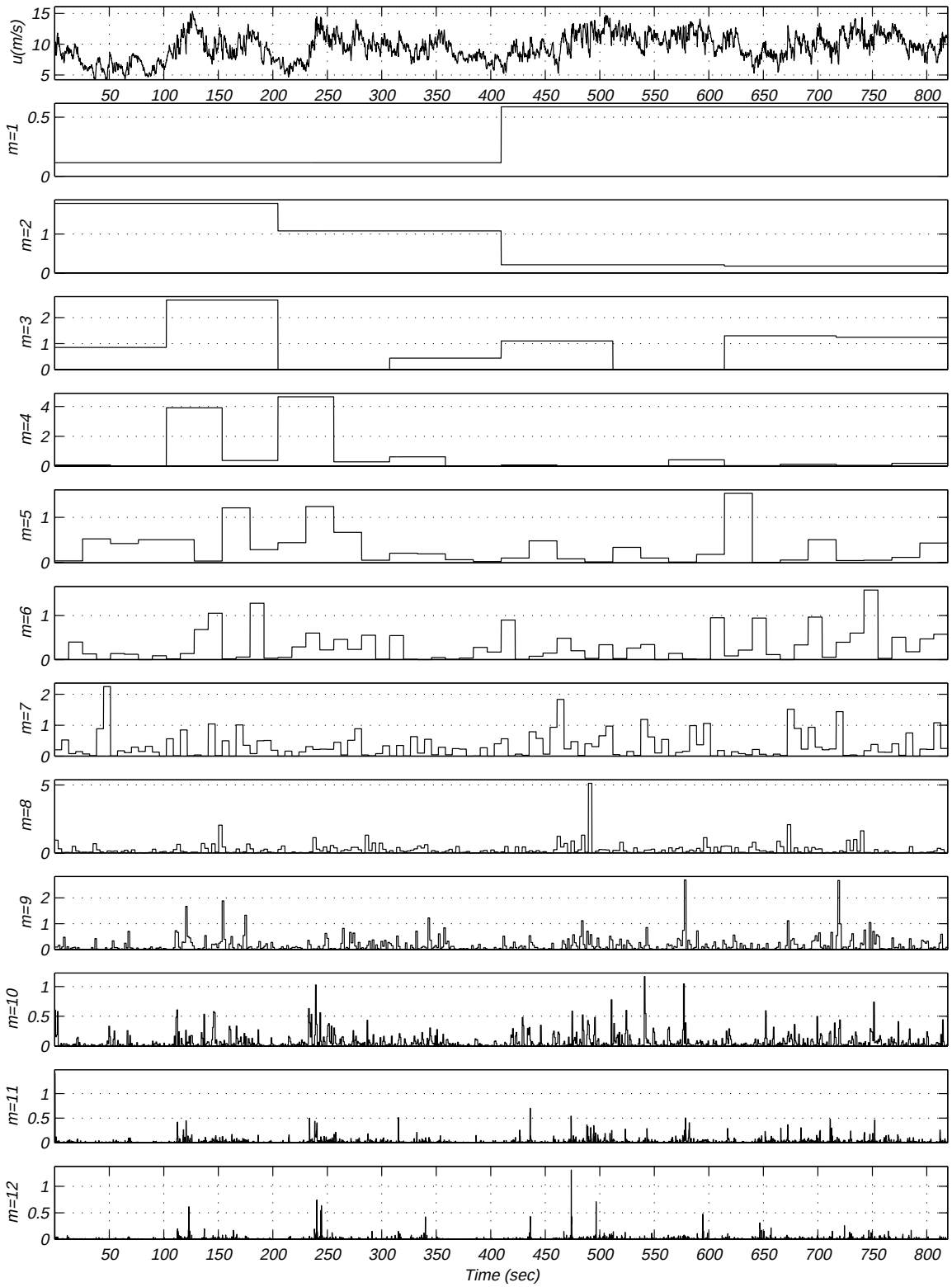

Figure 6.7a: Wavelet coefficients of the longitudinal velocity component for record M15N086.

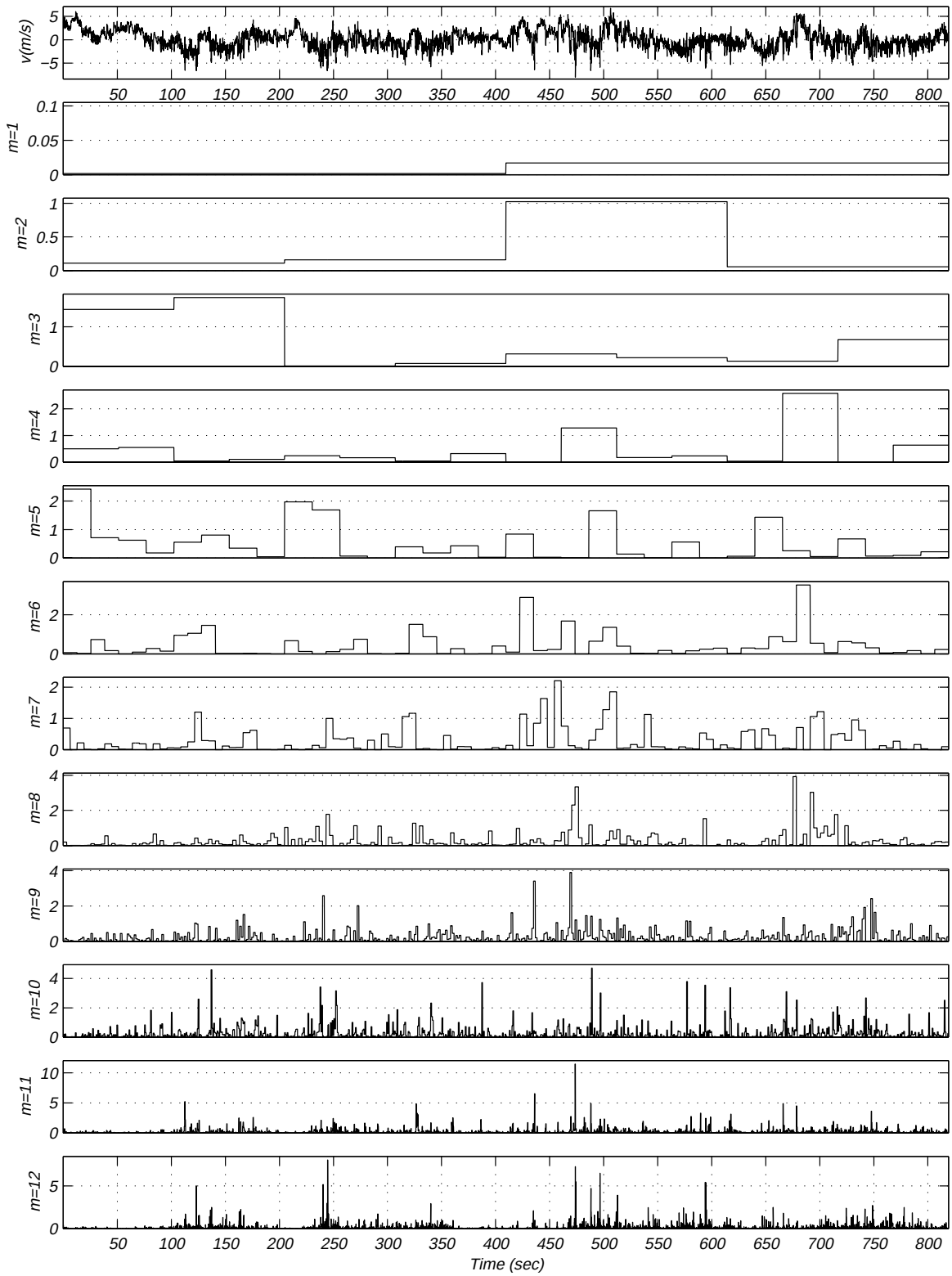

Figure 6.7b: Wavelet coefficients of the lateral velocity component for record M15N086.

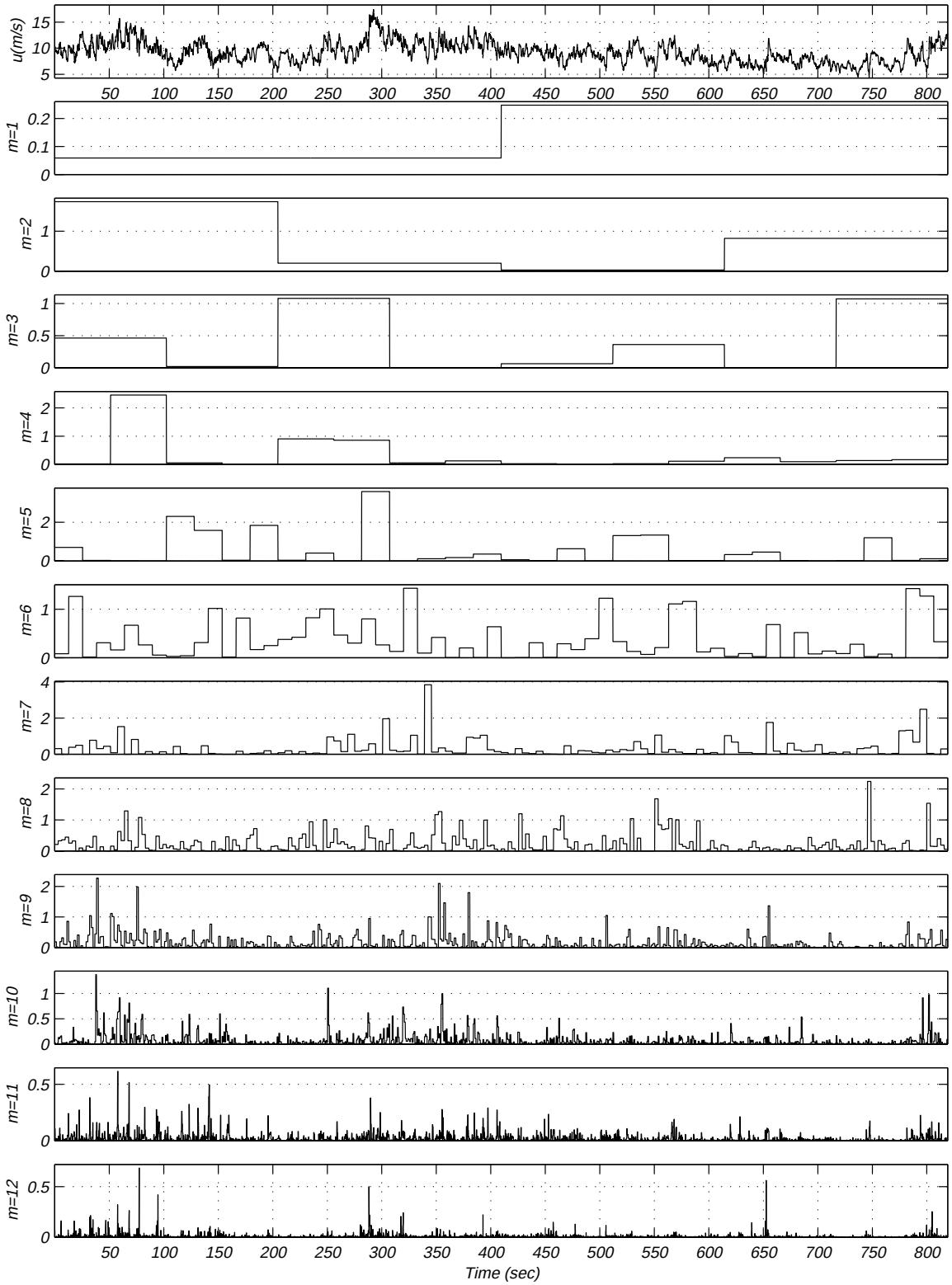

Figure 6.8a: Wavelet coefficients of the longitudinal velocity component for record M15N087.

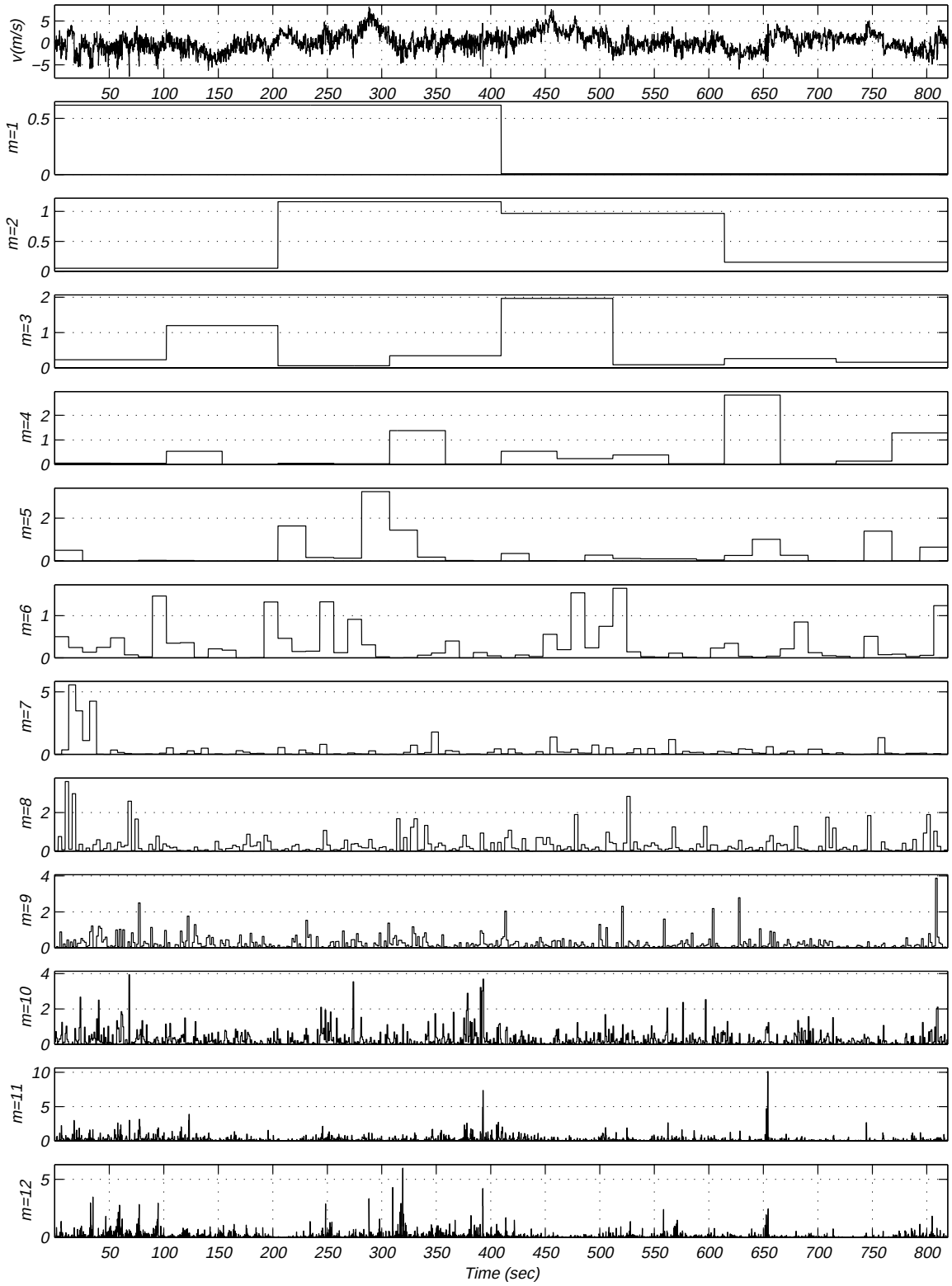

Figure 6.8b: Wavelet coefficients of the lateral velocity for record M15N087.

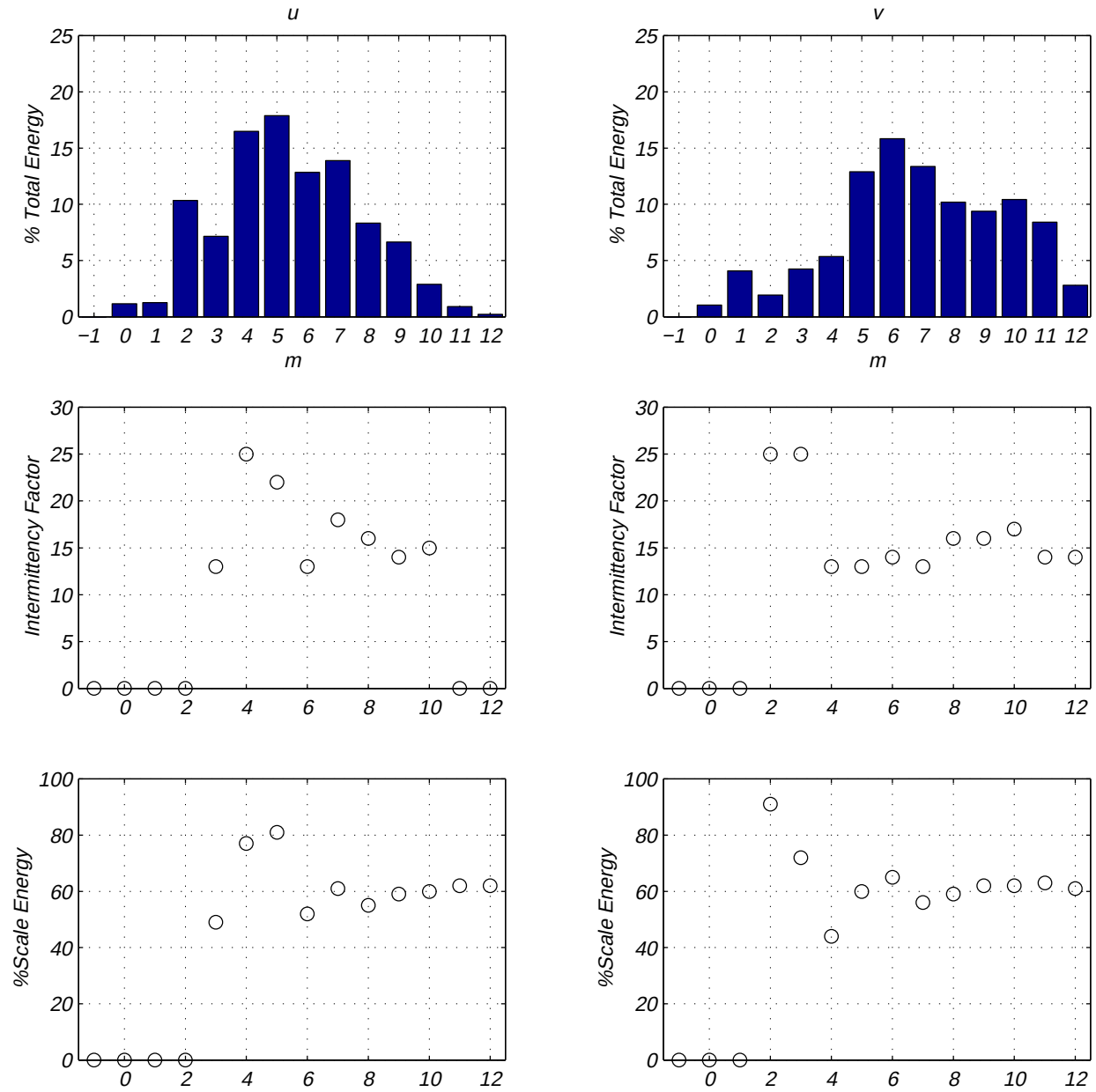

Figure 6.9: Total Energy, Intermittency Factors and % Intermittent Energy in scales of $u-$ and $v-$velocity components for record M15N468.

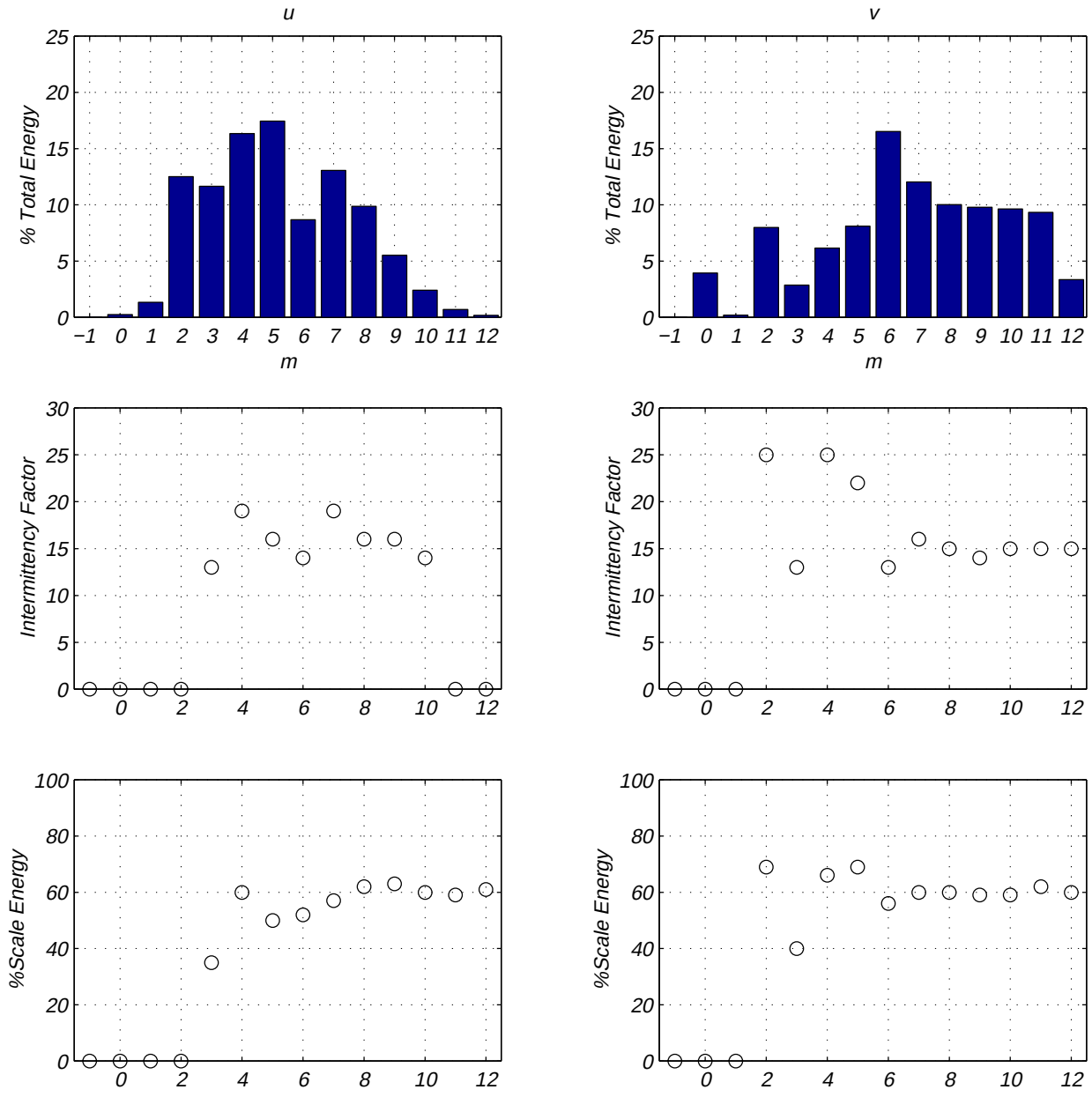

Figure 6.10: Total Energy, Intermittency Factors and % Intermittent Energy in scales of $u-$ and $v-$velocity components for record M15N471.

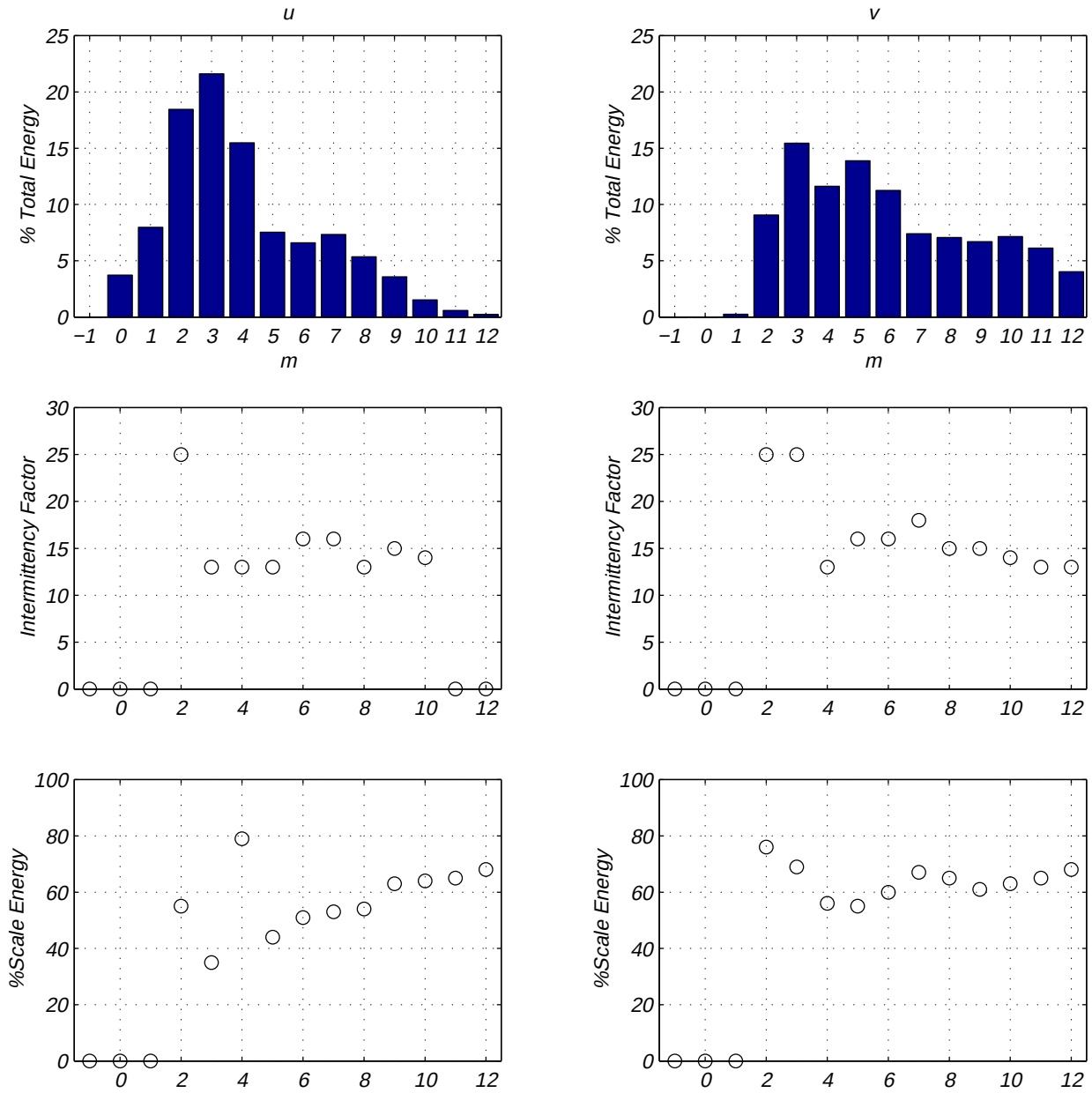

Figure 6.11: Total Energy, Intermittency Factors and % Intermittent Energy in scales of $u-$ and $v-$velocity components for record M15N086.

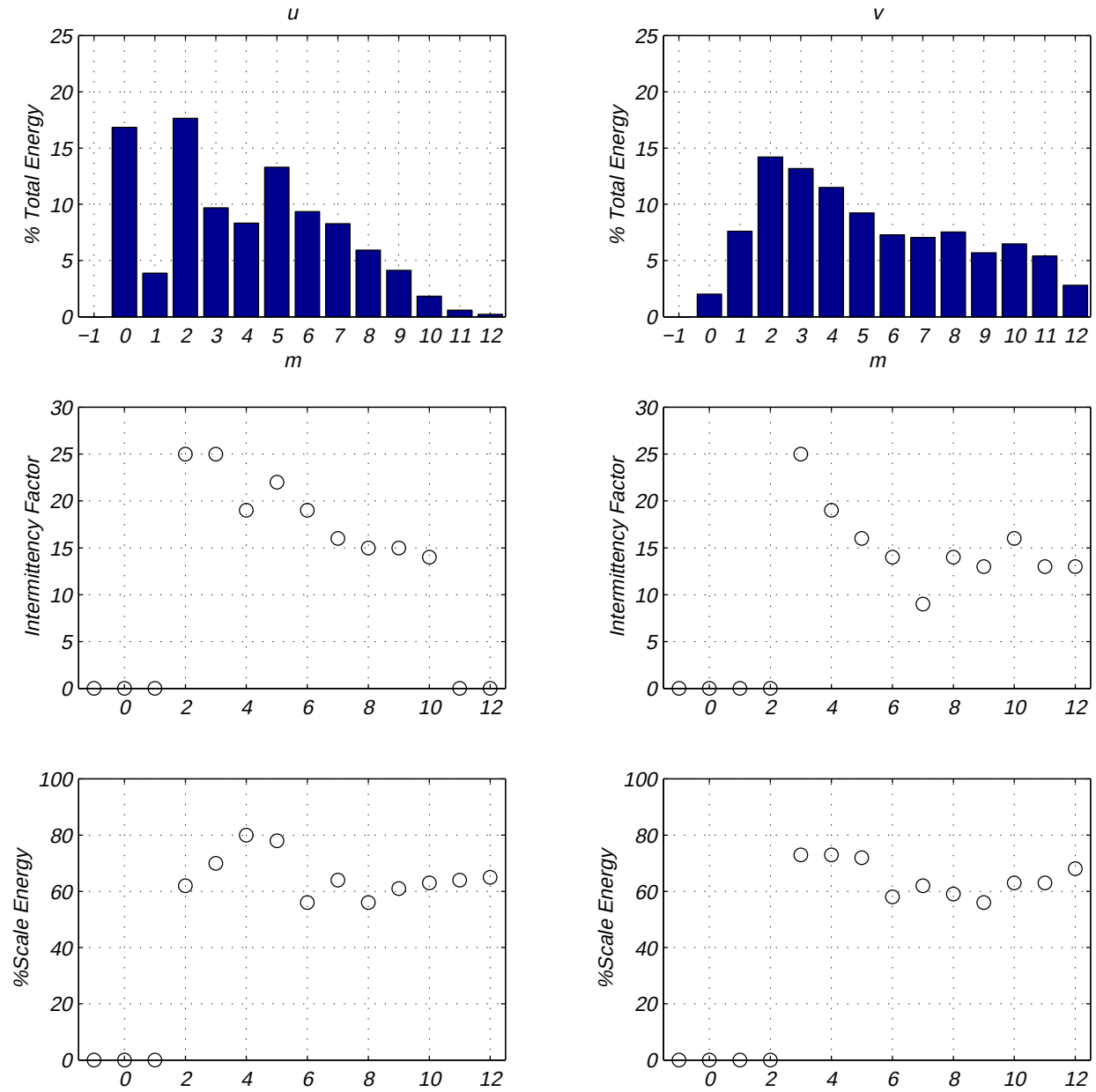

Figure 6.12: Total Energy, Intermittency Factors and % Intermittent Energy in scales of $u-$ and $v-$velocity components for record M15N087.

Chapter 7

Wavelet Analysis of Pressure Coefficients and Velocity-Pressure Relation

This chapter aims at providing answers to two fundamental questions. The first being, which scales in the pressure fluctuations are associated with low pressure peaks? This question is important because it determines the pressure scales which are associated with pressure peaks of a certain duration. The second question is: Are the scales associated with low-pressure peaks related to certain scales in the velocity fluctuations? A positive answer to this question is very important because it can be used to establish a quantitative relation between events in the atmospheric wind and extreme pressure loading on structures. Consequently, simulating such events becomes a necessity to reproduce pressure peaks in the laboratory and thus to predict extreme wind load.

In the following discussion we will consider two important cases of wind loading on structures. In one case, the wind is approaching the building at an angle of 90^o degrees, and it will be referred to as normal incidence case. In the second case, the wind is approaching the building at an angle of 45^o degrees, and it will be referred to as oblique incidence case. In the normal incidence case, a separation region is formed on the building roof where the shear layer rolls up to form a vortex. In the oblique case, two delta-wing-like vortices are formed on the corner of the building.

7.1 Characteristics of pressure peaks

7.1.1 Normal Incidence

Simultaneous time series of the u- and v-components of approaching wind and pressure coefficients, C_p from four different pressures taps on the roof for run M15N468 are shown in figure 7.1. These taps are referred to as taps # 50901, 50904, 50905 and 50907. The x and y coordinates for these taps are 2.64 and 0.36m for tap #50901, 2.64 and 1.27m for tap # 50904, 2.64 and 1.58m for tap #50905, and 2.69 and 2.18m for tap #50907. By inspecting the time series of pressure coefficients at these taps one can observe two distinct pressure peaks taking place near times 470 and 520 seconds in all time series. Peak C_p values at taps 50901 and 50905 of -3.5 are measured near 470 and near 520 seconds. At tap 50907 the peak C_p values are -2.5 at both times near 470 and 520 seconds. At tap 50904 relatively stronger peak Cp values of -3.8 near 470 seconds and -4.5 near 520 seconds are measured. Because these peak pressure coefficients are spread over a large area of the roof, they could have significant wind loading effects on the building roof. Examining the simultaneously measured time series of u- and v-velocity components one cannot determine any distinctive characteristics in u- or v-components that may directly be related to such peaks.

The time series of $u-$ and $v-$velocity components and the same four pressure taps for run M15N471, taken about half an hour later, are shown in figure 7.2. Pressure coefficients of these taps are characterized with simultaneous peaks pressures near 190, 410 and 720 seconds with Cp values of -3.8, -3.0 and -4.0 respectively at tap 50901. At tap 50904 the peak values are -3.2 near 190 and 410 seconds and -2.7 near 720 seconds. At tap 50905, the corresponding values are -2.5, -3.0 and -3.0. For tap 50907, the corresponding values are about -2.2. At tap 50904 the peak values are -3.2 near 190 and 410 seconds and -2.7 near 720 seconds. The appearance of peak pressure at the same time in several pressure taps again shows that a large area of the roof is being subjected to high pressure forces. Examining the simultaneously measured u and v velocity components of the approaching wind, once again, one cannot determine any specific variations in the time series of the velocity components that caused such pressure peaks.

To determine and quantify the scale of the pressure peaks, we computed the wavelet coeffi-

cients of the pressure coefficients measured for both records. The magnitudes of the wavelet coefficients at the four pressure taps for M15N468 are shown in figures 7.3a through 7.3d. In all figures, we notice high levels for the wavelet coefficients at times near 470 and 520 seconds. Other high-level wavelet coefficients can also be detected, however these events do not appear in each of these figures. For instance, the local peak pressure observed near 220 seconds in figure 7.3a does not appear in figures 7.3b, 7.3c, and 7.3d. Consequently, we limit the discussion here to peaks that appear simultaneously at all taps. The reason being that such peaks would have a greater impact on the wind load than an individual peak observed locally at a point with duration of a fraction of a second.

Based on the above approach and upon examining figures 7.3a through 7.3d one would notice two important features. First, the pressure coefficients are highly intermittent, i.e., the energy of the different scales in the pressure coefficients is changing significantly with time. Second, the peaks in the coefficients pressure appearing near 470 and 520 are accompanied by intermittent "pulses" of energy that extend over a scale range $5 \leq m \leq 9$ which corresponds to frequencies range $0.04 \leq \omega \leq 0.65$ Hz. The time axis in figures 7.3a and 7.3c show that the lowest scale associated with the peak at time 470 seconds is the m=8 scale, and with the peak at time 520 seconds is the m=7 scale. In figures 7.3b and 7.3d the lowest scale associated with the peak at time 470 seconds is the m=9 scale and with peak at time 520 seconds is the m=8 scale. Because the 470 peak is always appearing in one scale less the than the 520 peak, the 520 peak is broader than the 470 peak.

The above results can also be seen in the wavelet coefficients of M15N471 run, which are given in figures 7.4a through 7.4d. These figures show three important pressure coefficients events appearing in the form of pressure peaks near times 190, 410 and 720 seconds. Similarly to the results of run M15N468, other local and short duration peaks can be detected in figures 7.4a through 7.4d. Yet, by closely examining, figures 7.4a through 7.4d, the two observations made for run M15N468 hold. First, the energy of the wavelet coefficients is not evenly distributed in time. Second, high-level of wavelet coefficients at different scales are present near times 190, 410 and 720 seconds. Tap 50901 of figure 7.4a exhibit a peak pressure at time 190 seconds, which is captured in scales with $m = 10$ and m =12. It should be noted here that the very small scale represent peaks that may not be significant in relation to the wind loading effect due to their short duration effect. Henceforth, we well point out these

peak pressure in the relatively higher scale range to show their strength and duration. The peak pressures observed at 410 and 720 seconds are more broad and associated with scales with m is between 6 and 10. In figure 7.4b the scale of these peaks is at m=9 for the 190 and the 410 second peaks. The scale of the 720 is near m=8 scale.

Figure 7.4c shows that the observed peak at 190 seconds is captured in m=9 scale, the peak at 410 is captured in the m=10 scale and the peak at 720 seconds is captured in the m=7 scale. In Figure 7.4d the scales of the pressure peaks at 190, 410 and 720 are at scales with m=11, m=9 and m=7, respectively. This shows that the two peaks at 190 and 410 seconds are less broad than the peak near 720 seconds. By comparing the wavelet coefficients magnitudes the peak pressure near 720 seconds produces higher wavelet magnitudes compared to the peaks near 190 and 410. This shows that the peak near 720 seconds is stronger than the ones at times 190 and 410 seconds.

7.1.2 Oblique Incidence

The time series of simultaneously measured $u-$ and $v-$velocity components and pressure coefficients from three different pressure taps are shown in figure 7.5 for run M15N086. These taps are referred to as 50205, 50501 and 50509 and the x and y coordinates of these taps are 0.46 and 1.58m for tap 50205, 1.42 and 0.36m for tap 50501 and 1.47 and 2.79m for tap 50509. Inspecting the time series of the pressure taps 50205 and 50501, one can observe stronger and wider negative pressure peaks ($-10 \leq C_p \leq -2$) than the normal incidence case. This is expected since these taps are located underneath one of the two delta-wing-like vortices that form on the roof corner. The other tap 50509 is not located directly under one of these vortices. A coincidence of peak pressure coefficients between the three pressure taps is not expected due to large spacing between these taps. Yet, it should be emphasized that because of their magnitudes, these peaks may be significant in producing excessive wind loads. For instance the peak pressure coefficients near 120 seconds for 50205 tap is about -6.0, whereas for 50501 the peak that appears near 125 seconds has a C_p value of about -6.0 and for the 50509 tap the peak that appear near 110 seconds has a C_p value of about -2.0. We also note other peaks at 50205 tap. These are -5.5 at 250 second, -5 at 470 seconds and

-5.5 at 730 seconds. At tap 50501 peaks of about -7 appears at 175 seconds, -5.5 at 185 seconds, -6.5 at 250 seconds, -9 at 510 seconds, -4 at 630 seconds and -6 at 750 seconds. At tap 50509 other peaks are also observed. These are -2.0 at times 115, 240, and 340 seconds and peaks of about -3 C_p value at times 490, 650 and 730 seconds. As in the normal incidence case, by tracing these pressure peaks along the time axis and observing the simultaneously measured u and v velocity events one can not determine any of the velocity events that can be related to such pressure peaks.

The time series of $u-$ and $v-$velocity components and the same three cornering pressure taps for the M15N087 record are shown in figure 7.6. This record was taken about twenty minutes after M15N086 record. Figure 7.6 shows simultaneously measured velocity and pressure coefficients time series for the M15N087 record, taken immediately after the M15N086 record. The pressure coefficients of these taps are characterized with individual pronounced peaks with a C_p values between -10 and -2. At tap 50205 one can observe several pressure peaks with C_p values of about -7 at 65 second, -6 at 70, 250 and 800 seconds, and -5 at 510 seconds. Tap 50501 is characterized with several peaks of about -6.5 at 20 seconds, a more pronounced and broad peak of -10 at 290 seconds, and a -5 peak at 390, 570 and 810 seconds. At tap 50509 relatively weaker peaks are observed than the ones observed in the other taps and values of about -3.5 at 25 seconds and -2 at 155 and 640 seconds are measured.

In order to characterize these pressure coefficients peaks with scales and time duration we computed and plotted the magnitudes of the wavelet coefficients. Figure 7.7a through 7.7c show the wavelet coefficients of the three pressure taps of M15N086 run. Figure 7.7a shows high values of the wavelet coefficients coincide with high values of negative peak pressure. Inspecting figure 7.7a through 7.7c of the three corner pressure taps reveal that peak-negative pressure coefficients resulted in high wavelet coefficients. For instance in figure 7.7a of 50205 tap the pressure peaks near 125, 250, 470 and 735 seconds resulted in high values of wavelet coefficients at scales m=6, m=5, m=7 and m=6 respectively. These scales last over time duration between 6.4 and 24 seconds. Similarly, figure 7.7b of 50501 tap resulted in high value of wavelet coefficients at scale m=7 of the observed peaks near 185, 510, 6800 and 750 seconds. The peaks near 175, 250 and 740 seconds show high wavelet coefficients at scales of m=5, m=4 and m=6 respectively which last over a time duration near 25 seconds. In figure 7.7c the observed peak pressure near 115, 240, 340, 490, 650, and 730 seconds resulted in

high wavelet coefficients in the m=9, m=8 m=8, m=10, m=5 and m=7 scales, respectively. As can be seen in figures figure 7.7a through 7.7d the measured pressure coefficients are highly intermittent.

Similar results are observed in the examining M15N087 run. At tap # 50205, the observed peak pressure near 65, 250, 510 and 800 seconds resulted in high values of wavelet coefficients at $m = \{6, 9, 6, 8\}$ scales, respectively. At tap # 50501 the peak pressures near 20, 290, 575 and 815 seconds show high wavelet coefficients at scales m=7, m=5, m=7, m=8 and m=6, respectively. At the 50509 tap high values of wavelet coefficients were found to be also corresponding to peak pressure near 20, 50, 150 and 330 seconds as shown in figure 7.8c. The scale of these peaks are m=7, m=6 for the peaks near 20 and 50 seconds and m=4, m=8 for the peaks near 150 and 330 seconds, respectively. These high value of wavelet coefficients extend over a wide scales band. However, we choose to indicate the most energetic scale as the peak scale. For instance, the relatively narrow band peaks near 520 seconds in figure 7.8c extend over two scales m=8 and m=9 which corresponds to 3.2 and 1.6 seconds time duration.

The results of the wavelet analysis of the pressure coefficients show that the energy of the different scales is not evenly distributed in time. Moreover, large values for the coefficients correspond to the low pressure peaks observed in the time series. These peaks extend over a scale range between m=5 to m=9.

7.2 Velocity pressure relation

For the purpose of determining the relation between velocity and pressure fluctuations, the product of the wavelet coefficients is used to obtain an indication to the occurrence of fluctuations coinciding in scale and time. The interpretation of such a product follows from a basic property of the wavelet transform. If a given variable does not fluctuate at a certain scale at a certain time then its wavelet coefficients at that time is zero. In determining the relation between two variables, it is clear that there must be a significant fluctuation coincident in scale and time in each variable time series to obtain large values of the product providing that the time lagging time between the two variables is considered. One should note here that if either of the individual wavelet transforms is nearly constant everywhere

and the second is highly intermittent then the significance of the results are suppressed. Consequently, the results are more meaningful when there is a high degree of intermittency in time and scale as in the case of atmospheric wind and the observed pressure coefficients. The above multiplication exercise results in peaks where fluctuations from two time series coincide in scale and time. If fluctuations do not appear at the same time and same scale, the resulting product is very low. Consequently, such product can be used to examine the role of different turbulence scales in causing low pressure peaks, i.e. excessive wind loads.

7.2.1 Normal Incidence

The product of the wavelet coefficients of both velocity components (u and v) with wavelet coefficients of the pressure fluctuations are shown in figure 7.9a through 7.9h for run M15N468. These figures capture two distinct peaks near 470 and 520 seconds at scales between $m = 4$ and m=9. Nevertheless, the figures show other velocity scales that coincide with relatively weaker pressure peaks. For example, the observed high wavelet product magnitude in figure 7.9a at scale m=7 near 160 seconds is relating the peak pressure occurring at 160 seconds to turbulence event that have the same scale and occurred at the same time. Several other high product magnitude can be observed such as the ones near 130 seconds at m=6, near 450 seconds at m=7, and near 730 seconds at m=8 these are related to a significant gust events and consequently resulted in moderate pressure peaks as shown in figure 7.9a through 7.9d. These figures show that, longitudinal velocity events seem greatly attributed to the two pressure peaks near 470 and 520 seconds. These velocity events take place over a time duration that last 6.4 and 13.0 seconds, respectively.

In the same manner, we examine the relation between the lateral velocity and pressure by plotting wavelet coefficients products as shown in figure 7.9e through 7.9h for the same run, M15N468. The products reveal two high level of wavelet product centered at 470 and 520 seconds, and appearing at m=8 and m=7 scales, respectively. This is observed in figure 7.9e for 50901 tap and in both figure 7.9f for 50904 tap and figure 7.9h for 50907 tap . These velocity scales last over a time duration between 3.2 and 6.4 seconds. For tap 50905, the two peaks appear to be related to lateral velocity events at m=7, and m=6 scales that last for 6.4 and 12.8 seconds, respectively. The time duration of both velocity components which

related to the two peak pressure are nearly the same. Other relatively weaker wavelet product peak can be observed through these figures, for example the high wavelet product level in figures 7.9e and 7.9f near 730 seconds for 50901 and 50904 taps at the m=6 scale is also related to lateral turbulent gusts that last for 12.8 seconds. The result indicated that the two peak pressures near 470 and 520 seconds are associated with a relatively smaller scale in the lateral velocity components than the longitudinal components. The first scale that responsible for 470 pressure peaks last nearly 3.2 seconds, whereas the scale responsible for the 530 peak last nearly 6.4 seconds.

In the same manner, we present and discuss the results of M15N471 run. The product of the wavelet coefficients of the velocity components and pressure are given in figures 7.10a through figure 7.10h. In figure 7.10a of 50901 the peak pressure coefficients near 190, 410 and 720 seconds was captured in the scales m=7, m=7 and m=9, respectively. At tap 50904 , figure 7.10b shows high level of the wavelet product at m=$\{8, 8, 10\}$ scales for the peak pressure near 190, 410 and 720 seconds. In figure 7.10c of 50905 the peak pressure coefficients near 190, 410 and 720 seconds was captured in the scales m=10, m=8 and m=9, respectively. At 50907, figure 7.10d, the peaks scale are m=7, m=8 and m=10 with smaller product level than the other three taps due to the low value of C_p ($-2 \leq C_p$) near 190, 410 and 720 seconds. In general, longitudinal velocity events with duration between 1 and 6.4 seconds appear to be related to pressure peaks observed near 190, 410 and 720 seconds. Examining the lateral velocity events shows that the two peaks near 190, and 410 seconds are associated with the following: A strong and a relatively high level for tap 50901 in m=12 scale for both peaks (figure 7.10e). Weak velocity events at the lowest scales ($12 \leq m \leq 10$) for both 50904 and 50905 taps (figure 7.10f and 7.10g), and a strong level only for the peak near 190 for 50907 tap in m=11 scale (figure 7.10h). Whereas, the peak pressure near 720 seconds is related to stronger velocity events at m=6 and m=11 in all taps as shown in figures 7.10e through 7.10f. Near 410 seconds the peak was related to a longer duration scale in the velocity as can be seen in figure 7.10c, more clearly in figure 7.10d, at m=5 scale which corresponds to 25 seconds. The results show how variation of both velocity components are related to the pressure peaks, thus events in the longitudinal velocity and events in the lateral velocity are considered to be as important and they are related to these pressure peaks.

7.2.2 Oblique case

The wavelet coefficients product of velocity components with pressure coefficients for record M15N086 is shown in figures 7.11a through 7.11f. At tap 50205 in figure 7.11a, the observed peak pressure near 125 and 250 seconds appear to be related to longitudinal velocity scales at m=7 and m=4, and the observed peaks near 470 and 540 seconds appear to be related to scales at m=7. The peak near 735 seconds seems to indicate that there are two longitudinal velocity scales that are related to it, these scales are m=6 and at m=8. As far as the lateral velocity concerned of tap 50205 (figure 7.11d), these observed peaks near 125, 250 and 470 seconds found that are related to lateral velocity scales at m=$\{6, 5, 8\}$, and the peaks near 450 and 735 are both related to the same velocity scale of m=7.

At tap 50501, the observed peak pressure near 175, 85, 250, 510, 680 and 740 seconds are related to longitudinal velocity events observed at scales of m=$\{5, 7, 4, 7, 7, 6\}$ as shown in figure 7.11b, and lateral velocity events at scales m=$\{3, 3, 7, 7, 7, 6\}$, respectively as shown in figure 7.11e. It should be noted here that, the levels of the wavelet coefficients product is higher than the normal incidence case which due to the significance of these pressure peaks. At tap 50509 because the peaks are less pronounced the level of their product was also suppressed, yet still can be observed. For example the peak pressure near 115, 240, 340, 490, 650, 730 seconds show that are related to longitudinal turbulent events at m=$\{9, 8, 8, 10, 5, 7\}$ scales, respectively as shown in figure 7.11c. Except the first peak near 115 seconds, these peaks are related to lateral velocity events at the same corresponding scales of the longitudinal velocity as shown in figure 7.11f. The peak near 115 seconds seems to be related to lateral velocity events at m=6 scale.

For Run M15N087 the wavelet coefficients product of the velocity components and pressure coefficients are shown figures 7.12a through 7.12f. At tap 50205, shown in figure 7.12a, the peaks pressure observed near 72 and 800 seconds appear that, they are related to longitudinal velocity events at m=8 scale, and the peaks near 250 and 510 seconds are related to velocity events at m=6 scale. By examining the lateral velocity one find that the scales of lateral velocity events which related to these peaks are at the same scales of the longitudinal velocity as shown in figure 7.12d. At tap 50501, figures 7.12b and 7.12e, the observed peaks near 290, 575 and 815 seconds are related to velocity events at m=$\{5, 6, 6\}$ scales in both

velocity components. The peak near 290 seconds seems related to a larger scale in in the longitudinal velocity (m=7) than the scale of the lateral velocity (m=10). Again, we should stress that the level of wavelet product in the oblique case is more pronounced and energetic than the normal incidence case. At 50509 tap, which characterized with a weaker peaks than the above two taps, the observed peaks near 25 and 150 seconds are related to scales at m=7 and m=6 in both velocity components as shown in figures 7.12c and 7.12f, respectively. The peak near 640 seconds appear to be related in the longitudinal velocity to several scales that range between m=4 and m=7, whereas, this peak is related to only m=4 scale in the lateral components. It was reported by Tieleman [1992] and Scalan [1989] the existence of such peaks is attached with delta-wing vortices which assumed to be responsible for such very low peaks. In obtaining the value of the cross scalogram we did count for the lagging time between the measured pressure signal and velocity signal. One constraint in reaching to these results is that, the mean flow direction should be directed along a line through the meteorological tower and the center of the building. Hence, the lagging time is $\tau = \frac{L}{U}$, where L is the distance between the meteorological tower and the building center (46m). The constraint on the mean flow direction is necessary for prediction such a relation. Otherwise, only the very large scale turbulence will be counted for in reaching to a similar results.

7.2.3 Peak pressure versus turbulence events

The significance of the above results can be better assessed by studying individual pressure peaks. Figure 7.13 shows parts of the M15N468 time records of the pressure coefficients at tap # 50904 and the $u-$ and $v-$components of the wind. The interest is in the peak measured near 470 seconds. Obviously, there is no specific or well-defined change in the $u-$ and $v-$ components that can be related to the observed peak near 470 seconds. Along with these records, figure 7.13 shows the magnitudes of the wavelet coefficients at scale m=9, for the $u-$component, the pressure coefficients and their product. The figure also shows the magnitudes of the wavelet coefficients at scale m=8, for $v-$component, the pressure coefficients and their product. Upon examining these figures, it becomes clear that the pressure peak near 470 seconds is related to high-magnitude wavelet coefficients in the $u-$

and $v-$velocity components. Consequently, one can make the following important conclusion: Peak pressure coefficients can be defined by certain scales, in this case 8 and 9, and these peaks are related to events at the same scale in the $u-$ and $v-$velocity components of the approaching flow.

The above conclusion can be further strengthened by considering another portion of the record that shows another peak. Figure 7.14 shows another portion from the same time records of the pressure coefficients and $u-$ and $v-$velocity components. Along with these records, the magnitudes of the wavelet coefficients of the pressure coefficients and velocity components at scale m=8 and their products are shown. Again, simply examining the time series shows no specified event in the velocity that can be related to the pressure peak. In contrast, one can relate the relatively high magnitude of both $u-$ and $v-$ components of the wavelet coefficients at scale 8 to the peak pressure coefficient.

To further generalize the above results, we considered a peak measured under oblique incident flow condition. Figure 7.15 shows portions of the pressure coefficients at tap # 50501 and $u-$ and $v-$velocity components of record M15N086. The peak observed near 510 seconds cannot be clearly related to specific events in the $u-$ and $v-$components. On the other hand, by considering the magnitudes of the wavelet coefficients at scale m=7, one notices relatively high-level coefficients in both $u-$ and $v-$components near 510 seconds. Consequently, for both normal and oblique incident flows, the extreme peak pressure coefficients can be related to specific scales between m=7 and m=9 in the approaching flow.

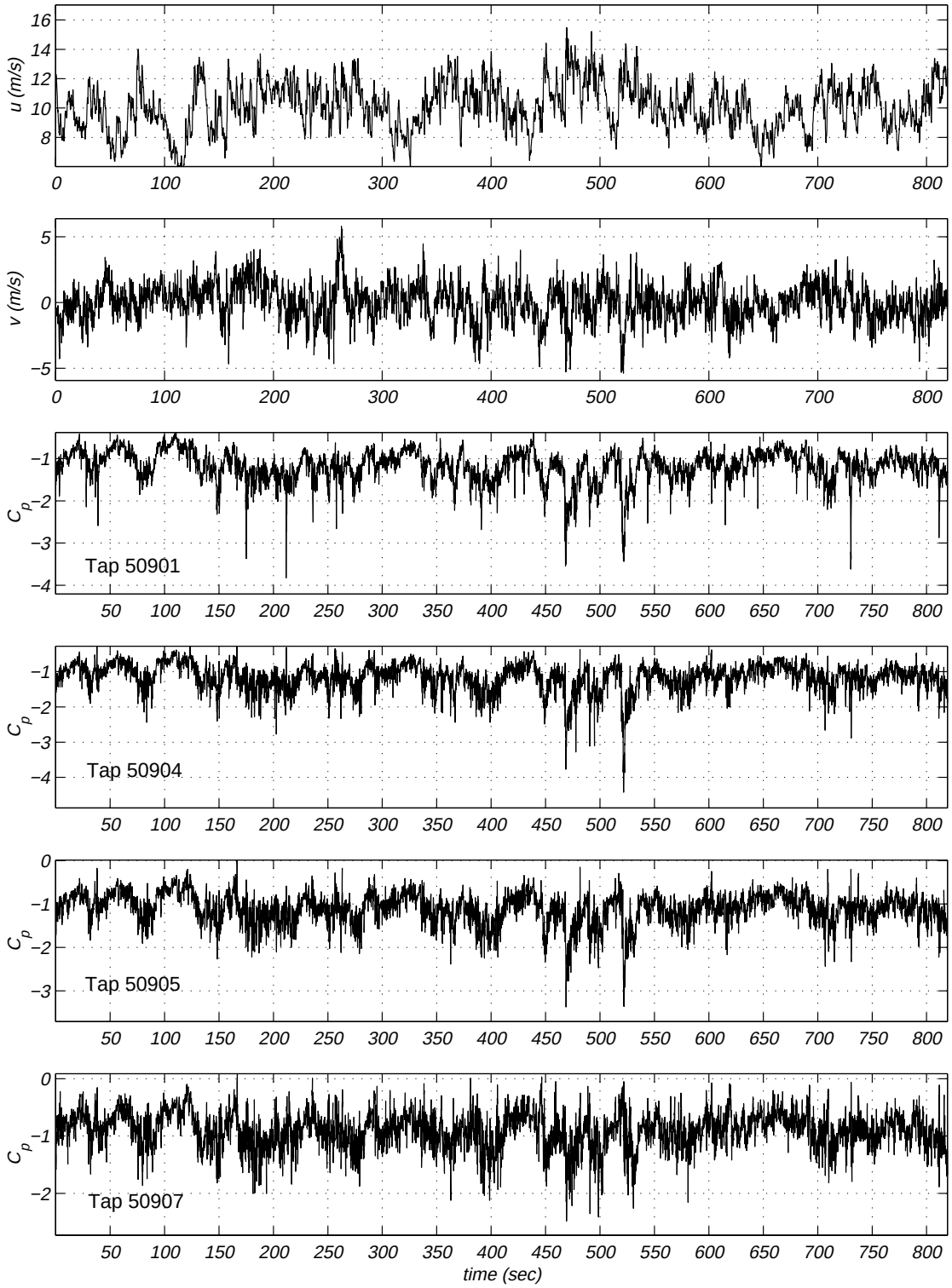

Figure 7.1: Time series of u and v velocity components and C_p of the four pressure coefficients (50901, 50904,50905 and 50907) on WERFL building for record M15N468.

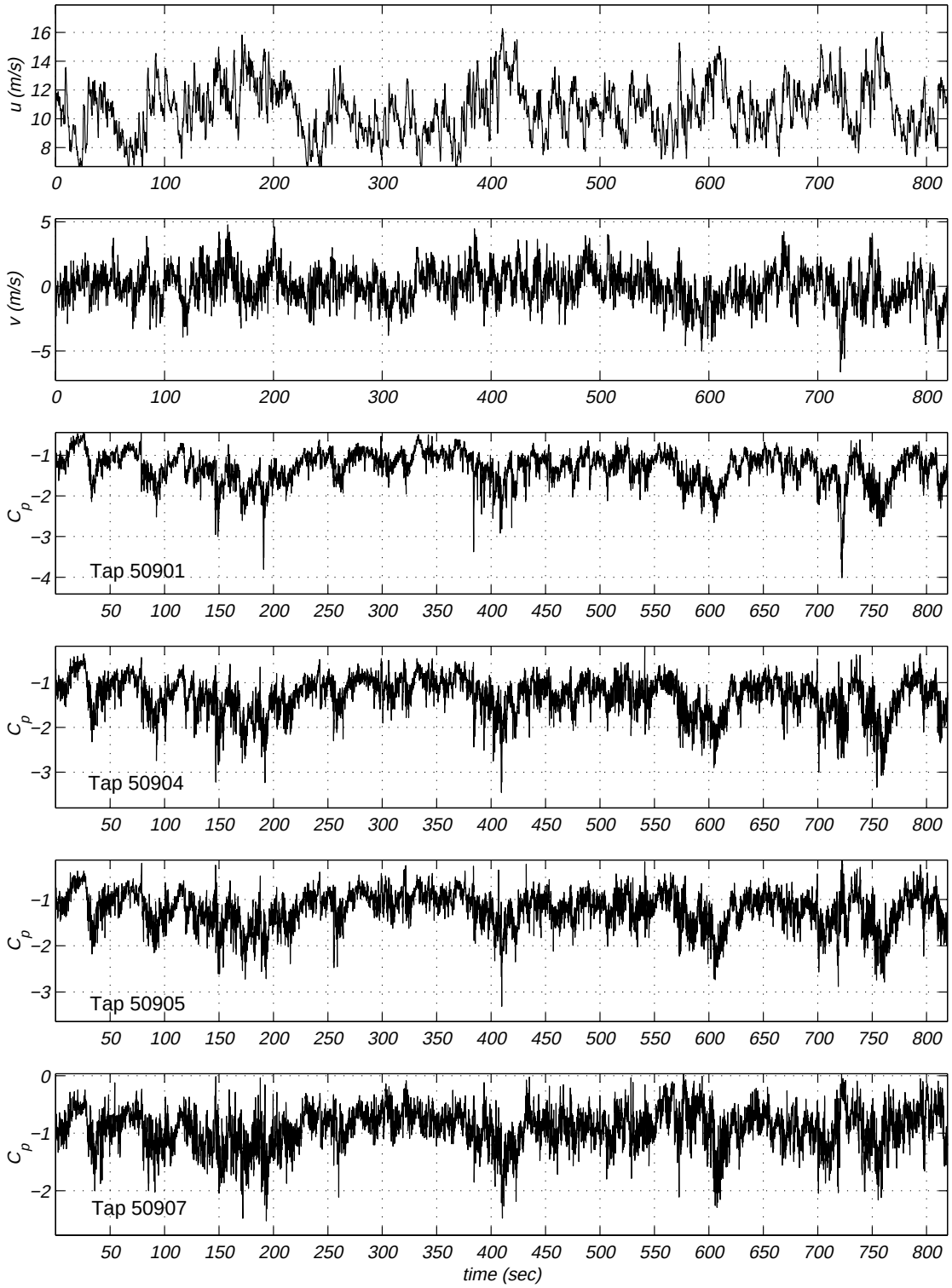

Figure 7.2: Time series of u and v velocity components and C_p of the four pressure coefficients (50901, 50904,50905 and 50907) on WERFL building for record M15N471.

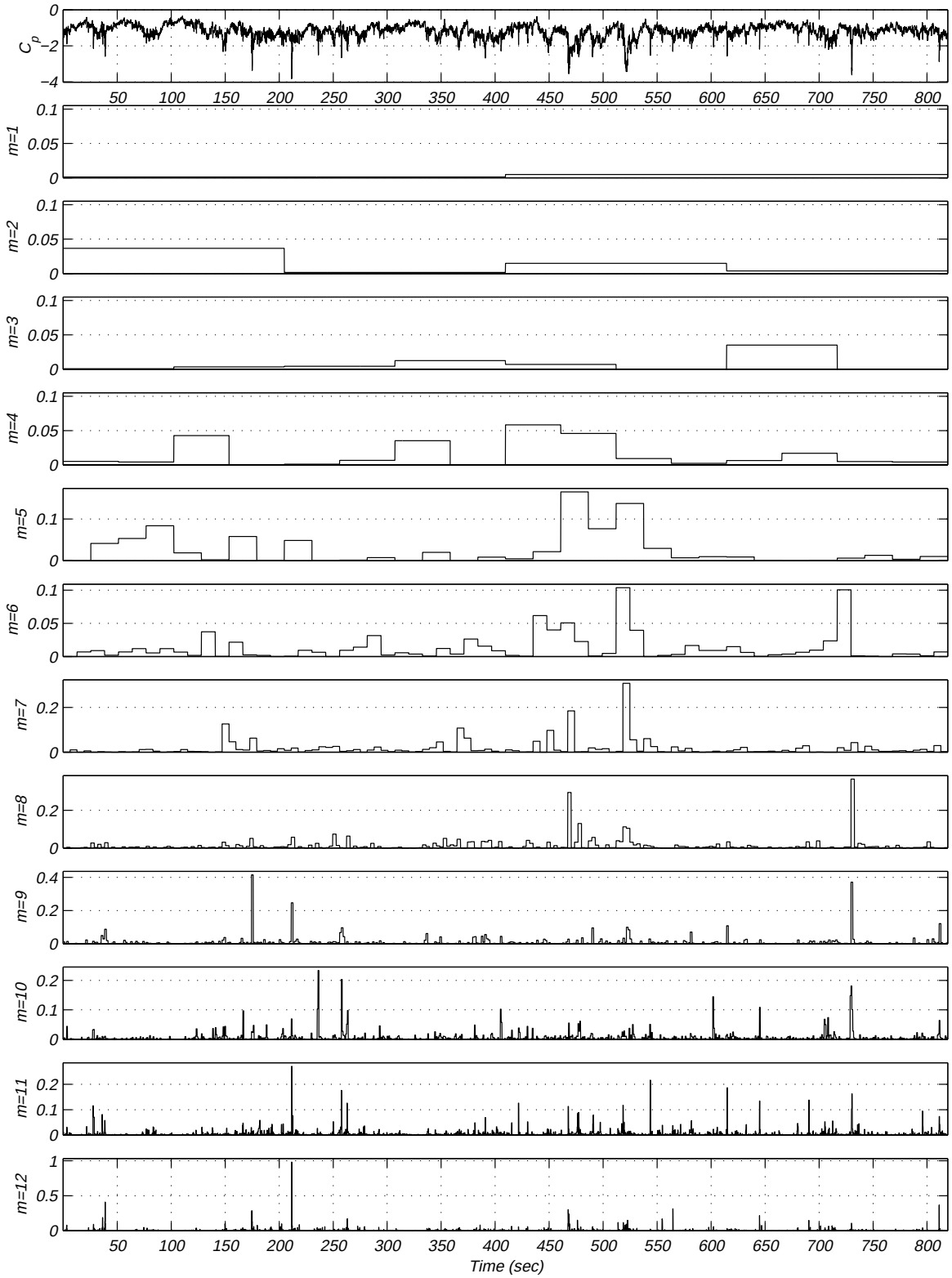

Figure 7.3a wavelet coefficients of pressure coefficients at tap # 50901 for record M15N468.

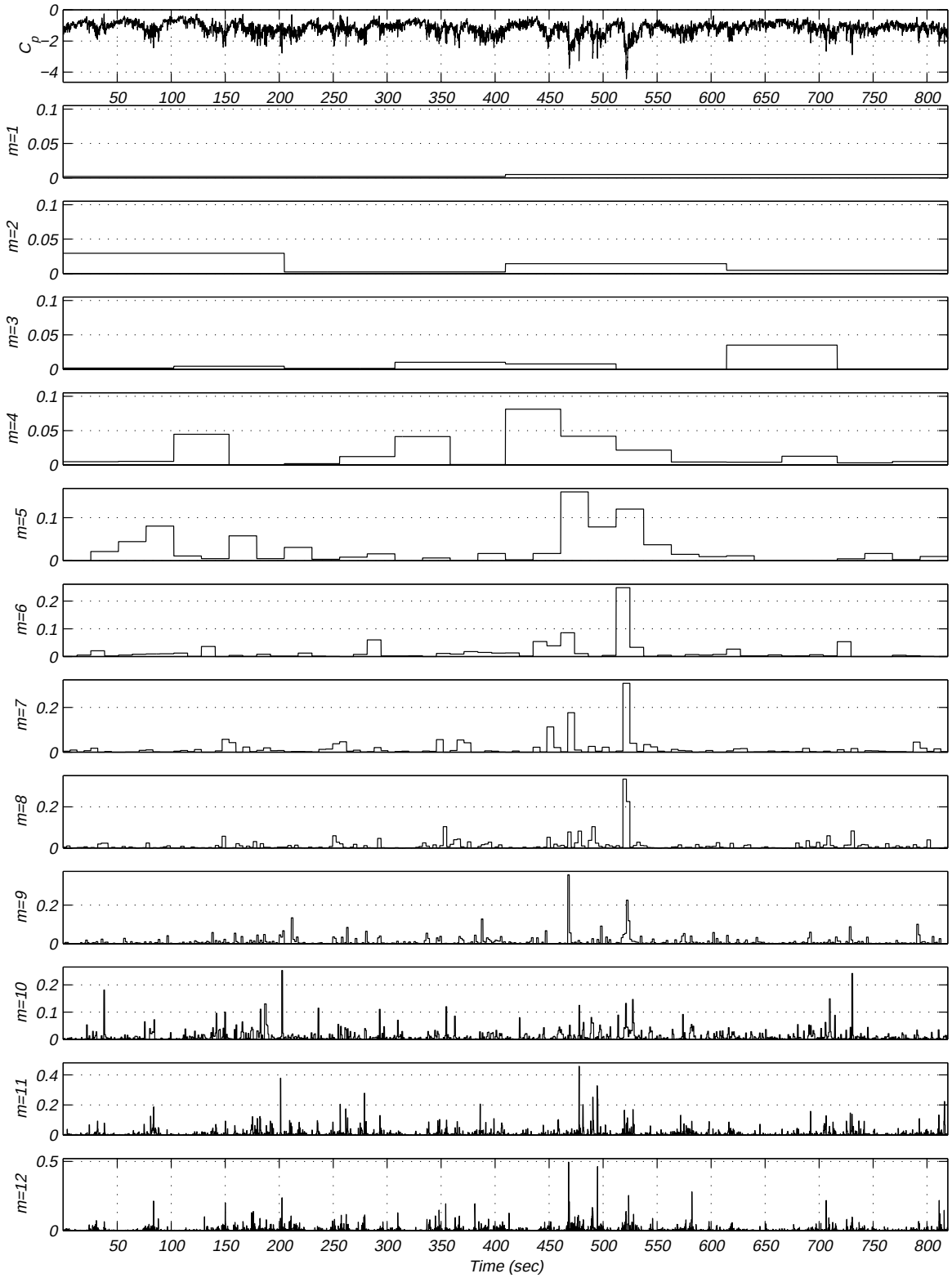

Figure 7.3b wavelet coefficients of pressure coefficients at tap # 50904 for record M15N468.

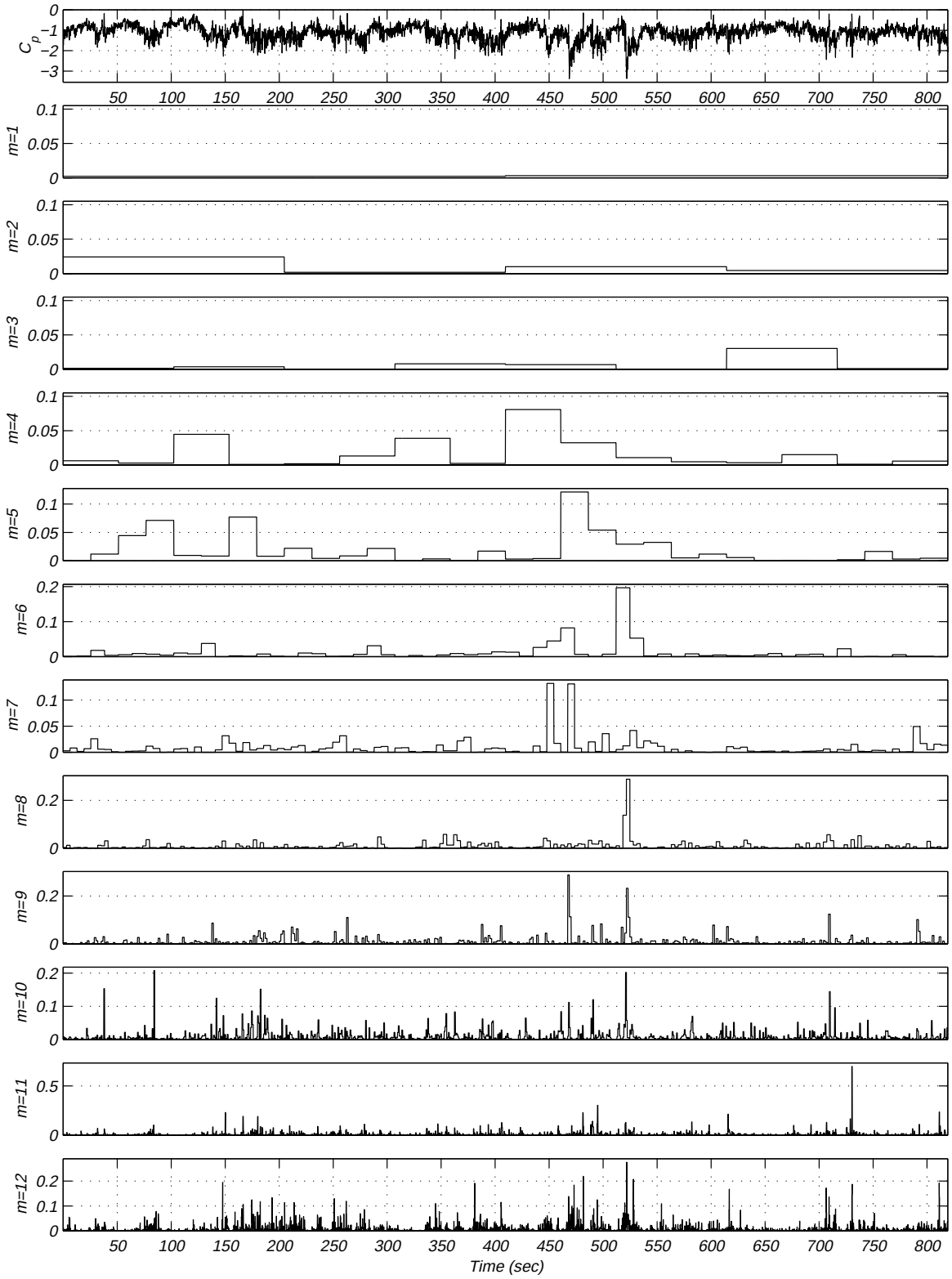

Figure 7.3c wavelet coefficients of pressure coefficients at tap # 50905 for record M15N468.

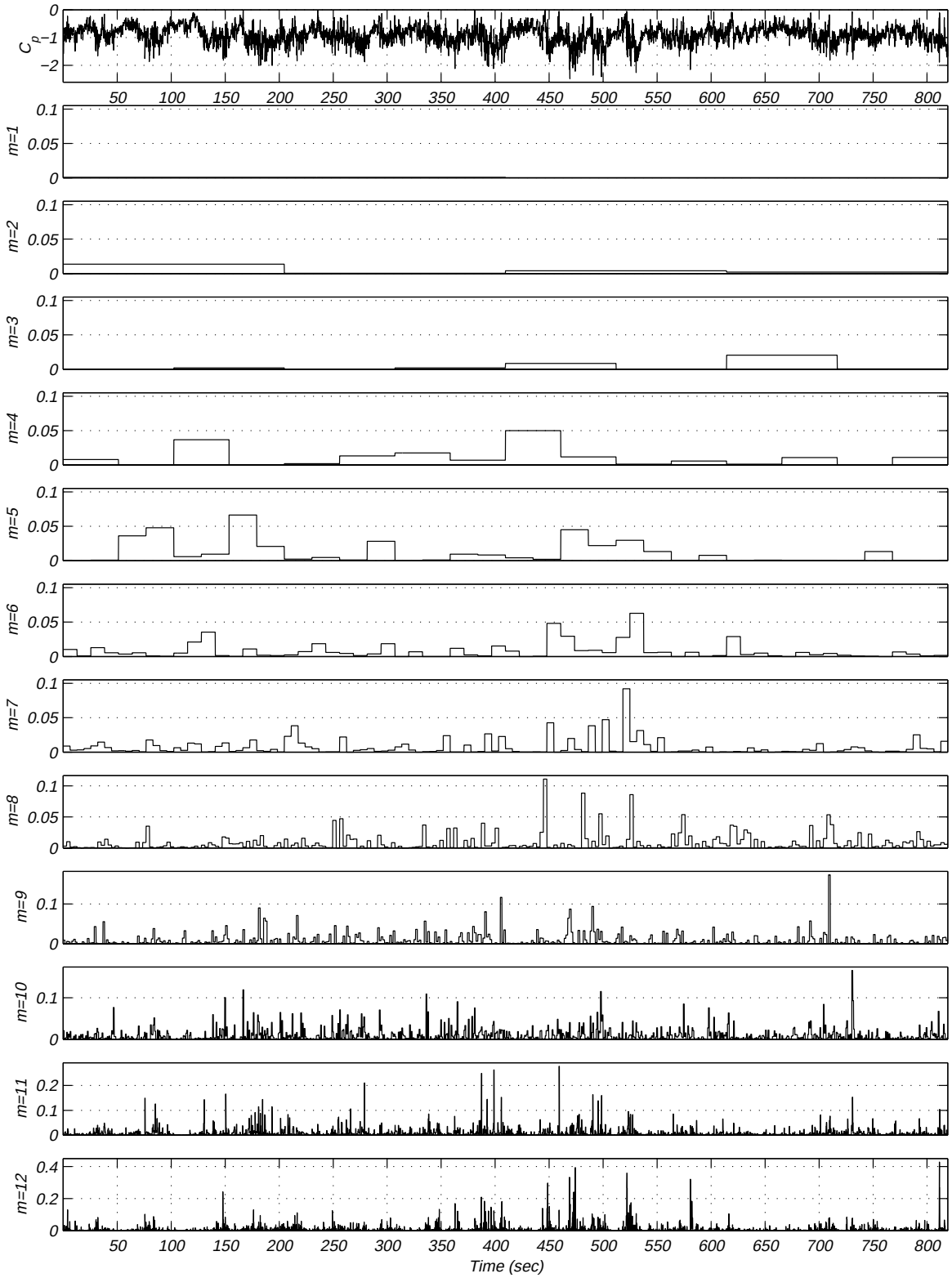

Figure 7.3d wavelet coefficients of pressure coefficients at tap # 50907 for record M15N468.

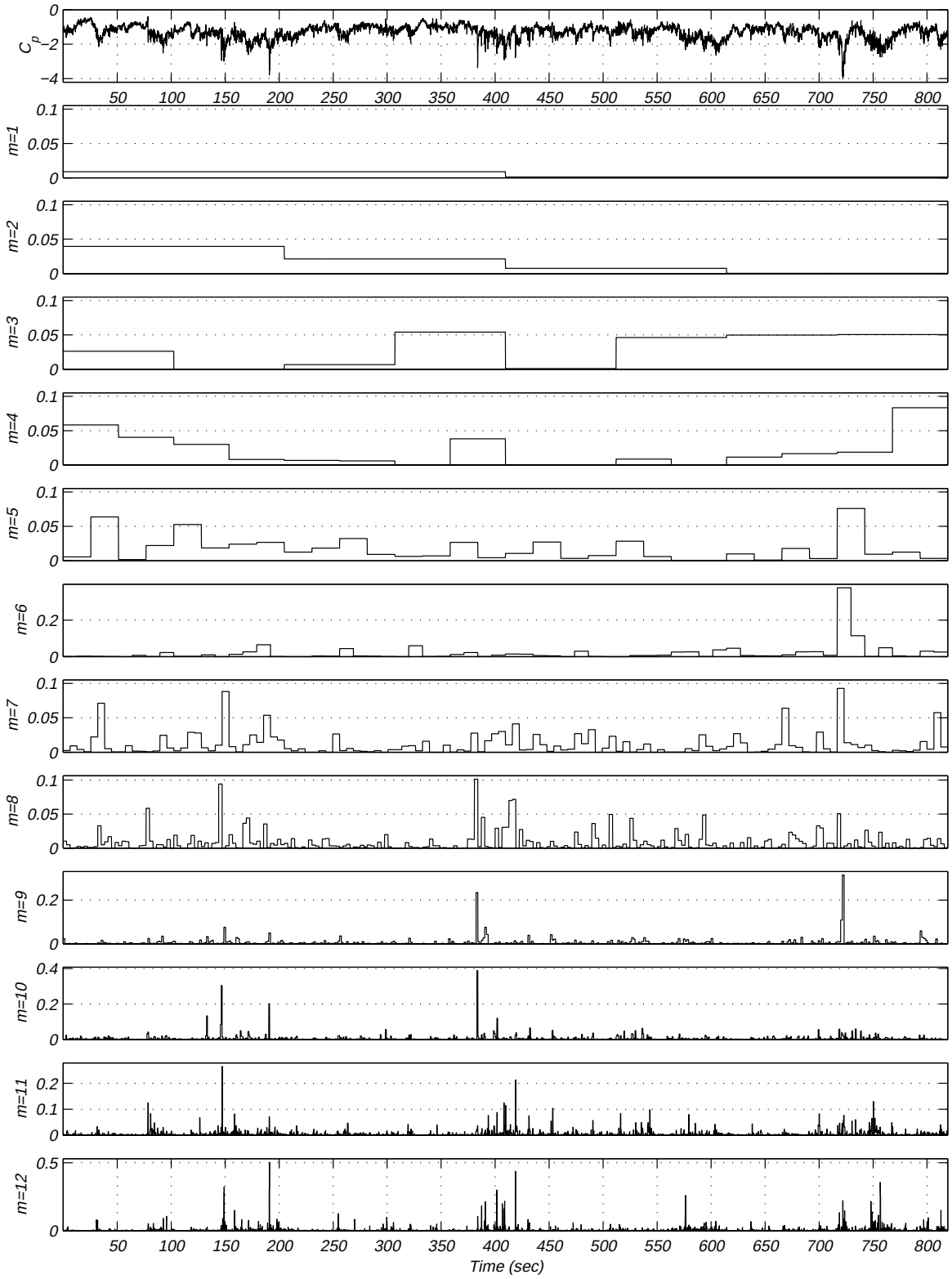

Figure 7.4a wavelet coefficients of pressure coefficients at tap # 50901 for record M15N471.

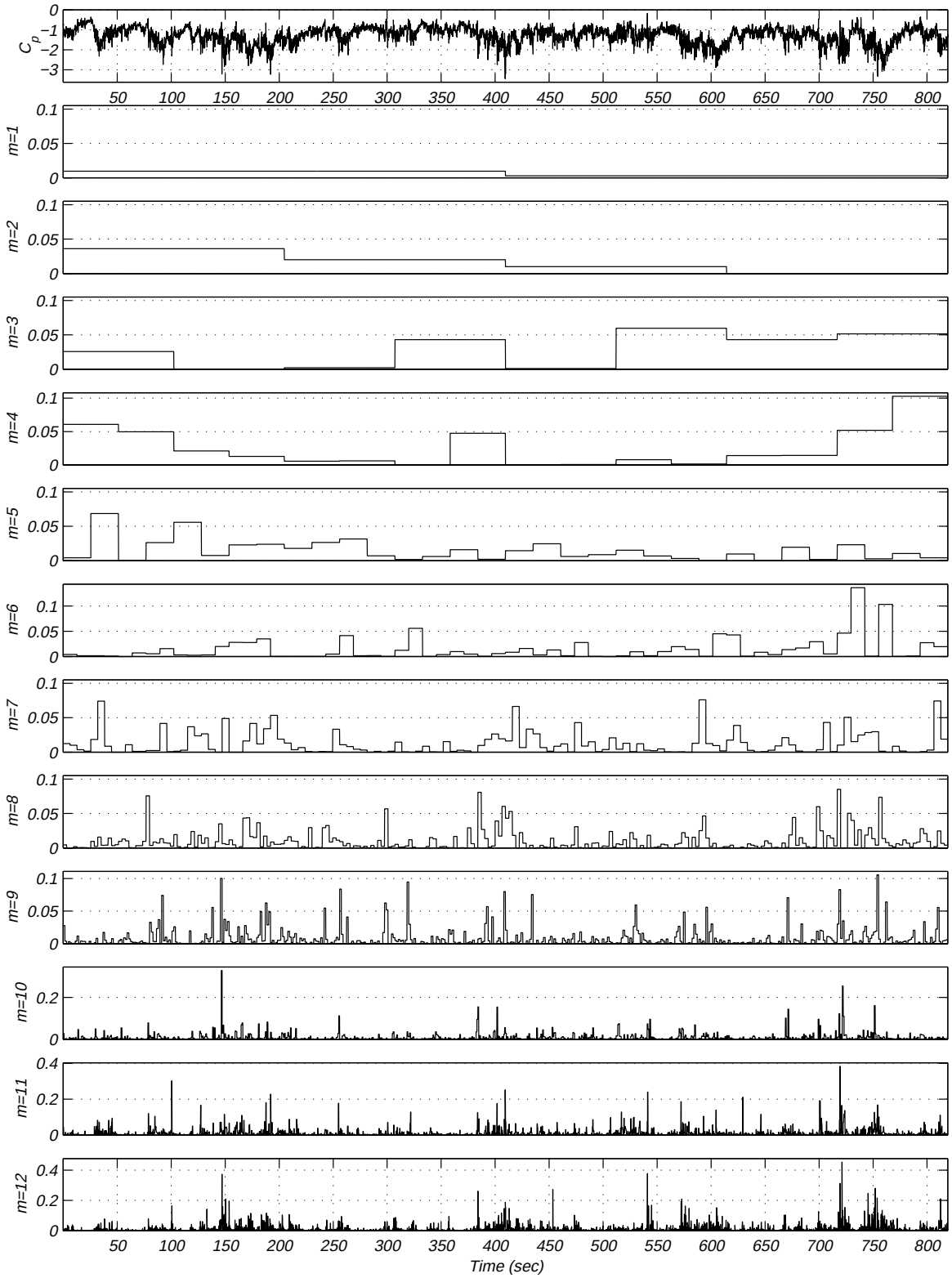

Figure 7.4b wavelet coefficients of pressure coefficients at tap # 50904 for record M15N471.

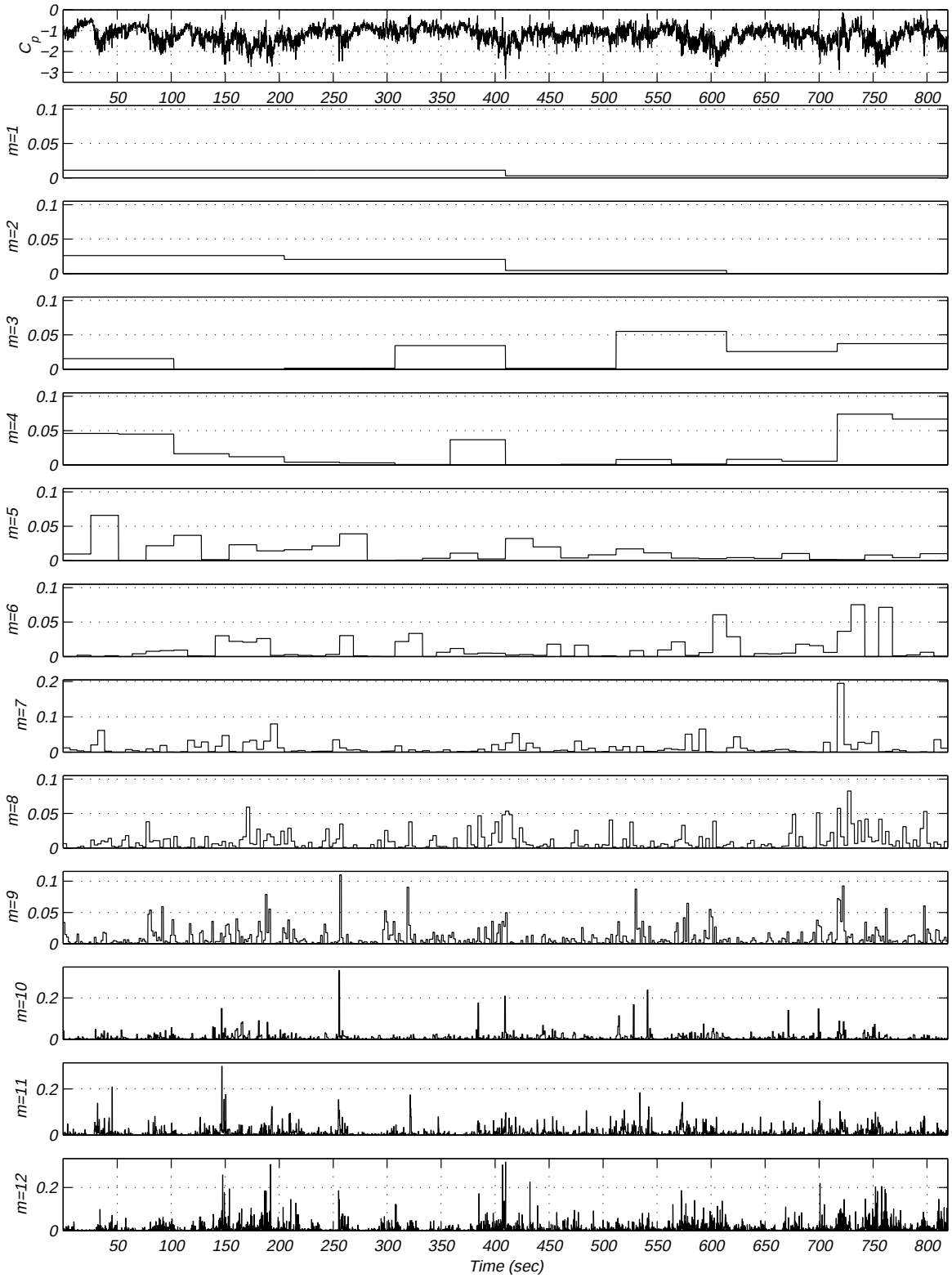

Figure 7.4c wavelet coefficients of pressure coefficients at tap # 50905 for record M15N471.

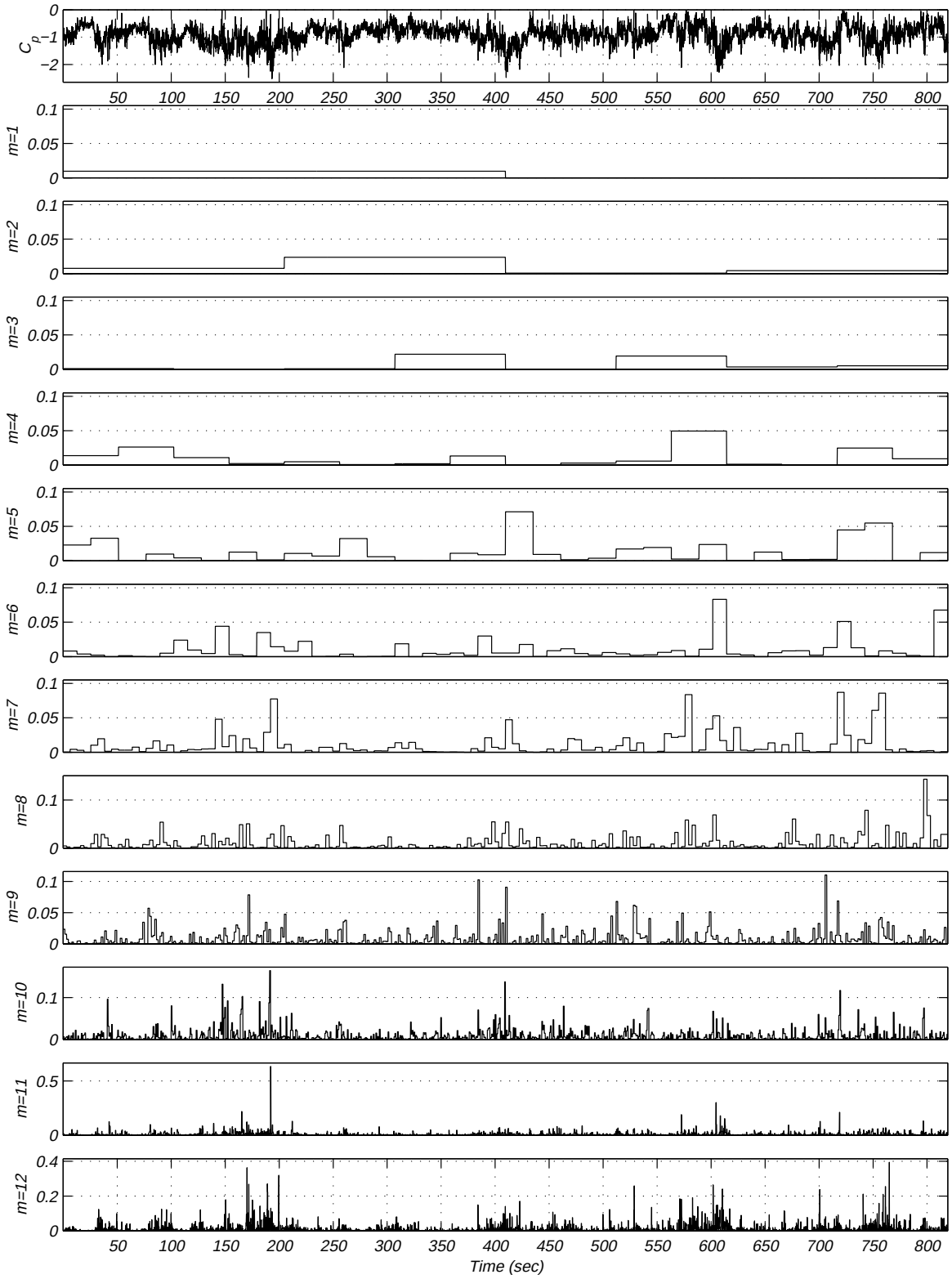

Figure 7.4d wavelet coefficients of pressure coefficients at tap # 50907 for record M15N471.

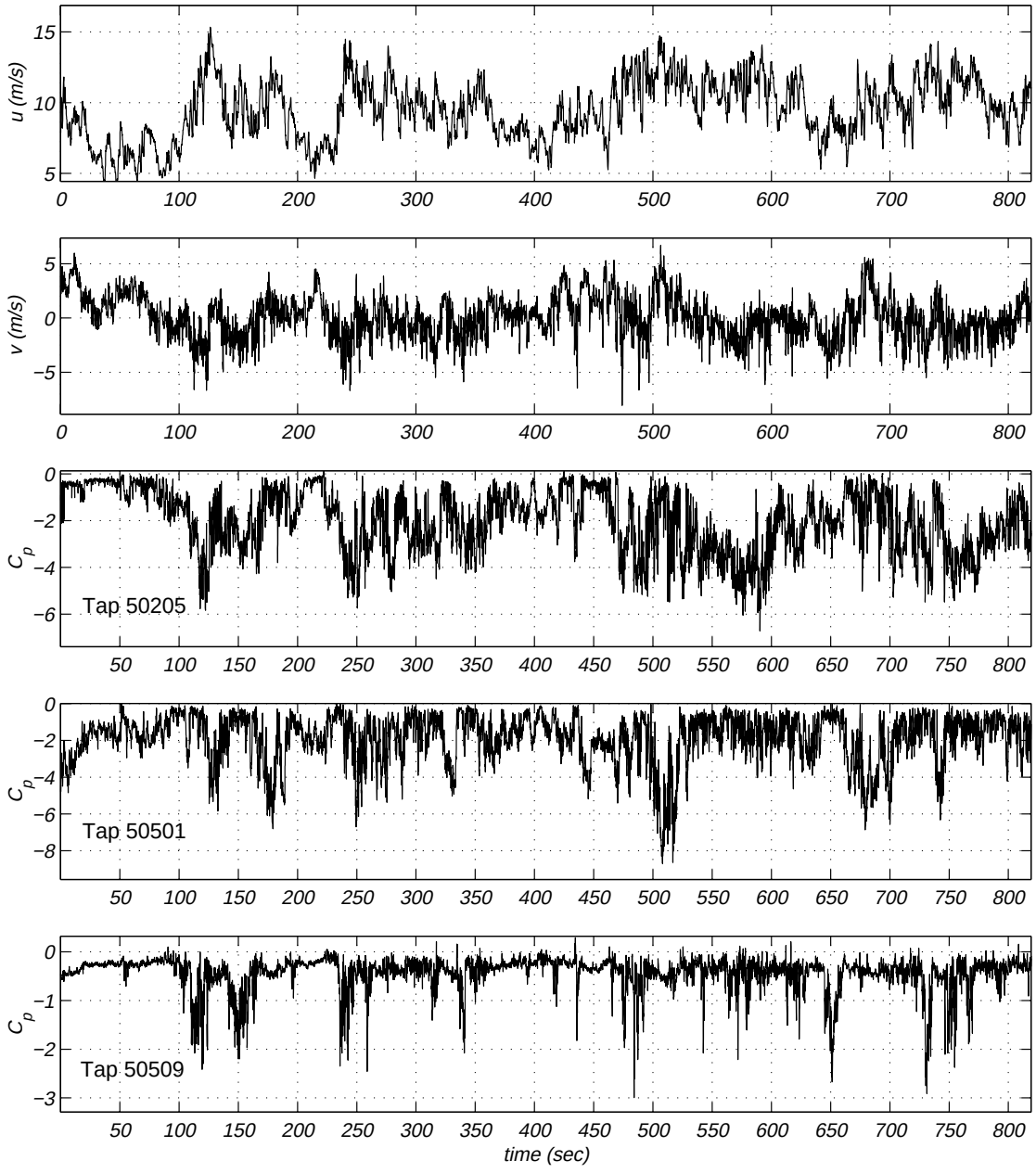

Figure 7.5: Time series of u and v velocity components and C_p of the three pressure coefficients (50205, 50501 and 50509) on WERFL building for record M15N086.

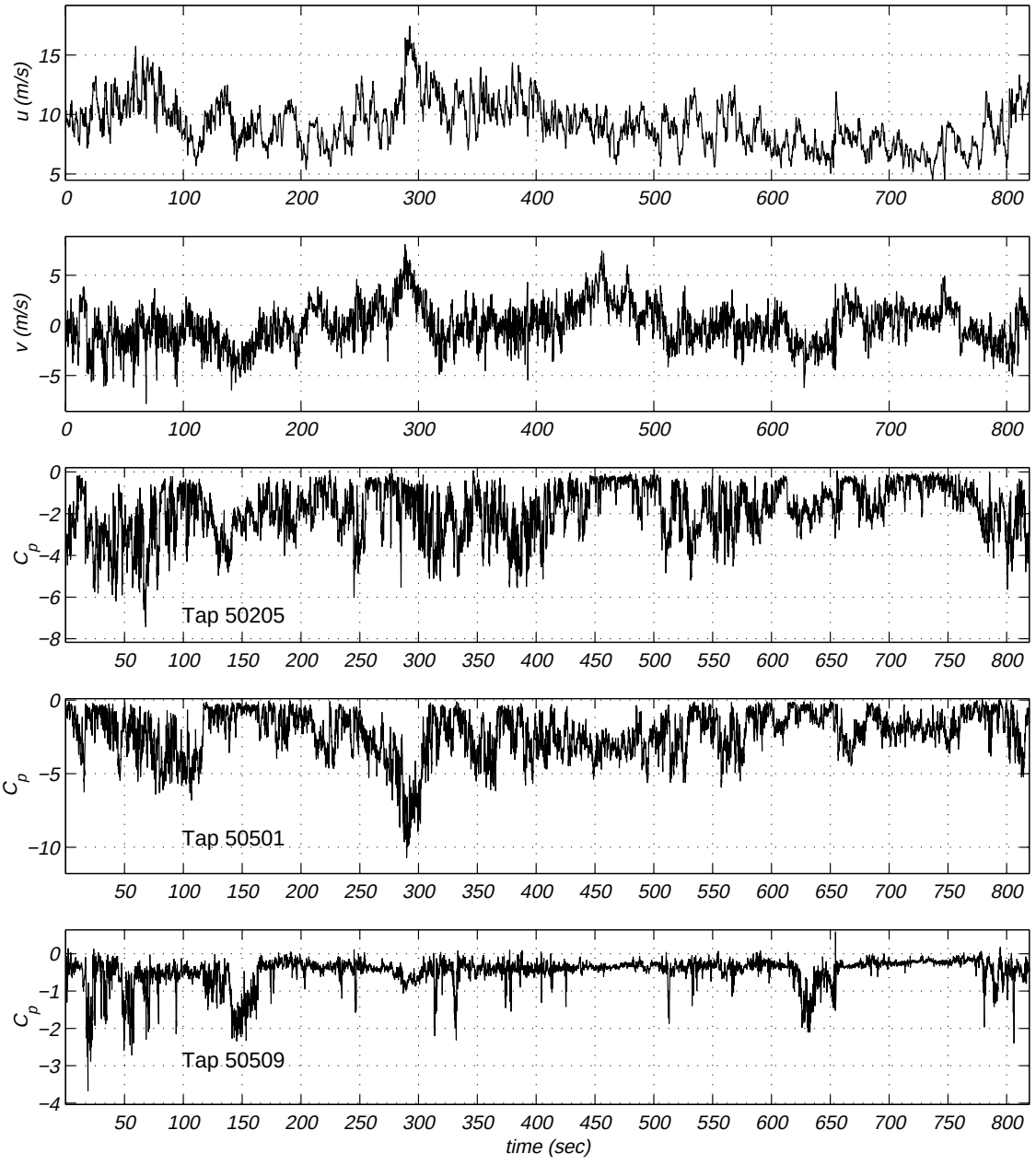

Figure 7.6: Time series of u and v velocity components and C_p of the three pressure coefficients (50205, 50501 and 50509) on WERFL building for record M15N087.

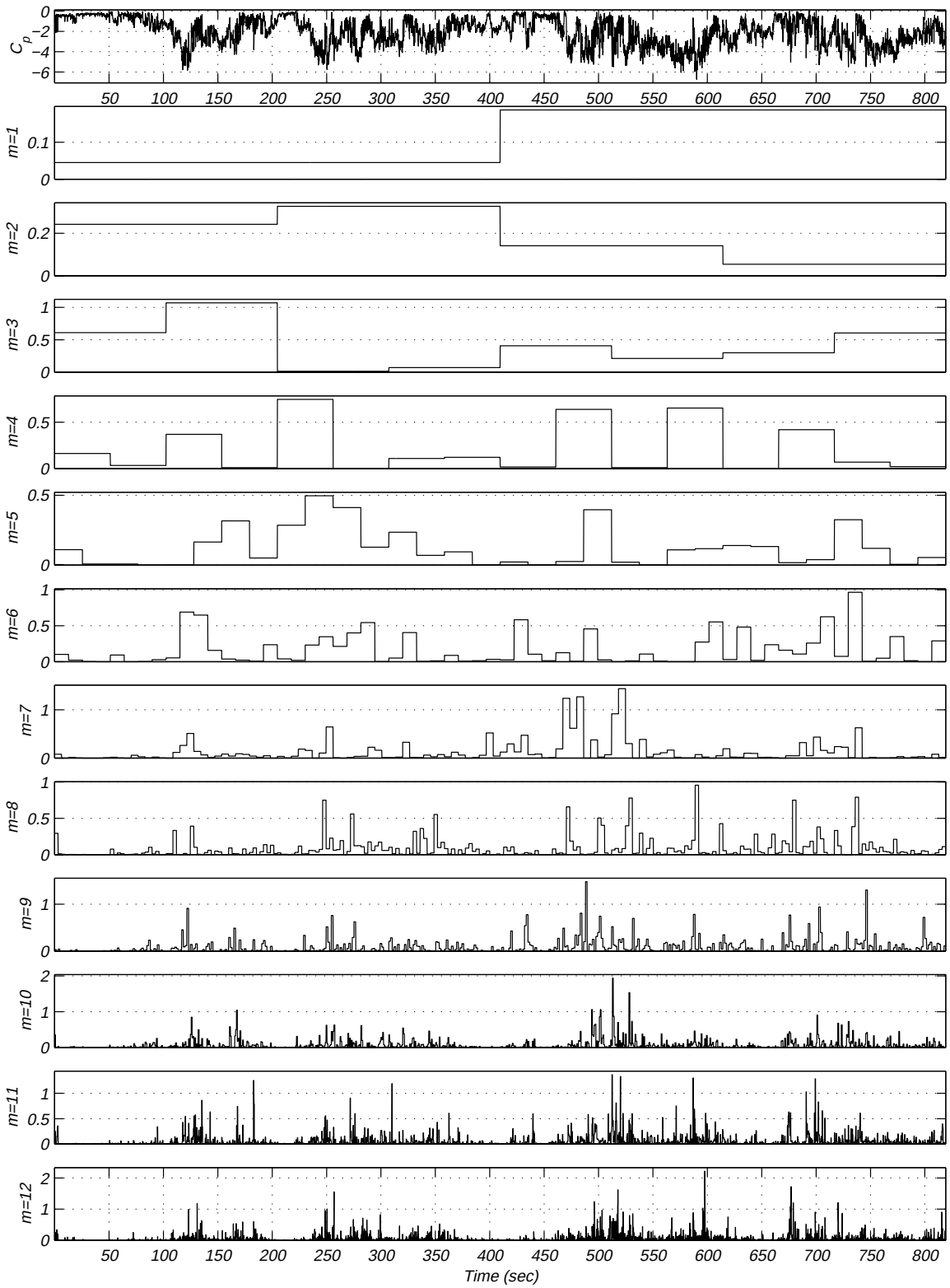

Figure 7.7a: wavelet coefficients of pressure coefficients at tap # 50205 for record M15N086.

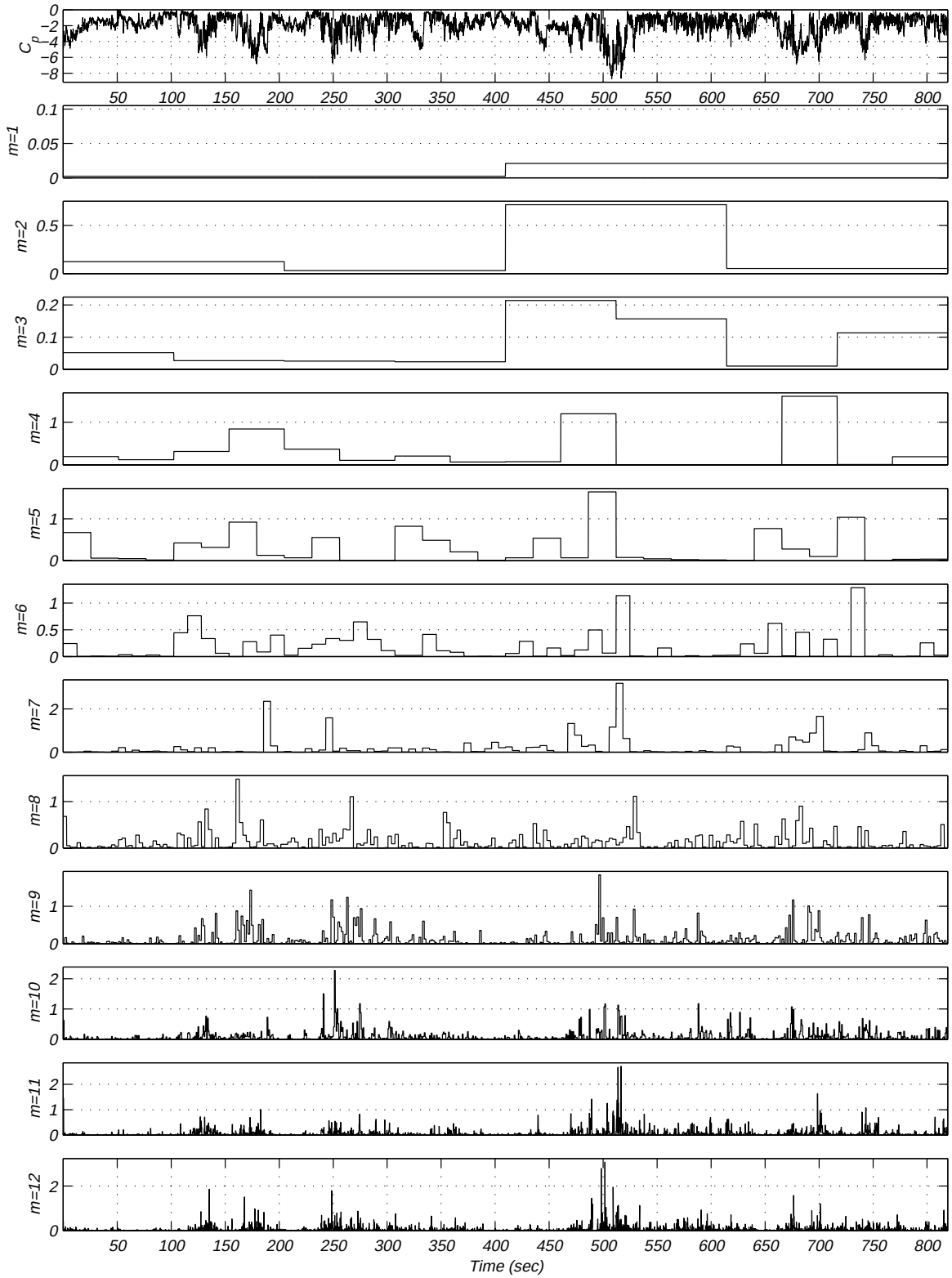

Figure 7.7b: wavelet coefficients of pressure coefficients at tap # 50501 for record M15N086.

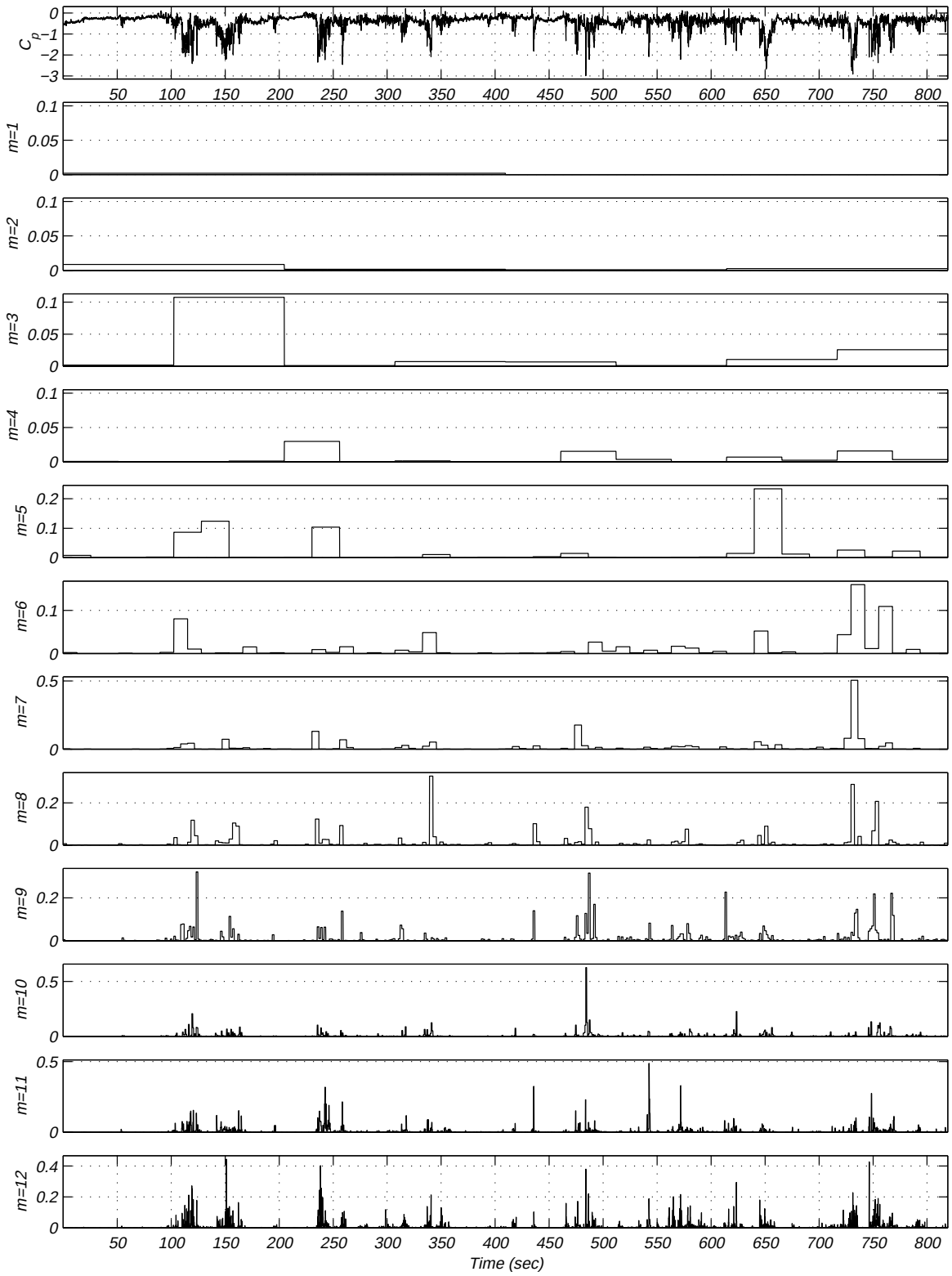

Figure 7.7c: wavelet coefficients of pressure coefficients at tap # 50509 for record M15N086.

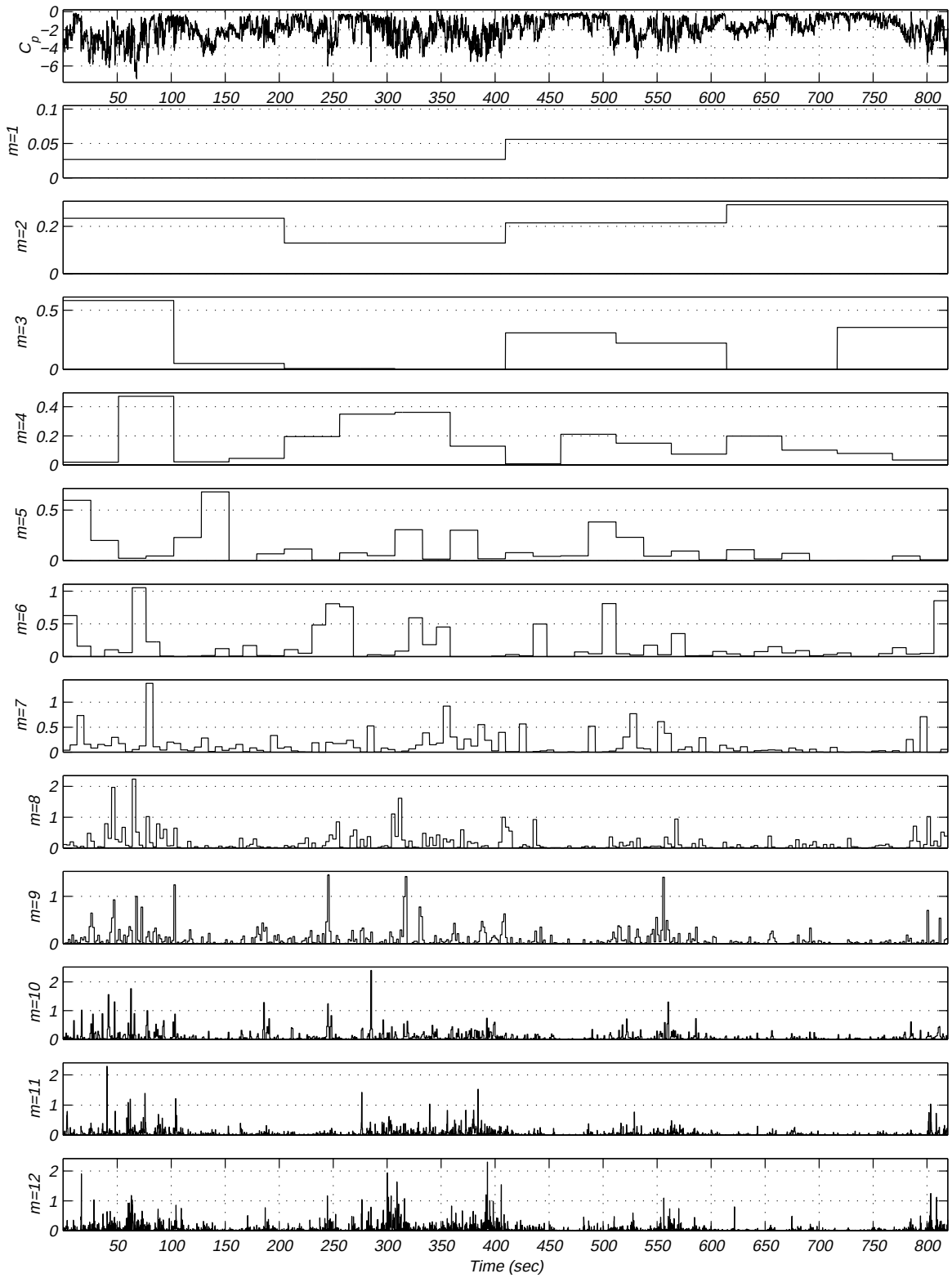

Figure 7.8a: wavelet coefficients of pressure coefficients at tap # 50205 for record M15N087.

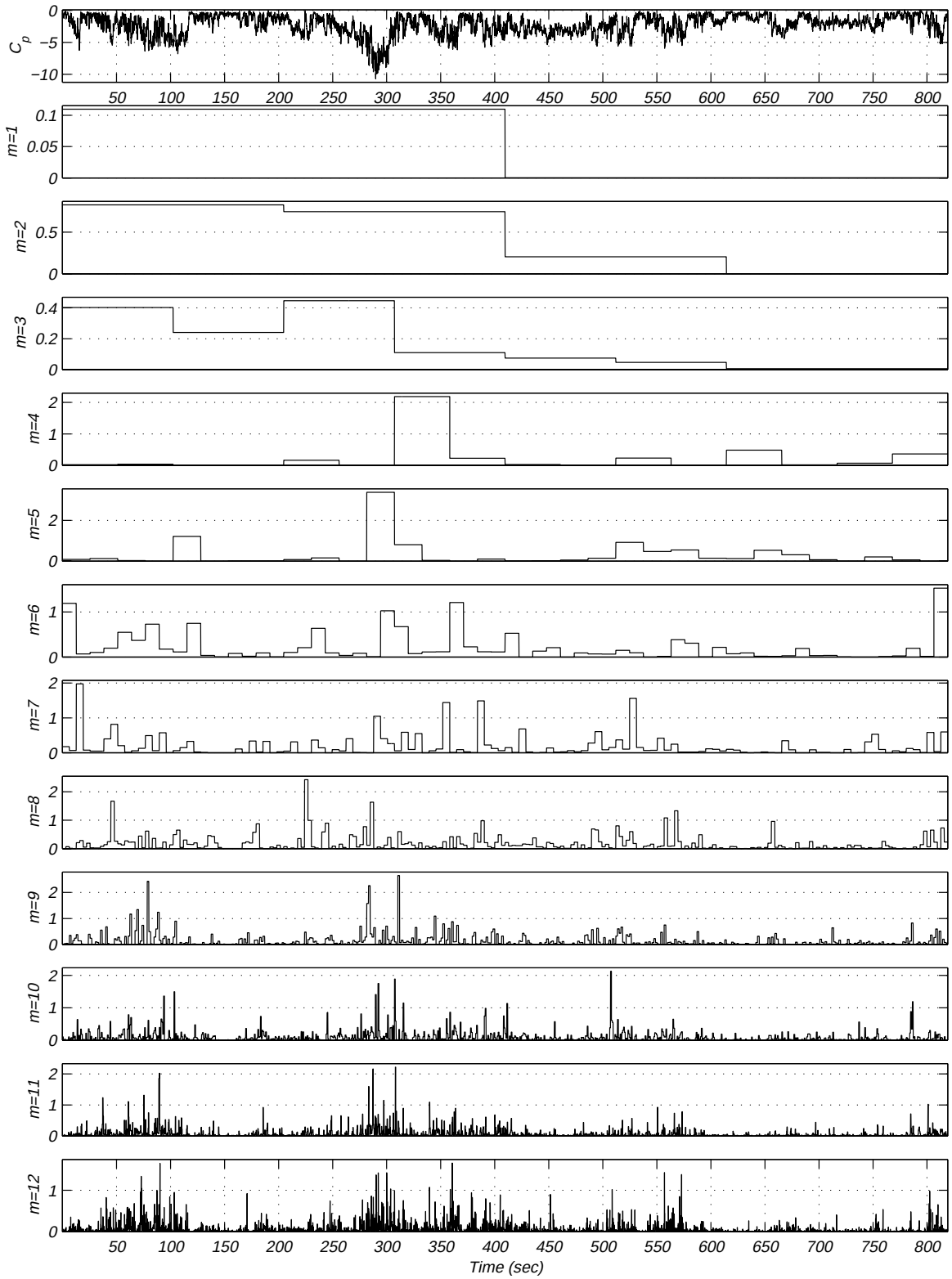

Figure 7.8b: wavelet coefficients of pressure coefficients at tap # 50501 for record M15N087.

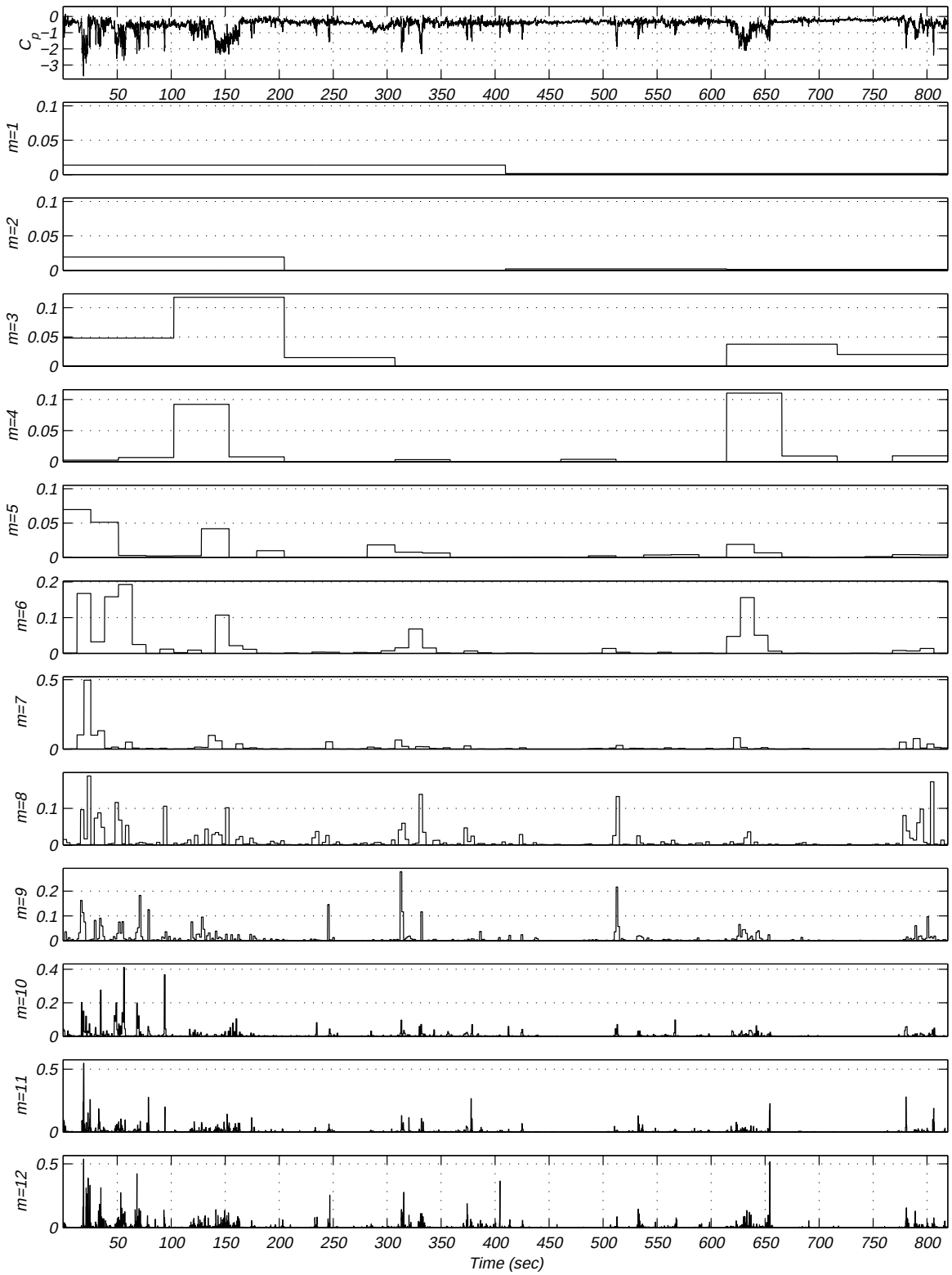

Figure 7.8c: wavelet coefficients of pressure coefficients at tap # 50509 for record M15N087.

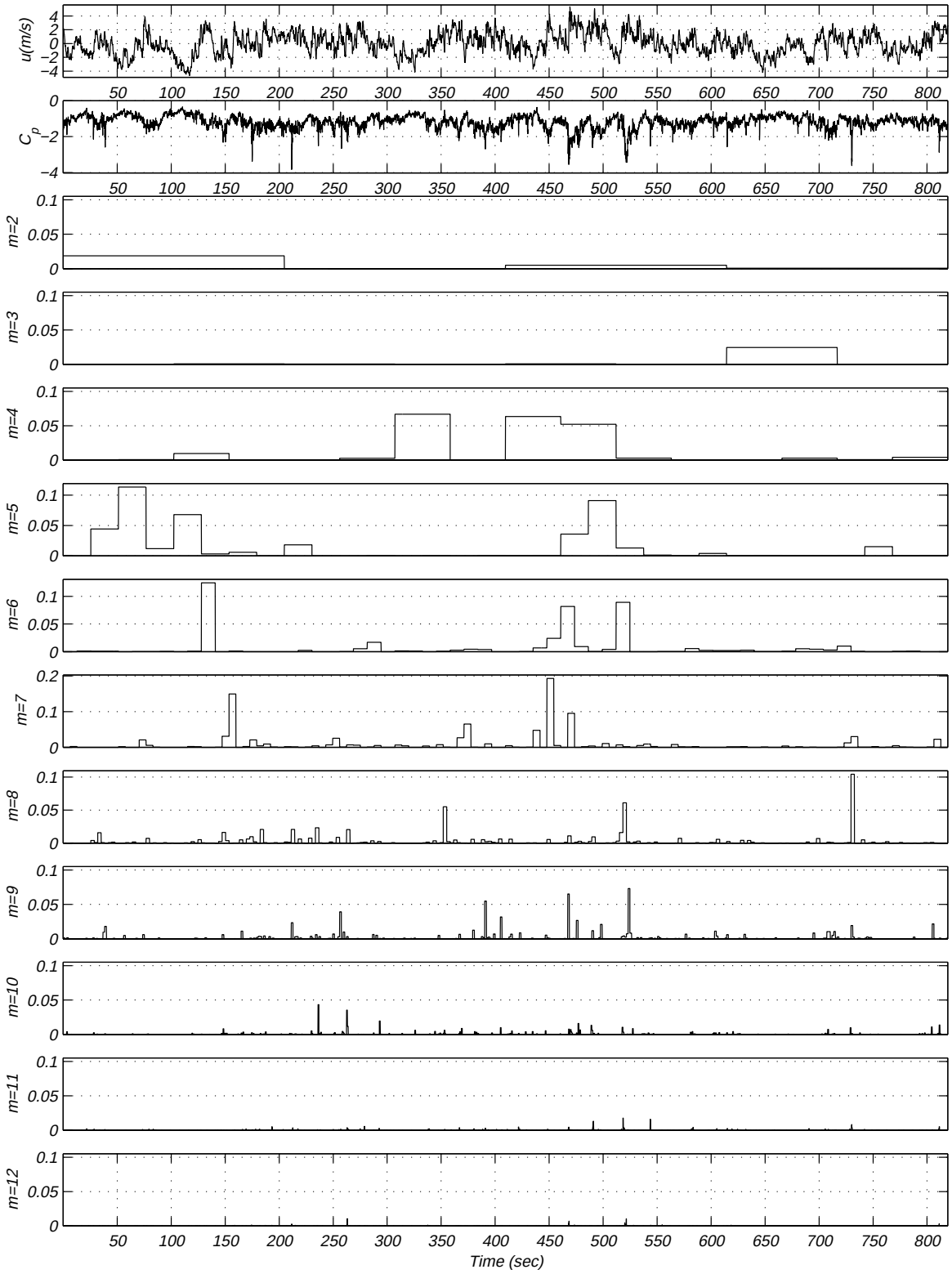

Figure 7.9a: Product of wavelet coefficients of u-component and pressure coefficients at tap # 50901 of record M15N468.

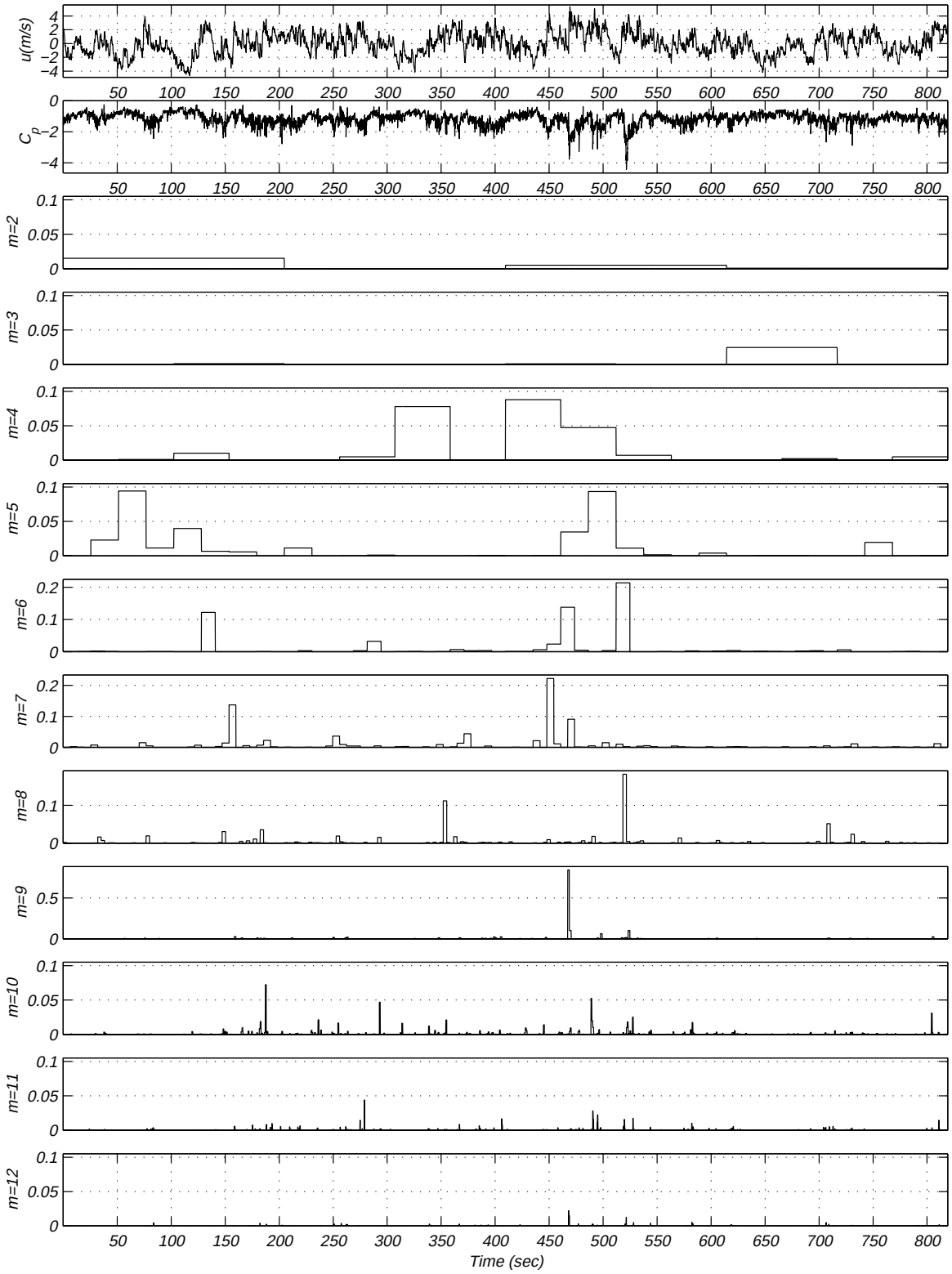

Figure 7.9b: Product of wavelet coefficients of u-component and pressure coefficients at tap # 50904 of record M15N468.

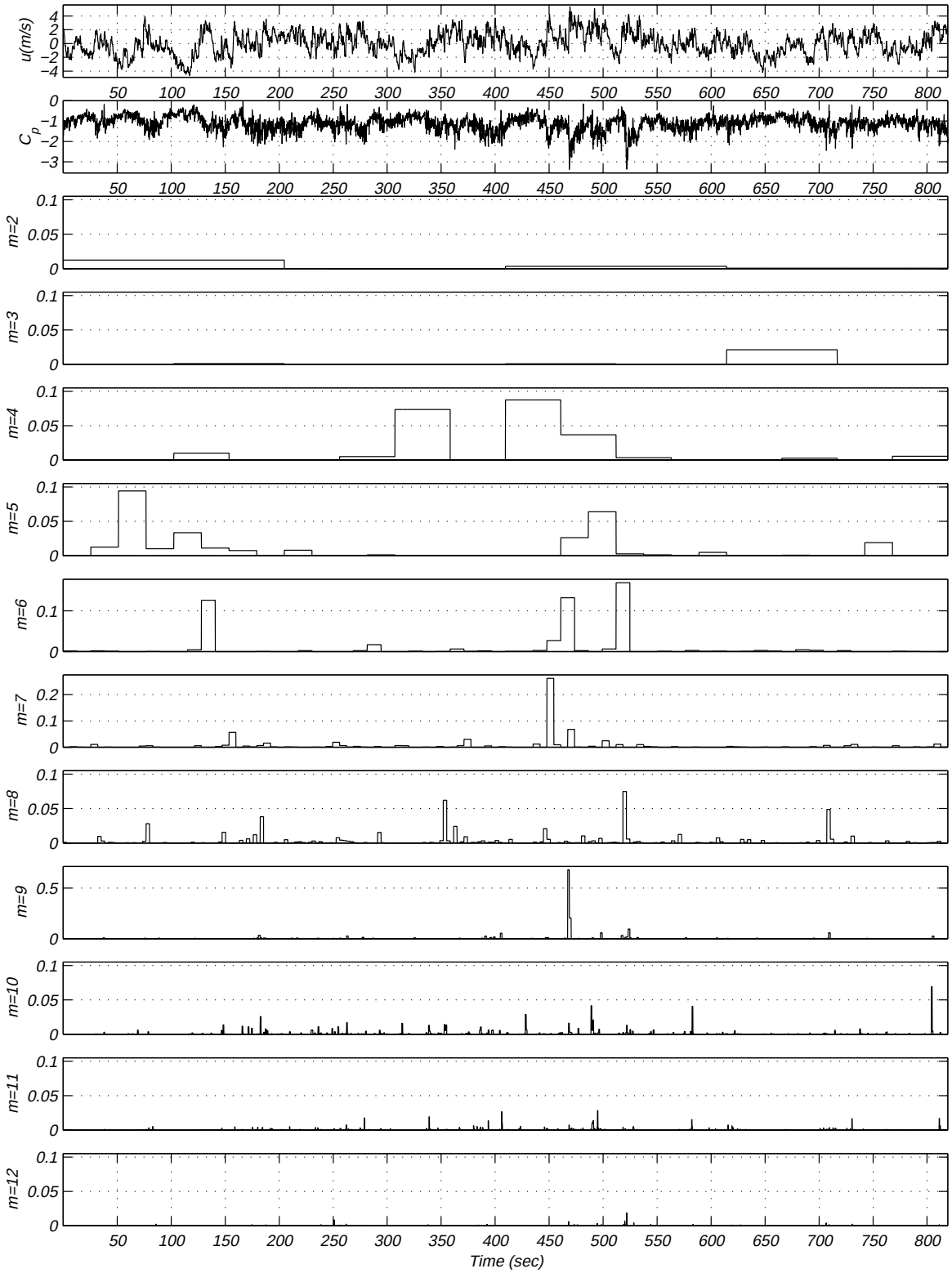

Figure 7.9c: Product of wavelet coefficients of u-component and pressure coefficients at tap # 50905 of record M15N468.

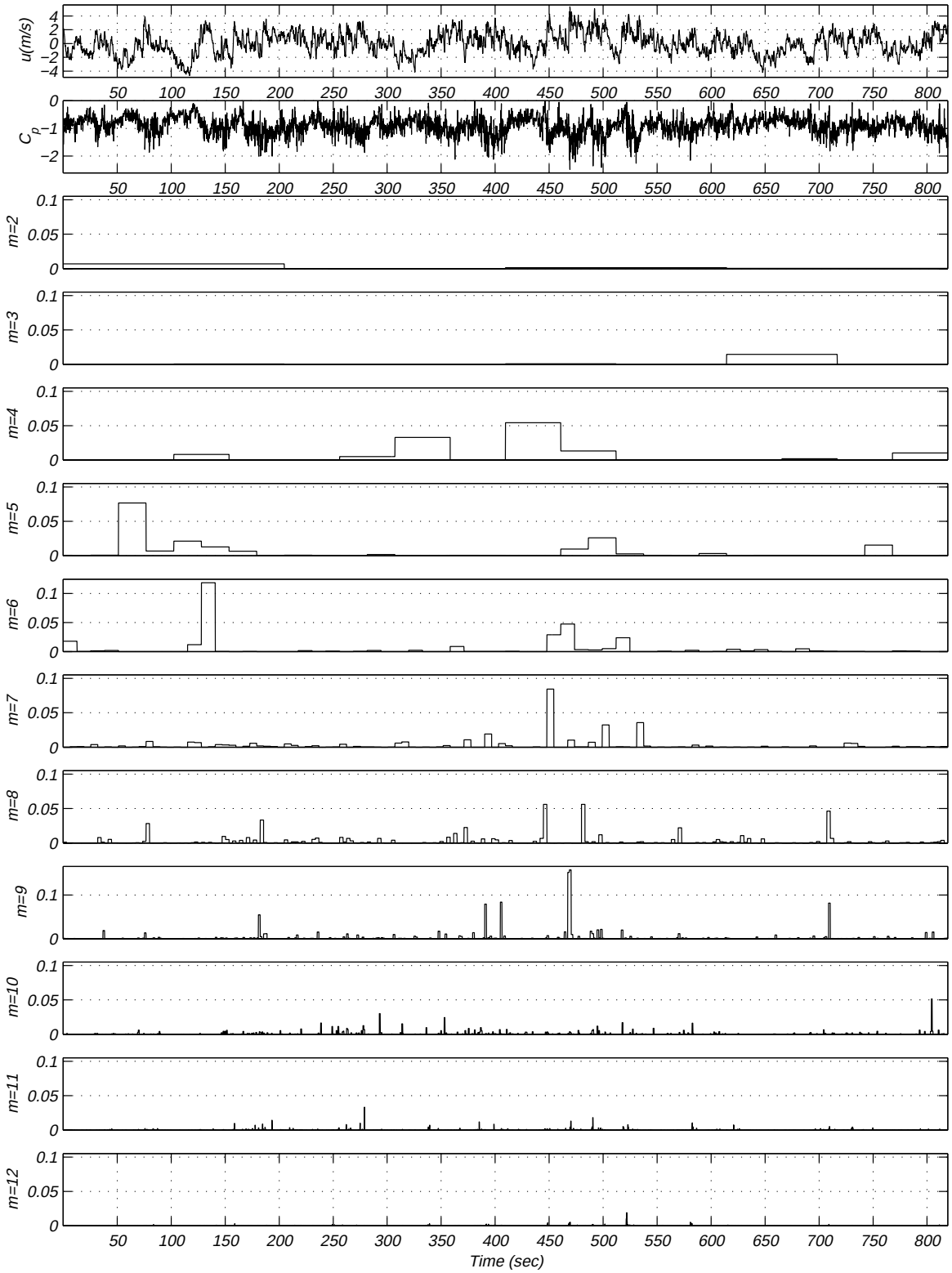

Figure 7.9d: Product of wavelet coefficients of u-component and pressure coefficients at tap # 50907 of record M15N468.

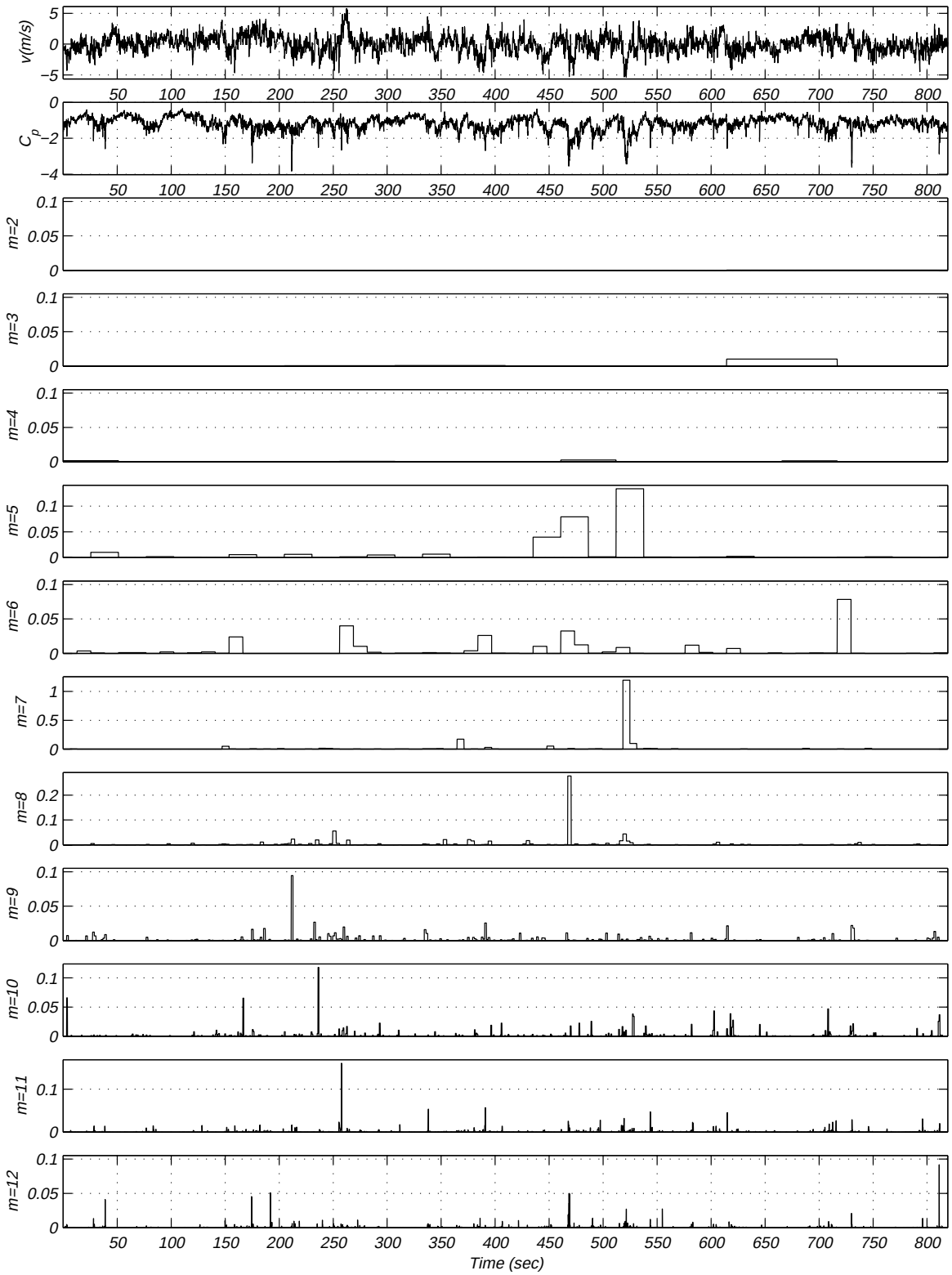

Figure 7.9e: Product of wavelet coefficients of v-component and pressure coefficients at tap # 50901 of record M15N468.

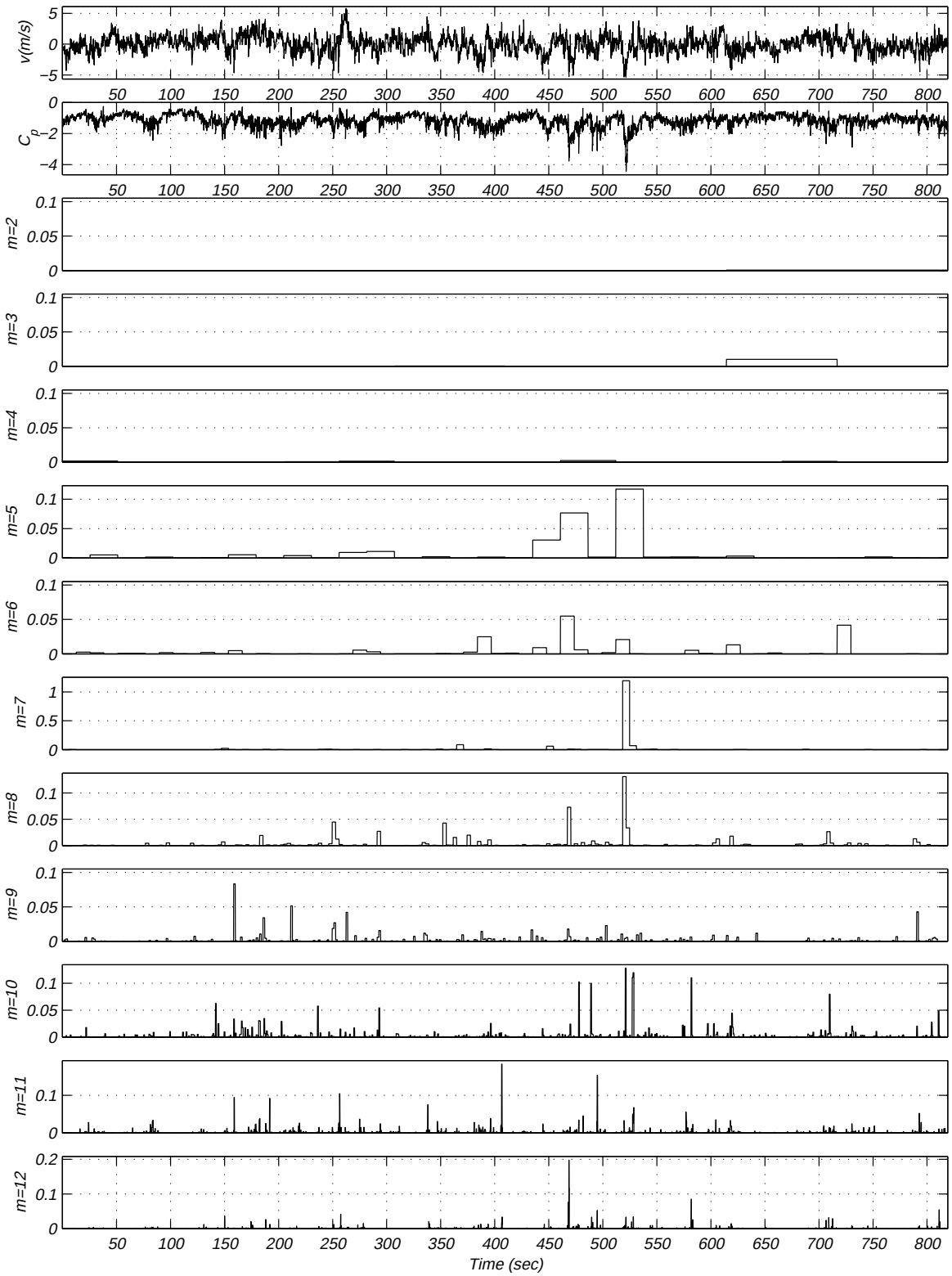

Figure 7.9f: Product of wavelet coefficients of v-component and pressure coefficients at tap # 50904 of record M15N468.

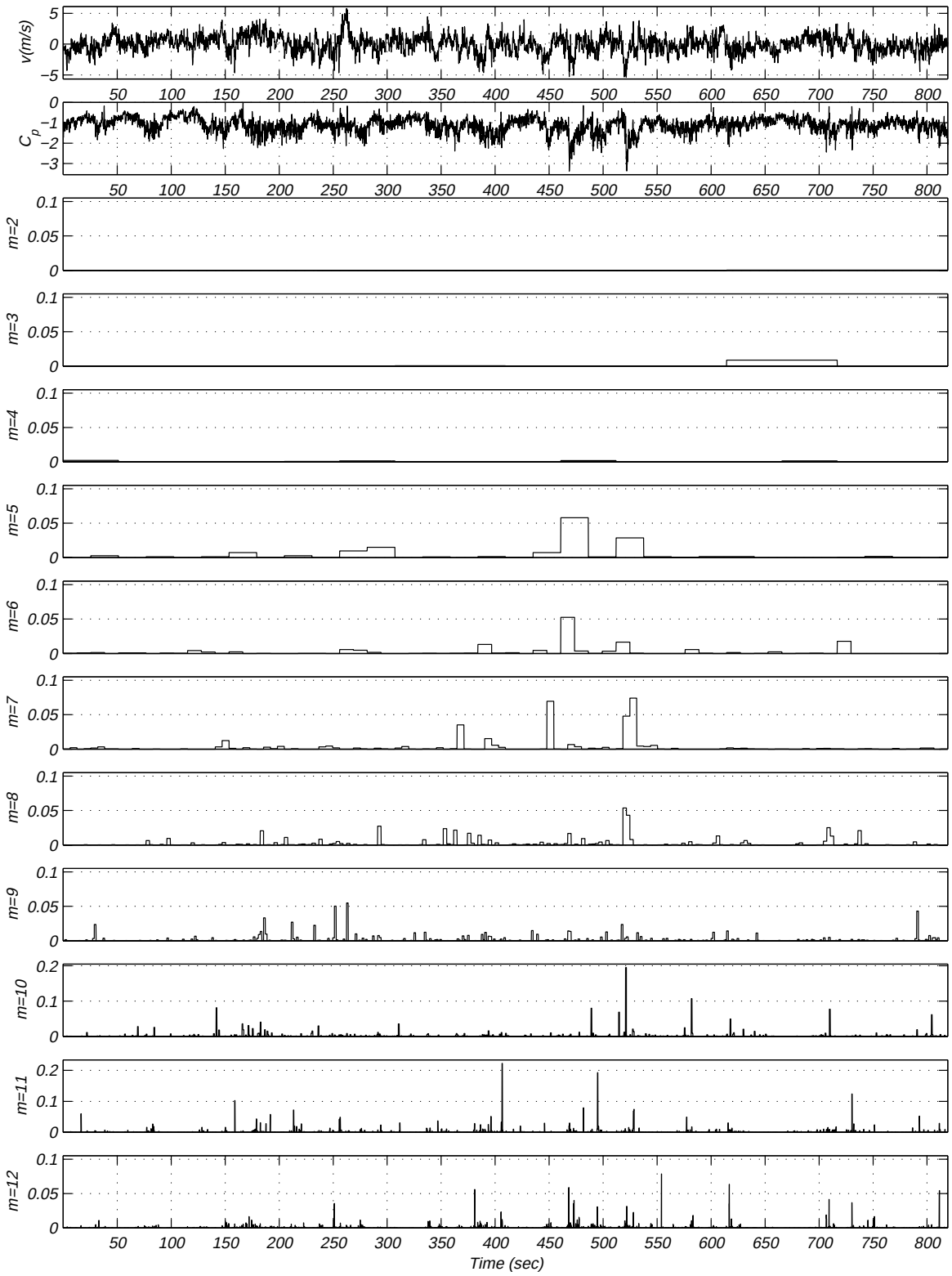

Figure 7.9g: Product of wavelet coefficients of v-component and pressure coefficients at tap # 50905 of record M15N468.

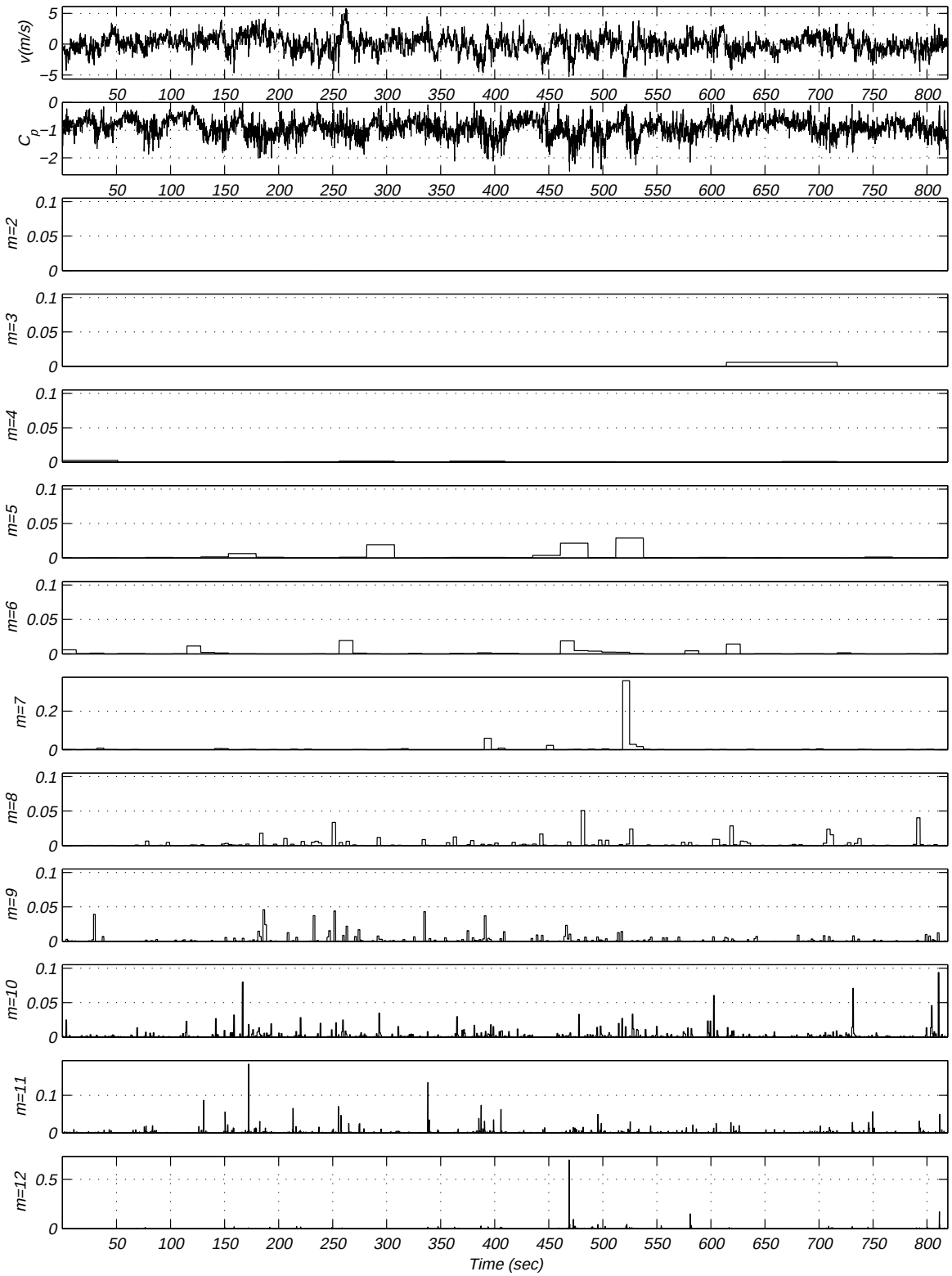

Figure 7.9h: Product of wavelet coefficients of v-component and pressure coefficients at tap # 50907 of record M15N468.

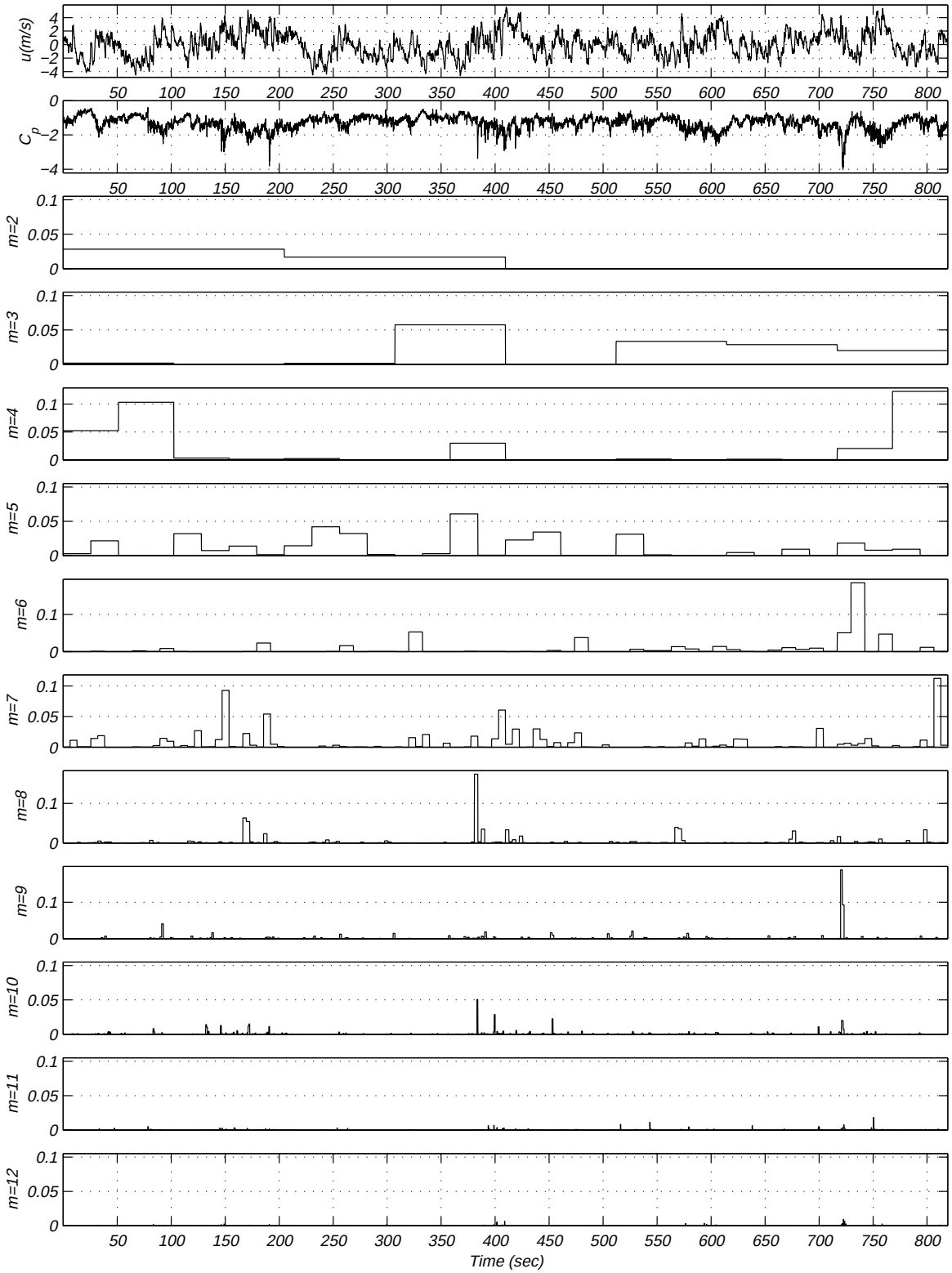

Figure 7.10a: Product of wavelet coefficients of u-component and pressure coefficients at tap # 50901 of record M15N471.

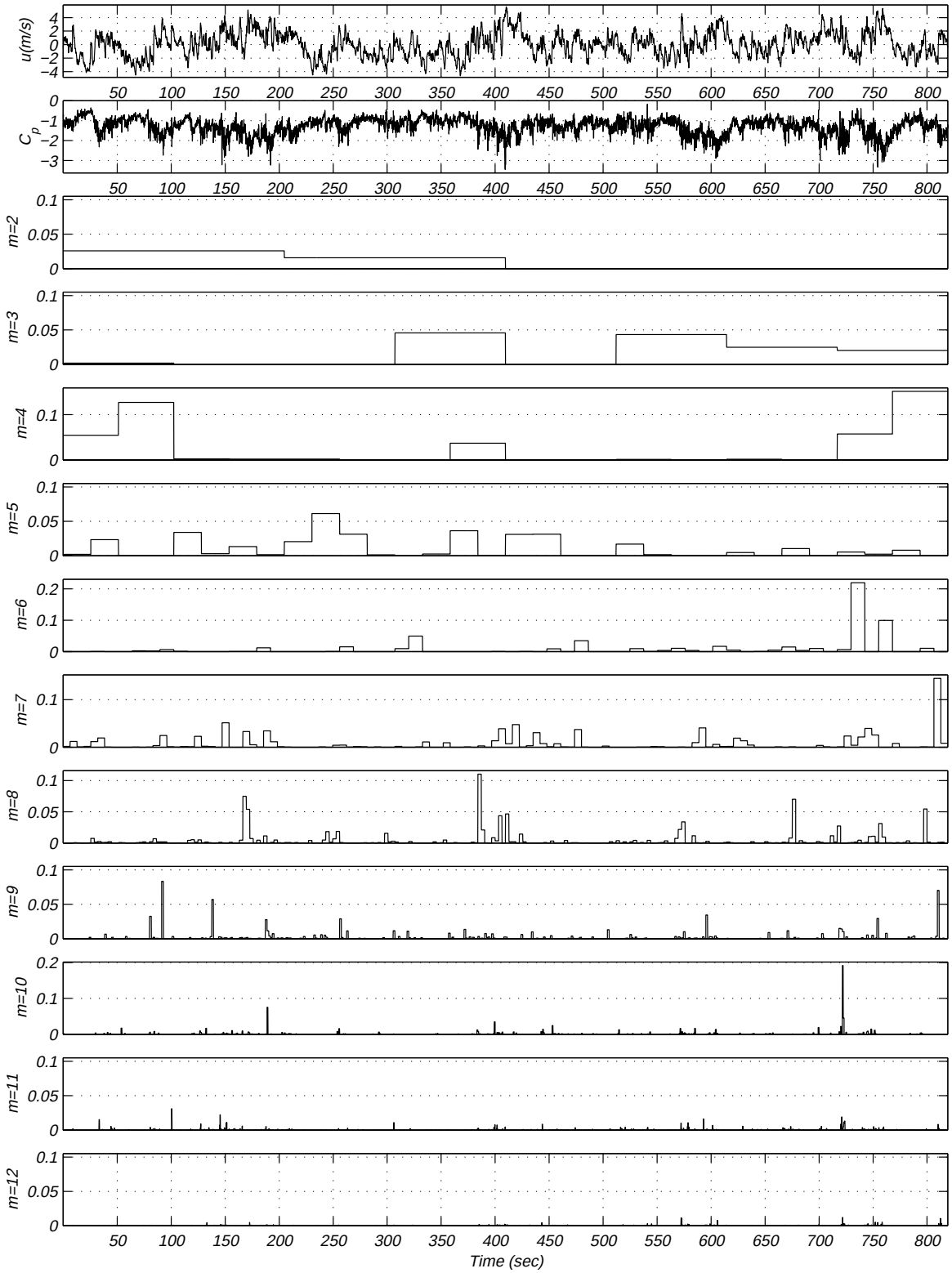

Figure 7.10b: Product of wavelet coefficients of u-component and pressure coefficients at tap # 50904 of record M15N471.

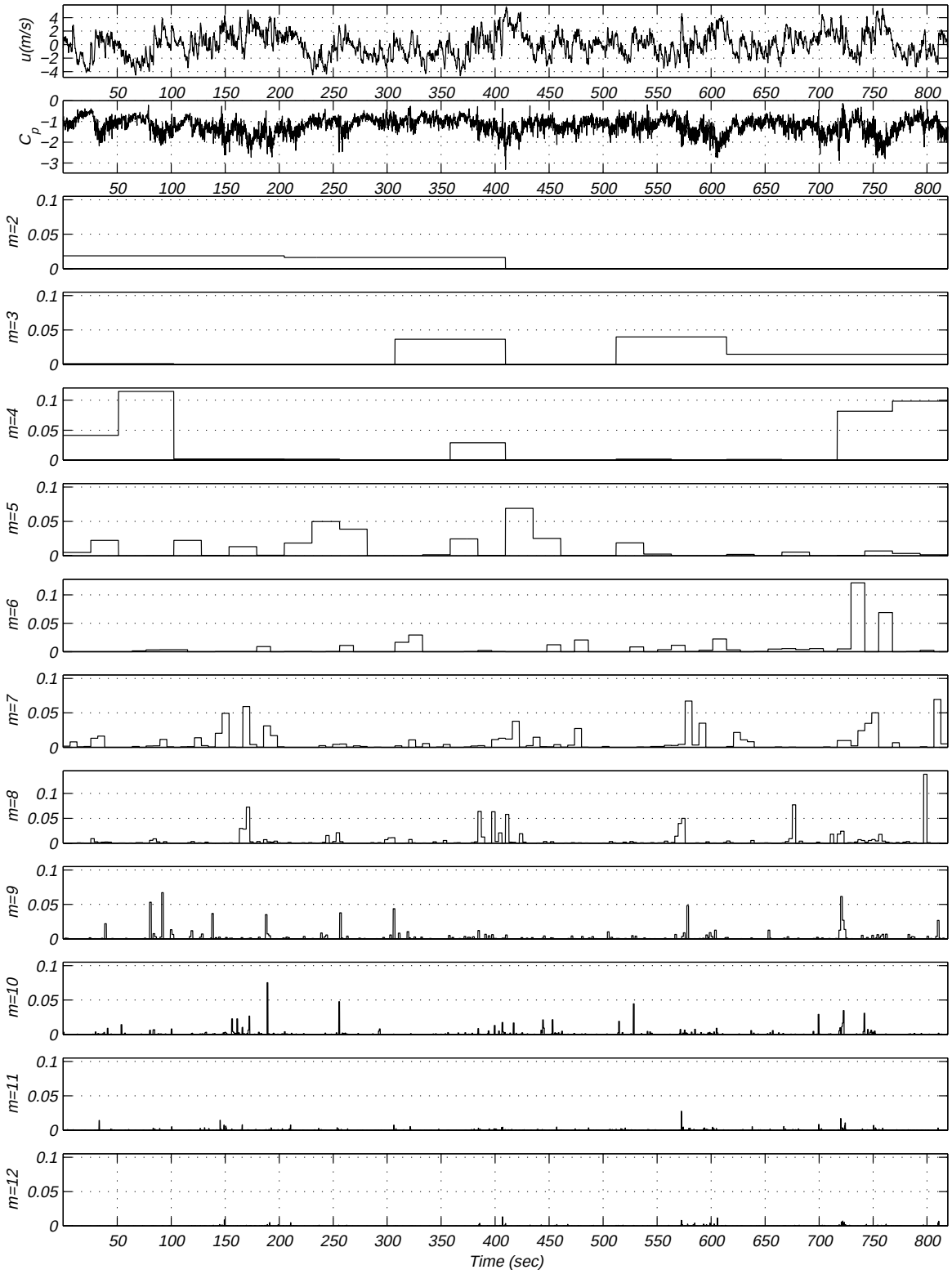

Figure 7.10c: Product of wavelet coefficients of u-component and pressure coefficients at tap # 50905 of record M15N471.

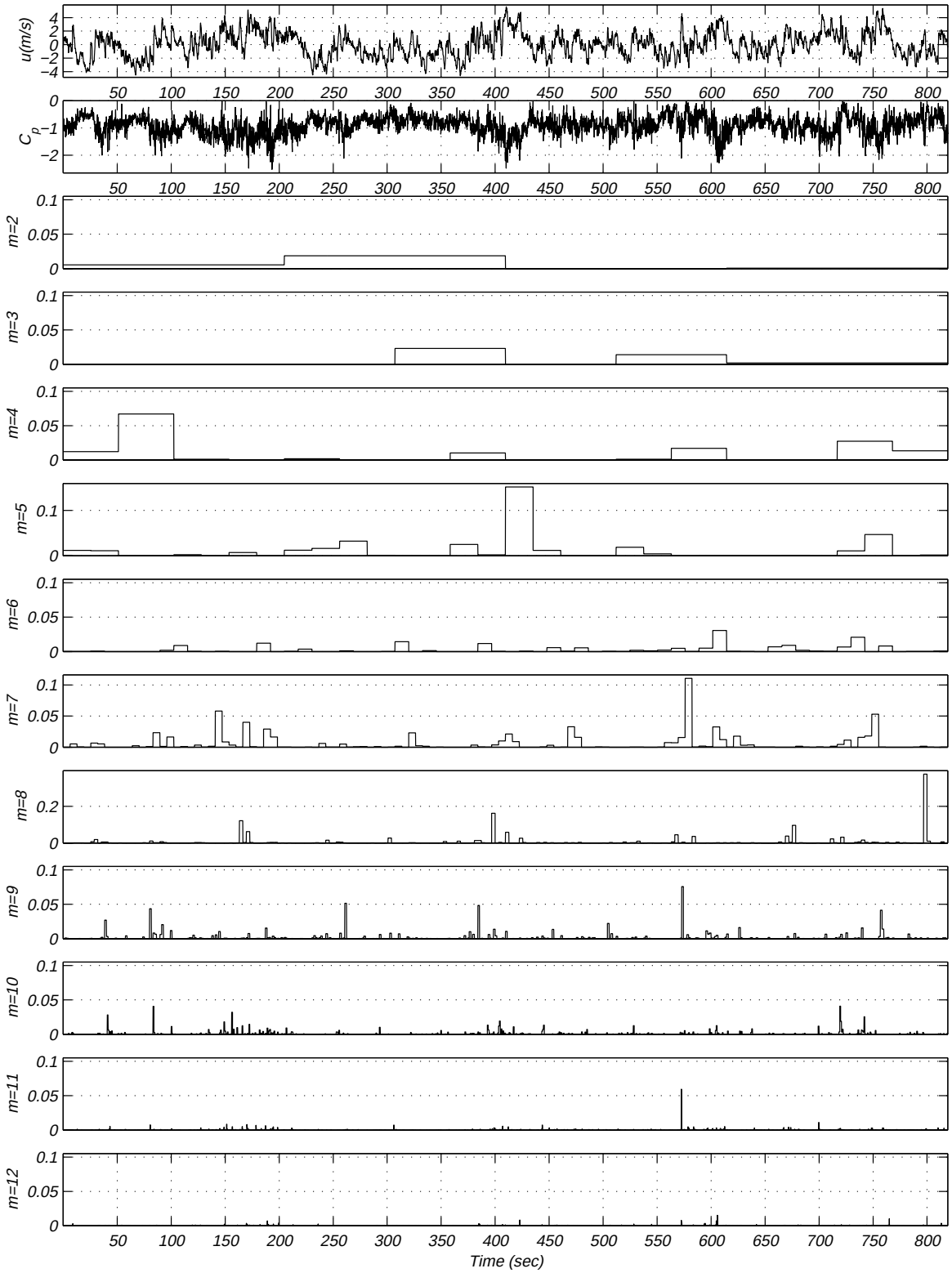

Figure 7.10d: Product of wavelet coefficients of u-component and pressure coefficients at tap # 50907 of record M15N471.

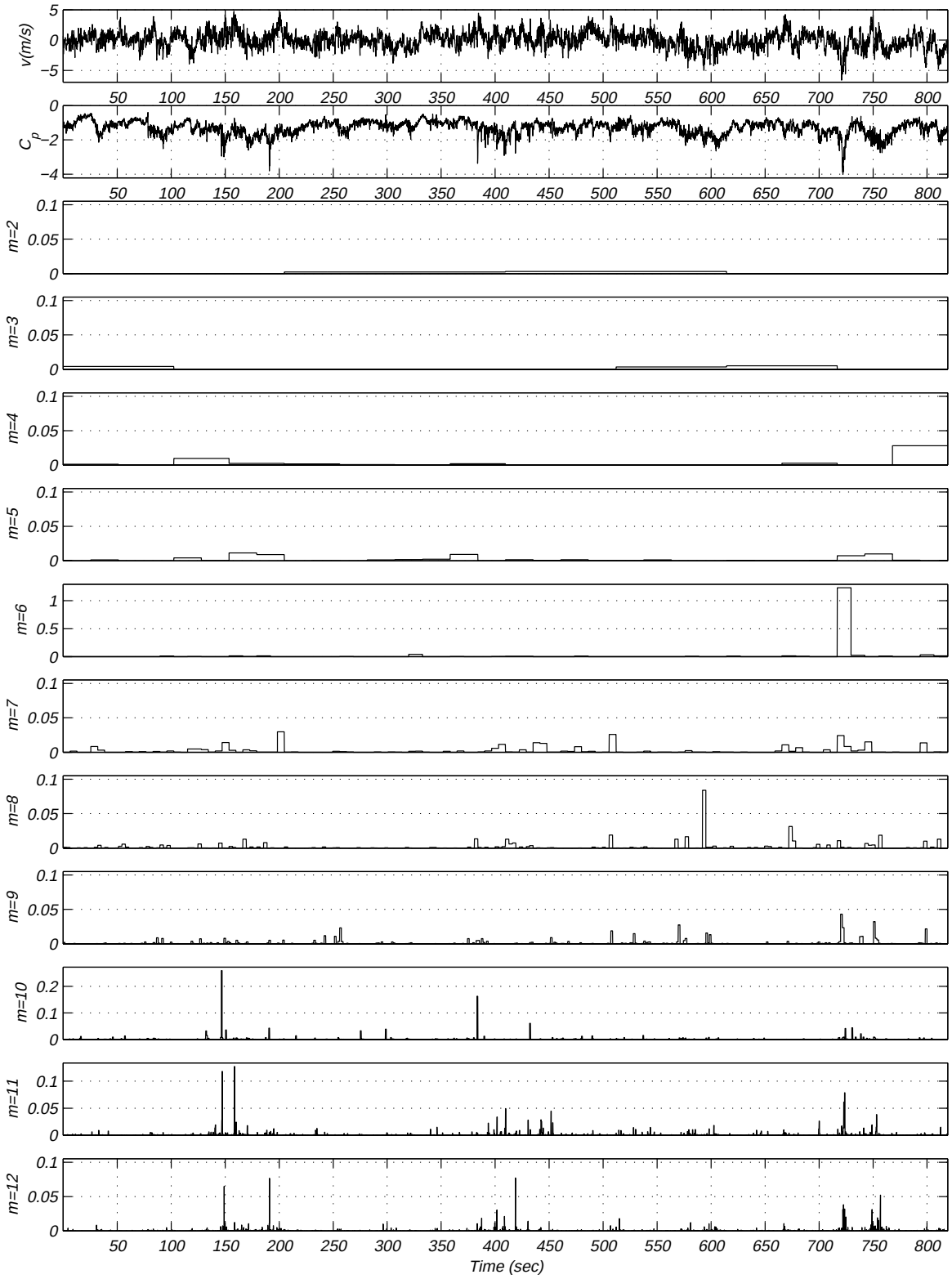

Figure 7.10e: Product of wavelet coefficients of v-component and pressure coefficients at tap # 50901 of record M15N471.

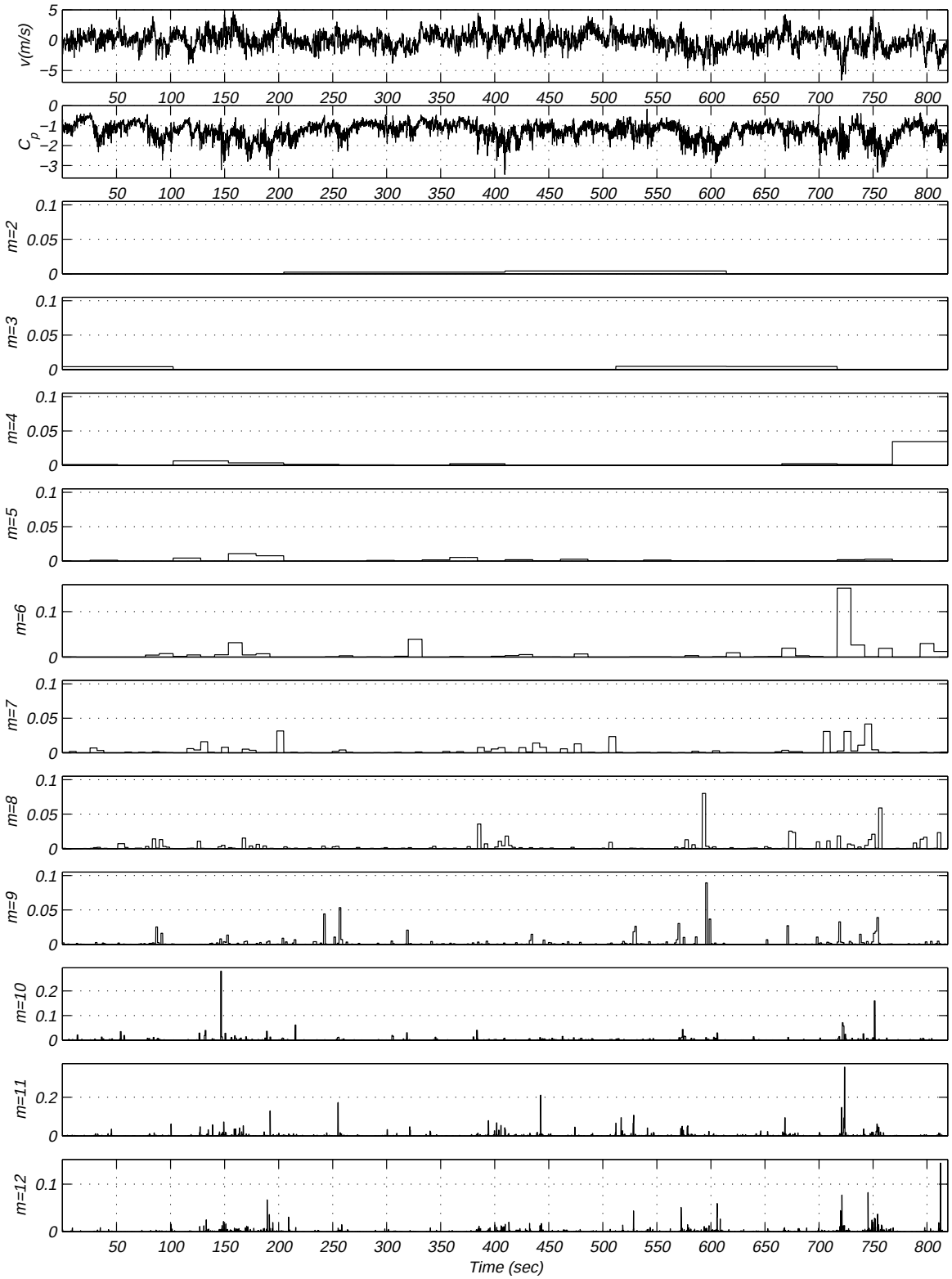

Figure 7.10f: Product of wavelet coefficients of v-component and pressure coefficients at tap # 50904 of record M15N471.

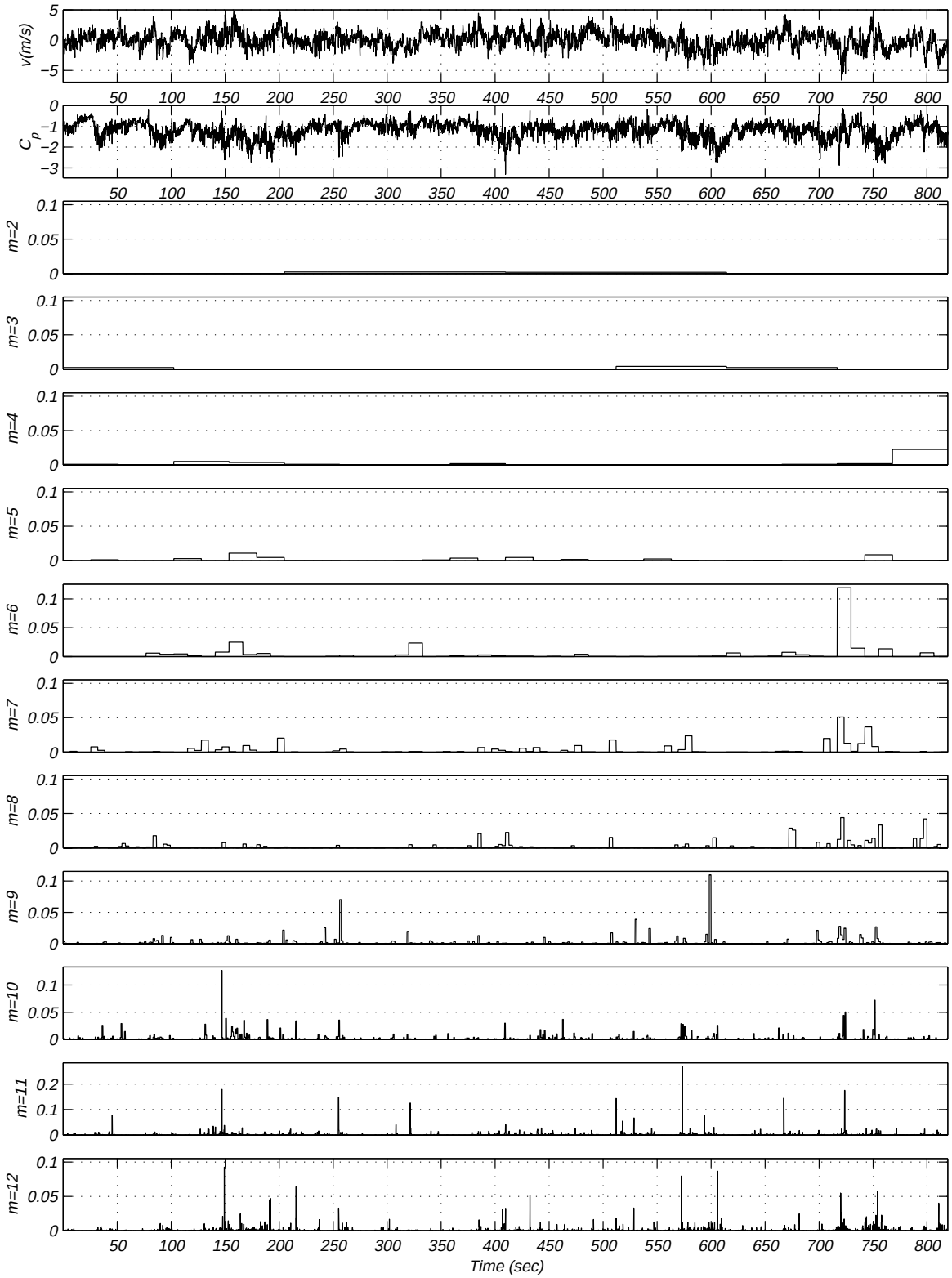

Figure 7.10g: Product of wavelet coefficients of v-component and pressure coefficients at tap # 50905 of record M15N471.

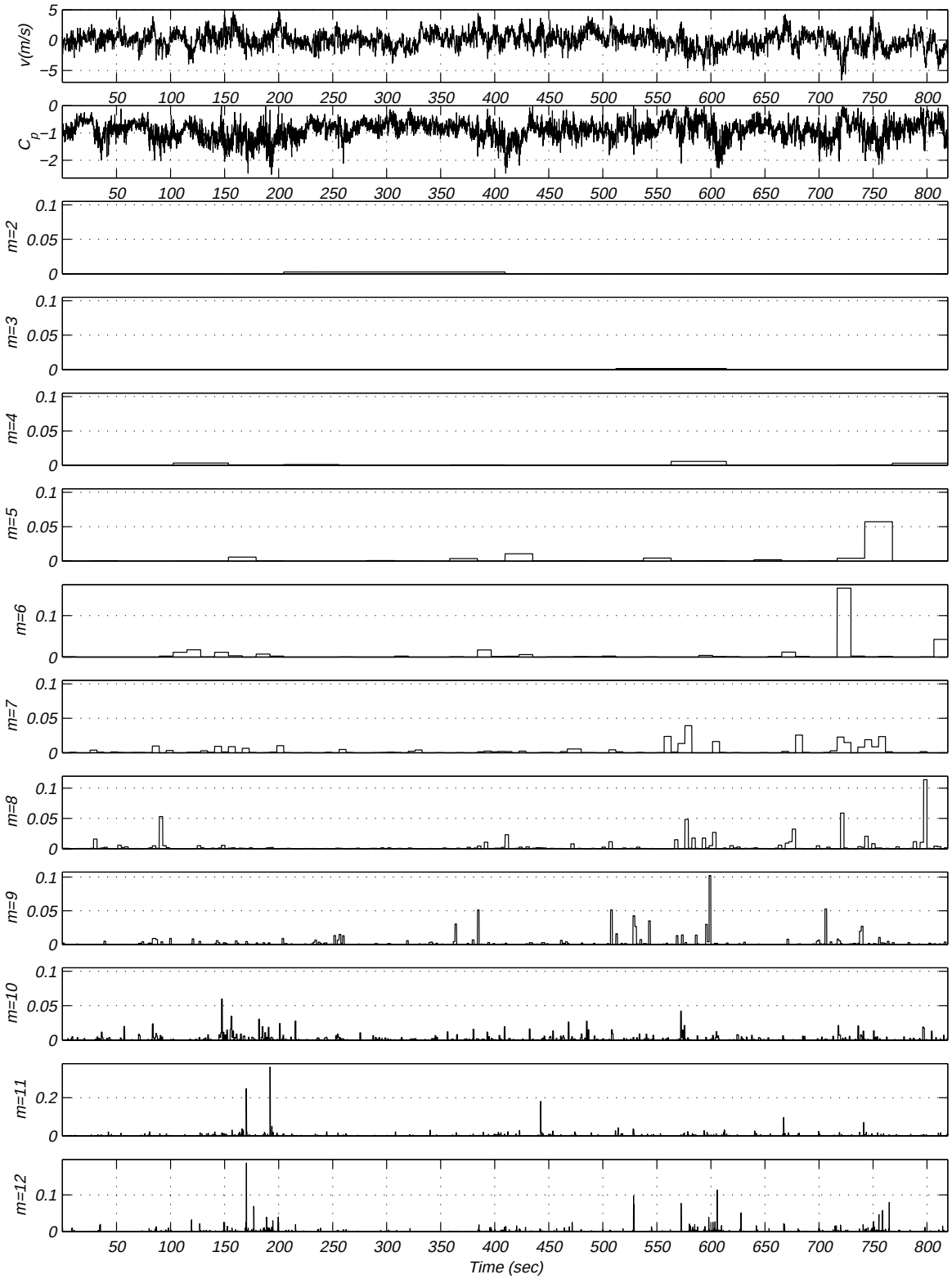

Figure 7.10h: Product of wavelet coefficients of v-component and pressure coefficients at tap # 50907 of record M15N471.

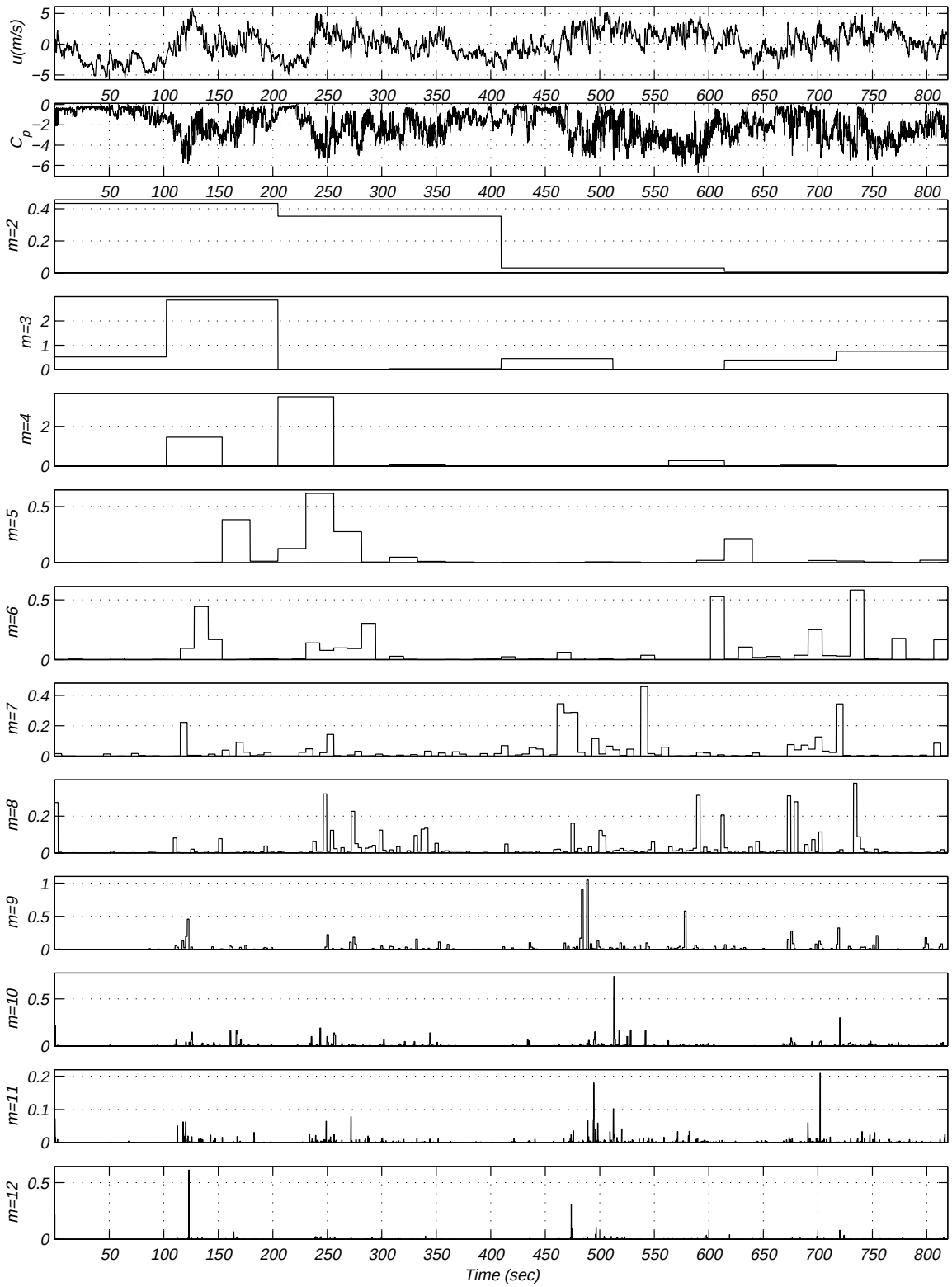

Figure 7.11a: Product of wavelet coefficients of u-component and pressure coefficients at tap # 50205 of record M15N086.

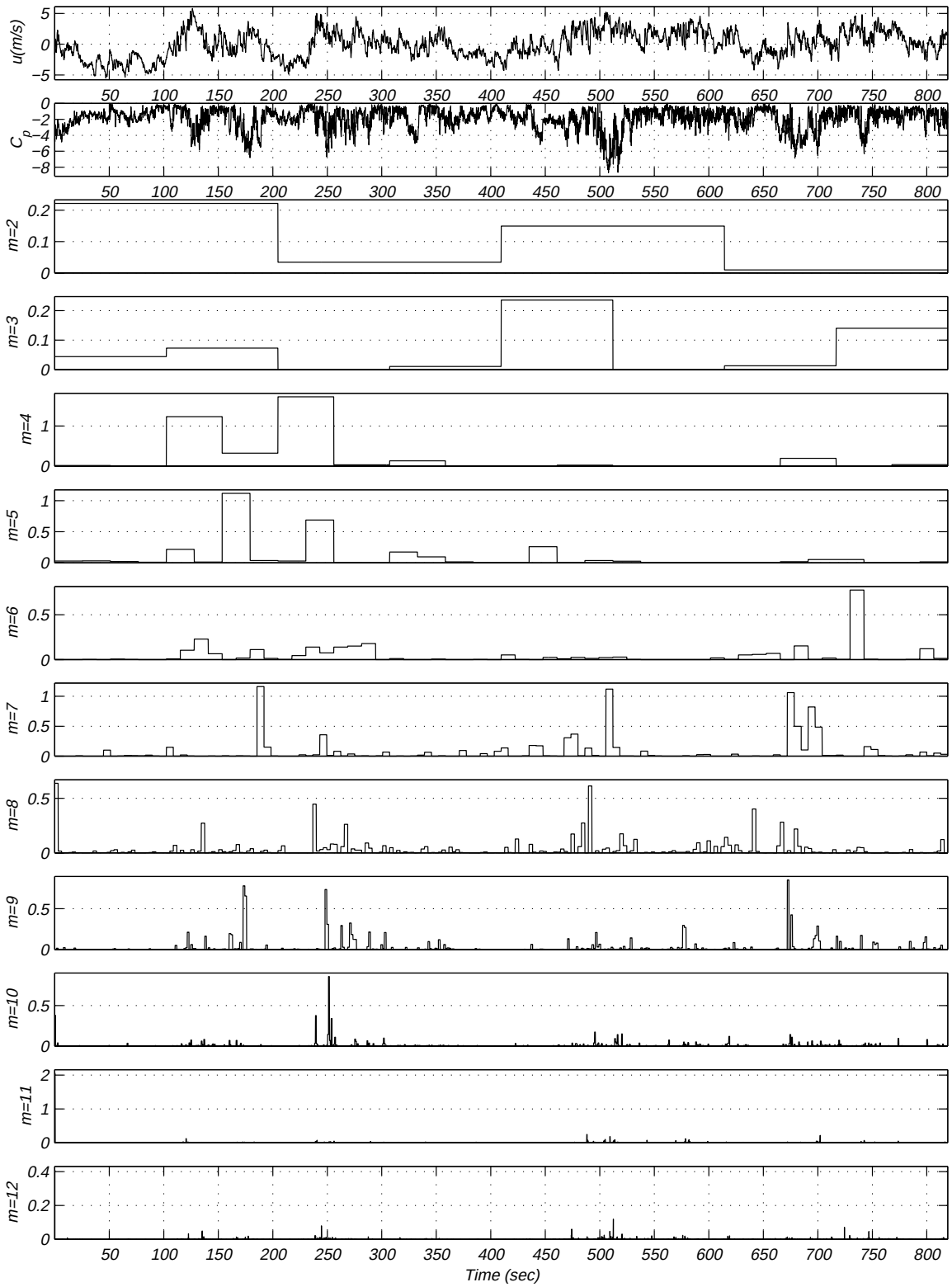

Figure 7.11b: Product of wavelet coefficients of u-component and pressure coefficients at tap # 50501 of record M15N086.

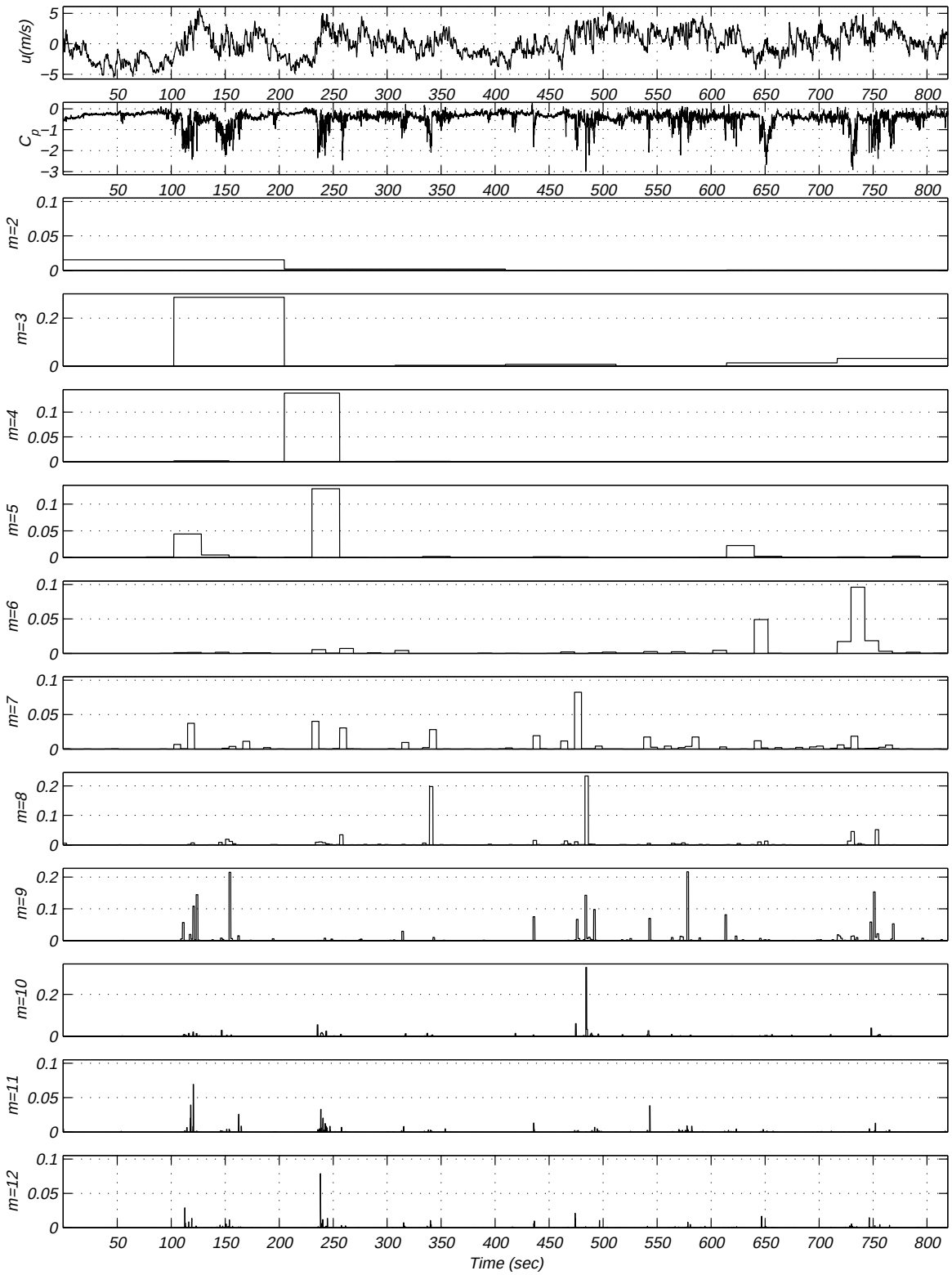

Figure 7.11c: Product of wavelet coefficients of u-component and pressure coefficients at tap # 50509 of record M15N086.

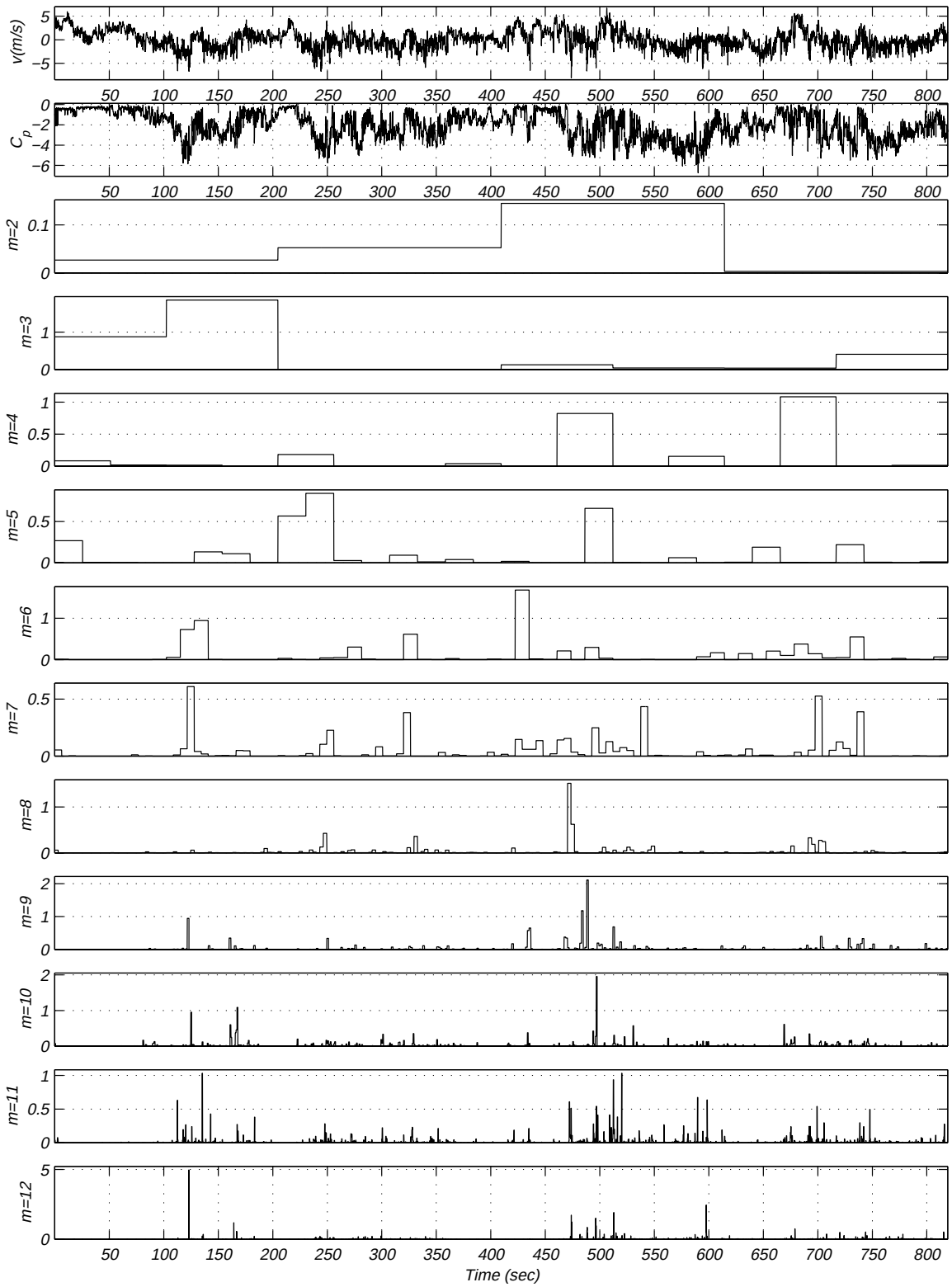

Figure 7.11d: Product of wavelet coefficients of v-component and pressure coefficients at tap # 50205 of record M15N086.

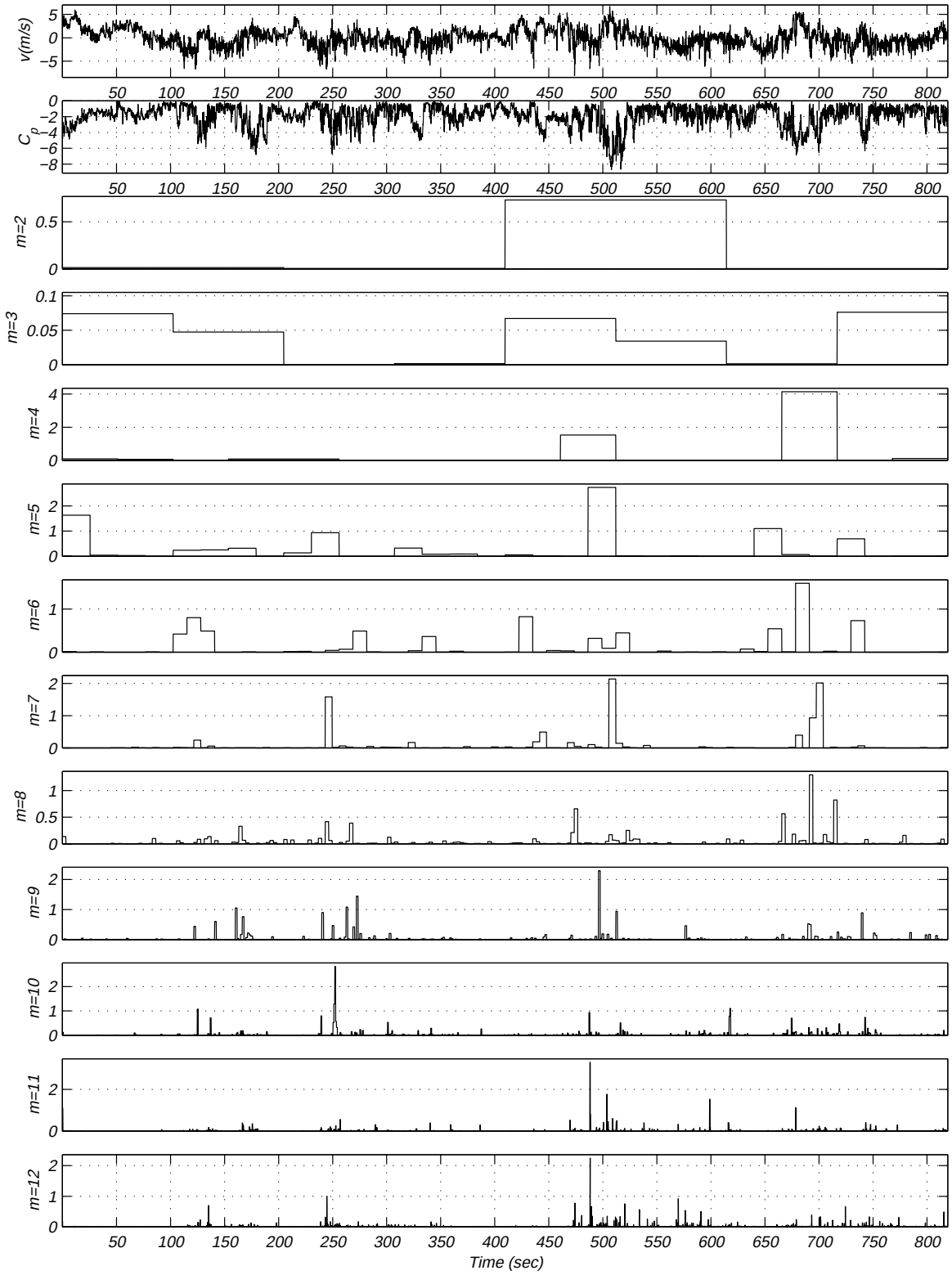

Figure 7.11e: Product of wavelet coefficients of v-component and pressure coefficients at tap # 50501 of record M15N086.

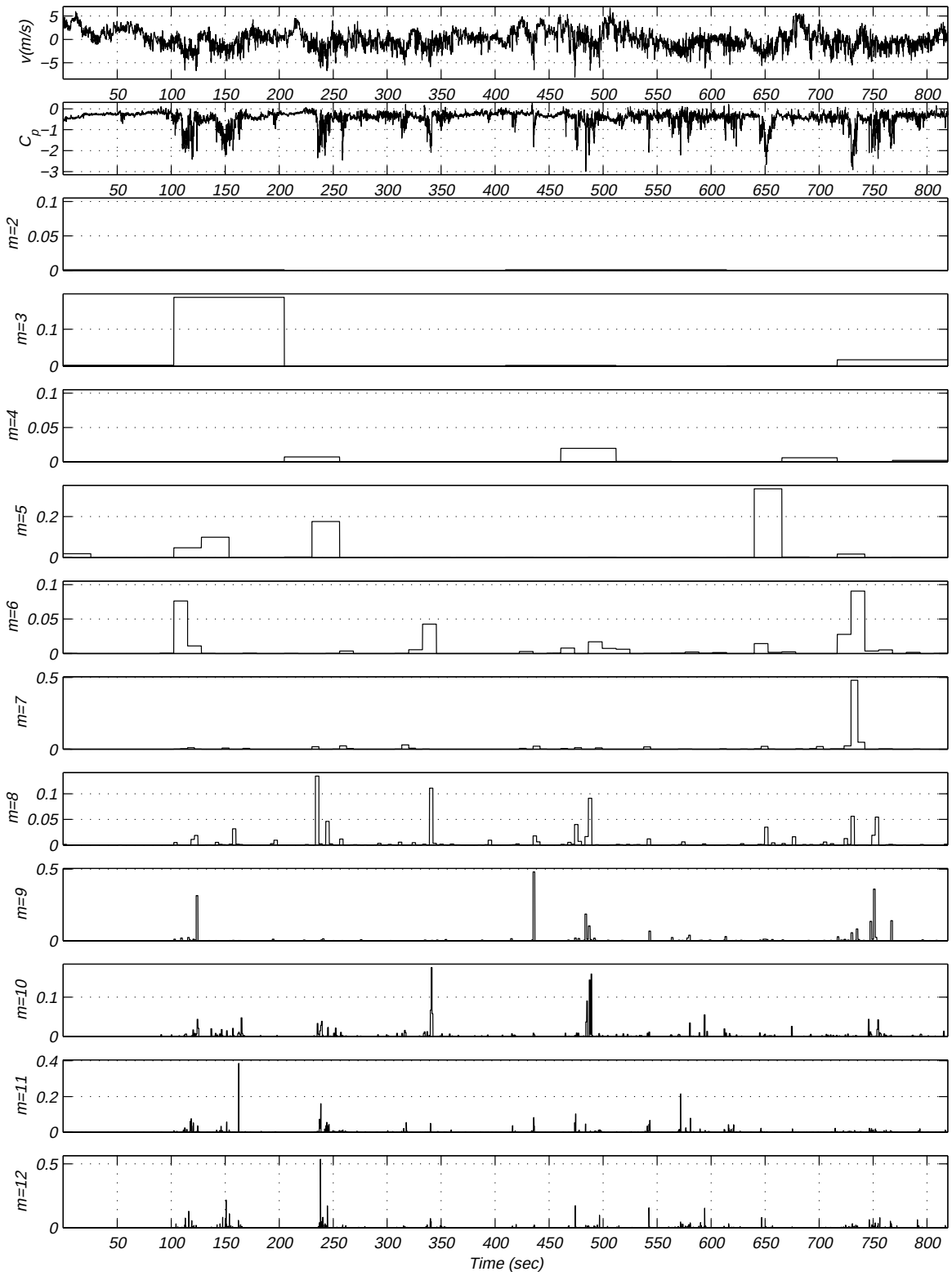

Figure 7.11f: Product of wavelet coefficients of v-component and pressure coefficients at tap # 50509 of record M15N086.

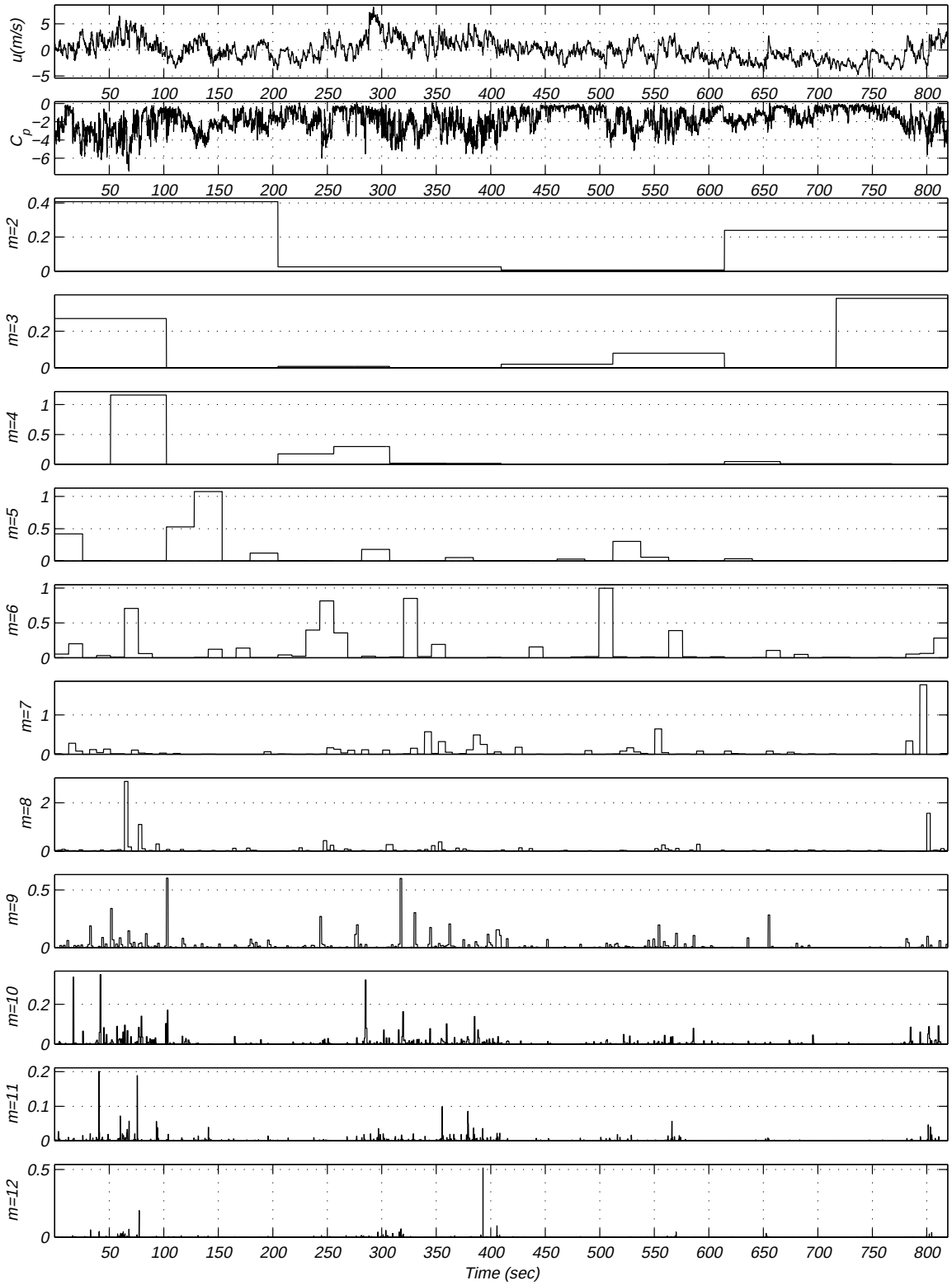

Figure 7.12a: Product of wavelet coefficients of u-component and pressure coefficients at tap # 50205 of record M15N087.

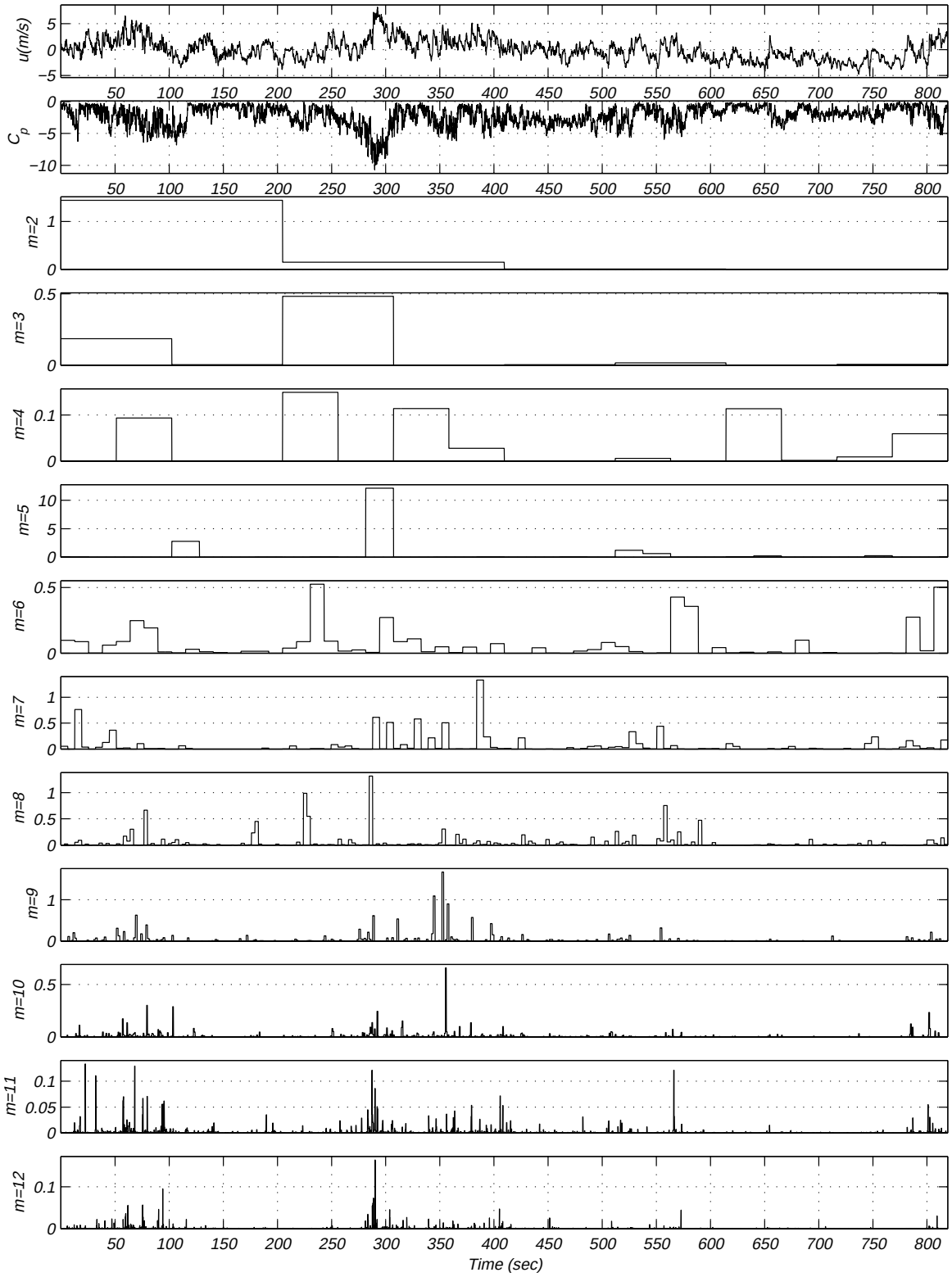

Figure 7.12b: Product of wavelet coefficients of u-component and pressure coefficients at tap # 50501 of record M15N087.

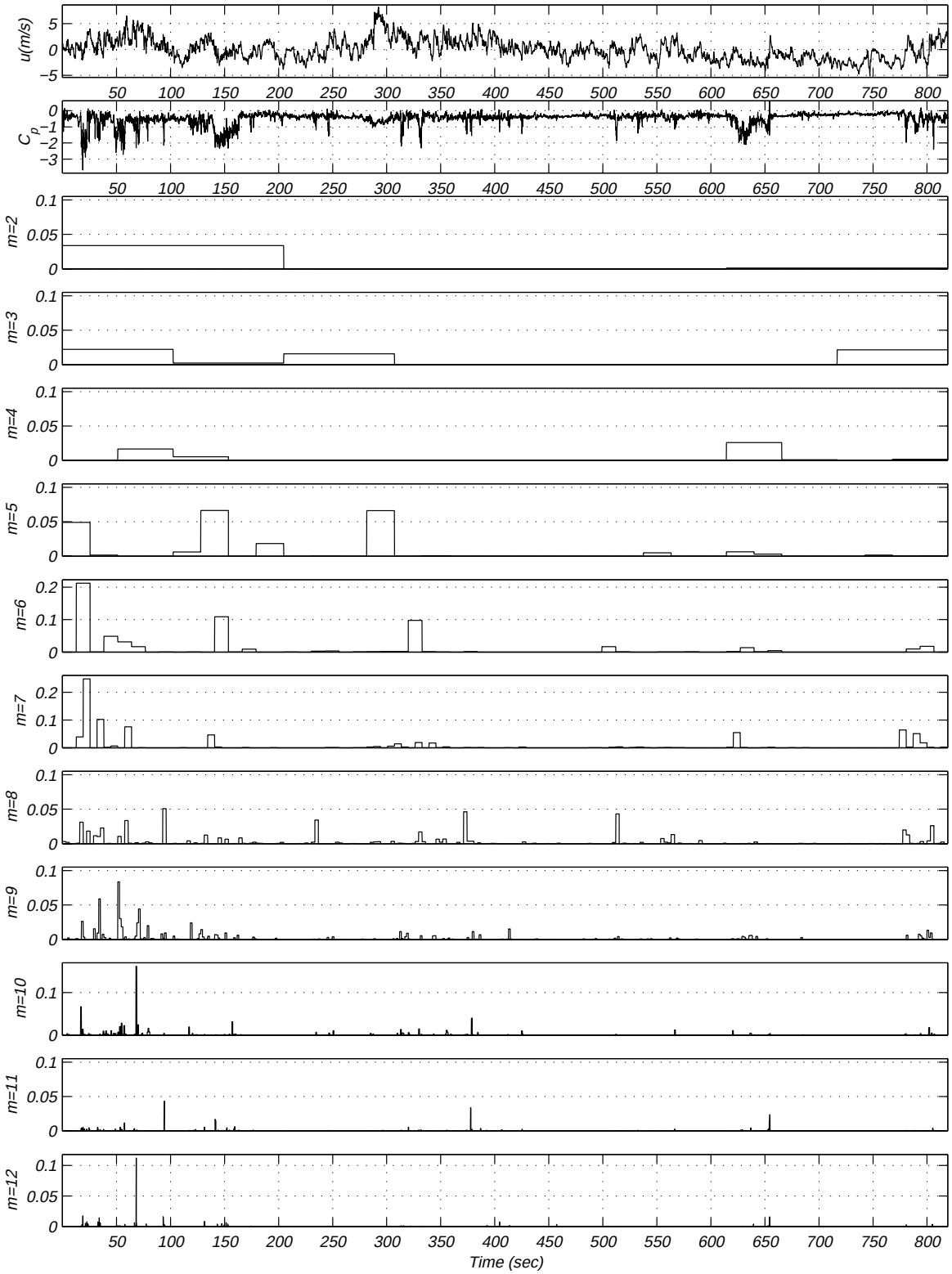

Figure 7.12c: Product of wavelet coefficients of u-component and pressure coefficients at tap # 50509 of record M15N087.

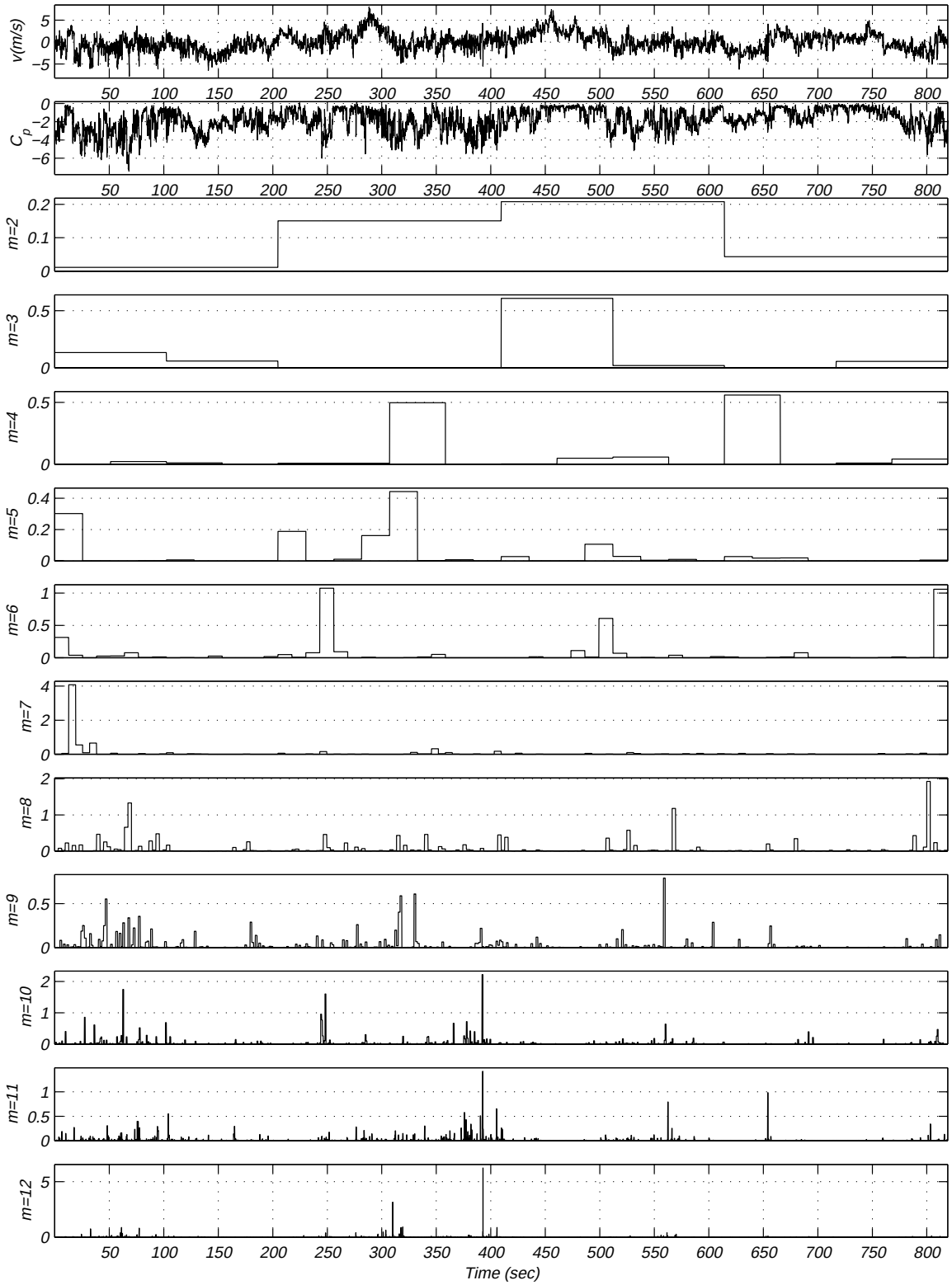

Figure 7.12d: Product of wavelet coefficients of v-component and pressure coefficients at tap # 50205 of record M15N087.

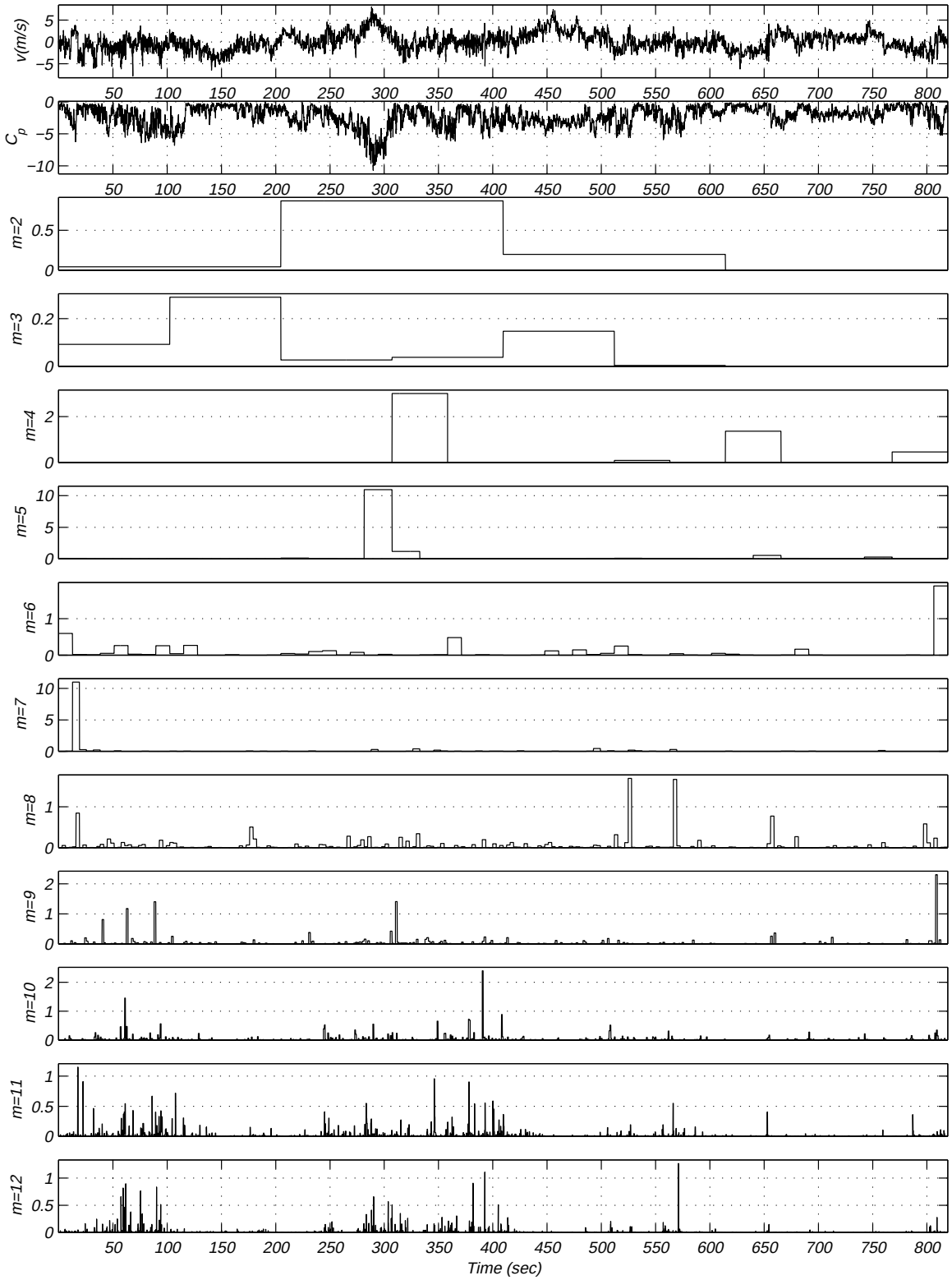

Figure 7.12e: Product of wavelet coefficients of v-component and pressure coefficients at tap # 50501 of record M15N087.

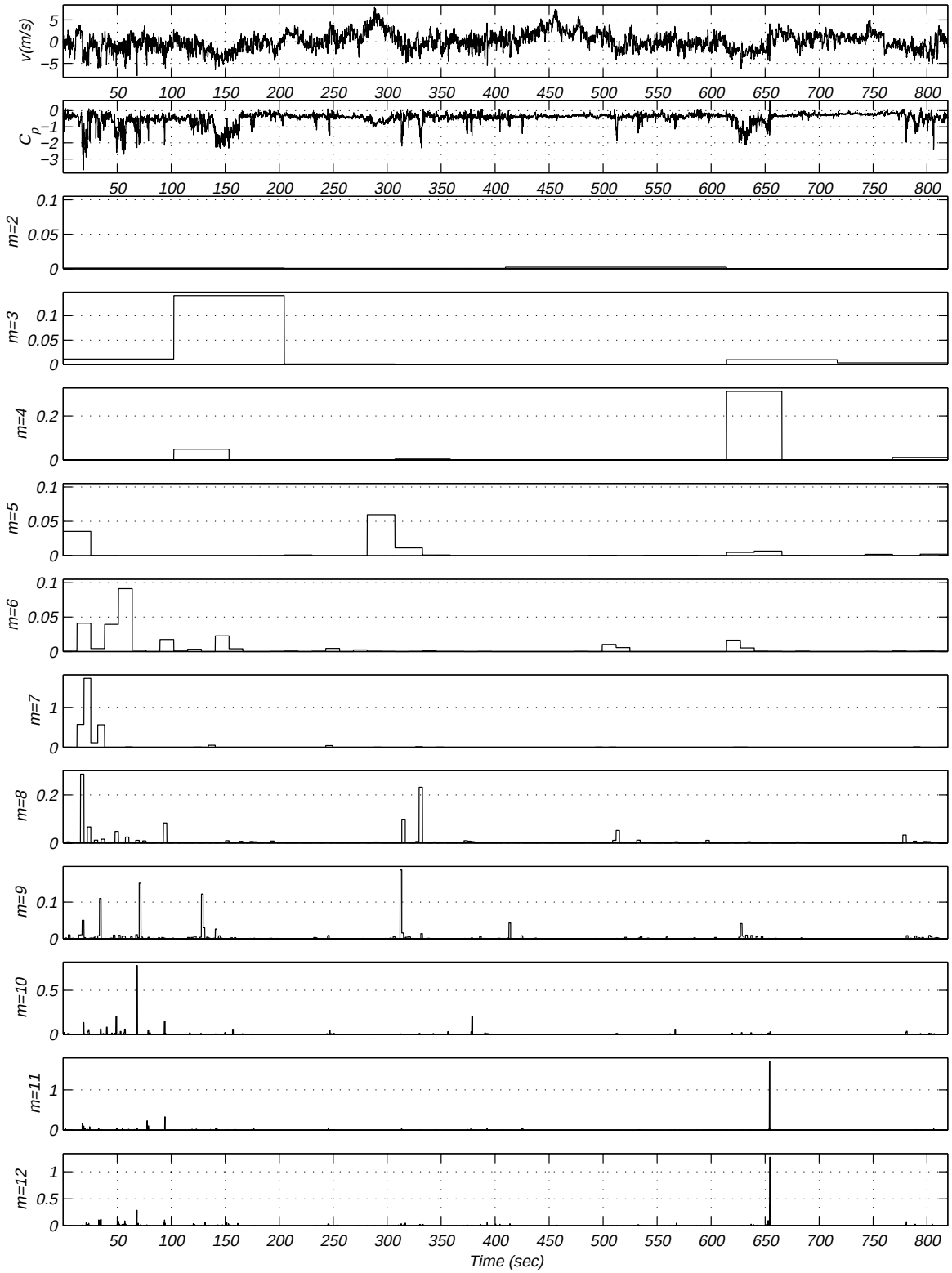

Figure 7.12f: Product of wavelet coefficients of v-component and pressure coefficients at tap # 50509 of record M15N087.

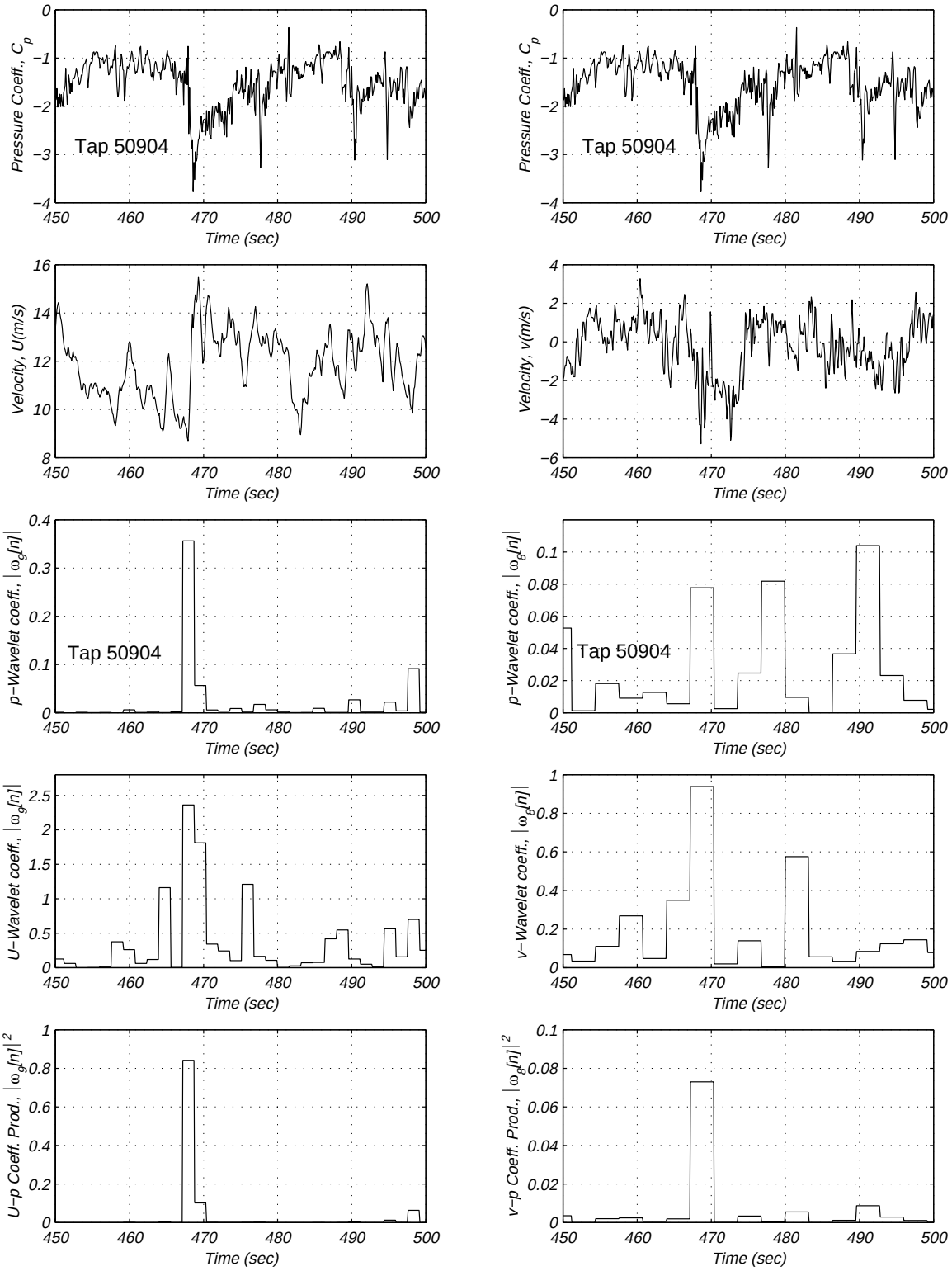

Figure 7.13: Time traces of pressure and velocity components and corresponding wavelet coefficients of record M15N468, tap#50904.

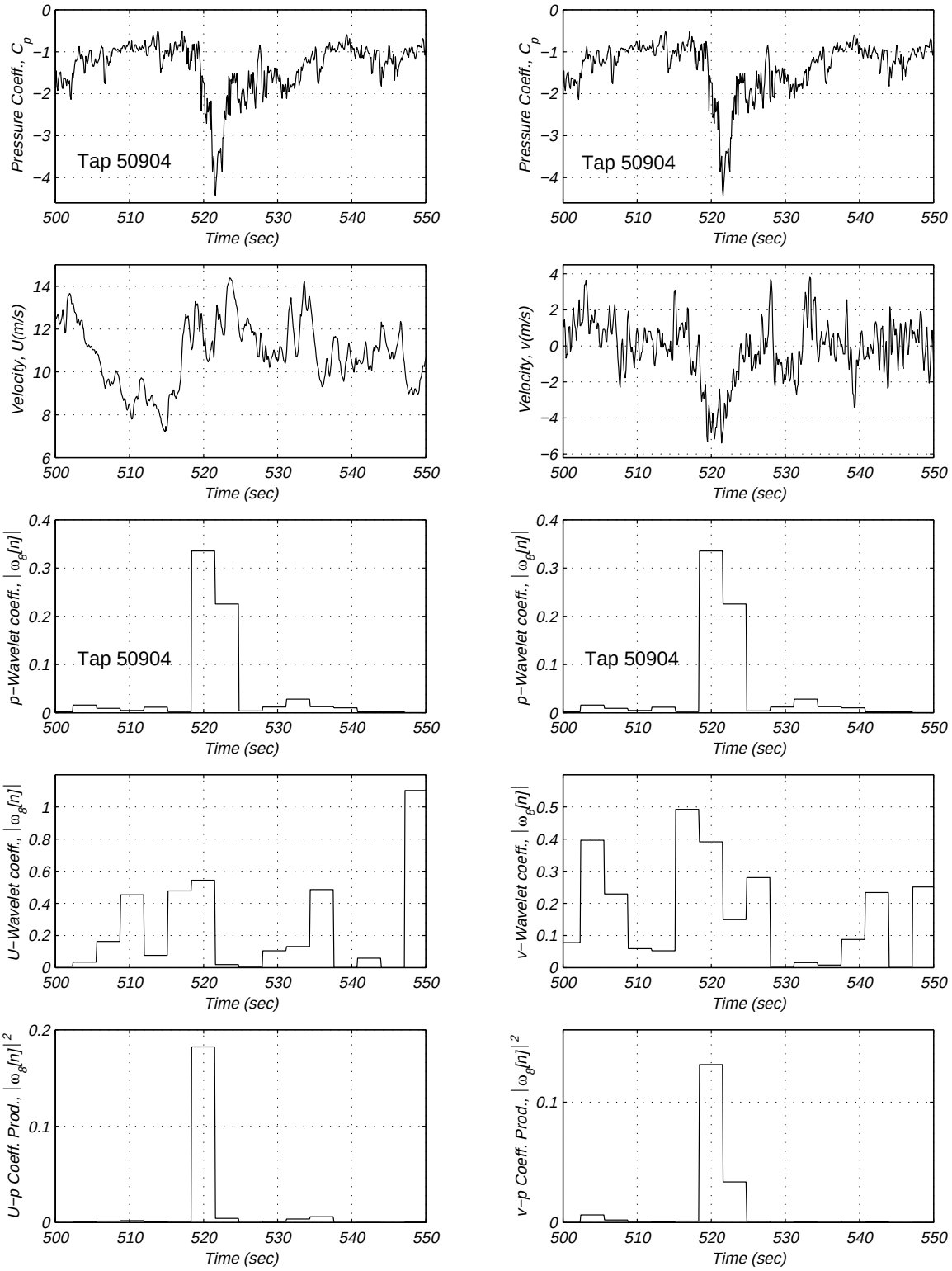

Figure 7.14: Time traces of pressure and velocity components and corresponding wavelet coefficients of record M15N468, tap#50904.

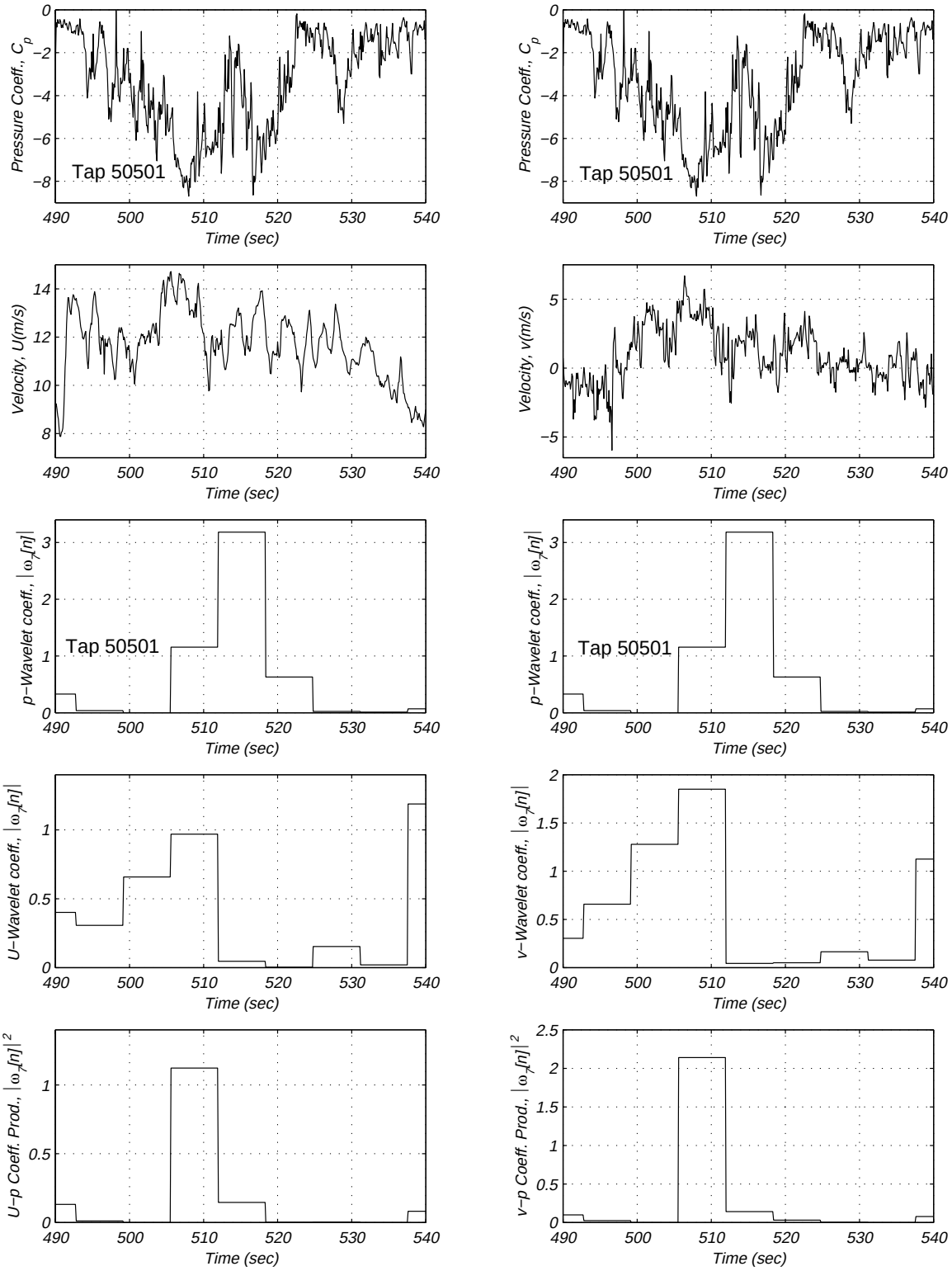

Figure 7.15: Time traces of pressure and velocity components and corresponding wavelet coefficients of record M15N086, tap#50501.

Chapter 8

Conclusions

The ultimate goal of this work is to assist in the mitigation against damage to low-rise structures caused by extreme wind storms. To achieve this goal we decided to (1) characterize turbulence events in the atmospheric surface layer and (2) relate observed negative peak pressure coefficients to certain turbulence events or scales. The results presented in this work show that:

- There are many shortcomings in the current Fourier-domain models and descriptions of atmospheric turbulence and for velocity-pressure relation. Mostly, these shortcomings are due to the fact that temporal information is not preserved.
- There are major discrepancies in the linear and nonlinear velocity-pressure spectral functions, namely admittance functions. Our results using spectral moments, show that these discrepancies exist because the linear coherence and the nonlinear cross-bicoherence between the frequency components of the velocity and pressure components are extremely low.
- Using wavelets, we were able to examine the time-varying characteristics of atmospheric flow and detect energetic events in atmospheric turbulence. We quantified these events by an intermittency factor and proposed that such factor be used in the simulation of the atmospheric boundary layer that aim at reproducing peak pressures.
- Applying wavelet theory, we were able to define pressure peaks that cause extreme wind

loads at a certain scales. We were also able to relate these scales to energetic turbulence scales in the $u-$ and $v-$velocity components. This relation between turbulence scales and low-pressure peaks supports the previous notion on the importance of simulating such turbulence events in wind tunnel experiments.

References

- [1] W.D. Baines, "Effect of velocity distribution on wind loads and flow patterns on Buildings," *Proceeding on the Conference on Wind Effects on Building and Structures*, Teddington, HMSO, 1963, pp.197-223.

- [2] J. C. K. Cheung, J. D. Holmes, W. H. Melbourne, N. Lakshmanan and P. Bowditch, "Pressure on a 1/10 Scale Model of the Texas Tech Building," *Third International Colloquium on Bluff Body Aerodynamics & Applications*, July 28-August 1, 1996, Virginia Tech, Blacksburg, Virginia, pp. A IX 5-A IX 8.

- [3] I. Daubechies, 10 Lectures on Wavelets, 1992, S.I.A.M.

- [4] N. Holscher, "A non-linear approach for the aerodynamic admittance of wind pressures," *Third International Colloquium on Bluff Body Aerodynamics & Applications*, July 28-August 1, 1996, Virginia Tech, Blacksburg, Virginia, pp. A VI 23-A VI 28.

- [5] M. Jensen and N. Frank, "Model-Scale Tests in Turbulent Wind," *Danish Technical Press*, 1965.

- [6] J. C. Kaimal and J. J. Finnigan, Atmospheric Boundary Layer Flows Their Structures and Measurements, Oxford University Press, 1994.

- [7] H. Kawai, "Pressure Fluctuations on Square Prisms-Applicability of Strip and Quasi-Steady Theories," *Journal of Wind Engineering and Industrial Aerodynamics*, Vol. 13, 1983, pp.197-208.

- [8] C. W. Letchford, R. E. Iverson and J. R. McDonald, "The Application of the Quasi-Steady Theory to Full Scale Measurements on the Texas Tech Building," *Journal of Wind Engineering and Industrial Aerodynamics*, Vol 48, 1993, pp. 111-132.

- [9] M. L. Levitan and K. C. Mehta, "Texas Tech field Experiments for wind loads part 1: Building and pressure measuring system," *Journal of Wind Engineering and Industrial Aerodynamics*, Vol. 41-44, 1992, pp.1565-1576.

- [10] M. L. Levitan and K. C. Mehta, "Texas Tech field Experiments for wind loads part 2: Meteorological instrumentation and terrain parameters,"*Journal of Wind Engineering and Industrial Aerodynamics*, Vol. 41-44, 1992, pp.1577-1588

- [11] Y. Meyer, Wavelets: Algorithms and Applications, 1993, S.I.A.M.

- [12] National Weather Service (NWS), " A summary of Natural Hazard Deaths for 1990 in the United States, National Oceanic and Atmospheric Administration, U.S. Dept. of Commerce,",1992, Silver Spring, MD.

- [13] D.E. Newland, An Introduction to Random Vibrations, Spectral and Wavelet Analysis, Third Edition, John Wiley & Sons, Inc., New York, New York, USA, 1993.

- [14] V. A. Sandborn, " Measurements of intermittency of turbulent motion in a boundary layer", *Journal of Fluid Mechanics*, vol. 6, part 2, pp. 221-240, 1959.

- [15] G. Steinmetz, "Andrew's Toll: As Insurance Rates From Hurricane Soar, Higher Rates Loom," *Wall Street Journal*, pp.A1-A3.

- [16] H. Tennekes and J. L. Lumley, A First Course in Turbulence, MIT Press, Cambridge, Massachusetts, 1972.

- [17] G. Thomas, P. P. Sarakar and Mehta, K.C., "Identification of Admittance Functions for Wind Pressures From Full-Scale Measurements,"91CWE, 1995, New Delhi, India.

- [18] H. W. Tieleman, "Model/Full Scale Comparison of Pressure on the Roof of the TTU Experimental Building", *East European Conference On Wind Engineering EECWE'94*, 4-8 July 1994 Warsaw, Poland.

- [19] H.W. Tieleman, "Universality of Velocity Spectra,"*Journal of Wind Engineering and Industrial Aerodynamics*, Vol 56, 1995, pp. 55-69.

- [20] H.W. Tieleman and M.R. Hajj, "Pressure on a Flat Roof - Application of Quasi-Steady Theory," *Proceeding of 10th Conference: Engineering Mechanics*, May 21-24,1995, University of Colorado at Boulder, Boulder, Colorado, pp. 557-559.

- [21] H. W. Tieleman, T. A. Reinhold and M.R. Hajj "Importance of Turbulence for prediction of Surface Pressure on Low-Rise Structures," *Third International Colloquium on Bluff Body Aerodynamics & Applications*, July 28-August 1, 1996, Virginia Tech, Blacksburg, Virginia, pp. A IX 1-A IX 4.

- [22] H. W. Tieleman, M. R. Hajj, and T. A. Reinhold, "The Laboratory Assessment of Surface Pressure Coefficients on Low-Rise Structures: The Effects of the incident flow",*presented at the* 3^{rd} *United Kingdom Conference on wind Engineering*, September 16-18, 1996, Oxford, UK.

- [23] USA Today, "Andrew Punishes Florida," *Engineering News Record.*, p. 8, August 31st, 1992.

(Vita)

Isam Mustafa Janajreh was born on the 14^th of February 1966 in Zarka, Jordan. During his teenage years he worked as a part time auto-mechanics and as carpenter for his family owned construction company. He received his BS in Mechanical Engineering from the Jordan University of Science and Technology in 1988.

After graduation, he worked as a field engineer at the Jordan Ports Corporations. In July 1992, he received a Master of Science in Mechanical Engineering at Virginia Tech with a concentration in Computer Aided Design (CAD). He worked as a system administrator for a Unix/Dos based operating system in the Materials Engineering department at Virginia Tech from July 1992 until March 1993. He then joined the Engineering Science and Mechanics department (ESM) at Virginia Tech in January 1993 and received an MS (with concentration in Fluid Mechanics) in June 1994. In January 1998 he received a Ph.D. in ESM with a concentration in Fluid-Solid interactions. Currently, he is serving as a visiting assistant professor in the ESM department and the Department of Mathematics.